Aerodynamic Design and Wind Tunnel Testing of Small Horizontal-axis Wind Turbines for Multirotor Configuration

A Thesis Submitted in Partial Fulfilment of the Requirement

for the Degree of

DOCTOR IN PHILOSOPHY

By

Ojing Siram (166151101)

Under the Guidance of

Prof. Niranjan Sahoo

School of Energy Science and Engineering

Indian Institute of Technology Guwahati

Guwahati-781039, India

May 2023

Dedicated to my parents…

Smti. Yagom Siram

And

Late. Nb. Sub. Takuram Siram
(31st Assam Rifle)

INDIAN INSTITUTE OF TECHNOLOGY GUWAHATI

CANDIDATE'S DECLARATION

I, **Ojing Siram**, hereby declare that the work presented in the thesis, entitled **"Aerodynamic Design and Wind Tunnel Testing of Small Horizontal-axis Wind Turbine for Multirotor Configurations"** in partial fulfilment of the requirements for the award of the Degree of **Doctor of Philosophy** and submitted to the School of Energy Science and Engineering, Indian Institute of Technology Guwahati is an authentic record of my research work carried out by me under the supervision of **Prof. Niranjan Sahoo**.

The matter presented in this thesis has not been submitted by me for the award of any other degree of this Institute or any other University/Institute/Organisation.

OJING SIRAM
Signature of Candidate

This is to certify that the above statement made by the candidate is correct to the best of my knowledge.

PROF. NIRANJAN SAHOO
Supervisor
Department of Mechanical Engineering
Indian Institute of Technology Guwahati

ACKNOWLEDGMENTS

First and foremost, I would like to express my deepest gratitude to my supervisor, **Prof. Niranjan Sahoo**, for his invaluable guidance, encouragement, support, and cooperation throughout my research work. I would also like to thank my Doctoral Committee members, **Prof. U. K. Saha**, **Prof. Vinayak Kulkarni**, and **Dr. Pankaj Kalita**, for continuously monitoring the progress of my work and providing valuable suggestions and encouragement. I would like to offer my special thanks to **Prof. U. K. Saha** for sharing his deep knowledge and techniques regarding article preparation and presentation. I would also like to thank the thesis reviewers, **Prof. A M Pradeep**, IIT Bombay, and **Prof. Rakesh Mishra**, University of Huddersfield, UK. Their valuable comments and suggestions have greatly helped me to Improve the quality of my Ph.D. Thesis.

I want to thank the **Department of Science and Technology-Govt. of India**, and **Technology Innovation and Development Foundation-IITG**, for the financial support. I am also thankful to the **School of Energy Science and Engineering** and the **Department of Mechanical Engineering, Indian Institute of Technology Guwahati,** for providing the necessary assistantship and infrastructure.

I thank my Ph.D. colleagues, **Dr. Mrinal Bhowmik**, **Dr. Anil K. Raout**, **Dr. Muniraja Tippa**, **Dr. Saibal Kanchan**, and **Dr. Samar Das**; they have given me much-needed encouragement. I would also like to acknowledge my lab mates: **Anand Verma, Umang Rathod, Abhishek Kamal, Bastav Borah, Kabita Naik, Ravi Kumar, Abhinav Rawat, Neha Kesharwani, Suchita Barhate, and Rishi Purohit**. They were my first family at IITG.

My Ph.D. life was not an easy journey, and I had been through lots of stress and adversity. During this period, I found much-needed stability and peace through yoga, music, and wildlife photography. Therefore, I thank **Isha Yoga**, I thank my Violin Guru, **Smt. Savita Borah**, and I thank **Shri. Dhiren Huzuri** for all those unplanned wildlife explorations and adventures.

My deepest gratitude goes to my family for their unwavering love and support throughout my life. I am always thankful to my mother, **Smt. Yagom Siram** for her immeasurable sacrifices and blessings. My elder sister, **Ms. Onam Siram**, and my younger brothers, **Kabang Siram** and **Martin Siram**, were always there with their encouragement and care. They always soften the life difficulties for me, and I owe all my achievements, including this, to them. It is due to all these individuals and unnamed Samaritans who had helped and pushed me to accomplish this uphill task.

Lastly, I would like to dedicate this thesis to my father, **Late Shri. Takuram Siram**, who always believed in my ability to be successful in the academic arena. You are gone, but your belief in me has made this difficult journey possible.

Ojing Siram

Abstract

The utility of small wind turbines (SWTs) covering horizontal and vertical-axis types as off-grid, standalone, and decentralized energy supplement systems has gained market attention. Such turbines primarily operate at low Reynolds number (*Re*) and low tip speed ratio (λ) conditions. Under such circumstances, the design, development, and testing of SWTs have become a tedious task, mainly due to the lack of precise aerodynamic knowledge of SWT at low *Re* and λ. With this aspect, the present investigation explores the applicability of small horizontal-axis wind turbines (SHAWTs) to be employed as a power-generating source in places where energy demand is minimal or as a potential off-grid power source.

This study explores the design and testing of SHAWT at low λ ($0.5 < \lambda < 6$) and low Re ($0.3\times10^5 \leq Re \leq 3\times10^5$) conditions. The SHAWT rotor blades were designed using the blade element momentum theory (BEMT) and fabricated using the 3D printer. The rotors' performance was tested in the wind tunnel using the rotary torque sensor (RTS). Based on the literature review, airfoil E216 (M1), SG6043 (M2), NACA63415(M3), and NACA0012 (M0) have been chosen for developing the model rotors. From BEMT analysis, the maximum coefficient of performance (C_{pmax}) of M1, M2, M3, and M0 at λ = 2.5 is found to be around 0.37, 0.36, 0.34, and 0.35, respectively, which is about 62.4%, 60.7%, 57.33%, and 59.02% of Betz's limit. The same developed rotors were tested in the wind tunnel at the designed pitch angle ($\theta_{p,design}$), and the C_{pmax} of 0.34, 0.30, 0.28, and 0.16 were obtained for M1, M2, M3, and M0, respectively. The anomaly observed for M0 could be attributed to relatively higher solidity and lesser aerodynamic characteristics at low *Re*. The complexity of the BEMT rotor necessitates the development of a non-BEMT rotor, which in the present study are straight and linear tapered (SLT rotors). The SLT rotors having the root- to-tip chord (C_r/C_t) of 1:1 shows favourable result.

Furthermore, an in-depth investigation of wake propagation and interaction with the nearby turbines has been carried out; this study intends to explore the applicability of model rotors as a multirotor system or in a small wind farm. In this regard, a dedicated downstream (x/R) wake study has been carried out using the constant temperature hot wire anemometry (CTHWA) and stereo particle image velocimetry (PIV). The wake flow study suggests that within the near wake regime (x/R < 6), the velocity deficit profile is marked by the formation of a W-shape. Furthermore, close to x/R = 12, the downstream flow recovers by about ~70% of upstream velocity. The time-resolve and time-averaged streamwise PIV assessment reveal Gaussian-like (skew) distribution and the presence of two opposite crests, marking the flow movement. The high-fidelity PIV data were then used to develop an ANN-based wake model. It is observed that experimental and ANN-based models can produce much better and more reliable results than their analytical counterparts.

TABLE OF CONTENTS

LIST OF FIGURES

LIST OF TABLES

NOMENCLATURE

Latin Symbols		Greeks Symbols	
a	Axial Induction Factor	λ	Tip Speed Ratio
a'	Tangential Induction Factor	$\emptyset$	Relative Angle
c	Chord Length (m)	α	Angle of Attack (Degree)
C_l	Coefficient Of Lift	ω	Angular Velocity
C_D	Coefficient of Drag	ρ	Density of Fluid (kg/m^3)
C_p	Coefficient of Power	μ	Dynamic Viscosity (Ns/m^2)
C_T	Coefficient of Thrust	β	Pitch Angle (Degree)
D	Rotor Diameter (M)	σ	Solidity of Turbine
F	Prandtl Constant	η_{WF}	Wind Farm Efficiency
F_D	Drag Force (N)		**Acronyms**
F_L	Lift Force (N)	ABL	Atmospheric Boundary Layer
F_T	Tangential force (N)	ANN	Articicial Neural Network
F_N	Normal Force/ Thrust Force (N)	BEMT	Blade Element Momentum Theory
g	Acceleration Due To Gravity (m/s^2)	FOV	Field of View
H_{hb}	Hub Height (m)	HAWT	Horizontal Axis Wind Turbine
N_B	Number of Blades	CTHWA	Constant Temp. Hot- Wire Anemometer
P	Power Output (W)	ML	Machine Learning
P_{max}	Maximum Power Output (W)	MNRE	Ministry of New and Renewable Energy
r	Radial Distance Form Hub (m)	NIWE	National Institute of Wind Energy
R	Rotor Radius (m)	PIV	Particle Image Velocimetry
T	Time Period (sec)	RE	Renewable Energy
V_x	x-Component Velocity (m/s)	RTS	Rotary Torque Sensor
u'	x-Component Velocity Fluctuation (m/s)	SLT	Straight and Linearly Tapered
$V_{x,avg}$	Mean Velocity Along x-axis (m/s)	SSWT	Small Scale Wind Turbine
V_y	y-Component Velocity (m/s)	SHAWT	Small Horizontal-axis Wind Turbine
v'	y-Component Velocity Fluctuation (m/s)	SWT	Small Wind Turbine
$V_{y.avg}$	Mean Velocity Along y-axis (m/s)	TSR	Tip Speed Ratio
V_z	y-Component Velocity (m/s)	VAWT	Vertical Axis Wind Turbine
U	Inlet Wind Velocity (m/s)	WPD	Wind Power Density

CHAPTER 1
INTRODUCTION

1.1 Motivation

The world has been witnessing a gradual increase in renewable energy share as a supplement for fossil fuels in the past two decades. This has opened the scope of research and development activities in renewable energy sectors. Among the various forms of renewable energy systems, wind energy has presented itself as a promising candidate, with a global installed capacity of about 743 GW as of 2021, and with a compounded annual growth rate (CAGR) of about 20% (IEA, 2021). This has come at the cost of decade-long research activities by the wind energy research communities, and to date, much of the research has been intended for the development of large wind turbines (LWTs). The contribution from LWT is undeniably admirable, as such turbines are capable of producing power in megawatt (MW) and gigawatt (GW) capacity having the rotor radius (R) as large as 80 - 100 m (Esteban et al. 2015; Diza and Soares, 2020). No wonder the prospect of LWT is promising, considering the population growth and energy consumption. However, for minimal energy demand, such as for off-grid individual households, rural communities, small-scale farms, and others, the implication of LWTs may not be viable and economical. Under such circumstances, the need for effective, efficient, and economical small wind turbines (SWTs) comes into the picture. These turbines, as such, are also best suited for urban/suburban regions.

During 2013-2018, the worldwide installation of SWTs had increased by 51.1%, and towards the end of 2020, SWTs market value reached about 161.9 million dollars, out of which China and the United States hold the significant market share (Orrell et al., 2021). Thus one can agree that the future of SWT is immense. From an economic point of view, the cost of installation, operation, maintenance, and repair of SWT is relatively lesser than LWT, making it one of the most reliable and affordable standalone or off-grid renewable energy systems. Such turbines primarily operate at low Reynolds number (*Re*) and low tip speed ratio (λ) conditions. Under such circumstances, the design, development, and testing of SWTs become a tedious task, mainly due to the lack of precise aerodynamic knowledge of SWT. This brings us to one of the primary objectives of the present study, to design and thoroughly investigate the aerodynamic behavior of SWT; small horizontal-axis wind turbine (SHAWT), in particular, as a standalone or integrated system. The integrated SWT system could be a configuration/arrangement of multiple turbines in the form of small wind farm or it could be a standalone system but with multiple rotors (Liu et al. 2019). A typical illustration of multirotor configurations is shown in Fig. 1.1.

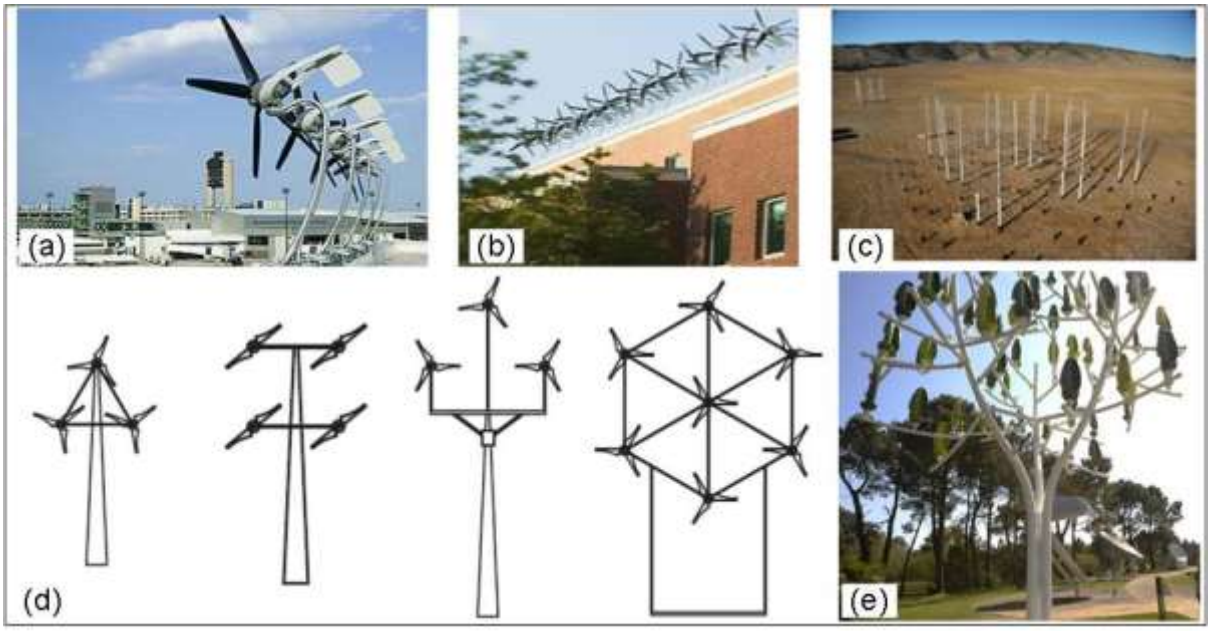

Fig. 1.1. Illustration of multirotor configuration (a) array of SWTs near terminal, (b) array of SWTs in the rooftop, (c) cluster of SWTs in open field, (d) multirotor turbine, and (d) tree wind turbine (Reproduced with permission from Casini et al. 2016; Liu et al. 2019; Dilimulati et al. 2018)

1.2 Classification of Wind Turbines

Broadly, the wind turbines are divided into HAWT (Horizontal-axis wind turbine) and VAWT (Vertical-axis wind turbine), which is mainly based on the perspective of their axis of rotation with respect to the wind direction (Burton et al. 2007). Such turbines are further classified on the basis of rotor size, hub heights, capacity, reliability and efficiency of the wind turbines, and siting of wind turbines. A typical illustration of turbine classification on the basis of hub height, rotor diameter, and capacity is shown in Fig. 1.2; some more detail is presented in Table 1.1. The SWTs, which is the main area of interest for the present study can be further classified into small HAWT and small VAWT. For the present investigation, small HAWT has been considered due to its relatively higher performance then VAWT (Tummala et al. 2016). The small HAWTs can be further categorized into small-scale, mini-scale, and micro-scale HAWTs. On the other hand, small VAWTs can be further categorized into Savonius, Darrieus, or hybrid rotors. In comparison to HAWTs, the VAWTs have a lesser power coefficient (C_p) (Jain and Saha, 2019; Treuren 2015); however, it is possible to enhance their performance by incorporating specific pitch control mechanisms, multi-rotor system, and various augmentation techniques (Sun et al. 2012; Zhao et al. 2019; Neagoe et al. 2020). The augmentation technique is a method of modifying the model's geometry without altering the rotor/airfoil body, basically to enhance the rotor performance. Further details on SWTs has been presented in the literature review section (Chapter 2).

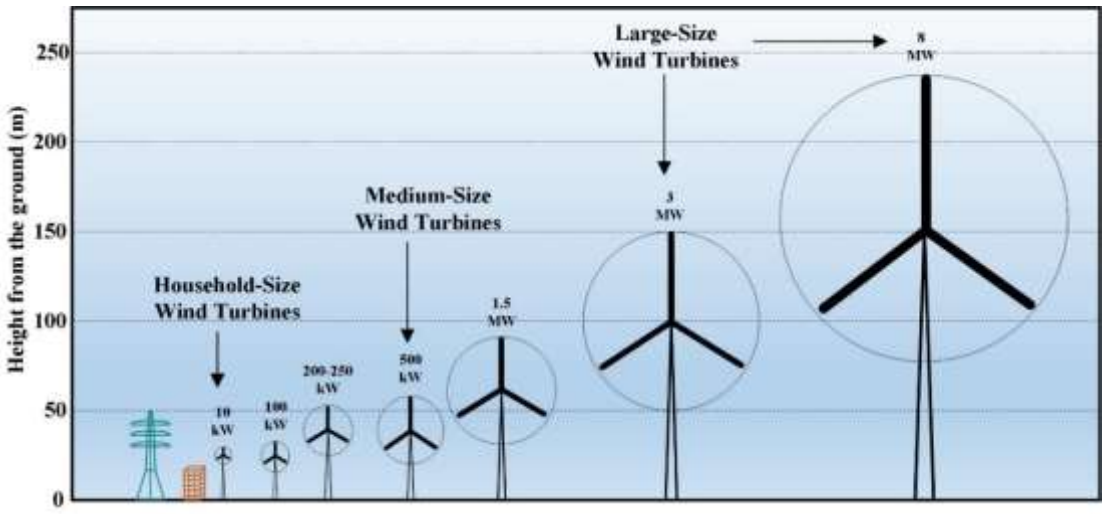

Fig. 1.2. Classification of wind turbines based on rotor diameter (Tummala et al.2016)

Table 1.1 Classification of wind turbines on the basis of size and capacity

Type of Turbine	Model Examples	Rotor Dia. (m)	Standard Power Output (kW)	Wind Condition	Application
Large commercial wind turbines	Vestas V164-8 MW, Siemen SWT-8.0-154, Siemens SWT-2.3-101 Nordex N80, N90, N100, V120-2.0 MW, etc.	≥ 50	1000 – 8000	Very high	Large scale production, Offshore Wind farm, Onshore windfarm
Medium Commercial wind turbines	Nibe A and Nibe BDK, Mod-OA US, Tvind DK 54 etc.	20 - 50	100 - 1000	High	Mini wind farm
Small commercial wind turbines	MG4520, Small HAWT, American wind energy association (AWEA), etc.	10 - 20	25 - 100	Good	Residential Power
Domestic Scale wind turbines	Savonius Type, Darrieus Type, twisted Savonius, small HAWT, QR5 Gorlov type VAWT etc.	3 – 10	1.4 – 16	Moderate	Hybrid System
Mini Scale wind turbines	Bornay 600, TAOS 600, AC 240, Air-x marine etc.	1.25 – 3	0.25 – 1.4	Low	Building Integrated rooftop
Micro Scale wind turbines	NE-100 S, NE-200S, NE-300S, µF500m, Superwind350, Rutland 913 etc.	0.50 – 1.25	0.004 – 0.25	Very Low	Low power application

1.3 Changing Landscape of Global Renewable Energy

At the end of 2019, the world has produced more than 162000 TWh or equivalent to about 14 GToe through various sources, out of which oil, natural gas, and coal have a significant contribution in terms of generation potential (Ritchie and Roser, 2020; IEA, 2021). However, a decrease in energy production is witnessed post-COVID-19 detection and subsequent restriction, particularly from fossil fuels. As per as consumption is concerned, as depicted in Fig. 1.3(a), about 31% of the world's total energy consumption comes from oil, followed by coal (27.3%), natural

gas (24.7%), hydro (6.9%), nuclear (4.4%), and RE (5.65%) (Kowalskia et al., 2019; IEA, 2021). Fossil fuels being limited on earth, opting for RE is the ultimate necessity, and so far, it is already making significant progress. About 5.6% of energy share is contributed through RE in consumption. Moreover, in the past few decades, a significant amount of RE installation has been made, with about 2500 GW of power produced through various RE sources as of 2020, as shown in Fig. 1.3b(b). As per the IEA, the major countries producing electricity through RE are Europe, Asia Pacific, Central and South America, and North America (IEA, 2021).

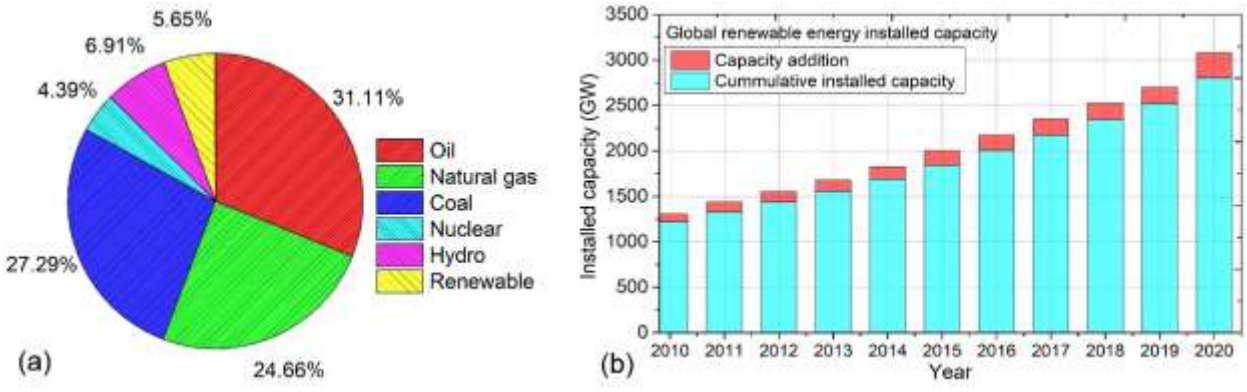

Fig. 1.3. Global energy consumption by fuel as of 2020, and (b) Progress in renewable energy installation in the world (IRENA 2020; IEA, 2021; Siram et al. 2022a).

Globally, the total installed wind power capacity stood around 743 GW, with about 90 GW established in 2020-2021 (Fig. 1.4a). A 20% CAGR in installed capacity has been recorded since 2000, suggesting a positive node towards wind energy growth (IEA, 2021). Among the top 10 wind power countries, China has the highest wind energy-producing country, with an installed capacity of about 236 GW at the end of December 2019, which is about 36.3% of wind power among other global wind power countries (Fig. 1.4b). It is followed by the USA, Germany, India, Spain, and the UK, which share about 16.2%, 9.4%, 5.8%, 4.0%, and 3.6%, respectively, by the end of 2020 (Ritchie and Roser, 2020; IEA, 2021). India, the fourth-largest wind power producer, had a total installed capacity of about 35.61 GW at the end of March 2019 (IEA, 2021; Irfan et al., 2019). Furthermore, demographically, it is noted that asia-pacific has the high consumption (Fig. 1.5a), at the same time share maximum RE generation (Fig. 1.5b). There are two modes of wind power generation: onshore wind farms (inland) and offshore wind farms (sea/coastal regions). A wind farm is an array or a cluster of multiple turbines that is often employed for substantial energy extraction. One of the largest inland wind farms is the 20 GW Gansu wind farm, which is located in desert areas near Joaquin, China (IEA, 2021). Onshore wind farms face many challenges like land usage, non-uniform wind field, the noise produced by large wind turbines, rugged/complex terrain, and other logistical issues (Alhmoud and Wang, 2018). In contrast, the offshore wind farm can produce much higher energy than onshore wind farms because of relatively uniform and constant wind flow conditions. The knowledge gained from

various offshore projects suggests a higher initial expenditure than onshore wind power generation (Schwanitz and Wierling, 2016; Li et al., 2018).

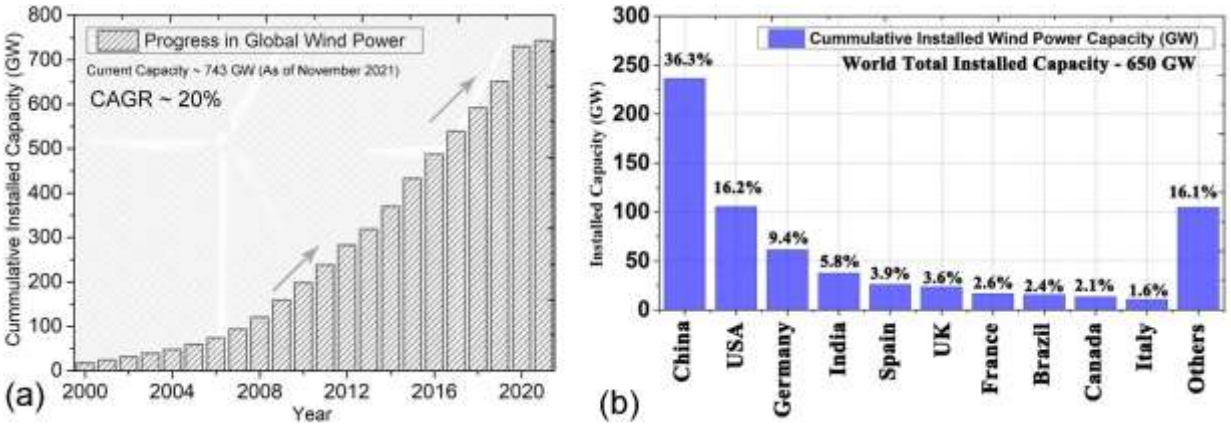

Fig. 1.4 (a) Progress in global wind power installation since past two decades, and (b) share of total installed wind power capacity of the world as of 2020 (IEA, 2021; Siram et al. 2022a)

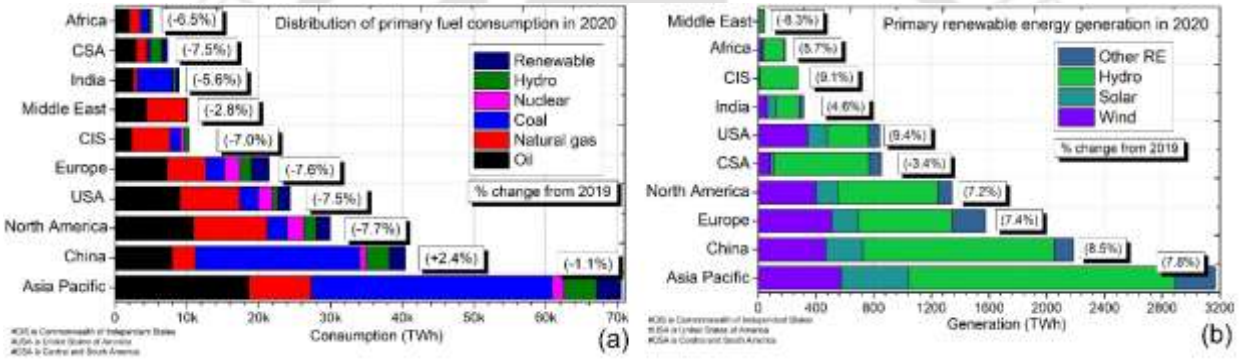

Fig. 1.5 (a) Share of primary fuel consumption, and (b) share of primary renewable energy generation, as of 2020 (IEA, 2021; Siram et al. 2022a))

1.4 Changing Landscape of India's Renewable Energy and Contribution of Wind Energy.

A country of billion people, India has witnessed a sharp increase in its economic activities in the past few decades, fulfilling the needs of its ever-growing population, which has come at the expense of a considerable sum of energy and carbon emissions. With rising global concern on climate change and India's commitment to reducing carbon emissions, the country is gradually shifting towards harnessing energy through renewable energy (RE). In recent times, electricity generation via RE, including large hydro, covers about 20%. The road towards RE comes with many challenges, especially when most of its economic activities heavily rely on conventional energy sources. Being the most contributor among all the RE in India, wind energy has a significant role. Being the second-most populous country globally (Roser, 2019; Kober et al., 2020), India is the third-largest in terms of energy production and consumption, with about 2061TWh/year and 1547 GWh/year, respectively, through all possible means (IEA, 2019). The distribution of energy sources across the country varies significantly, partly due to the demand

and supply scenario. Through Fig. 1.6, it can be observed that most of India's major power generating plants are localized in the western and Southern zone, having a combined share of about 63% (NLDC, 2018-19; CEA- LGBR, 2018-20). As of 31 March 2020, India's cumulative installed power capacity is about 370 GW, out of which RE sources share about 23.39% (87 GW). The share of wind and solar power installed is about 38 GW (43%) and 35 GW (40%), respectively (Fig. 1.7). And it is expected that a major share of wind and solar will come from large wind farms and large solar parks (Chowdhury et al. 2022).

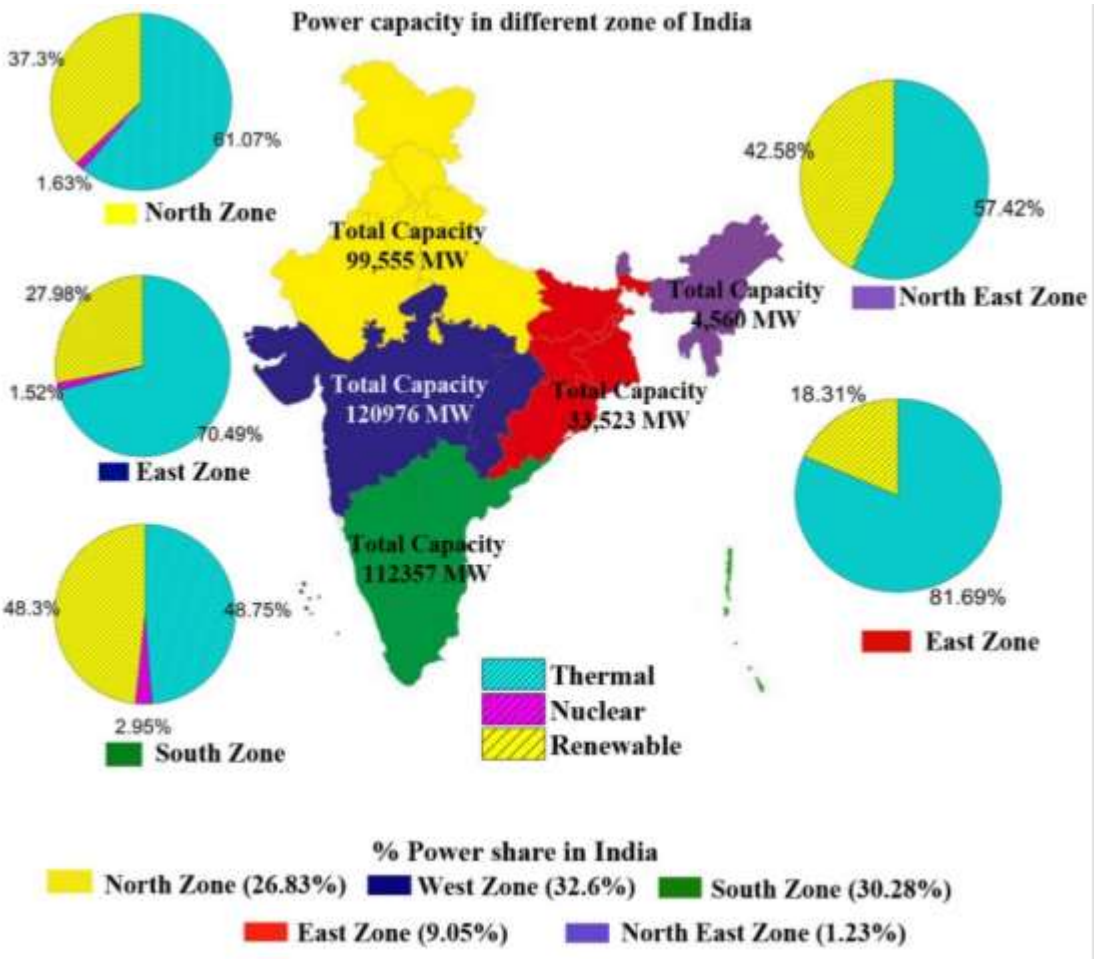

Fig. 1.6. Power share by different zones of Indian states as of March 2020 (Siram et al. 2022a).

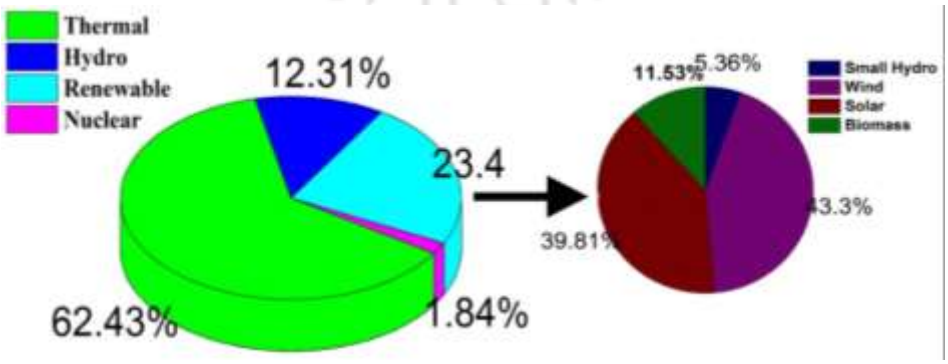

Fig. 1.7. Share of energy production in India as of 31 march 2020 (Siram et al. 2022a)).

The National Institute of Wind Energy (NIWE) has commissioned 50 m, 80 m, 100 m, and 120 m meteorological masts to acquire reliable wind resource data across the country. A typical wind power potential at 100 m above sea level (agl) is shown in Fig. 1.8 (MNRE, 2019-20). The major potential regions for wind power generation are the cost of Gujarat, Western India. Although the assessment shows a promising capacity utility factor (CUF) of more than 28% in the Himalayan range, the region's complex terrain makes installing large wind turbines difficult; however, in such places, the application of SWTs will be promising. Furthermore, the wind power potential increases with altitude; a typical potential wind flow layout at 120 m agl is shown in Fig. 1.7(a). The predicted data presented in Figs. 1.8(a) through 1.8(d) rely on numerous meteorological masts. Thus, India has installed more than 850 masts across the states at different height ranging from 20 m to 120 m agl. India has witnessed a gradual increase in wind power installation over the past few decades with an average annual addition of about 2.2 GW, as depicted in Fig. 1.9. The total installation is over 37.7 GW at the end of March 2020, having over 3500 WTs of all categories (NIWE, 2020-2021). In the fiscal year 2019-2020, about 2050 MW of installation was made compared to 1570 MW in 2018-2019, with a growth rate of 5.7 % (Fig. 1.9). With this pace, it is expected that India's wind industry will meet its 60 GW target by 2023.

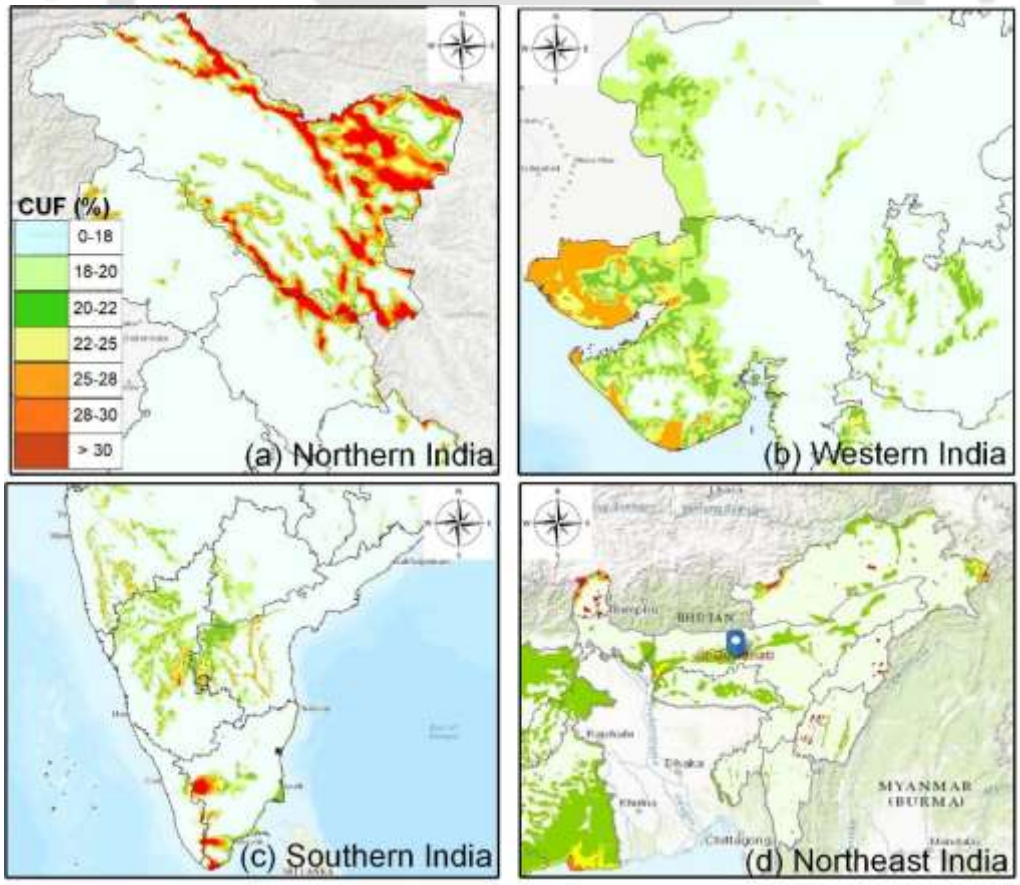

Fig. 1.8. Wind resource potential at 100 m agl across (a) northern; (b) western; (c) southern; and (d) northeastern part of India (Siram et al. 2022a)).

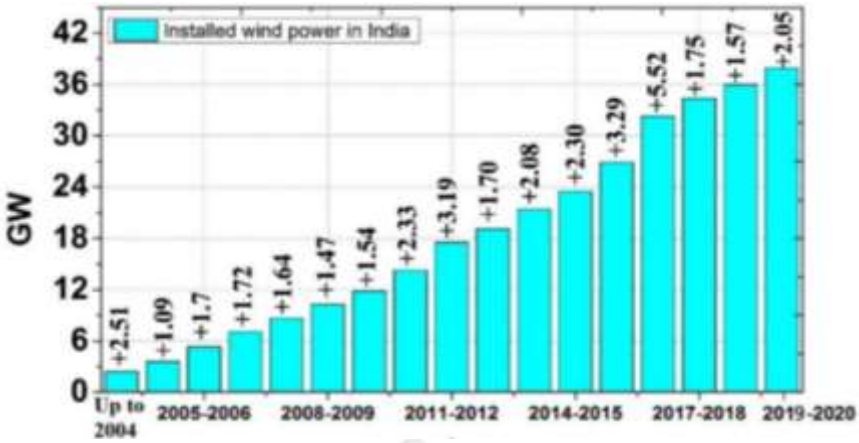

Fig. 1.9. Progress in wind power installation in India since 2004-2020 (Siram et al. 2022a))

1.5 Research Objectives and Road Map

Inspired by the concept of multirotor system, consisting of SWTs (Fig. 1). The present work is primarily focused on the design and development of small horizontal-axis wind turbine (SHAWT) for low Reynold number (Re) and low tip speed ratio (λ) conditions. To achieve this goal, set of design, development, and testing proposition were laid out. The key objectives of the present research work have been mentioned below, and the research road map is shown in Fig. 1.10.

- Design and Development of SHAWTs.
- Testing of Developed SHAWTs Under Low λ Conditions.
- Study on SHAWT Wake Propagation Under Low λ Conditions.
- Study on Implication of Data-Driven Wake Modeling and Estimation.

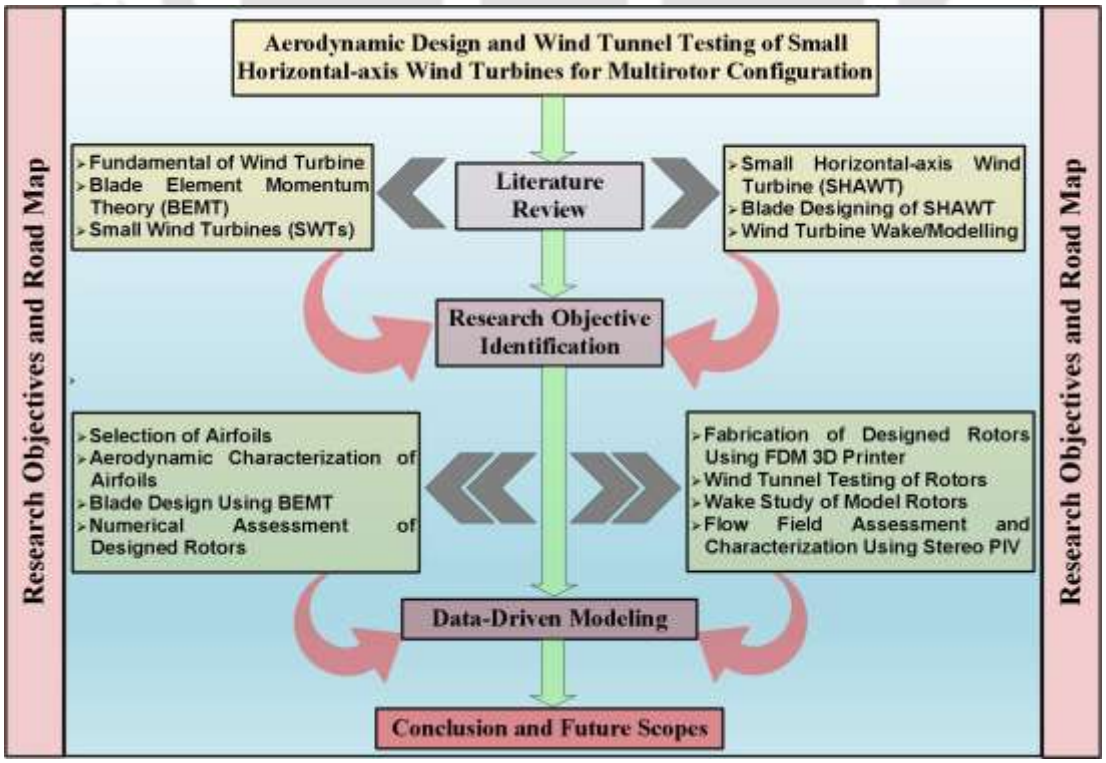

Fig. 1.10. Illustration of research objectives and road map

The information obtained from this research can be potentially employed in the design of small horizontal-axis wind turbines, which then can be used in the design and modeling of multirotor configurations or small wind turbine integrated systems. A pictorial depiction of the research objectives and road map is highlighted in Fig. 1.9, also illustrates some of the essential research considerations to achieve the objectives. Different variations are also discussed in short and will be taken care of at proper length in the upcoming chapter.

1.6 Organization of the Thesis

The Thesis has been organized into 10 chapters and several subsections to address the objectives of the present study. A brief highlight on the global energy scenario and the changing landscape of renewable energy in India has been addressed in Chapter 1, this chapter provides a broader outlook on the research objective and road map. Chapter 2 presents the fundamental theories of the wind turbine and its related aerodynamic concepts, which will serve as the background for the subsequent literature reviews. In chapter 2, the last five subsections present the core literature review of the present study. After every literature review, a brief summary of the review has been presented. Chapter 3 presents the experimental setup and methodology adopted to carry out the research objectives. Chapter 4 to Chapter 9 presents the result and discussion of the experimental and numerical work carried out as per the research objective highlighted in chapter 1. And finally, Chapter 10 summarizes the major outcome and conclusion of this thesis, and also highlight the future scopes and opportunities. Apart from the major content presented in chapters, an Appendix section has also been added that includes some mathematical formulations, governing parameters and constants, and uncertainty analysis formulation.

CHAPTER 2
THEORY AND LITERATURE REVIEW

2.1 Wind Turbine Aerodynamics

A wind Turbine is a power generating system that can extract the kinetic energy of wind and convert it to mechanical energy, thereby, with the help of a generator, to electrical energy. The wind turbines can broadly be divided into lift and drag-based machines based on the direction of the wind and force acting on the blade. Fundamentally, the wind turbine operation relies on its shape and aerodynamic behavior. The HAWTs are mainly lift-based; whereas the VAWTs are mostly drag-based, and the combination of both lift and drag has an important role in providing the initial torque (McTavish et al. 2013; Wood, 2015). Thus, it is important to understand the fundamental aspects of wind turbine, prior to the design and development of wind powered system.

2.1.1 Calculation of Energy Available in the Wind

Fundamentally, there are three major factors that determine the power output from a wind energy system. These are the wind speed, swept area of the rotor, and overall conversion efficiency of the rotor, transmission system and generator. The energy available in the wind is equal to the kinetic energy of the wind, and the wind power (P_a) available for a rotor can be expressed as per Eq. (2.1).

$$P_a = \frac{1}{2}\rho_f A U_\infty^3 \tag{2.1}$$

Where, ρ_f is the fluid density, A is the swept area of the rotor, and U_∞ is the freestream velocity. The above equation shows that the wind power varies with the cube of the wind velocity, considering that the density is constant. However, a system cannot totally convert the available power into useful power because of the losses and from the fact that one cannot reduce the downstream wind velocity to zero, otherwise there would be no flow through the turbine which is the main criteria of the Betz limit. The analogy of Betz limit can be obtained from the actuator disc model (Fig. 2.1) as mentioned below:

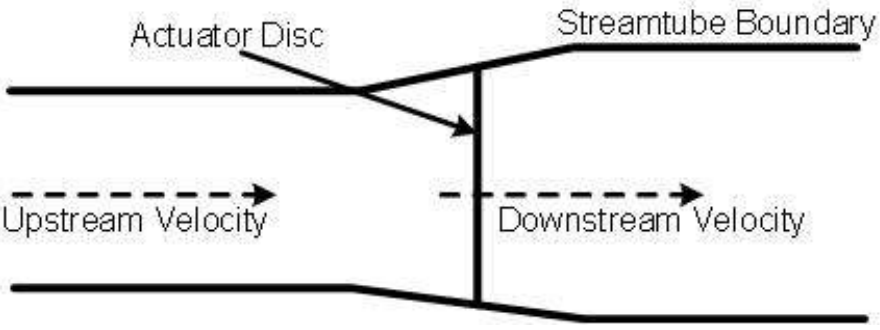

Fig. 2.1 Betz actuator disc model

If, V_i = inlet velocity upstream of actuator disc.

V_o = Outlet velocity or downstream velocity just after the actuator disc.

m_w = mass flow rate across the actuator disc.

$m_w = \rho A_D V_{av}$; V_{av} = Average velocity across the actuator disc = $\frac{(V_i + V_o)}{2}$

(Considering A_D = A)

Since the power recovered from the wind (P_{out}) is equal to the rate of change in the kinetic energy. Therefore, one can also express the power relation as per Eqs. 2.2 through 2.8.

$$P_{out} = \frac{1}{2} m_w \left(V_i^2 - V_o^2\right) \tag{2.2}$$

$$P_{out} = \frac{1}{2} \rho A V_{av} \left(V_i^2 - V_o^2\right) \tag{2.3}$$

$$P_{out} = \frac{1}{2} \rho A \frac{(V_i + V_o)}{2} \left(V_i^2 - V_o^2\right) \tag{2.4}$$

$$P_{out} = \frac{1}{2} \rho A \frac{(V_i + V_o)^2}{2} \left(V_i - V_o\right) \tag{2.5}$$

$$P_{out} = \frac{1}{2} \rho A \frac{\left(V_i^3 + V_o^2 V_i + 2V_o V_i^2 - V_o V_i^2 - V_o^3 - 2V_o^2 V_i\right)}{2} \tag{2.6}$$

$$P_{out} = \frac{1}{4} \rho A V_i^3 \left[1 - \left(\frac{V_o}{V_i}\right)^2 + \left(\frac{V_o}{V_i}\right) - \left(\frac{V_o}{V_i}\right)^3\right] \tag{2.7}$$

Assuming, $x = \frac{V_o}{V_i}$; from equation (2.1), $P_a = \frac{1}{2} m_w V_\infty^2 = \frac{1}{2} \rho A V_\infty^2$; $V_i = V_\infty$

$$P_{out} = \frac{1}{2}\left(1 + x - x^2 - x^3\right) P_a \tag{2.8}$$

Differentiating the above equation with respect to *x* and equating to zero, we get the optimum value of x for the maximum power output, as per Eq. (2.9).

$$\frac{dP_{out}}{dx} = 0 \tag{2.9}$$

We get, $3x^2 + 2x - 1 = 0$; $x = 1/3$

Substituting the value of *x* in Eq. (2.8), we get,

$$P_{out\,\max} = 0.593 P_a \tag{2.10}$$

Or, $$C_{P\max} = 0.593 \tag{2.11}$$

This criterion is called Betz Limit in the wind turbine aerodynamics, which can be stated as no wind turbine system could generate mechanical energy from a stream-tube with uniform velocity, more than 59% of the available wind energy. Or in terms of the rotor performance, which can be expressed as the power coefficient (C_p) will not exceed 0.593, known as the Betz limit due to several losses. Okulov and van Kuik, (2012) have briefly examined the past studies on this limit (0.593). They noted that this constrain is actually the legacy of Betz and Joukowsky's work; therefore, it should be renamed as the Betz-Joukowsky limit. The losses in the turbine could be from the tip region, hub region, transmission, and others. Zhong et al. (2020) have briefly examined the effect of tip loss and the implication of the correction factor, popularly known as the "Prandtl tip loss factor". A WT blade developer has to consider all such factors and constraints that could potentially depreciate the WT generation capability and the market value addition over the years. In the present study, the HAWT type of wind turbine has been considered, thus, most of the aerodynamic description mentioned in the article are related with regards to HAWT.

2.1.2 Governing Forces Acting on the Wind Turbine Blade

The angular momentum imposed on the wind turbine blade are the consequence of the aerodynamic forces acting on the blade sections. Unlike the static airfoils where its aerodynamic characteristics are governed by the angle of attack (α) for every corresponding *Re*. In a rotating rotor, its aerodynamic and performance parameters are governed by the relative α that is the angle between the relative velocity (U_{rel}) of the rotating blade section and the chord line (Manwell et al. 2009). A typical representation of wind turbine blade section subjected to uniform inflow, the fundamental forces acting are shown in Fig. 2.2. The wind turbine performance is often described with respect to tip speed ratio (λ) and *Re*, as given by Eq. (2.12). The aerodynamic forces acting on the airfoil are expressed in Eqs. (2.13) through (2.16), and the subsequent velocity distribution over the sectional airfoil is expressed by velocity triangle representation (Manwell et al. 2009). The force components and the velocity diagram (Fig. 2.2) play an important role, particularly with regards to the designing of the HAWT blade through blade element momentum theory (BEMT). The methodology involves the assessment of axial (a) and tangential (a') induction factor in calculating the necessary twist, pitch, and others across the blade section (Manwell et al. 2009).

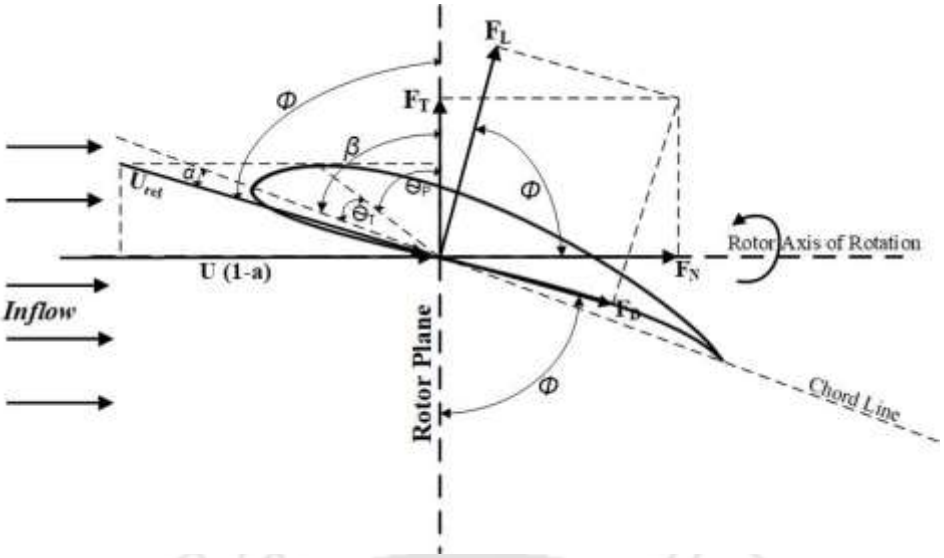

Fig. 2.2. Illustration of various aerodynamics forces (Manwell et al. 2009)

$$\lambda = \frac{R\omega}{U} = \frac{R2\pi N/60}{U}; \quad and, \quad \mathrm{Re} = \frac{\rho U c}{\mu} \tag{2.12}$$

$$C_l = \frac{F_L}{\frac{1}{2}\rho U_{rel}^2 . A_p}; \text{ and } C_d = \frac{F_D}{\frac{1}{2}\rho U_{rel}^2 . A_p} \tag{2.13}$$

$$F_L = \frac{1}{2}\rho U_{rel}^2 . c . C_l ; \text{ and } F_D = \frac{1}{2}\rho U_{rel}^2 . c . C_d \tag{2.14}$$

$$F_N = F_L \cos\phi + F_D \sin\phi \tag{2.15}$$

$$F_T = F_L \sin\phi - F_D \cos\phi \tag{2.16}$$

The aerodynamic forces acting on a rotating blade are lift force (F_L), drag force (F_D), thrust force (F_N), and tangential force (F_T), which are acting with respect to U_{rel} (Fig. 2.2). The U_{rel} is the result of streamwise velocity (U) and angular velocity (ω). The subsequent power coefficient from the rotor is express by Eq. (2.18) (Manwell et al. 2009).

$$U_{rel} = \sqrt{U^2 + (r\omega)^2} \tag{2.17}$$

$$C_p = P/(0.5\rho U^3 . A) \tag{2.18}$$

where, A represents the swept area.

2.2 Blade Element Momentum Theory (BEMT)

The BEMT is the combination of blade element theory and momentum theory. In this theory, some assumptions are made where the blade is divided into N number of strips along the blade span (Fig. 2.3), and there is no interaction between the strips (Manwell et al. 2009).

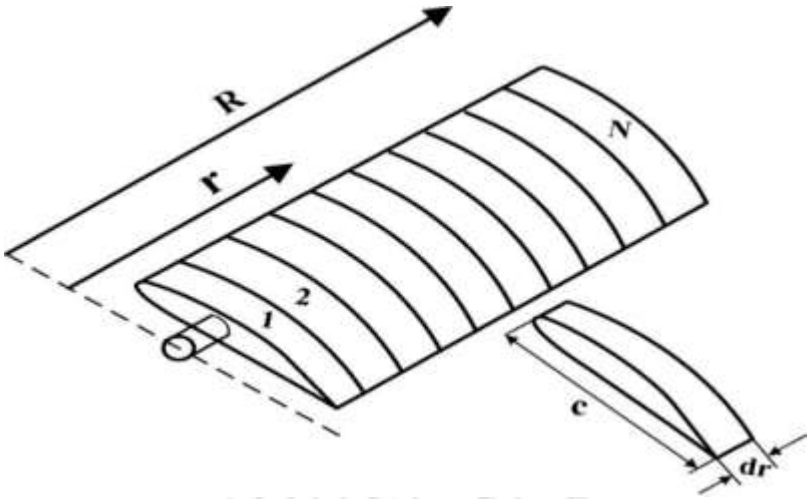

Fig. 2.3 Blade divided into *N* strips

The momentum theory is based on the conservation of linear and angular momentum that estimates the thrust and torque at different locations of the rotor. The blade element theory determines the forces on the blade elements as a function of blade geometry and using sectional lift and drag coefficient data from the performance of airfoils corresponding to α. Figure 2.4 shows the blade element and the forces acting on it. The relative angle (φ), θ_p and twist angle (θ_t) of the blade section can be obtained by Eqns. (2.19) through (2.21).

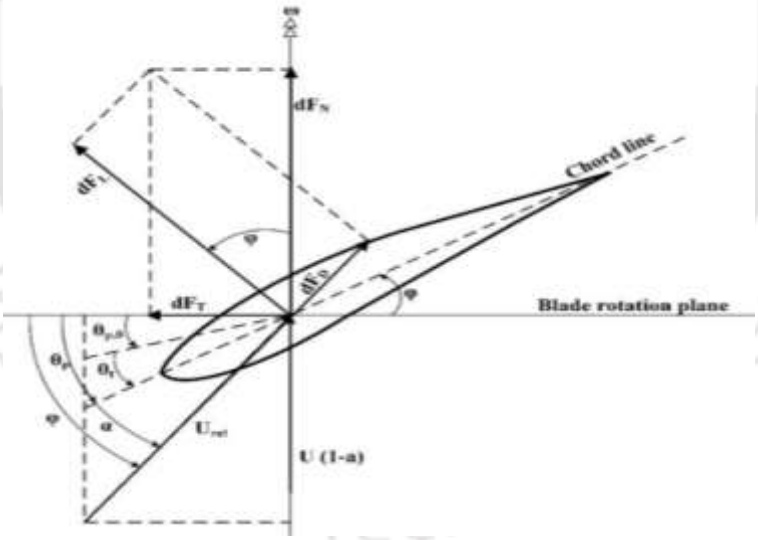

Fig. 2.4 Velocity triangle representation of wind turbine rotor blade section

$$\varphi_{i,j} = tan\left(\frac{1-a_{i,j}}{(1+a'_{i,j})\lambda_{r,i}}\right) \tag{2.19}$$

$$\theta_p = \varphi - \alpha \tag{2.20}$$

$$\theta_t = \theta_p - \theta_{p,o} \tag{2.21}$$

where a is axial induction factor, a' is tangential induction factor, $\theta_{p,0}$ is pitch angle at the tip, λ_r is local tip speed ratio and subscript i and j represents the no. of section and iteration step respectively. The BEMT relationship was developed by balancing momentum forces and relations with the local blade forces. The BEMT analysis has been evaluated by considering the wake rotation, it is implemented to get the blade shape for an optimum rotor. During the process, the implementation is usually carried out through a convergence scheme, starting with assumed values of a and a'. By summing the contribution from each blade section, the rotor thrust and torque are found through an iterative process (Manwell et al. 2009; McTavish et al. 2013).

2.2.1 Design of SHAWT Blade Using BEMT

The design procedure of the rotor begins with the choice of airfoil and rotor parameters, as shown in Table 2.1. Assuming wake rotation for the optimum blade shape, an initial blade shape is determined. Here, the blade design under wake rotation considers the axial and tangential induction factors. The optimum condition implies the state when the rotor can produce the maximum power efficiently. Under this assumption, the optimum angle of attack (α) occurs at the maximum value of C_l/C_d (Dehouck et al. 2018; Song and Luitz et al. 2014), and accordingly, the corresponding chord length, pitch and twist distribution can be calculated. The twist in the blade ensures that α is either equal or close to the design α at each section.

Table 2.1 Input parameters for blade shape design

Sl. No	Parameters	Notations
1	Tip speed ratio	λ
2	Number of blades	B
3	Blade span	b
4	Number of blade element	N
5	Radius	R
6	Design lift coefficient @ max C_l/C_d	$C_{l,design}$
7	Design angle of attack @ max C_l/C_d	α_{design}

The foremost step is to define the required geometric parameters such as rotor radius (R), blade span length (b), and the number of blades (B). This is followed by selection of operational limit of λ, optimum value of λ and number of blade element (N). The empirical relation for the rotor λ and the power output (P_{out}) can be express by relation as Eq. (2.22).

$$\lambda = \frac{R\omega}{U}; \quad and \quad P_{out} = C_p 0.5 \rho_{air} \pi R^2 U^3 \tag{2.22}$$

where, P_{out} is turbine output power (W), C_p is power coefficient, ρ_{air} is density of air (kg/m^3), R is radius of the rotor (m) and U is upstream wind speed (m/s). The detailed iterative procedures

involved to evaluate the rotor geometric parameters and subsequently to estimate/predict the performance of the rotor have been mentioned in Chapter 3.

2.3 Literature Review on Small Wind Turbines (SWTs)

The utility of small wind turbines (SWTs) covering horizontal and vertical-axis types as off-grid, standalone, and decentralized energy supplement systems has gained market attention. Such turbines primarily operate at low Reynolds number (*Re*) and low tip speed ratio (λ) conditions. Under such circumstances, the design, development, and testing of SWTs have become a tedious task, mainly due to the lack of precise aerodynamic knowledge of SWT. As a part of the research objective, this section reviews the fundamental aspects of SWT, including airfoil selection criteria, blade design, and aerodynamic improvement through passive flow control and augmentation techniques. The article also reports several classes of potential airfoils that can be employed in the design of SWTs. The airfoils considered operate mainly in the range of $Re = 0.3 \times 10^5$ to 3×10^5 and $\lambda = 0.5$ to 6. Besides the classical approach, the article showcases the prospects of several bioinspired profiles/shapes that are meant for SWTs operating at low *Re* and λ conditions.

On the basis of past studies (Nguyen and Metzger, 2017; Tummala et al. 2016; Jain and Saha, 2019; McTavish et al. 2013), the SWTs can be made available through horizontal-axis wind turbines (HAWTs) and vertical-axis wind turbines (VAWTs), as shown in Fig. 2.5. The small HAWTs can be further categorized into small-scale, mini-scale, and micro-scale HAWTs. On the other hand, small VAWTs can be further categorized into Savonius, Darrieus, or hybrid rotors; and these turbines have a rotor diameter (*D*) of less than 5 m. In comparison to HAWTs, the VAWTs have a lesser power coefficient (C_p) (Jain and Saha, 2019; Treuren, 2015); however, it is possible to enhance their performance by incorporating specific pitch control mechanisms, multi-rotor system, and various augmentation techniques (Zhao et al. 2019; Sun et al. 2012; Neagoe et al. 2020). The augmentation technique is a method of modifying the model's geometry without altering the core rotor/airfoil body, which is basically meant to enhance the rotor performance. As reported in literatures (Tummala et al. 2016; Jain and Saha, 2019; McTavish et al. 2013), the wind turbines vary from large to micro levels (Table 1.1). One can categorize the wind turbines into large wind turbines (LWTs), medium wind turbine (MWTs), and small wind turbines (SWTs), as represented in Fig. 2.5. The SWT can be further categorized into small HAWTs and VAWTs; these rotors will have a diameter (D) of less than 5 m. Figure 2.6 shows various types of vertical-axis and horizontal-axis SWTs such as H-type Darrieus, Darrieus Turby, Gorlov, Twisted Savonius, and others (Casini et al. 2016; Dilimulati et al. 2018). Such SWTs can also be modelled into an integrated system, as shown in Fig. 2.7, which can effectively serve as off-gird power generating source. The contribution from LWTs is undeniably admirable and bright, especially when there is a spontaneous rise in renewable energy demand. However, these turbines are known for occupying substantial area because of their larger size (Wang and Prinn, 2010; Fiedler and

Bukovsky, 2011; Kievanpour et al. 2017). In such scenario, the scope of SWTs is very much promising.

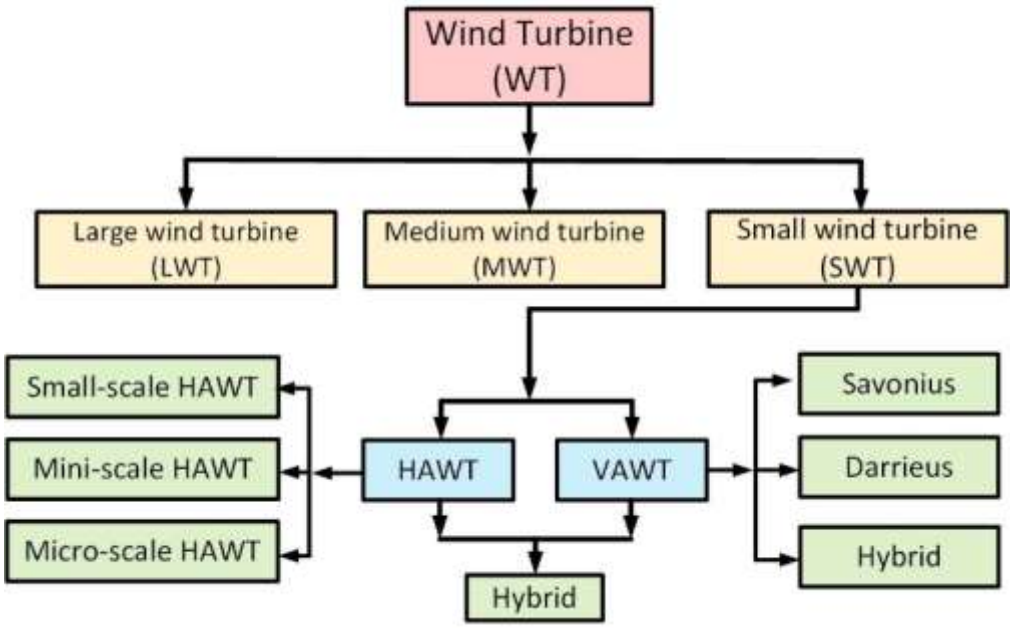

Fig. 2.5 Categories of wind turbines

Fig. 2.6 Typical vertical-axis and horizontal-axis wind turbines (Casini et al. 2016; Dilimulati et al. 2018). Reproduced with permission from J. Wind Engg and Industrial Aerodynamics, 175, 179-192 (2018). Copyright 2018 Elsevier.

Fig. 2.7. Cluster arrangement of small wind turbine (Reproduced with permission from Casini et al. 2016; Liu et al. 2019; Dilimulati et al. 2018)

2.3.1 Past studies on SWTs

The selection and design of SWTs is a challenging task as they need to operate at low *Re* and low λ conditions. Initial studies with several classes of airfoils for their use in wind turbines have been performed by National Renewable Energy Laboratory and Delft University (Karthikeyan et al. 2015; Tangler and Rooij, 2003). They have shown that some of the profiles have potential implications in small turbines. In their findings airfoils operating at $Re = 5 \times 10^5$ has been reported (Karthikeyan et al. 2015; Tangler and Rooij, 2003; Giguere and Selig, 1997,1999); however, the study on turbines operating below $Re < 10^5$ is scarce. Hitherto, a host of airfoils have been examined for wind turbine blades, however, the study of SWT airfoils operating at low λ is very much limited. The design of the wind turbine blade and its aerodynamic performance is mostly evaluated through the blade element momentum theory (BEMT), nonetheless, blades of SWT could also be of Non-BEMT (NBEMT) type with straight forward. Further, performance optimization can be processed through genetic algorithms, Xfoil, or computational fluid dynamics (CFD) tools. In this context, the aerodynamic shape optimization of twisted SWT blades has been studied by Shen et al. (2016). Table 2.3 summarizes the previous studies carried out in the area of SWTs under different operating and geometric conditions. The results reported are mostly regarding blade design and its aerodynamic characterization. Details of the electrical system, drivetrain resistance, or any related control system have not been considered in these studies.

Nevertheless, the data provided in Table 2.3 would provide a great deal of information on the aerodynamics of SWTs.

Table 2.3 List of research activities carried out on small wind turbines (SWTs)

Investigators	Evaluation method	SWT description	Key observations
Duquette et al. (2003)	Numerical	Airfoil: SG6043	Increase of C_p at low λ with increase in solidity (σ). With 5-7% increase of σ enhances the C_p by 15-25%.
Hirahara et al. (2005)	Experimental U = 4 – 23 m/s Blockage Ratio (BR): 3.4 %	Airfoil: NACA2404 Nos. of blade (B) = 4; Radius (R) = 0.25 m	Net efficiency of rotor: 0.25; C_{pmax} = 0.41 when at λ = 2.7. For the design rotor, its performance is found to be best while operating U = 8 – 12 m/s
Wang et al. (2008)	Experimental and CFD BR: 13.5 %; U = 9.1, 11.25, and 13.9 m/s	Airfoil: Rutland 913 B = 6; R = 0.285 m Non-BEMT rotor.	Implication of scoop is examined. P_{max} = 132 W; C_{pmax} = 0.308 at 13.9 m/s (λ = 2.58). Cutting the original blade reduce the performance and efficiency. C_{pmax} = 0.19 is observed using scoop.
Zhang e al. (2009)	---	Airfoil: S822-S823	Tested at U = 5 m/s at 50 rpm; Max. C_p = 0.43 is obtained.
Freere et al. (2010)	Experimental U = 13 m/s; TI: 3%	Airfoil: MG4520 B = 3; R = 1.05 m; Non-BEMT	Rotor speed: 50 – 600 rpm; C_{pmax}: 0.22 at λ_{opt} = 6; Range of λ = 2 -8 Effect of yaw is observed; C_p decrease with increase in yaw angle.
Matsumiya et al. (2010)	Experimental field tests	SD7037 B = 3; R = 0.9 m	Rated power: 1 kW at 12.5 m/s and 3.2 kW at 20 m/s Rotor speed: 2.5 - 50; Field test: 319 W at 9.7 m/s; C_{pmax}: 0.36
Lanzafame and Messina (2010)	Experimental U = 7 - 15 m/s	Airfoil: NACA4415 B = 3; R = 0.225 α = 0˚, 3˚, 6˚, 9˚	Blade twist modification is employed to lower the blade tip stall at high wind speed. High angle of attack (α) causes excessive inverse tangential force, creating resistive torque thus lower the C_p. They obtained C_{pmax} = 0.49 at λ_{opt} = 4.71
Krogstad and Lund (2012)	Experimental and computational (BR: 11.8%)	Airfoil: S826 B = 3; R = 0.45 m; BEMT rotor	C_{pmax} = 0.448 at λ=6; CFD over-predict the C_p by about 2%
Wu et al. (2012)	Experimental and simulation U = 1 m/s	Airfoil: NACA63415 B = 3; R = 0.3, 05, and 0.6 m;	Rotor rotation: 200 – 300 rpm; C_p (0.6 m) > C_p (0.5 m) > C_p (0.3 m). Increasing the nos. of blade is less significant. Obtained average C_p of 0.33
Refan et al. (2012)	Experimental U =1 - 11 m/s BR: 21.7% and 41.77%	Airfoil: Wortmann FX63-137 (Tip)– NACA6515 (root) B = 3; R = 1.1 m; BEMT rotor.	Rotor speed: Max. 1200; Rated power = 900 W at 12.9 m/s P_{max} = 470 W at 9 m/s; C_{pmax} = 0.277. Experimental results show slightly different optimum λ as predicted by BEMT.
Chen et al. (2012)	Experimental BR: 4% and 10% (with flange)	Airfoil: NACA4415 B = 6; R= 0.15 m Non-BEMT rotor	Effect of σ and use of flange are examined; Max. rotor speed = 6000 rpm. C_{pmax} = 0.29 (without flange) and C_{pmax} = 0.67 (with flange) at 12 m/s. With flange shows C_p exceed Betz's limit.
Singh et al. (2012, 2013)	Experimental U = 4, 5, and 6 m/s	Airfoil: AF300 B = 2; R= 0.63 m; BEMT rotor	$C_{pmax} \approx$ 0.30 at θ_p = 18º and 20º at U= 6 m/s; Average C_p = 0.1, 0.22, and 0.255 at U = 4, 5, and 6 m/s, respectively at 18º compared to C_p =0.052, 0.11, and 0.15 for the baseline rotor. Effect of pitch angle is observed.
Rocha et al. (2014)	Computational and field tests Hub height: 5 m	Airfoil: NACA0012 B = 3; R= 1.5 m; BEMT rotor	Field tests show $C_{pmax} \approx$ 0.14 at λ = 7.25. k-ω SST numerical model is employed.
Kishore and Priya (2013)	Experimental U =1.8 - 5 m/s; BF < 10%	Airfoil: NACA0012 B = 3; R = 0.197 m; Non- BEMT	P_{max} = 0.83 W at U = 5 m/s; C_{pmax} = 0.14 at U = 2.9 m/s; Ducted turbine produces 1.4 – 1.6 time more power than the unducted turbine.
Kishore and Priya (2013)	Experimental and theoretical study U = 4 m/s; Re = 40,000	Airfoil: Symmetric airfoil B = 3; R = 0.20 m Non-BEMT rotor.	Rated power = 1 W but capable of producing 2.2 W at 5.5 m/s. C_p =0.31 – 0.34, at U = 3 – 5.5 m/s. C_{pmax} = 0.32 at λ = 4.1 (U = 4 m/s); Overall efficiency: 21% at U = 4 m/s

Song and Lubitz (2014)	Field Tests U < 3 m/s	Airfoil: SD7062 B = 3; R = 1.25 m; Non-BEMT	Tested for two pitch angle (+5º and +9º) and obtained C_p of 0.282 and 0.263, respectively. (σ: 30%)
Huang et al. (2015)	Experimental U = 6, 8, and 10 m/s	Airfoil: SD80000 B = 3; R = 0.15 cm; Non-BEMT	Examined the effect of leading edge protuberance (LEP). Improvement in C_p due to LEP is found to be effective only at low λ. NOT preferable for high wind speed condition.
Shen et al. (2016)	Numerical Cut-in wind speed: 4 m/s Cut-out wind speed: 20 m/s	Airfoil: S809 B = 3; R = 0.9 m Non-BEMT rotor	Scope of lifting surface with free wake model is examined. Micro genetic algorithm (μGA) is used as optimization algorithm. The 3D optimized blade has higher C_p and C_t then 2D. High C_p close to 0.5 at 8 m/s was predicted.
Jackson et al. (2017)	Experimental and numerical study BF: 2.25%; TI: 0.32%	Airfoil: NACA4424 Three sets of rotor were tested. B = 3; R= 0.1015 m; Non-BEMT rotor	Sets of experimental examines the near and far wake characteristics for 3 array of model turbines. Spacing of 2D and 4D from first turbine. Employed Reynold stress transport model in numerical simulation for solving RANS equations.
Akour et al. (2018)	Experimental and numerical study U = 2.7 – 5.9 m/s	Airfoil: BW3, A18 and SG6043 B = 3; R = 0.5 m BEMT rotor	Simulation study using QBlade tool shows BW3 rotor has better performance over A18 and SG6043 at Re = 25,000. C_{pmax} = 0.38 at λ = 4.4 via numerical study and C_p = 0.34 at λ = 3.5 via experimental study.
Evans et al. (2018)	Experimental U = 8 - 22 m/s	Airfoil: SD7062 B = 2; R= 2.5 m	Significance of aeroelastic modelling of SWT is studied. Power generated ~ 4.7 kw (at U ~ 17 m/s), therefore, C_{pmax} = 0.08.
Rocha et al. (2018)	Field tests Hub height: 5 M Hub diameter: 300 mm	Airfoil: NREL S809 B = 3; R = 1.5 m; BEMT rotor	λ_{opt}= 8; β= 31.63°, 25.63°, 22.63°, and 19.63°. For, λ = (2-4), C_p = (0.07-0.319) and when λ = (4-8), C_p = (0.18-0.45), C_{pmax} at β = 25.63° Examined the significance of blade pitch angle on performance.
Lipian et al. (2016)	Experimental U = 8 - 18 m/s. BF: 16%	Airfoil: SG6040 and SG6041 Two model test. Rotor separation: 0.1D – 0.62D; R = 0.16 m	Effect of augmentation on SWT performance. Increase in efficiency by 11 – 13%. C_p variation negligible at high velocity. C_p: 0.23 (open rotor) for λ = 0 – 6, whereas, C_p = 0.554 (ducted rotor) for λ = 0 – 10. Increase of Cp with the use of second rotor for unshrouded turbine.
Macphee and Beyene (2019)	Experimental BF: 56.15% U = 2.05, 2.60, and 3.15 m/s	Airfoil: NACA0015 B = 3 (rigid and flexible or morphing blades); R = 571 mm; Non-BEMT rotor	C_{pmax} (rigid blade) = 0.254 and C_{pmax} (flexible blade) = 0.256 at 2.05 m/s and β = 3°. Flexible blade has wide range of operational potential than rigid blades. With increase in β, the performance of the rigid rotor degrades much faster than with that of the flexible rotor.
Li et al. (2020)	Numerical study. Analysis of two models of HAWT and optimization of mixed airfoil HAWT.	Airfoil: DU96W180 and NACA4412 LWT to SWT modelling B = 3; R = 0.32 m; BEMT rotor	Optimization of scale down 2.5 MW turbine to 0.32 m rotor base on Lifting-line theory was examined. Aerodynamic performance of rotor with NACA4412 is found to better than DU96W180 at low Re. Final optimized model shows C_p of ~0.35 at λ ~6.5
Abdelsalam et al. (2021)	Numerical and experimental studies U = 5,6,8, and 10 m/s	Airfoil: E216 B = 3; R = 0.50 m; BEMT Rotor	C_{pmax} = 0.426 at λ = 5.1 (U = 10 m/s). The proposed models deviated from exp. value at 5 m/s. However, similar results were seen at higher velocities. Linear model predicts C_p = 0.401. Significant change in C_p values of linear model at different pitch angle.
Liu et al. (2020)	Numerical study	Airfoil: NACA4415 B = 3; R= 3.5 m; Non-BEMT rotor	Examined the concept of delaying the laminar separation bubble through surface grooves at low Re SWT. About 2% increase in C_p is observed with the inclusion of surface groove.

2.3.2. Airfoil Selection for SWTs

For the design and fabrication of turbine blades through BEMT, the selection of airfoil is of great concern. In most scenarios, the selection of rotor blade profile is based on aerodynamic characteristics, size, and shape. In the classical approach, the selection of airfoil is made based on the optimum value of C_l/C_d for the desired *Re*. Now, one has to judiciously consider these values since the operation of SWT generally falls under low *Re* conditions. Based on the studies reported (Tummala et al. 2016; Treuren, 2015; Wood, 2015; McTavish et al. 2013), the low Re is considered in the range of $0.3 \times 10^5 \leq Re \leq 3 \times 10^5$. Now, relying on this criterion, different types of airfoils have been explored. Only those airfoils have considered that find their application in the design of SWT blades. Some of these airfoils and their corresponding aerodynamic characteristics at $Re = 0.5 \times 10^5$, 1.0×10^5, and 2.0×10^5 are shown in Table 2.4. There are different types, sizes, and shapes of airfoil available in the aerodynamic community; though most of them are developed for their use in traditional aviation or in large wind turbines. But for SWTs, only a few are known to the wind energy community. Some of these are repeatedly investigated or utilized in exploring their feasibility in various applications. A host of researchers have explored airfoils such as SG6043, E387, SD7062, NACA0012, S822, and NACA4418 (Table 2.4) for their utilization in SWTs. At the same time, airfoils like AF300, E216, A18, E387, NACA63415, and others are least examined, although they exhibit promising results in SWT applications (Singh et al. 2012; Rocha et al. 2014; Akour et al. 2018; Abdelsalam et al. 2021).

The NACA series of airfoils, initially meant for aviation, have also been explored for their usage in SWTs in mid-1980s (Tummala et al. 2016; Treuren, 2015; Giguere and Selig, 1997, 1999). Some of the NACA airfoils have shown good aerodynamic characteristics in both VAWT and HAWT (Sheldahi and Klimas, 1981). The NACA44XX, NACA00XX, and NACA24XX are certain sets of airfoils that have been explored for their application in SWTs. SG60XX series, developed by Selig and Giguere, (Giguere and Selig, 1997, 1999) on the other hand, are the different segments of airfoils that have shown some promising characteristics mainly due to their high lift and low drag behavior while operating at low *Re*. They have also suggested the usage of SG60XX airfoils for the design of SHAWTs. From the literature survey as well as from the data (Tables 2.3 and 2.4), the airfoils that could be used in SWT are shown in Fig. 2.8. It will be of great interest for the researchers and developers to explore such potential airfoils.

Table 2.4 List of airfoils used in the SWT blade design

Airfoil	Max. C_l/C_d	α (°)	Investigators	Airfoil	Max. C_l/C_d	α (°)	Investigators
A18	43.99 (Re ~ 0.5 x 10^5)	5.25	Karthikeyan et al. (2015); Akour et al. (2018)	SG6043	39.71 (Re ~ 0.5 x 10^5)	8.75	Giguere and Selig (1998); Duquette et al. (2003); Migliore et al. (2004); Ahmed et al. (2011); Wata et al. (2011); Pourrajjabian et al. (2014); Akour et al. (2018); Rahgozr et al. (2020)
	64.96 (Re ~ 1.0 x 10^5)	4.50			66.47 (Re ~ 1.0 x 10^5)	7.00	
	86.33 (Re ~ 2.0 x 10^5)	3.25			98.00 (Re ~ 2.0 x 10^5)	5.50	
	79.60 (Re ~ 3.0 x 10^5)	--					
AF300	54.00 (Re ~ 1.0 x 10^5)	8.20	Singh et al. (2012, 2013)	SG6040	26.06 (Re ~ 0.5 x 10^5)	11.50	Giguere et al. (2021);
					50.51 (Re ~ 1.0 x 10^5)	9.00	Karthikeyan et al. (2015);
					72.93 (Re ~ 2.0 x 10^5)	7.75	Lipian et al. (2016)
BW-3	46.72 (Re ~ 0.5 x 10^5)	5.50	Karthikeyan et al. (2015); Akour et al. (2018); Suresh and Rajkumar (2020).	SG6041	35.45 (Re ~ 0.5 x 10^5)	5.75	Giguere et al. (1998);
	67.60 (Re ~ 1.0 x 10^5)	4.50			53.46 (Re ~ 1.0 x 10^5)	5.00	Karthikeyan et al. (2015);
	74.66 (Re ~ 2.0 x 10^5)	4.00			72.82 (Re ~ 2.0 x 10^5)	4.00	Lipian, et al. (2016)
	69.60 (Re ~ 3.0 x 10^5)	--					
E387	38.09 (Re ~ 0.5 x 10^5)	8.50	Guglielmo and Selig (1997); Selig and MacGranahan (2004, 2004a); MacTavish et al. (2013); Karthikeyan et al. (2015); Suresh and Rajkumar (2020)	SD7062	12.09 (Re ~ 0.5 x 10^5)	4.00	Song and Lubitz (2014);
	50.98 (Re ~ 0.8 x 10^5)	8.00			47.63 (Re ~ 1.0 x 10^5)	7.00	Karthikeyan et al. (2015);
	60.66 (Re ~ 1.0 x 10^5)	7.50			70.04 (Re ~ 2.0 x 10^5)	6.25	Evans et al. (2018)
	84.35 (Re ~ 2.0 x 10^5)	6.75			77.50 (Re ~ 3.0 x 10^5)	--	
	81.70 (Re ~ 3.0 x 10^5)	--					
E216	40.73 (Re ~ 0.5 x 10^5)	8.00	Abdelsalam et al. (2021);	SD7037	34.48 (Re ~ 0.5 x 10^5)	6.50	Matsumiya et al. (2010);
	68.50 (Re ~ 1.0 x 10^5)	6.00	Gupta et al. (2017);		55.22 (Re ~ 1.0 x 10^5)	5.25	Karthikeyan et al. (2015);
	99.17 (Re ~ 2.0 x 10^5)	4.00			74.75 (Re ~ 2.0 x 10^5)	4.75	Zhang et al. (2020)
					76.30 (Re ~ 3.0 x 10^5)		
E422	5.27 (Re ~ 0.5 x 10^5)	7.75	Wata et al. (2011)	SD7032	31.95 (Re ~ 0.5 x 10^5)	7.50	Giguere and Selig (1998);
	29.50 (Re ~ 1.0 x 10^5)	2.25			56.30 (Re ~ 1.0 x 10^5)	5.50	Karthikeyan et al. (2015)
	60.01 (Re ~ 2.0 x 10^5)	9.50			77.87 (Re ~ 2.0 x 10^5)	4.75	
					83.40 (Re ~ 3.0 x 10^5	--	
E555	27.83 (Re ~ 0.5 x 10^5)	10.50	Gupta et al. (2017)	S833	27.54 (Re ~ 0.5 x 10^5)	9.50	Prasad at al. (2014); Hasan et al. (2017)
	51.15 (Re ~ 1.0 x 10^5)	8.50			39.40 (Re ~ 1.0 x 10^5)	8.50	
	69.11 (Re ~ 2.0 x 10^5)	7.50			54.83 (Re ~ 2.0 x 10^5)	6.50	
NACA 2414	29.23 (Re ~ 0.5 x 10^5)	8.75	Karthikeyan et al. (2015)	S822	27.66 (Re ~ 0.5 x 10^5)	9.50	Selig and MacGranahan (1998); Zhang et al. (2020); Prasad et al. (2014); Karthikeyan et al. (2015); Hasan et al. (2017)
	47.77 (Re ~ 1.0 x 10^5)	7.50			42.69 (Re ~ 1.0 x 10^5)	8.50	
	65.07 (Re ~ 2.0 x 10^5)	6.75			68.55 (Re ~ 2.0 x 10^5)	7.00	
	66.60 (Re ~ 3.0 x 10^5)				69.40 (Re ~ 3.0 x 10^5)	--	
NACA 2408	37.42 (Re ~ 0.5 x 10^5)	5.50	Hirahara et al. (2005); Tummala et al. (2016)	NREL S826	34.60 (Re ~ 0.5 x 10^5)	9.50	Krogstad and Lund (2012)
	52.56 (Re ~ 1.0 x 10^5)	5.00			60.86 (Re ~ 1.0 x 10^5)	8.25	
	66.55 (Re ~ 2.0 x 10^5)	4.00			82.99 (Re ~ 2.0 x 10^5)	7.25	

Table 2.4 List of airfoils used in the SWT blade design (contd.)

Airfoil	Max. C_l/C_d	α (°)	Investigators	Airfoil	Max. C_l/C_d	α (°)	Investigators
NACA 63415	29.96 (Re ~ 0.5 x 10^5) 53.05 (Re ~ 1.0 x 10^5) 75.56 (Re ~ 2.0 x 10^5)	9.50 8.25 7.25	Wu et al. (2012)	NREL S809	15.53 (Re ~ 0.5 x 10^5) 23.41 (Re ~ 1.0 x 10^5) 51.73 (Re ~ 2.0 x 10^5)	12.25 10.00 8.25	Butterfield et al. (1992); Shen et al. (2016); Rocha et al. (2018)
NACA 63621	---	--	Habali and Saleh, (2000)	S1210	14.88 (Re ~ 0.5 x 10^5) 59.29 (Re ~ 1.0 x 10^5) 86.32 (Re ~ 2.0 x 10^5)	2.50 8.00 6.50	Singh et al. (2012, 2013)
NACA 4415	7.41 (Re ~ 0.5 x 10^5) 48.43 (Re ~ 1.0 x 10^5) 71.07 (Re ~ 2.0 x 10^5)	9.00 9.00 6.50	Vardar and Alibas (2008); Chen et al. (2012); Liu et al. (2020)	S1221	27.07 (Re ~ 0.5 x 10^5) 45.22 (Re ~ 1.0 x 10^5) 70.04 (Re ~ 2.0 x 10^5)	3.25 3.75 11.50	Singh et al. (2012, 2013)
NACA 4412	33.44 (Re ~ 0.5 x 10^5) 56.09 (Re ~ 1.0 x 10^5) 78.14 (Re ~ 2.0 x 10^5)	9.75 8.50 7.00	Vardar and Alibas (2008); Aung et al. (2016); Khaled et al. (2017); Tian et al. (2017)	S1223	33.05 (Re ~ 0.5 x 10^5) 47.46 (Re ~ 0.8 x 10^5) 54.48 (Re ~ 1.0 x 10^5) 73.64 (Re ~ 2.0 x 10^5)	2.00 2.00 3.25 3.75	Guglielmo and Selig (1997); Wata et al. (2011); Suresh and Rajkumar (2020)
NACA 0012	25.67 (Re ~ 0.5 x 10^5) 33.43 (Re ~ 0.8 x 10^5) 36.68 (Re ~ 1.0 x 10^5) 47.43 (Re ~ 2.0 x 10^5)	5.00 5.00 5.00 5.00	Vardar and Alibas (2008); Rocha et al. (2014); Rocha et al. (2018); Kishore and Priya (2013); MacTavish et al. (2013); Migliore and Oerlemans (2004)	S7012	33.73 (Re ~ 0.5 x 10^5) 51.93 (Re ~ 1.0 x 10^5) 70.30 (Re ~ 2.0 x 10^5) 72.10 (Re ~ 3.0 x 10^5)	7.00 6.50 5.75 --	Karthikeyan et al. (2015)
NACA 0015	24.69 (Re ~ 0.5 x 10^5) 37.49 (Re ~ 1.0 x 10^5) 49.63 (Re ~ 2.0 x 10^5)	6.25 6.00 6.25	Nigim and Jabbar (1989); Macphee and Beyene (2019)	S6062	34.59 (Re ~ 0.5 x 10^5) 50.44 (Re ~ 1.0 x 10^5) 65.25 (Re ~ 2.0 x 10^5) 73.10 (Re ~ 3.0 x 10^5)	5.75 5.25 4.25 --	Song and Lubitz (2014); Karthikeyan et al. (2015)
NACA 4424	1.96 (Re ~ 0.5 x 10^5) 30.84 (Re ~ 1.0 x 10^5) 53.65 (Re ~ 2.0 x 10^5)	9.75 4.50 6.00	Jackson and Amano (2017)	SH3052	---	--	Corbus and Praschar (2004); Singh et al. (2012, 2013)
NACA 4418	5.31 (Re ~ 0.5 x 10^5) 43.30 (Re ~ 1.0 x 10^5) 67.02 (Re ~ 2.0 x 10^5)	4.75 10.00 7.50	Selig and MacGranahan (2004, 2004); Migliore and Oerlemans (2004); Refan and Hangan (2012); Singh et al. (2013); Suresh and Rajkumar (2020)	SH3055	47.00 (Re ~ 1.0 x 10^5)	10.32	Selig and MacGranahan (2004, 2004a); Migliore and Oerlemans (2004); Singh et al. (2012, 2013)
Wortmann FX63-137	26.82 (Re ~ 0.5 x 10^5) 46.65 (Re ~ 0.8 x 10^5) 62.09 (Re ~ 1.0 x 10^5) 90.58 (Re ~ 2.0 x 10^5)	11.00 9.00 7.50 6.25	Singh et al. (2013); Refan et al. (2012); Suresh and Rajkumar (2020)	LS (1)-0421	23.79 (Re ~ 0.5 x 10^5) 33.10 (Re ~ 1.0 x 10^5) 52.38 (Re ~ 2.0 x 10^5)	10.25 8.50 6.50	Habali and Saleh (2000)

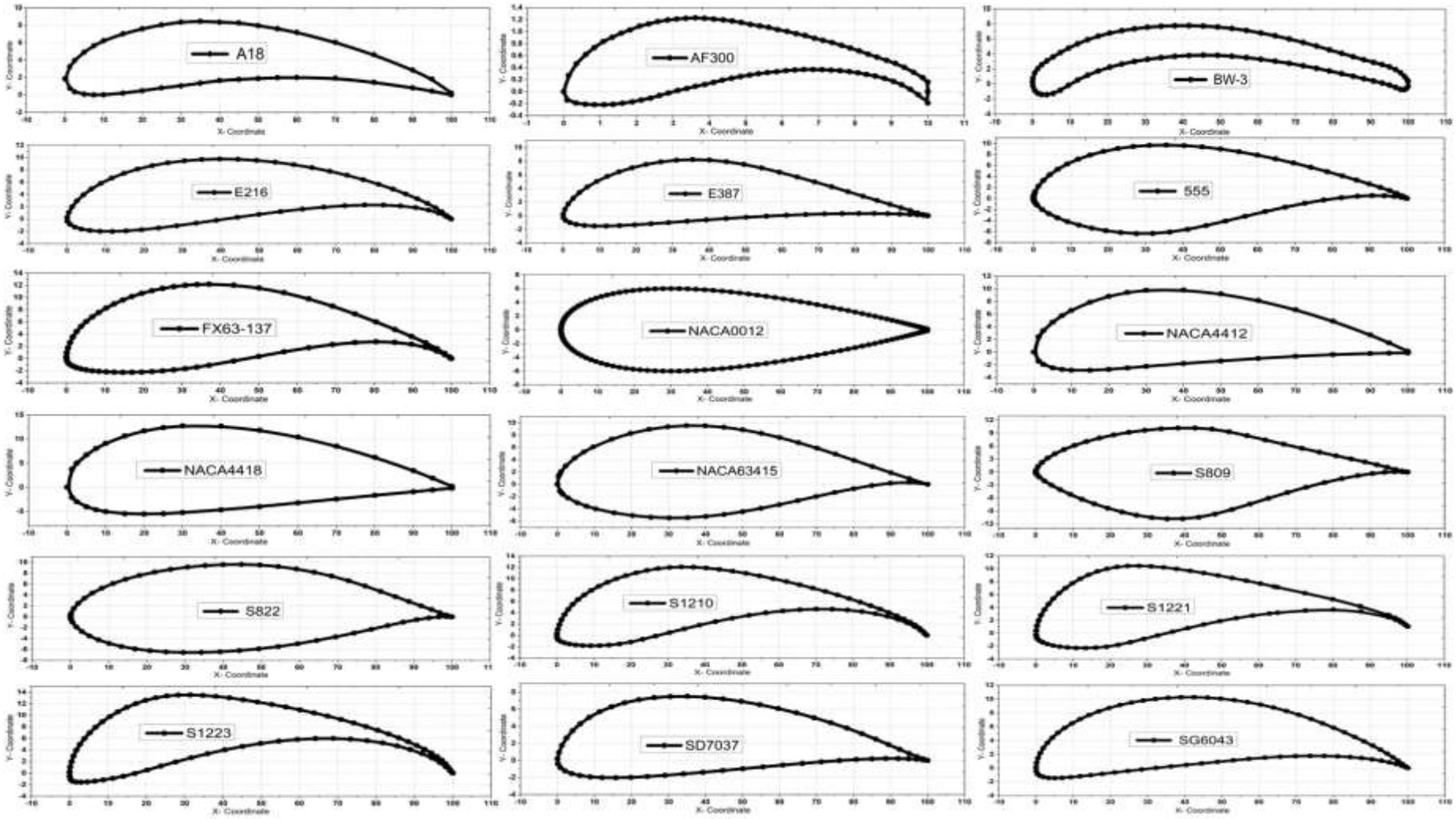

Fig. 2.8 Some potential airfoils for SWTs

Aerodynamic properties of the wind turbine blade rely on the type of airfoil selected. One can examine the aerodynamic characteristic of the airfoil through the classical approach for the concerned Re, which can be achieved through XFoil, Qblade, ANSYS, and other tools apart from the experimental method. Furthermore, there are several flow control mechanisms or attachment by which the performance of the airfoil can be further enhanced. In the aerospace study, such flow control techniques are incorporated into the wings, fans, rudders, turbines and others (Gad-el-Hak, 2007). As reported by Green, (2008), the attached flow over airfoil surfaces at a high α ensures better operational capability, performance, range, and endurance. Gad-el-hak, (2007) have acknowledged the possibility of flow control mechanism through passive, active and hybrid techniques. The former two techniques are differentiated on the basis of without and with actuators mechanisms, whereas the combination of both is classified as a hybrid technique. The passive flow control techniques include geometric modification of the rotor blade/airfoil, such as vortex generator, boundary layer strip, surface groove, tubercles, and others. On the other hand, the active flow control technique includes the use of energized flow control devices like actuators, synthetic jets, and others. The implementation of such attachments/provisions drives the flow separation process, which are often described by the separation bubbles. The consequence of flow separation is the alteration of aerodynamic properties such as lift, drag, transition, and reattachment processes since they are related to each other, as shown in Fig. 2.9 (Gad-el-hak, 2007; Aftab et al. 2016). This section showcases some past studies examining the influence of airfoils/wind turbine flow control techniques.

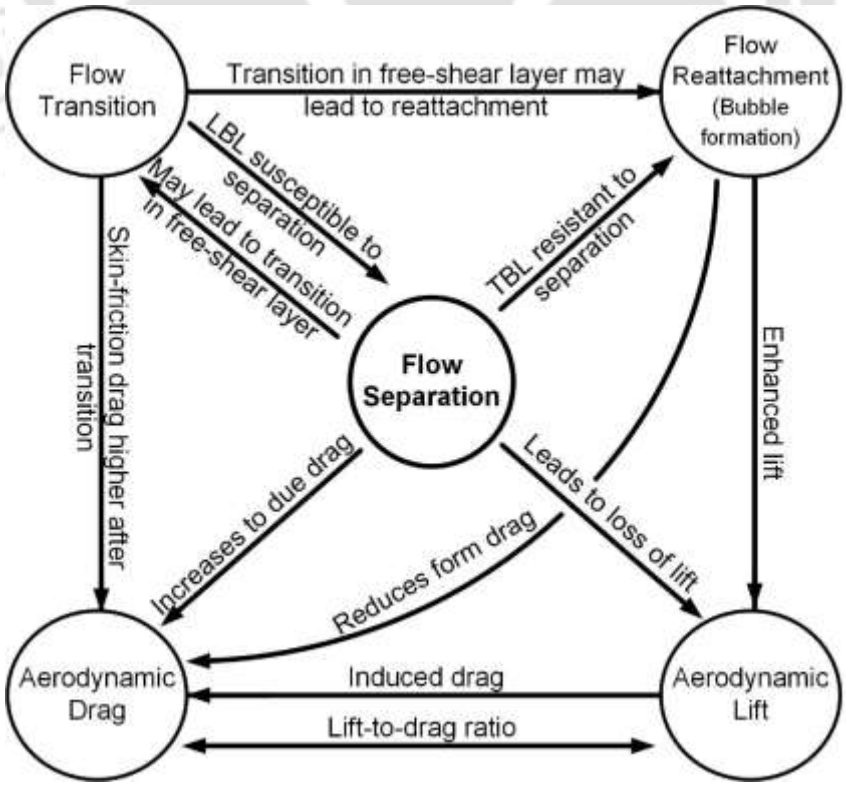

Fig. 2.9. Interrelation between flow separation and aerodynamic features (Gad-el-hak, 2007; Aftab et al. 2016).

2.3.3. Effect of Rotor Geometric Configuration

For a given SWT, the effect of rotor geometric variability on its performance is often discussed in terms of the number of blades (B), solidity (σ_s), yaw angle (γ), and pitch angle (β) configurations (Tummala et al. 2016; Zhao et al. 2020). Some of the earliest discussions on the effect of such parameters were reported (Tummala et al. 2016; Jain and Saha, 2019; Costello et al. 2015; Guo et al. 2021; Karthikeyan et al. 2015); however, those reported work were mainly focused on LWTs.

2.3.3.1. Effect of Number of Blades and Airfoil Shape

Xisto et al. (2016) have investigated the effect of B on the performance of wind turbines. Their examination involves the effect of solidity. They have also examined the effect of airfoil thickness on the rotor performance using different symmetric NACA00XX airfoil (NACA0006, NACA0010, NACA0015, and NACA0018). The indented range of wind turbine operation was kept at $0.5 < \lambda < 1.5$, and $B \leq 6$. The C_p variation has been acknowledged through B and λ as shown in Fig. 2.10; for low λ utility VAWT, the $C_{pmax} > 0.25$ is noted for $B \geq 4$. Furthermore, with such a configuration, the C_{pmax} response is observed to be saturating as B is increased gradually for a given λ. The investigation suggests that symmetric airfoil having higher thickness/chord (t/c) ratio produces superior power, and among the opted NACA symmetric profiles, NACA0018 (18% thickness) shows higher performance, as shown in Fig. 2.11(a). The airfoils depict an increase in C_p with t/c as seen through Fig. 2.11(b), and this observation suggests that for a given λ, upon increasing the blade thickness, the performance of the rotor seems to be promising. Apart from this, they have also examined the effect of β through a controlled pitching mechanism as suggested by Leger et al. (2015). Their findings suggest that using the proposed pitching mechanism, the rotor generates a relatively higher torque compared to fixed β while operating a low λ. Furthermore, it is to be noted that the rotor with six blades produces a higher torque compared to lesser number of blades. This shows the relevance of higher number of blades at low λ conditions.

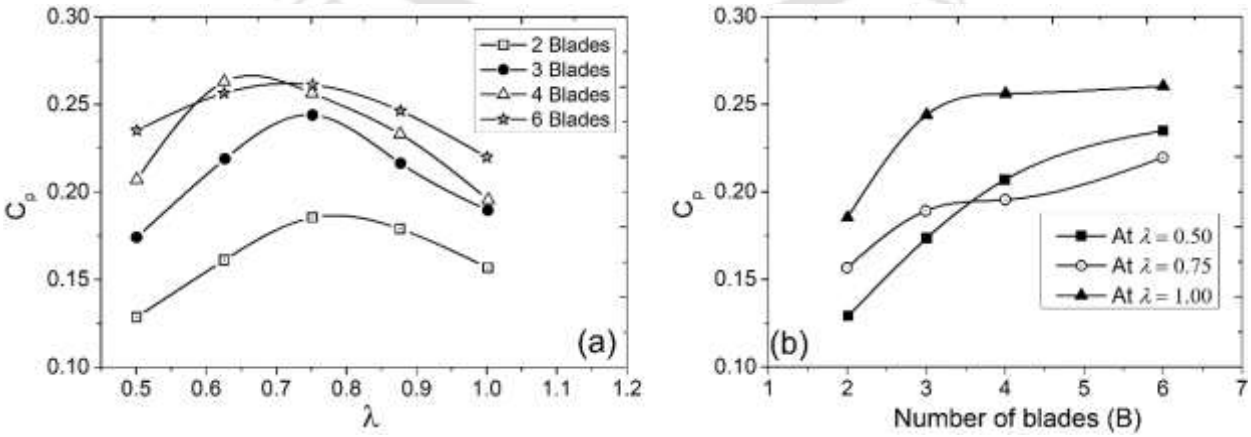

Fig. 2.10. Performance of rotor (a) with different number of blades, and (a) at defined λ (Xisto et al. 2016)

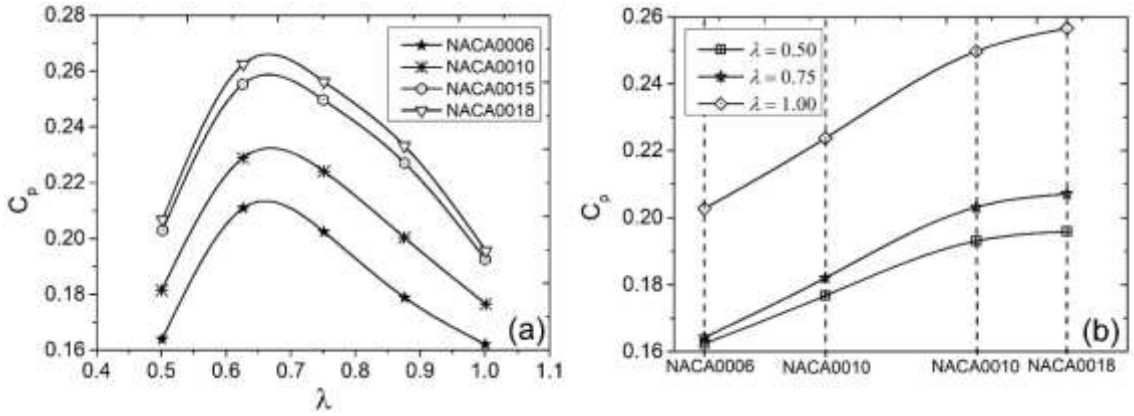

Fig 2.11. Performance of rotor (a) with different airfoil thickness, and (a) at a defined λ (Xisto et al. 2016)

2.3.3.2. Effect of yaw

During the preliminary analysis, most wind turbine models do not incorporate the effect of yaw (γ) or wake deflection. The implication of γ comes from the fact that under the omnidirectional wind gust, the effect of precise yawing would be helpful in maintaining the rotor performance. In recent times, the importance of γ on the overall wind farm performance has been studied (Grant et al. 2000; Medici and Alfredson, 2008). However, with regards to SWTs, its effect is found to be minimal. The significance of γ on the HAWT rotor performance has been presented by Bahaj et al. (2007), and their examination involves simultaneous incorporation of γ and β. The examination is performed in a water tunnel at a hub pitch angle of 20° and 25°, and the typical response at these angles is presented in Fig. 2.12 and 2.13. In both cases, it is noted that the rotor performance decreases with increases of γ, and this decrease in power is observed to be approximately a function of the cosine of γ^2 and the corresponding thrust as the cosine of γ (Bahaj et al. 2007). Furthermore, it is observed that an increase of β degrades the overall rotor performance. This can be acknowledged from the fact that it is highly unlikely to see a BEMT rotor outperformed from its design condition.

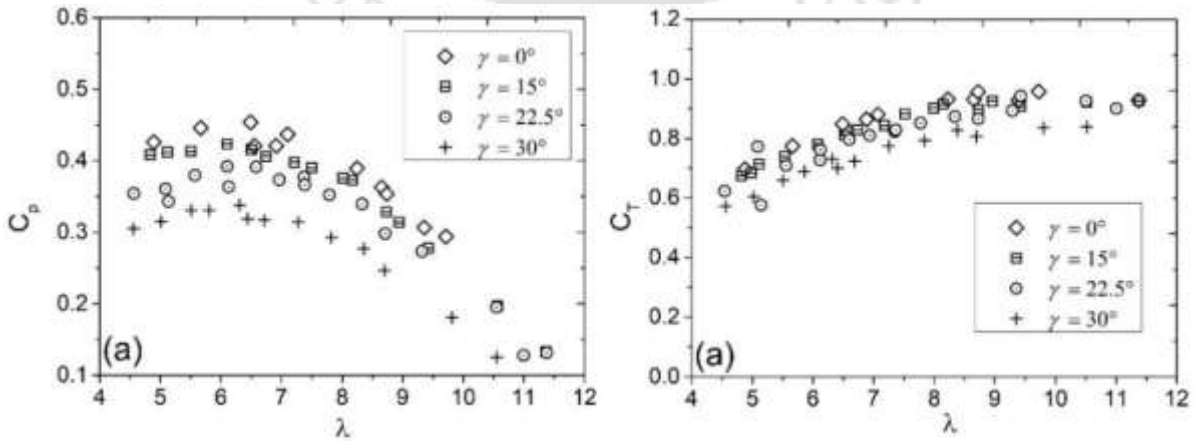

Fig. 2.12. Represents the rotor performance at β = 20° (a) *Cp* vs λ (b) C_T vs λ at different yaw angle (Bahaj et al. 2007)

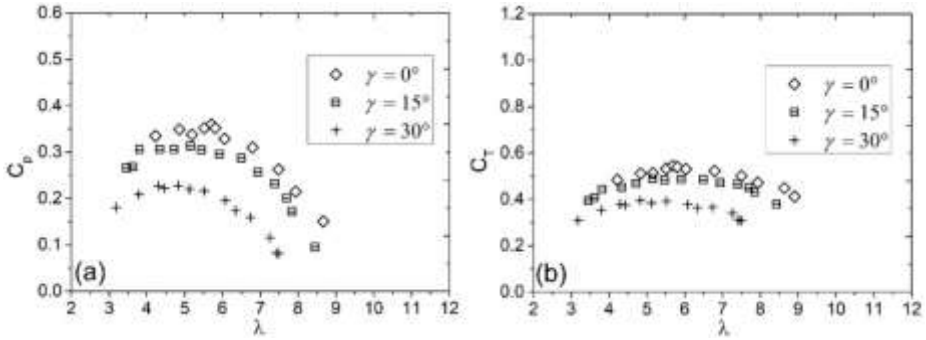

Fig. 2.13. Represents the rotor performance at β = 25° (a) *Cp* vs λ (b) C_T vs λ at different yaw angle (Bahaj et al. 2007)

Thus, one could see the degrading nature of the γ effect; however, it has a promising effect as reported (Grant et al. 2000; Medici and Alfredson, 2008) when multiple rotors are installed in a cluster/array. Similarly, one may examine the effect of yawing for the cluster of SWTs that are subjected to an omnidirectional wind gust. Thus, it is also necessary to understand the flow dynamic of wind turbine wake, when kept in cluster formation; a detailed review related to the wind turbine wake has been discussed in next section.

2.3.4 Summary and Knowledge Gaps

There are many factors which may govern the characteristics of SWTs, following are some of the principle observations:

a) The size of SWT can be put under the range of D < 5 m and with a generation capacity of a few kilowatts and the operational limit can be kept at $0.3\times10^5 \leq Re \leq 3\times10^5$ and $0.5 < \lambda < 6$.

b) The blade of SWTs is usually of constant profile as compared to LWTs. Therefore, a precise airfoil selection for the rotor blade needs to be undertaken considering low *Re* and low λ. Though at low *Re*, the rotor performance with mixed airfoil seems to be slightly improving the overall $C_{p,}$ there is not enough data/information on mixed airfoil for low λ rotor.

c) The provision of passive flow control devices can be explored on high *Re* airfoils for their application in low *Re*.

d) The symmetric airfoil having a higher *t/c* ratio seems to provide promising results.

e) For lower λ application (λ < 1.5), a higher number of blades seems to be promising; however, in the range of $0.5 < \lambda < 6$, the number of blades does not play an insignificant role in improving the rotor performance.

f) For a single rotor, the influence of yaw angle is not recommended; however, the yaw arrangement can be beneficial for multiple rotors.

g) The ducted SWT is promising, however, further research is needed to optimize and improve the flow acceleration process towards the LE of the duct.

h) Scaling down of LWT/MWT rotor blade length to meet SWT size is not promising.

i) Blade twist lowers the blade tip stall at high wind speed. If the twist increases, so is the α, this results in increase of resistive torque thus lower the C_p.

2.4 Literature Review on Wind Turbine Wake

A wind turbine as a standalone system could serve has a potential energy source. However, for an integrated system like the wind farm, staggered wind turbines, or multirotor system where the presence of nearby turbines could potentially govern the nature of whole system will require indepth understanding of wake interfereance. In this aspect, as a part of the research objective for the designing of multirotor configuration turbines, it is essential to understand the aerodynamic wake behaviour of a turbine. Thus, in this literature review section, extensive literature survey has been carried out, examing the exsisting model and their limitations.

Wind energy is one such renewable energy technology that has evolved over the years, from the Sistan windmills (7^{th} century) to 8 MW Viestas 164 (21^{st} century) large wind turbine, suggesting that a great deal of technological transition has occurred over the years (Lucas, 2005). The majority of wind power generation is anticipated to be contributed by the onshore and offshore wind turbine installations in the form of wind farms (Tasneem et al. 2020). Wind farms are clusters of large, medium, or small wind turbines often installed to generate substantial electric power. In most cases, the blades of such wind turbines are usually designed from the concept of blade element momentum theory (Bilgili et al. 2021). The overall capacity of a large wind farm is mostly in megawatt or gigawatt, and hence they play a significant role in mitigating the power requirement to a great extent. Large wind farms such as Gansu wind farm, London Array, Mupandal wind farm, and others are some of the most extensive wind energy producing facilities that occupy as much as 100 km^2 of the area (IEA, 2021; Lucas, 2005; Tasneem et al. 2020). Therefore, considering the amount of land usage, it is of utmost importance for a wind farm developer to propose a kind of layout that can not only accommodate the maximum number of turbines but also can maintain the optimum wind farm efficiency.

Maintaining an optimum wind farm efficiency is one of the critical aspects for many developers, and this has also gained significant interest among the research communities over the years. The key challenges that come in the path of wind farm modelling are the wind turbine wake expansion and prediction. Different analytical wake models have been evolved over the years to comprehend such wake propagation process. Assessment by analytical wake models comes from the fact that the turbines in the array/cluster are subjected to different sources of aerodynamic loadings. These loading can be discretized into the wind turbine wake, atmospheric boundary layer (ABL), inflow turbulence, and others. A schematic of all these flow fields is represented in Fig. 2.14. Due to the confluence of several flow field structures (Fig. 2.14) give rise to an overall wind farm boundary

layer (WFBL), and minimizing the domain of WFBL is a challenge for wind farm layout developer. Several factors determine the extent of WFBL and its subsequent implication in wind farm development; however, the most important factors that play an essential role in the wind farm modelling are shown in Fig. 2.15.

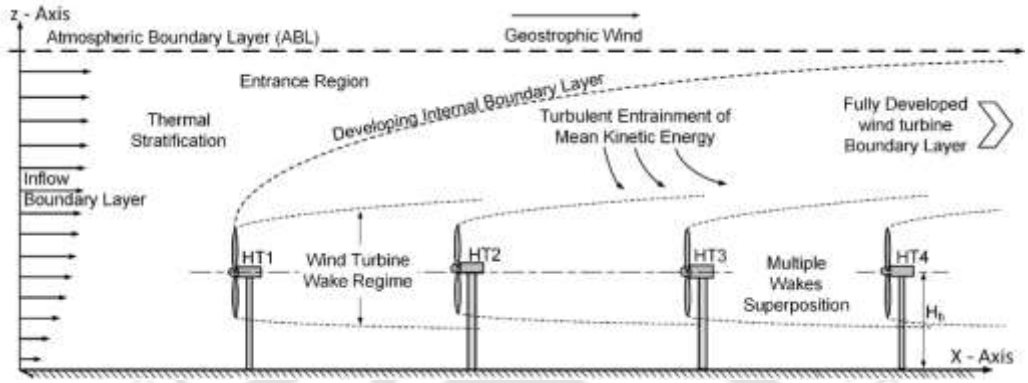

Fig. 2.14. Depiction of wind turbine array boundary layer (Steven and Meneveau, 2017)

Fig. 2.15. Important factors of wind farm modelling

2.4.1 Significance of Wake Studies

A wind turbine converts the kinetic energy of wind into mechanical energy and, further with the help of a generator, to electrical power. As per the aerodynamic law of wind turbines, a turbine can only extract about 59% of total wind energy, which is often referred to as Betz's limit (Manwell et al. 2009). This constrain is due to the fact that when wind flow passes from upstream to downstream of the turbine, it becomes slower due to losses in its momentum. As a result, the downstream turbines could experience their generating potential to be about 20-46% compared to operating under unobstructed conditions (Adaramola and Krogstad P-Å, 2011). An analogous observation was also made by McKay et al. (2013) through supervisory control and data

acquisition for a six months' duration, where a drop of about 35% in the first downstream turbine was observed. This drop in performance heavily relied on the separation distance, such as the field investigation conducted by Barthelmie et al. (2007) at Middelgrunden wind farm, Denmark where they found about 10% drop for 4D (D being the rotor diameter) separation. On the other hand, Sorensen et al. (2002) have noted a 12.4% drop in performance when the separation is 8D; the investigation was carried out at Horns Rev wind farm, Denmark. The scenario would be different for the offshore and onshore wind farms that are usually differentiated on the basis of ambient turbulence (T_a). Typically, the T_a for offshore is found to be between 6 to 8%; however, it is relatively higher at the onshore (Barthelmie et al. 2002). Indeed, one can certainly acknowledge the importance and need for accurate wake modeling that will help estimate the annual energy production of a wind farm.

2.4.2 Wind Turbine Wake Regimes

The wind turbine wake is often discretized into two regimes: the near wake and the far wake. The near wake is the regime taken just behind the rotor plane, as shown in Fig. 2.16, where the flow field properties are examined usually till 2D or 3D. In Fig. 2.16, R is the rotor radius, non-dimensional distance x/R, z/R, and y/R represents the streamwise, lateral and vertical direction, respectively. Within this regime, the wake properties could be associated with the rotor blade geometry and aerodynamics (Kumar et al. 2021; Vermeer et al. 2003). The near wake region investigation mainly focuses on the behavior of vortex patterns without considering the topographical features. Most wake models consider the near wake regimes as uniform, steady, and parallel flow conditions. However, in the actual scenario, the situation is much more complex while considering the wind shear, rotor tower interaction, nacelle influence, yawed effect, dynamic stall, and aero-elastic behaviors essential for the long term power estimation of the wind turbine and the wind farm (Sørensen and Shen, 2002; Steven and Meneveau, 2017). On the other hand, the far wake is the wake regime where continuous helical vortex structure disappears, and this regime is mainly associated with wind farm modelling (Steven and Meneveau, 2017; McKay et al. 2013; Vermeer et al. 2003). The end of the far wake regime is often marked by the advancement of fully developed flow or when normalized velocity reaches unity. Although most of the models suggest 70-90% flow recovery in the range of 8D-12D from the rotor plane, a minimum of 5D is usually recommended for turbine spacing to subdue the influence of wake considering the cost of operation, land, and transmission losses (Chen and MacDonald, 2012; Manwell et al. 2009). The wind turbine placement becomes more perplexing when there is limited allotted land for the wind farm setup.

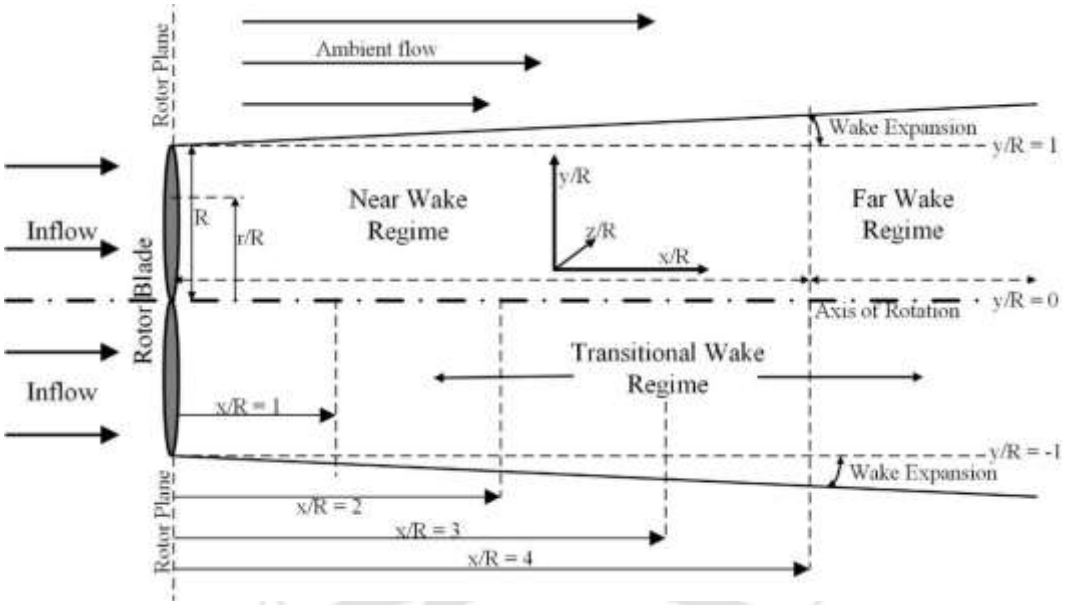

Fig. 2.16. Wind turbine downstream wake regime distribution

2.4.2.1 Near Wake Regime

As the name suggests, the near wake regime defines the flow field close to the rotor. As of now, there are not many empirical relations that define the near wake characteristics. One of the foremost correlations is given by Vermeulen et al. (1980), where the length of the near wake in terms of wake growth rate (dr/dx) is expressed by Eq. (2.23).

$$x_n = \frac{nr_0}{\left(\frac{dr}{dx}\right)} \tag{2.23}$$

where, $r_0 = R\sqrt{\frac{m+1}{2}}$

$$m = \frac{1}{\sqrt{1-C_T}}; \quad n = \frac{\sqrt{0.214+0.144}\left(1-\sqrt{0.134+0.124m}\right)}{\left(1-\sqrt{0.214+0.144m}\right)\sqrt{0.134+0.124m}}$$

The wake growth rate $\left(\frac{dr}{dx}\right)$ is expressed by Eq. (2.24)

$$\frac{dr}{dx} = \sqrt{\left(\frac{dr}{dx}\right)_a^2 + \left(\frac{dr}{dx}\right)_m^2 + \left(\frac{dr}{dx}\right)_\lambda^2} = \sqrt{G_a^2 + G_m^2 + G_\lambda^2} \tag{2.24}$$

where, $\left(\frac{dr}{dx}\right)_a = G_a = 2.5I_a + 0.005$; $\left(\frac{dr}{dx}\right)_m = G_m = \frac{(1-m)\sqrt{1.49+m}}{(1+m)9.76}$

and, $\left(\frac{dr}{dx}\right)_\lambda = G_\lambda = 0.012B\lambda$

where G_α, G_m, and G_λ define the wake growth rate due to ambient turbulence, wake shear-generated turbulence, and mechanical turbulence, respectively. The parameter C_T and λ are the thrust coefficient and tip speed ratio, respectively, whereas I_a and B represent the ambient turbulence and the number of blades. Another earliest empirical relation on the near wake is presented by Lissaman, 1979. This model assumes the wake growth by turbulent entrainment at its edge that introduces the free stream momentum as well as mass into the wake and considers the idealistic constant pressure field. As per the *Lissaman* model, the radius of the near wake regime at the beginning can be expressed by Eq. (2.25).

$$r_o = R\sqrt{\frac{(m_w + 1)}{2}} \tag{2.25}$$

The radius of wake at the end of near wake regime is expressed by Eq. (2.26)

$$r_c = \frac{r_o}{(0.214 + 0.144 m_w)^{0.5}} \tag{2.26}$$

Here, m_w is the ratio of freestream velocity to the velocity of wake (U_{cw}) at the core of turbine wake as given by Eq. (2.27).

$$m_w = \frac{U_\infty}{U_{CW}} \tag{2.27}$$

Moreover, Lissaman argues that the wake growth is defined by three turbulent components within the near wake regime. In contrast, in the far wake regime, the development of the wake is driven mainly by ambient turbulence (I_a). Furthermore, the transversal wake profile is characterized by the shear layer outside the wake core. On the contrary, the near wake regime terminates when the outer shear layer meets the centerline of the wake. As a result, the velocity deficit decreases with increasing distance from the rotor plane.

2.4.2.2 Far Wake Regime

The far wake regime, on the other hand, is the regime of the wind turbine flow field beyond 3D to 5D (Fig. 2.16). This flow domain is often discussed up till when the normalized velocity reaches unity that is often expressed to be around 8D-12D (Vermeer et al. 2003; Steven and Meneveau, 2017). The far wake regime is mostly considered for the wind farm modeling, and the information on this regime helps in the optimization of a wind farm. Tracking the limit of the far wake regime can be acknowledged by assessing the normalized velocity; however, its initiation segment is always doubtful. One may dictate the starting regime after the near wake or towards the end of

the transitional regime. Schepers, (2003) have discussed the initialization of far wake from 2.25D with a hat-shaped velocity deficit, however, this limit seems to be debatable. In any case, most of the models predict the flow recovery by 70-90% between 8D to 12D. Although, considering the cost of installation, land usage, and transmission losses, a minimum space of 5D is usually recommended for turbine spacing to subdue the influence of wake (Chen and MacDonald, 2012; Manwell et al. 2009). The major discrepancy associated with the far wake comes from considering the wake generated shear from the turbine nacelle, supporting tower, and atmospheric boundary layer (ABL). Al Sam et al. (2017) have noted the effect of ABL that significantly alters the far wake. As per their findings, the velocity magnitude is relatively higher for higher ABL and indicates higher TI with large eddy viscosity but with lesser isotropic nature. Furthermore, with an increase in the ABL height, the overall energy production and the power coefficient (C_p) also increase. Various wake models like that of the kinematic and field models are meant for far wake analysis, and more details of these models are discussed in subsequent sections.

2.4.2.3 Transitional Near-to-Far Wake Regime

Apart from the near and the far wake regimes, the study on the transitional regime is also a matter of discussion for the wind turbine wake modelling. Although there is not much research work available on this regime, this regime is likely to fall within 2D-4D, where the helical vortex structure starts losing its integrity. Perhaps with precise instruments like the particle image velocity, and light detection and ranging, one may be able to dictate this regime. Understanding this regime shall help predict the wind turbine wake and its expansion process more accurately. One of the few studies that gave some information on the transitional regime is presented by the Lissaman model (Lissaman, 1979). In this model, the velocity deficit in the transitional region is expressed as a linear combination of flow profiles. The radii of turbine wake at the beginning (r_c) and at the end of the transition (r_F) are expressed by Eqs. (2.28) and (2.29).

$$r_c = \left(\frac{dR_w}{dx}\right) x_c + r_o \tag{2.28}$$

$$r_F = \frac{r_o}{\left(0.134 + 0.124 m_w\right)^{0.5}} \tag{2.29}$$

And the extent of transition regime (x_t) is expressed by

$$x_t = \frac{x_c \left(0.214 + 0.144\right)^{0.5} \left(1 - \left(0.134 + 0.124 m_w\right)^{0.5}\right)}{\left(\left(0.134 + 0.124 m_w\right)^{0.5}\right)\left(1 - \left(0.214 + 0.144\right)^{0.5}\right)} \tag{2.30}$$

where R_w is radius of wake, x_c is the extent of near wake downstream of the rotor, dR_w/dx is the wake growth rate, and r_o is the near wake radius close to the rotor plane.

2.4.3 Wind Turbine Wake Models

The wind turbine wake models are categorized into the Kinematic, Field, and Wake added turbulence models, as depicted in Fig. 2.17. These models could be for single or for multiple turbines.

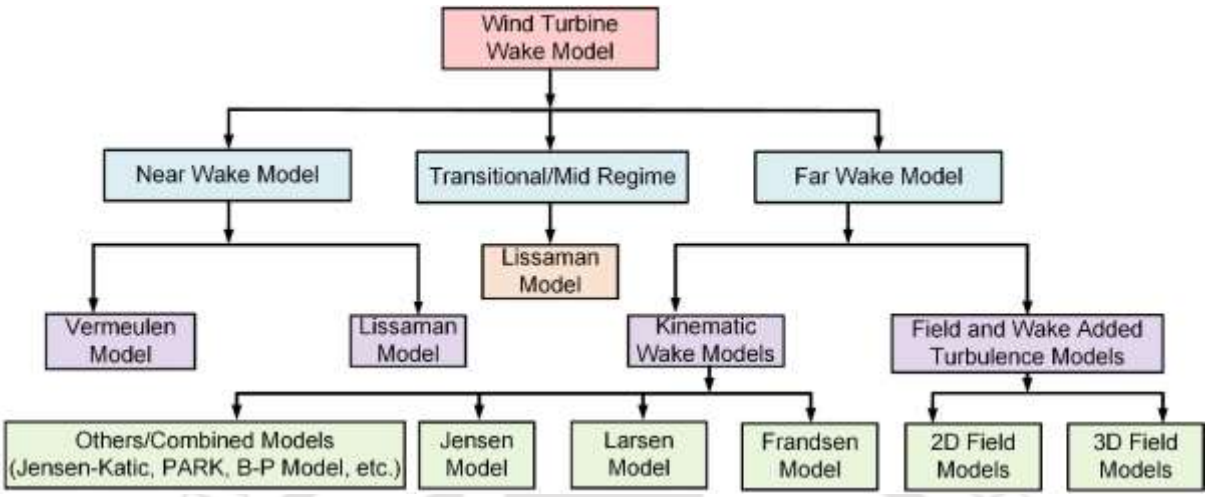

Fig. 2.17. Wind turbine wake models

2.4.3.1 Kinematic Wake Models

The kinematic wake model uses the momentum equation to model the velocity deficit of the wake behind a turbine. The model does not cover the change in turbulence intensity (TI), and therefore, the model has to be coupled with a turbulence model. Furthermore, the model does not include the ambient turbulence; as a result, the velocity deficit perturbation is considered negligible. The TI is considered axisymmetric, and hence, the wake has self-similar distribution. The self-similarity of the velocity, velocity deficit, or TI profiles is the fundamental feature of the kinematic model describing the wind turbine wakes (Vermeer et al. 2003). Some of the pioneering Kinematic models are proposed by Larsen, Jensen, Frandsen, and others (Fig. 2.17). These models are described below.

2.4.3.1.1 Jensen Wake Model

The Jensen's wake model is one of the pioneering and extensively explored wake model (Vermeer et al. 2003; Steven and Meneveau, 2017). This simplest model proposed for a single rotor was initially coined by Jensen, (1983) and later modified by Katic (Katic et al. 1987). The model is only meant for far wake estimation, so it does not include any information on the helical vortex shedding. The wake deficit or velocity deficit is considered linearly distributed, which is mostly expressed in terms of distance from the rotor plane. In recent times, the applicability of the Jensen model has been reviewed extensively (Shakoor et al. 2016), where the model assumes the turbine wake to be turbulent and does not consider the participation from the tip vortices. The model is

found to be applicable to the offshore wind farm as it gives a reasonable energy prediction with minimum error. Some other assumptions made in the Jensen model are:

- The near field behind a wind generator is neglected.
- The areal spread of momentum deficit of a feature like this is such that linear momentum is proportional to downwind distance *x*.
- The wake expansion is linear.
- The velocity behind the rotor is axisymmetric (Fig. 2.18).
- The velocity just behind the rotor is 0.33*U* in accordance with the classical Betz's theory.
- The entrainment constant is taken as 0.1.

For a single turbine Jensen wake model (Fig. 2.18), the wake radius is given by Eq. (2.31) (Jensen, 1983).

$$R_w = R(1+2kx) \tag{2.31}$$

And the velocity in the fully developed wake expressed by Eq. (2.32) (Jensen, 1983).

$$U_d = U_\infty \left(1 - \frac{1-\sqrt{1-C_T}}{(1+2k\mu)^2}\right) A_w \tag{2.32}$$

$$\text{where, } k = \frac{0.5}{\ln(H_b / h_o)}$$

where μ is the relative distance behind the rotor, $\mu = x/D$, k is the wake decay constant, C_T is thrust coefficient and A_w is area of the wake. And as per Eq. (2.32), the value of U_d in the wake is constant for a defined μ, and here the velocity profile is expressed as 'hat-shaped'. The value of k is a function of the turbine's hub height (H_b) and surface roughness height (h_o). For most the onshore wind farm, k is taken as 0.075, whereas for the offshore wind farm, it is considered to be 0.04. Now, just behind the rotor plane where the wake expansion is negligible ($k \approx 0$), the downstream velocity can be expressed by Eq. (2.33).

$$U_d = U_\infty \sqrt{1-C_T} \tag{2.33}$$

Since the Jensen model does not include the influence of vortex shedding, Eqs. (2.32) and (2.33) are mostly considered for the far wake regime. As per Hans (Han, 2011), these equations are applicable in the range of 3D to 5D for the onshore and 6D to 8D for the offshore wind farms. Further, one can see through Eq. 2.33 that to have a real value of U_d, the value of C_T must be less than unity.

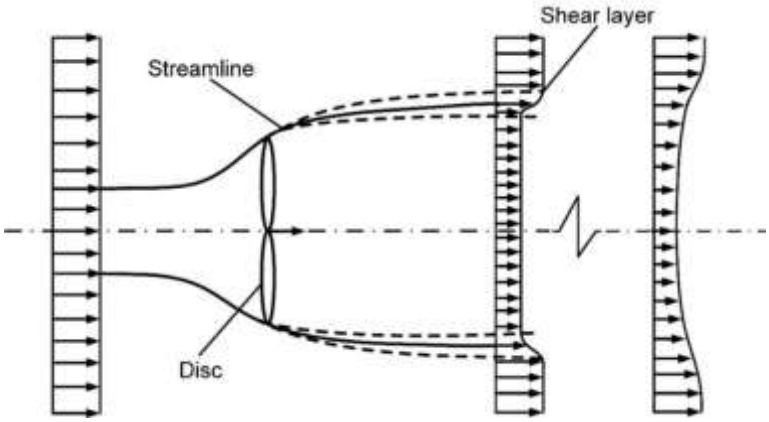

Fig. 2.18. Schematic representation of wind turbine wake

2.4.3.1.2 Larsen Wake Model

Larsen (Larsen, 1988) gave an analytical model that was mainly based on the wake theory discussed by Schlichting, (2014). This model was also initially formulated for the single turbine. The model includes the Prandtl turbulent boundary layer equations, and its close form solution produces the width of turbine wake and the velocity profile that includes the axial and radial velocity fields. The schematic of the Larsen wake model coordinate system is shown in Fig. 2.19.

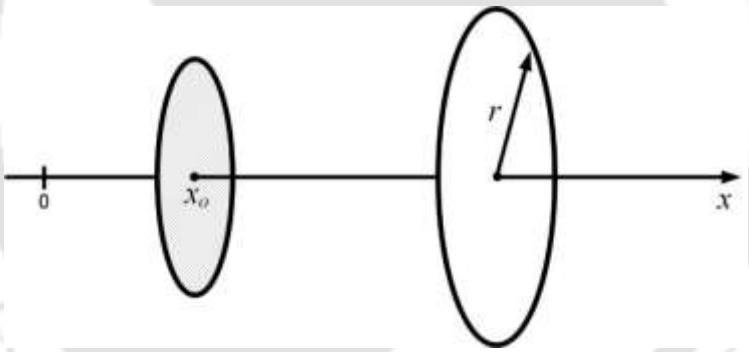

Fig. 2.19. The coordinate layout of Larsen wake (Larsen, 1988)

Larsen gave the first and second order model of the wake behind a wind turbine that is based on the turbulent equations. The profile is considered axisymmetric, and a single self-similar velocity profile is considered for the overall wake. From the analytical solution of Larsen's first order model, the downstream axial and radial velocities at some axial and radial distance within the wake are obtained from Eqns. (2.34) and (2.35), respectively. Further, the radius of wake at any downstream axial position $R_w(x)$ can be expressed by Eq. (2.36).

$$U_d(x,r) = -\frac{U_\infty}{9}\left(c_T A x^{-2}\right)^{1/3}\left[r^{3/2}\left(3c_1^2 c_T A x\right)^{-1/2} - \left(\frac{35}{2\pi}\right)^{3/10}\left(3c_1^2\right)^{-1/5}\right]^2 \quad (2.34)$$

$$U_r(x,r)=\frac{U_\infty}{3}\left(c_T A\right)^{1/3} x^{-\frac{5}{3}} r\left[r^{3/2}\left(3c_1^2 c_T A x\right)^{-1/2}-\left(\frac{35}{2\pi}\right)^{3/10}\left(3c_1^2\right)^{-1/5}\right]^2 \tag{2.35}$$

$$R_w(x)=\left(\frac{35}{2\pi}\right)^{1/5}\left(3c_1^2\right)^{1/5}\left(c_T A x\right)^{1/3} \tag{2.36}$$

where,

$$c_1=\left(\frac{R}{\alpha_1}\right)^{5/2} x_o^{-5/6};\ \alpha_1=\left(\frac{105}{2\pi}\right)^{1/5}\left(c_T A\right)^{1/3} \text{ and } x_o=\left(\left(\frac{R}{\alpha_1}\right)^{-3}\left(\frac{\beta_1}{(U_\infty-U_m)}\right)^{3/4}-1\right)^{-1}\Delta x$$

The measure of axial velocity that depends on Δx (distance measured from the wind turbine rotor) is expressed by Eq. (2.37) (Larsen, 1988).

$$U_m=U_\infty\left(1-\beta_1 c_1^{-4/5}\left(x_0+\Delta x\right)^{-2/3}\right) \tag{2.37}$$

where,

$$\beta_1=\left(\frac{1}{9}\right)(3)^{-2/5}\left(\frac{35}{2\pi}\right)^{3/5}\left(c_T A_w\right)^{1/3}$$

where A_w is the area of the wake. The velocity deficit decay in Larsen model is similar to one presented by Crespo and Hernandez, (1993, 1996). The decay rate is proportional to downstream position $x^{-2/3}$ and turbulence intensity decay as $x^{-1/3}$. In the later part of Larsen wake model research (Larsen and Réthoré, 2009), the model was modified with the inclusion of wake interaction that helps in quantifying the performance of the wind farm. At the same time, the proper calibration of the wake model through the rotor's full-scale experimental observation on its flow field was performed. The updated governing equations are expressed as per Eqs. (2.38) through (2.41).

$$u_x(x,r)=-\frac{U_\infty}{9}\left(c_T A\left(x+x_0\right)^{-2}\right)^{1/3}\left[r^{3/2}\left(3c_1^2 c_T A\left(x+x_0\right)\right)^{-1/2}-\left(\frac{35}{2\pi}\right)^{3/10}\left(3c_1^2\right)^{-1/5}\right]^2 \tag{2.38}$$

$$R_w(x)=\left(\frac{35}{2\pi}\right)^{1/5}\left(3c_1^2\right)^{1/5}\left(c_T A\left(x+x_0\right)\right)^{1/3} \tag{2.39}$$

where, C_1 represents the non-dimensional mixing length express as per Eqns. (2.40) and (2.41).

$$c_1=\left(\frac{105}{2\pi}\right)^{-1/2}\left(d_1 R\right)^{5/2}\left(c_T A x_o\right)^{-5/6}=l\left(C_T A(x)\right)^{1/3} \tag{2.40}$$

where, l is the Prandtl's mixing length

$$x_o = \left(\frac{9.6D}{\left((2R_{9.6} / d_1 D)^3 - 1 \right)} \right) \tag{2.41}$$

where, $d_1 = \left\{ \left(1 + \frac{1}{\sqrt{1 - C_T}} \right) / 2 \right\}^{0.5}$

where, $R_{9.6}$ is the radius of wake at a downstream distance of x/D = 9.6 from the rotor plane. The corresponding expression of the wake radius is obtained empirically from the field data as per Eq. (2.42).

$$R_{9.6} = 2a_1 \exp\left(a_2 c_T^2 + a_3 c_T + a_4 \right)\left(b_1 I_a + 1 \right) R \tag{2.42}$$

In Eq. (2.42), the a_1, a_2, a_3, a_4, and b_1 are constants assumed in the updated Larsen model (Larsen, 1988). Since the updated model considers the interference of wakes, the mean effective wind speed at such a scenario is given by Eq. (2.43).

$$U_{eff}^2 = \frac{1}{A} \int U^2 dA \tag{2.43}$$

Further, the effective wind speed within the wind farm is calculated using a linear superposition of wakes as expressed by Eq. (2.44).

$$U_w^{eff} = U_{eff} - \sum_{i=1}^{N_u} u_{x_i} \tag{2.44}$$

where, N_u defines the number of upstream wind turbines in a wind farm.

2.4.3.1.3 Frandsen Wake Model

Another single wind turbine wake model is presented by Frandsen et al. (2006). The model is evolved from the Betz-Lanchester theory that provides the relation for thrust coefficient (C_T) and power coefficient (C_p) of the wind turbine. The model considers a cylindrical control volume having a cross-sectional area that is equal to the area of wake, as shown in Fig. 2.20.

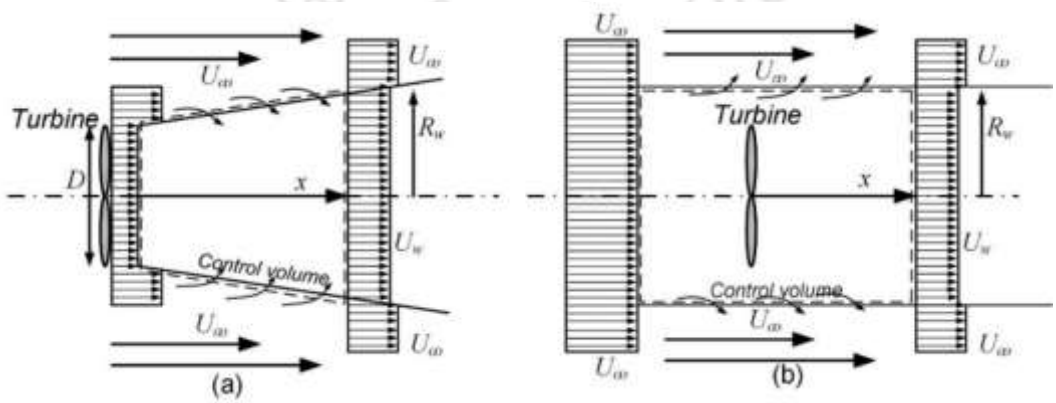

Fig. 2.20. Schematic of the two control volumes: (a) downwind of the wind turbine, and (b) around the wind turbine

The velocity deficit is evaluated through the momentum balance equation between the upstream/freestream flow and the downstream wind turbine wake. Furthermore, the model considers a simplified integral version of the momentum equation for evaluating the momentum deficit in the wake. The Frandsen model is also axisymmetric and has a top-hat velocity/velocity deficit profile as expressed by Eq. (2.45) (Frandsen et al. 2006).

$$\frac{U_w(x)}{U_\infty} = \frac{1}{2} \pm \frac{1}{2}\sqrt{1-2\frac{A}{A_w(x)}c_T} \tag{2.45}$$

where A is the swept area of the rotor, and A_w is the wake area at downstream distance x. In Eq. (2.45), the "+" is implied when the range of is $0 \leq C_T \leq 0.75$ and considered as "-" when $C_T \geq 0.75$. The size of the wake downstream of the rotor is expressed by Eq. (2.46).

$$R_w(x) = \left(\beta^{\frac{k_s}{2}} + \alpha_s s\right)^{\frac{1}{k_s}} R \tag{2.46}$$

The wake decay factor (α_s) is expressed as per Eq. (2.47)

$$\alpha_s = \beta^{\frac{k_s}{2}}\left(\left(1+2\alpha_{noj}s\right)^{k_s} - 1\right)s^{-1} \tag{2.47}$$

$$\textit{where,} \qquad \beta = \frac{\left(1+\sqrt{1-c_T}\right)}{\left(2\sqrt{1-c_T}\right)};\ \alpha_{noj} \approx 0.05 \text{ and } s = \frac{0.5x}{R}$$

One can express the initial size of the wake as per Eq. (2.48).

$$R_w(x=0) = R_w^I = \sqrt{\beta}R \tag{2.48}$$

The Frandsen model can be used in three different scenarios of a wind farm that are a very handful in predicting the performance of turbines in a regular array. In the first scenario, a single or multiple wake profile is obtained without considering the interference from nearby turbines. The second scenario is taken when two nearby turbine wake interacts, and the wake expansion is only subjected to the vertical direction. In the third scenario, as the turbine wake expands, it is balanced with the Planetary Boundary Layer.

2.4.3.1.4 Jensen-Katic Wake Model

This model is the update from the earliest Jensen model, although this model still relies on axisymmetric self-similar velocity distribution. This model has been widely implemented in the engineering wake model (Jensen 1983; Katic et al. 1987; Ainslie, 1988). The velocity deficit defined by this model is expressed by Eq. (2.49) (Katic et al. 1987).

$$Vel\_def = \frac{\Delta U}{U_\infty}(C_T, x) = \frac{1-\sqrt{1-C_T}}{\left(1+\frac{0.5 I_a x}{R}\right)^2} \tag{2.49}$$

$$where, \qquad I_a = 2\alpha = \frac{1}{\ln\left(\frac{H_b}{h_o}\right)}$$

Here, I_a is the ambient turbulence intensity, which is often expressed as $I_a = 2\alpha$, α denotes the momentum entrainment constant (or decay coefficient). The model describes that the wake expansion is proportional to the downstream distance from the rotor plane and can be expressed as per Eq. (2.50).

$$R_w(x) = \alpha x + R \tag{2.50}$$

2.4.3.1.5. B-P Wake Model

This model, proposed by Bastankhah and Porté-Agel, (2014), is evolved from the mass and momentum conservation theory applied across the rotor. Although, the derivation procedures and the governing equations employed are somewhat similar to the Frandsen model Frandsen et al. 2006). This model presents a Gaussian distribution profile for the velocity deficit as expressed by Eq. (2.51).

$$Vel\_def(x,r) = \frac{\Delta U}{U_\infty} = \left(1-\sqrt{1-\frac{C_T}{8(0.5k^* x/R+\varepsilon)^2}}\right) \times \exp\left(-\frac{1}{2(0.5k^* x/R+\varepsilon)^2}\left\{\left(\frac{h-H_b}{2R}\right)^2+\left(\frac{y}{2R}\right)^2\right\}\right) \tag{2.51}$$

Here,

$$\varepsilon = 0.25\sqrt{\beta}\,; \quad \beta = \frac{\left(1+\sqrt{1-c_T}\right)}{\left(2\sqrt{1-c_T}\right)}$$

The wake radius is given by Eq. (2.52)

$$r_x = R\sqrt{(\beta + 0.5\alpha x/R)} \tag{2.52}$$

where k^* is the growth rate, H_b is the height of rotor hub, α is the wake decay coefficient, h and y are vertical and spanwise coordinates, respectively. The model assumed that the velocity deficit just after the rotor plane is uniformly distributed; however, as per Eq. (2.51), it transforms into a Gaussian shape as it moves far from the rotor plane.

2.4.4 Multiple Wake Model

The models discussed above are best suited for characterizing the single wake model. However, a wind farm encompasses multiple turbines, and as a result, any turbine within the domain of a wind farm could be exposed to flow field directed from nearby turbines. Such as the case of the T7 rotor, as shown in Fig. 2.21. Understanding the superposition of multiple wakes is complicated due to its imperceptibility under normal observation and complex turbulence phenomena (Steven, and Meneveau, 2017; Manwell et al. 2009; Vermeer et al. 2003). There are several approaches to deduce the wake interaction model; however, as reported (Kuo et al. 2015), four governing techniques are primarily listed in Table 2.5 suitable for the multiple wake superposition. The following subsection discusses the multiple wake models mainly formulated on these conditions. In Table 2.5, u_i represents the wind speed upstream (close to rotor plane) of turbine i, u_{ij} is the wind speed at turbine i under the wake influence of turbine j and 'n' is number of turbines.

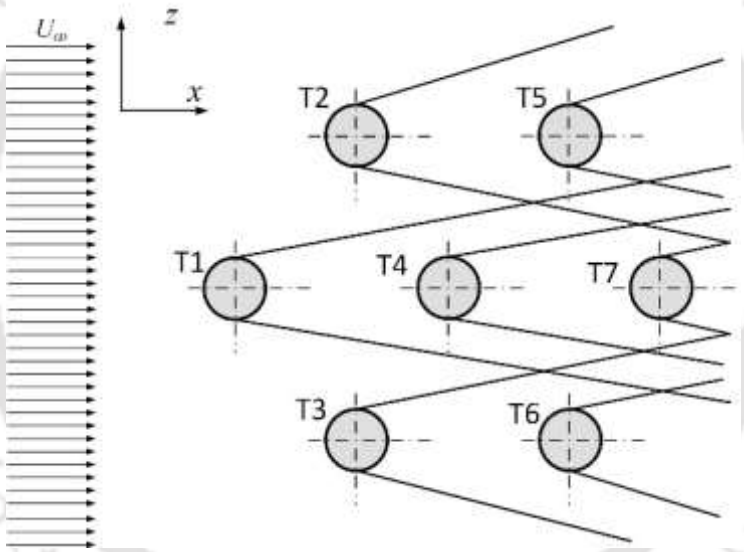

Fig. 2.21. Multiple wake effect in windfarm

Table 2.5 List of some wake interaction models (Kuo et al. 2015; González-Longatt et al. 2012)

Sl. No.	Description	Expression
1.	Geometric superposition	$\frac{u_i}{U_\infty} = \prod_{j=1}^{n}\left(\frac{u_{ij}}{u_j}\right)$
2.	Linear superposition of velocity deficit	$\left(1-\frac{u_i}{U_\infty}\right) = \sum_{j=1}^{n}\left(1-\frac{u_{ij}}{u_j}\right)$
3.	Sum of squares	$\left(1-\frac{u_i}{U_\infty}\right)^2 = \sum_{j=1}^{n}\left(1-\frac{u_{ij}}{u_j}\right)^2$
4.	Sum of energy deficits	$\left(U_\infty^2-u_i^2\right)^2 = \sum_{j=1}^{n}\left(u_j^2-u_{ij}^2\right)$

2.4.4.1 Jensen-Multiple Wake Model

Inspired by the Jensen single wake model (Jensen, 1983), González-Longatt et al. (2012) presented a multiple wake effect, where the wake interferences are analogues to the shadowing effect. A typical overview of shadowing on the downstream turbine is presented in Fig. 2.22. The model considers that any arbitrary wind turbine (*j*) is affected by the nearby upstream turbine (*i*) as well as by other upstream turbines, say T1, T2, and T3. The downstream wind speed from the turbine (*i*) and other upstream turbines are combined to form a single wake effect. This single wake effect from multiple rotors is expressed in terms of the shadowed area (A_{shadow}), which is considered to measure the degree of overlap between the area spanned by the wakes shadow cone and the turbine swept area under shadowing (A_o). The area of shadow on a turbine is expressed as per Eq. (2.53), considering that all rotors have the same diameter.

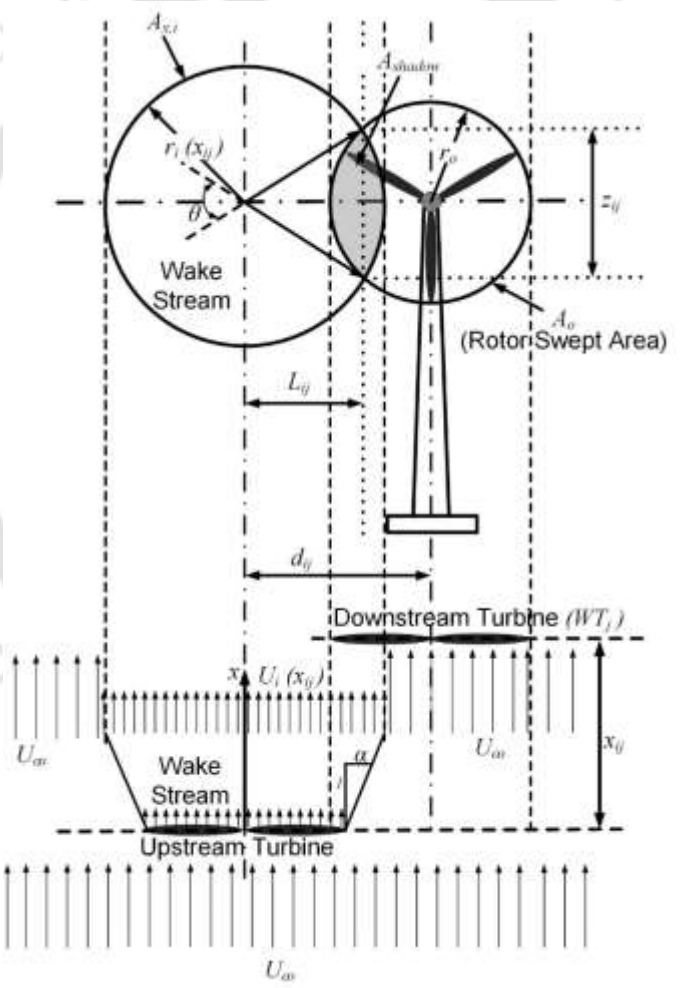

Fig. 2.22. Typical representation of wake interference (González-Longatt et al. 2012)

$$A_{shadow,i} = [r_i(x_{ij})]^2 \cos^{-1}\left(\frac{L_{ij}}{r_i(x_{ij})}\right) + r_o^2 \cos^{-1}\left(\frac{d_{ij} - L_{ij}}{r_i(x_{ij})}\right) - d_{ij} z_{ij} \tag{2.53}$$

The effective wake speed upstream of turbine (*j*) is expressed as per Eq. (2.54).

$$U_j(x_{ij}) = U_i\left[1-\sum_{i=1}^{n}(1-\sqrt{1-C_T})\left(\frac{r_o}{r_i(x_{ij})}\right)^2\frac{A_{shadow,i}}{A_o}\right] \quad (2.54)$$

where x_{ij} is the separation distance between upstream turbine (i) and downstream turbine (j), $r_i(x_{ij})$ is the radius of wake shadow behind the upstream turbine (i) at a distance of x_{ij}, L_{ij} is the distance between the wake shadow centre and the point of interference of shadow and turbine (j), and d_{ij} is the distance between the centre of the downstream turbine (j) and the centre of shadow that is $d_{ij} = r_i(x_{ij}) + r_o$.

2.4.5 Wind Turbine Wake Studies

In an array/cluster of rotors, the wake characterization is a critical consideration that must be examined precisely. The various analytical models as discussed in previous subsections though addresses the fundamental procedures of wake characterization, often overestimates. Hitherto, the most reliable approach to address such issues is through experimental or numerical analyses. Subsequently, necessary correction in the formulations can be incorporated based on the data collected. Grant and Parkin, (2000) have performed wake investigation using a non-blade element momentum theory rotor that suggests the dependence of trailing vortex circulation on the rotor phase and yaw angle (γ). The tangential velocity is found to be relatively higher within 15-30% of radial distance. The dependence of γ on performance is also acknowledged by Adaramola and Krogstad (2011). They noted the enhancement of overall C_p while keeping the upstream turbine at yaw condition ($\gamma \neq 0°$), and in this case, the C_{pmax} of the downstream rotor increased by about 12%. Further, the improvement of C_{pmax} is seen upon enhancing the separation distance (x/R). A wind tunnel investigation by Jackson and Amano, (2017) has observed the near wake regime to be around $x/R < 6$. They have observed asymmetric deficit distribution within $x/R \leq 4$ and towards the lower half of the turbine, where more erratic and higher deficit magnitude is observed due to the turbulence created by the tower and its interaction with the wakes of rotating blades. For dual rotors (4R apart), a relatively higher velocity deficit is noted after the second rotor (for $x/R < 4$). Similarly, for three rotors in arrays (4R apart), the maximum velocity deficit is observed after the third rotor (for x/R < 4). There is a substantial deviation between experimental and simulation, mostly towards the centerline (hub region). Medici and Alfredson, (2006,2008) have noticed that towards the outer part of the tip vortex, a relatively higher velocity peak occurs at every vortex passage. Furthermore, the propagation of tip vortices along the streamwise direction is found to be around 0.75U close to 3D, and beyond this, the streamwise velocity (U_x) vanishes. Duo et al. (2019) have performed experimental investigation on two scale-down wind turbine models that are aligned in an array with a spacing of 5D. The upstream rotor can produce a C_{pmax} = 0.23, whereas the C_{pmax} of the downstream turbine varies with λ. Their examination of the wake study suggests the occurrence of maximum velocity deficit when the rotor is operating at optimum λ.

Further, the power loss of about 70% to 40% is noted while the downstream rotor is kept from 5D to 7D. The downstream optimum λ decreases under the influence of upstream wake. They have noticed that the spanwise offset turbine separation is more beneficial than streamwise separation w.r.t power extraction potential.

Apart from the geometric reliance on the wake characteristics, the wind turbine wake subjected to the surface boundary layer effect or atmospheric boundary layer (ABL) effect is also a critical factor. For large wind turbines having a hub height of more than 50 m, the result may not be much of significance, but for small turbines with lesser height, the effect of ABL cannot be totally neglected. Hancock et al. (2014) have examined the influence of ABL under three categories viz., (a) base-line neutral case, (b) stable, and (c) unstable. They observed large and small velocity deficits under the stable and unstable ABL. The field study performed at a potential wind site in Chile by Becerra et al. (2017) has examined the wake flow at the height of 15 m. A software program like the HOMER can be extensively used in demand and supply curve characterization Hancock et al. (2014). Wei et al. (2014) have examined the effect of counter-rotating down-scale wind turbines and their subsequent wake interaction. Interestingly, they have observed a 20% improvement in performance while the rotors are in counter-rotating configuration compared to the co-rotating arrangement. Beyond 6.5D, the counter-rotating effect on the downstream turbine diminishes. Annoni et al. (2016) have examined the wake expansion using particle image velocimetry on the array of three rotors kept at 5D spacing. The measurement at the 3D downstream location of the rotor suggests the wake expansion from 0.5 to 0.82D and 0.5 to 0.74D at de-rated and rated conditions, respectively. The wake expansion is less in the case of the rated condition. Tian et al. (2017) have tested models rotors (D = 0.25 m and H_b = 0.225) for a set of three wind farm layouts. Their investigation suggested the presence of developing, developed, and equilibrium wake states. Some more critical findings/observations on the wind turbine wake through experimental and numerical analysis are summarized in Table 2.6. Once the velocity field are mapped, one can evaluate the wind farm efficiency as per Eq. (2.55), which is described as the ratio of total wind power produced by all the turbines to total power produced individually without the wake effect.

$$\text{Wind farm efficiency } (\eta_{WF}) = \frac{\text{Total power or energy generated by turbines in the layout}}{\sum_{i=1}^{N}(0.5\rho A_i U_{io}^3)} \tag{2.55}$$

where N is the number of turbines in the layout, A_i is the i^{th} turbine, and U_{io} is the upstream velocity of i^{th} turbine. The definition described in Eq. (2.55) is insufficient to deal with onshore wind farms or complex terrain. It often so happens that the best performing turbine may not be the one towards the upstream location (Astolfi et al. 2019). Therefore, a more elaborated η_{WF} relation is needed considering the terrain, cost of energy production, and wind turbine layout (Chen and MacDonald, 2012; Chen et al. 2014; Astolfi et al. 2019).

Table 2.6 Some key experimental and numerical observations on the wind turbine wake

Wake parameter	Observation remarks
Near wake regime	• Defined the near wake regime between 1D and 3D (Grant and Parkin, 2000). • End of the near wake regime is observed when the shear layer reaches the wake axis around 2D–5D (Crespo et al. 1999). • Induced axial velocity downstream of the rotor is found to be high. Presence of individual rotor blade in the wake disappears after 1D, however, the tip vortices remains intact (Massouh and Dobrev, 2007). • Strong flow rotation and highly asymmetric velocity deficit and turbulence structure exist within the near wake regime (Kocer et al. 2011). • Phase-average method is used to extract the shedding response; beyond $x/D > 5$, the phase-averaged is lost (Eriksen and Krogstad, 2017). • Streamwise velocity measurement shows a drop of 80% and 50% at $x/D = 2.4$ and 4, respectively (Hyvärinen and Segalini, 2017). • Consistent vortex ring can be observed till the near-wake region of $x/R < 8$ (Sedaghatizadeh et al. 2019). • Normalized time-averaged velocity deficit measurement shows W-shape flow profile within the near wake.
Far wake regime	• Downstream measurement shows the occurrence of maximum velocity deficit close to hub height (Barthelmie et a. 2002). • Single-bladed rotor does not give rise to meandering, whereas the influence of 2 and 3-bladed rotors in the wake meandering are notable. A large wake meandering suggests a larger thrust on the rotor (Medici, D., and Alfredsson, 2006, 2008). • Dependence of inlet TI on wake propagation is highly felt (Li et al. 2017; Talvera and Shu, 2017). • Large scale diffusion is observed by $x/D = 5$ leading to loss of sharp edge of the wake (Eriksen and Krogstad, 2017). • A complete flow recovery at $x/D = 14.5$ is observed while operating at $\lambda = 2.5$ (Hasan et al. 2019). However, the numerical analysis shows velocity recovery of about 80% around 7D at $\lambda = 2.5$ (Hasan et al. 2019), suggesting an early prediction. • About 60-70% flow recovery is noted beyond $x/R > 12$ while operating at low λ.
Wake deficit	• Roll-up of tip vortex is found to be affected by the vortex sheds from the inboard trailing edge (Grant and Parkin, 2000). • Vertical flow mapping within $x/R \leq 2$ shows asymmetric velocity deficit. Furthermore, vertical TI distribution is asymmetrical and is found to be high towards the root section, $r/R < 0.3$ (Jackson, R. S., and Amano, 2017). • The maximum deficit does not occur in the center of the wake but close to $0.5R$ (Magnusson, 1999). • The velocity deficit of ~65% is observed along the centerline (0.5D–1.75D), however, at $x/D = 2.5$, it decreases to ~25% (Kocer et al. 2011). • Far from the rotor plane, the increase of lateral and vertical velocities is observed close to the rotor and vice versa (Zhang et al. 2013). • Lateral measurement of velocity deficit shows axisymmetric nature with maximum value around $y/R = 0.2$ (Eriksen and Krogstad, 2017). • Increase of TI is observed from the rotor plane to $x/R \leq 6$. Between $6 < x/R < 8$, a slight decrease of TI is observed, however, it increases again beyond $x/R \geq 10$ due to disintegration of the wake (Mo et a. 2013). • Wake instability is observed at $x/R \geq 8$. Region of wake instability increases with freestream velocity (U_∞) (Mo et a. 2013). • Prediction of wake instability through computational approach highly depends on the mesh quality (Carrión et al. 2015). • Velocity deficit in the wake reduces with increase in TI. The maximum velocity deficit is obtained at $z/R = 0.50$ (lateral) and $y/R = -0.25$ (vertical). This value of deficit also increases with increase in λ (Li et al. 2017).
Helical and tip vortex	• Trailing vortex circulation depends on the phase angle and the yaw angle, which is found to be high at $\gamma = 0°$ and at high azimuth angle (Grant and Parkin, 2000).

	• Towards the outer part of the tip vortex, a higher velocity peak is obtained at every vortex passage. The tip vortex moves radially with a low frequency (Medici, D., and Alfredsson, 2006, 2008). Tangential velocity direction same as the rotor rotation (Massouh and Dobrev, 2007). • Influence of tip vortices is higher on axial velocity than on tangential velocity. The velocity induced by bounded circulation stay in same azimuth position. The tip vortices remained intact with the helical vortex till 1D (Massouh and Dobrev, 2007). • Persistent vortices are observed till 2D–3D, however, beyond $x/D \geq 5$, the wake rotation starts diminishing (Zhang et al. 2013). • The helical vortex structure interacts and pair-up, merge and breakup within $x/D = 3$ (Eriksen and Krogstad, 2017). • There is consistent vortex ring within $x/R < 8$. The ring of tip vortices is visible up to $x/R = 16$ in uniform flow (Sedaghatizadeh et al. 2019).
Vortex shading frequency	• Shedding frequency near the tip region is about ~60-80 Hz compared to ~4-10 Hz close to hub at $x/D = 1$. This is considered as low frequency shedding (< 100 Hz) with $St \approx 0.35$. Frequency response is found to be consistent at $x/D = 0.5$, 1 and 2 (Zhang et al. 2013). • Streamwise velocity produces low frequency (~10 Hz). The shedding frequency depends on x/D, inlet TI and ABL (Aubrun et al. 2013). • When $4 < x/R < 5$, high frequency signatures are noted, indicating the onset of instabilities with vortex pairing (Carrión et al. 2015). • St is found to be decreasing with increase of λ, however, it increases with γ (Medici, D., and Alfredsson, 2006, 2008). • Shedding frequency and helical tip vortex frequency responses vary with change in blade pitch angle.
Effect of yaw	• In an array of rotors, the C_{pmax} of downstream rotor increases by about 12% under yaw (γ) (McKay et al. 2013). • At $\gamma = 0°$, the vortex size increases due to continuous vorticity feeding from the entire blade span. Moreover, a constant vortex circulation is obtained, which is independent of azimuth angle. At $\gamma \neq 0°$, the overall vortex size is smaller compared to $\gamma = 0°$ (Grant and Parkin, 2000). • The wake deflection under yaw condition produces wake skew that lasts till far-wake regime. At this condition, the progress of vortex dissipation is further enhanced resulting in an early velocity recovery (Uemura et al. 2017). • Yaw control in maneuvering the wake meandering is found to be highly interactive with the η_{WF} (Castellani et al. 2018).
Effect of λ	• Axisymmetric distribution is noted at high λ (= 10) (Eriksen and Krogstad, 2013). Lateral and vertical deficits also increase with increase of λ (Li et al. 2017). • At high λ (>11), the rotor wake starts losing its helical stability from near to far wakes (Troldborg et al. 2012; Okulov et al. 2017). Wake size increases with increase of λ (Talavera and Shu, 2017). Upon increasing the λ from 2.5 to 7, the flow recovery distance drops to 6.5D from 14.5D (Hasan et al. 2019).
Effect of inlet TI	• High inlet TI leads to relatively higher wind velocity distribution, causing an entrainment of the inflow and wake (Li et al. 2017). • Performance and wake characteristics are found to be highly dependent on the inlet TI (Talavera and Shu, 2017). • There is not much significant change in the recovery distance upon increasing the U_∞ (Hasan et al. 2019).
Effect of ABL	• Wake growth is the largest for the stable ABL compared to unstable ABL. Streamwise velocity (U_x) recovers much faster (0.75 U_∞) in unstable compare to stable ABL (0.6 U_∞) at $x/R = 10$ (Hancock et al. 2014). • There is an increase of inflow velocity by 13% at the hub height for hilly surface compared to plain surface (Hyvärinen and Segalini, 2017). • Consistent and stronger vortex ring is observed till $x/D < 4$ under stable boundary layer (Sedaghatizadeh et al. 2019).
Others	• Effects from turbine tower and nacelle are found diminishing beyond $x/D = 2.5$ (Kocer et al. 2011). The downstream rotor losses its power by about 50-60%, and an improper alignment could lead to 10-20% loss in the annual energy production (Barthelmie et al. 2007, 2010). • Downstream rotor shows $C_p = 0.12$, 0.13, and 0.15, when installed at $x/R = 6$, 8, and 10, respectively. • A simple relationship can be obtained between the decay law of the velocity deficit and the C_p of the downstream rotor (Troldborg et al. 2010)

2.4.6 Limitation of Wake Models

The various analytical formulations on the wind turbine wake and their implication in wind farm modelling come with several limitations. The deviation in the wake behaviour comes from the classical narrative of well-structured velocity fields and their propagation, which can be well understood from the findings presented in Table 2.6. The Larsen model (Larsen, 1983) first and second-order wake models do not include the pressure term in the boundary equation; however, it is possible to consider this in a third-order model. Similar to the Ainslie model (Ainslie, 1988), Larsen models do not account for the ground effects or the tower effects in their basic formulations (Larsen, 1988; Larsen and Réthoré, 2009). Gaumond et al. (2014) stated that for the row of wind turbines with narrow space of 3° to 5°, the Larsen wake model underestimates the energy production. This is because the uncertainty in the direction of the wind is not modelled.

Tong et al. (2012) have investigated the performance of different analytical models to estimate power production; there results are mostly differentiated from the far wake characteristics. Further, it is observed that the Frandsen wake model predicts a larger initial wake expansion and highest wind speed for the single and multiple wakes compared to the other analytical models (Frandsen et al. 2006). This shows that the model provides additional power drop for the downstream turbines. Apart from considering a top-hat profile and axisymmetric wake, the Frandsen model equation has neglected the pressure gradient, gravity force, viscous forces, rotational effects, and incompressible effects. Such factors need to be included considering the latest trend in the installation of large and small wind farms at different climatic conditions.

The Jensen-Katic model considered that the far wake starts at an axial distance of about 3-4D downstream of a wind turbine, which is debatable. Like the Frandsen wake model (Frandsen et al. 2006), the Jensen-Katic wake model (Katic et al. 1987) disregards pressure gradients, the gravity force, rotational effects, viscous forces (e.g., shear forces in the edge of the wake), surface boundary layer effects, and vertical support tower effects. The wake model assumes the flow profile to be axisymmetric and has a constant top-hat transversal profile. This model is derived from the concept of momentum conservation for a fully developed wake field, and hence, the model's validity is mainly limited to the far wake regime. Although the legacy of the Jensen model is undeniably one of the pioneering correlations for many wind farm designers, its several assumptions often make it unreliable for the multiple wake interaction models. Kuo et al. (2015) noted one such discrepancy through experimental investigation of multiple wake interaction. They

observed that the downstream flow recovers much earlier, close to 9.4D instead of 10.4D predicted through the Jensen multiple interaction model. This faster-than-expected and non-monotonic recovery case is not a product of the proposed wake interaction model; however, it is the Jensen's model inability to imitate the observed wake recovery. According to Carrión et al. (2015), the main disadvantage of the wake models is that they need analytical expressions for the expansion region and the near wake region, which are employed as the boundary conditions. In addition, they incorporate a set of constants that are adjusted to match the experimental data. Most models suggest that the maximum normalized velocity deficit at each downwind location occurs at the center of the wake (Bastankhah and Porté-Agel, 2014); however, the experimental investigation produces contradicting results.

Determining the optimal layout of a set of wind turbines in a given area is a complex problem. The wind farm layout problems can be modelled in two ways, namely (a) continuous and (b) discrete. In discrete models, the turbines can only be placed in a countable set of pre-determined locations inside the wind farm, while in continuous models, they can be placed anywhere in the farm, considering their coordinates as continuous variables. Metaheuristic algorithms such as evolutionary algorithms (Chen et al. 2012; Mittal and Taylor, 2010; Chen and MacDonald, 2014), particle swarm optimization (Chowdhoury et al. 2012, 2013), and extended pattern search (Du and Cagan, 2012) have been the primary tools to solve the continuous models. Although powerful in tackling non-linear problems, a metaheuristic cannot guarantee global optimality.

Most wake models employed in wind farm modelling rely on the far wake assumptions. These models assume that the wake behind a turbine has a starting diameter equal to the turbine diameter and spreads linearly as a function of downwind distance. This simplification means that the wake velocity cannot be found accurately at all downwind positions. It is often assumed that the velocity is considered constant inside the wake model or has a commonly seen Gaussian distribution. This simplification is made because the aim of the model is to estimate the energy content in the wind field seen by the downwind turbines rather than accurately describe the velocity field. However, for better and more precise wind farm modeling, it is essential to understand the wake flow field downwind and its interaction with other wake produced by the nearby turbines or any natural or artificial obstacles. Although, it is quite understandable that incorporating all the subdue parameters in the analytical formulation will make the empirical relation more complex.

2.4.7 Summary and Knowledge Gaps

There are many factors which may govern the characteristics of wind turbine wake, following are some of the principle observations:

a) Numerous wind turbine wake models have been proposed over the past decades, some of which are the legacy of Jensen, Larsen, Lissaman, Frandsen, Ainslie and others. Although they are very quick to calculate and avoid the need for 3D computational fluid dynamics, the models often overestimate the flow characteristics because of assumptions like top-hat shape, linear expansion, Gaussian profile, axisymmetric deficit, negligible atmospheric boundary layer effect, and others.

b) It is observed that there are many discrepancies in defining the near wake regime and far wake regime. Based on the literature review, the near wake regime could be trance till 1.5D – 3D, and the far wake could be observed beyond 3D–5D.

c) Limited research articles are available that have briefly discussed the transitional regime; however, a few experimental observations suggest that one may dictate this regime between 2D–3D. The extent of these regimes highly depends on the rotor geometric configuration and inflow characteristics.

d) The effect of ABL is minimal for the near wake regime, but its effect cannot be ignored beyond this regime. It is noted that inlet TI plays a positive role in the early recovery of the velocity deficit.

e) Some of the critical experimental observations that showed inconsistent results from the analytical prediction are the asymmetric distribution of the velocity deficit, non-linear wake expansion, presence of negative velocity deficit beyond the core flow, non-existence of maximum deficit at the center of the wake, high deficit towards the lower haft of turbine wake, early development of fully developed flow, and others. In view of this, there is always room for developing a better correlation for a single and multiple wake interaction model that would precisely predict the performance and comprehend the fatigue loads on the turbines.

CHAPTER 3
EXPERIMENTAL SETUP AND METHODOLOGY

The experimental investigations have been carried out in a subsonic open-circuit wind tunnel. This facility is installed at the premises of the Department of Mechanical Engineering, IITG. The salient features of this facility, instrumentations, experimental setup, rotor blade design and fabrication, and the related methodology adopted have been discussed in this chapter.

3.1 Wind Tunnel and Instrumentations

For assessing the performance of model turbines, a low turbulence level wind tunnel facility has been used. The wind tunnel is a subsonic wind tunnel, the tunnel fan is powered by a 3-phase 30 HP induction motor, the dimensional layout of the tunnel is shown in Fig. 3.1. The wind tunnel is an open-circuit type and can produce a maximum wind speed of 50 m/s at the test section. The velocity measurement is performed using an electronic manometer which has a sampling frequency of 100 Hz. The tunnel test section has a width of 600 mm, height of 600 mm, and length of 2000 mm. Based on the size of the turbine models and the expected λ, the test section inlet velocity is maintained between 6–10 m/s. In this velocity range, the maximum rotational speed of the rotor can reach up to 3200 rpm. The average standard deviation (SD) in wind flow measurement using a pitot-static tube is found to be close to 1.2%, while that of the rpm is found to be about ~2%. In the range of velocity considered and the expected rotor rpm, the corresponding λ value falls in the range of 0.5 – 6. In most of the LWTs, the λ value is found in the range of 3 – 15 (Fuglsang et al. 2004; Butterfield et al. 1992), and thus the present model turbine rotors will fall under the category of low λ. Various associated instruments are shown in Fig. 3.2(a), and the related acquisition layout is shown in Fig. 3.2(b).

The level of turbulence in the tunnel is estimated through a hot-wire anemometry system. The turbulence intensity is observed to be less than 0.3% for the present wind tunnel studies and this is good enough to ensure that all the flow physics phenomena and aerodynamic characterization of models are acceptable (Bruun, 1995). The SHAWT model is mounted at a distance of 500 mm from the inlet of the test section. The vertical support structure of the model is kept at a distance of 300 mm from the side wall of the tunnel, and the hub height of the model is 300 mm. The blade radius (R = 120 mm) is kept the same for all the models, and this creates the blockage ratio (BR) of the rotor to be ~12.5%, which is found to be low and close to the acceptable limit of 10% as reported (Treuren, 2015).

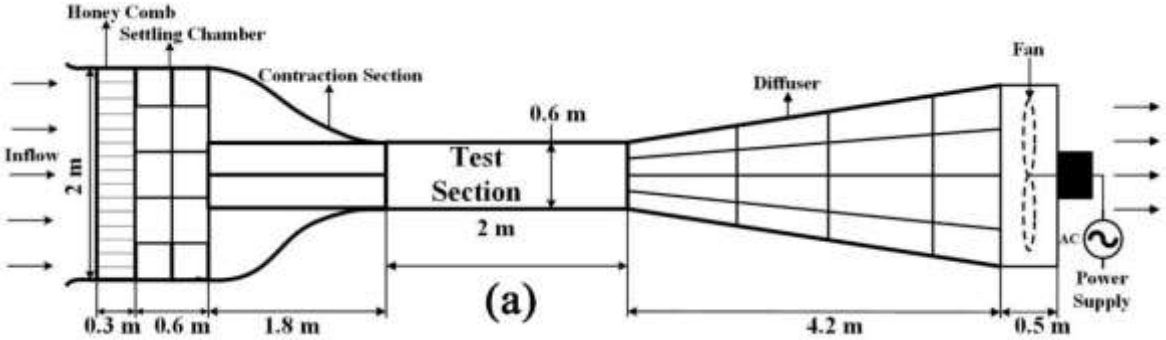

Fig. 3.1. Dimensional layout of subsonic wind tunnel at IITG

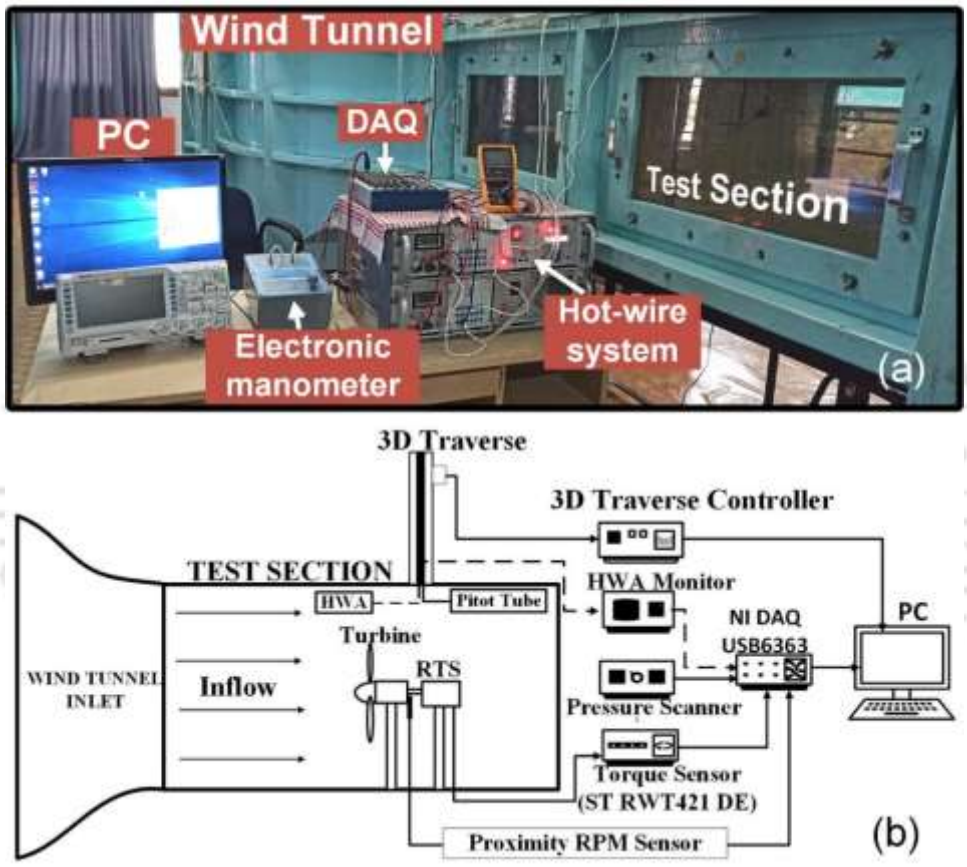

Fig. 3.2. View of (a) subsonic wind tunnel and (b) acquisition system

3.1.1 Measurement systems

To measure the rpm of turbine rotor, a n-p-n type proximity sensor is used. The sensor has an accuracy of ±0.1% and a sensing distance of 10 mm. Though, the sensor is pre-calibrated by the manufacturer, the corresponding sensor RPM has also been mapped with a hand handle tachometer and with the RPM of the rotary torque sensor. Under a uniform flow, the proximity sensor has an accuracy of ±0.1% and about ±0.3% deviation with the torque sensor rpm data. To measure the performance of model SHAWTs, a rotary torque sensor (RTS), as shown in Fig. 3.3 is used. The RTS is coupled with the rotor using a flexible coupler that helps in countering and constraining any slight miss alignment (< 2˚) while rotating. The torque data

are acquired directly through sensor software installed on the PC or through the analog output using the data acquisition (DAQ) system. The RTS model (RWT421 DE), capable of measuring torque up to 10 Nm and rotational frequency up to 20000 rpm, is supplied by the Sensor Technology Ltd., U.K. In wind turbine aerodynamics, the rotor performance is often expressed in terms of the non-dimensional parameter, C_p (Eq. 4). On the other hand, the mechanical efficiency considers the final output taking care of transmission, gear mechanism, and other losses. The mechanical efficiency parameter is mostly helpful in describing the performance of a machine from the industrial perspective, because the final output heavily relies on the optimum design condition of other systems apart from the turbine rotor blade (McTavish et al. 2013; Liu et al. 2013). Since, the present study does not include any complicated gearing mechanism, and hence, the power output is directly measured by a torque sensor. The rotor performance thus is expressed in terms of the C_p.

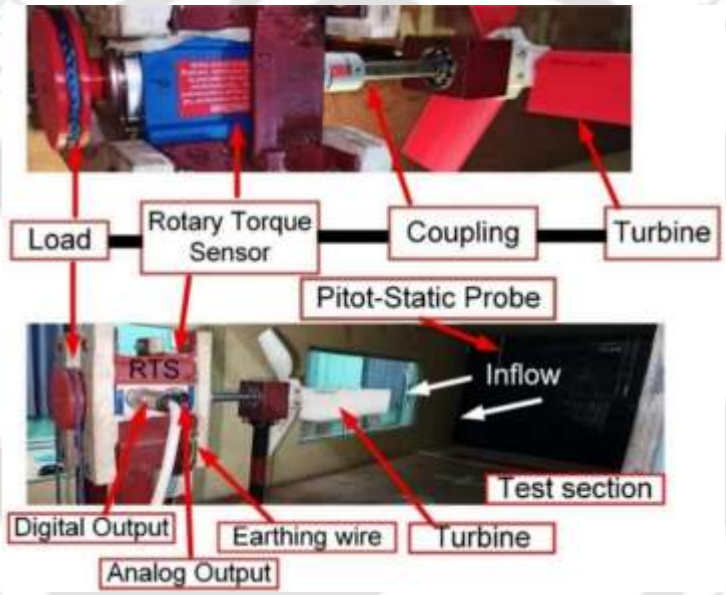

Fig. 3.3 Turbine and torque measurement setup

3.1.2 Wind Tunnel and Hot-wire Anemometry Characterization

3.1.2.1 Wind Tunnel Characterization

The wind speed inside the tunnel can be measured through a Pitot-static probe. The differential pressure measured through a Pitot-static probe is taken through a single channel electronic manometer, and the resultant pressure difference is also known as dynamic pressure (Cengel and Cimbala, 2005). Subsequently, the wind velocity inside the test section could be evaluated through Eq. (3.1). The electronic manometer has a sampling frequency of 100 Hz, and in present study, acquisition has been made for a sampling duration of 30 s. Figure 3.4(a) represents the calibration of HWA for the range of Pitot-Static probe velocity, which is evaluated through the dynamic pressure relation (Eq. 1). The voltage response from the HWA probe closely follows a linear response with a change in inflow velocity. The respective

standard deviation of velocity response of the pressure probe is found to be within the limit of acceptable tolerance, as shown in Fig. 3.4(b). The velocity sampled through the Pitot-Static probe is further used to calibrate the wind tunnel.

$$P_d = P_o - P_s = \frac{1}{2}\rho U^2 \tag{3.1}$$

where P_d, P_o, and P_s are dynamic pressure, total pressure, and static pressure, respectively, and ρ and U are air density and velocity, respectively. The present study deals with a heat transfer associated probe while deducing the velocity. So, it is required that the fluid (air) temperature variation is negligible in the test section. The temperature variation has been precisely monitored using a *k*-type thermocouple, and a typical response is shown in Fig. 3.5(a). The variation in the fluid temperature is presented in the normalized form: expressed as the ratio of fluid temperature at wind-on mode (T_{wo}) to wind-off mode (T_{wof}) in Fig. 3.5(b). It can be observed that the fluid temperature fluctuation is very negligible even with the change in freestream velocity. Thus, ambient temperature variability is negligible for the present wind tunnel, and it almost remains constant for the duration of the study.

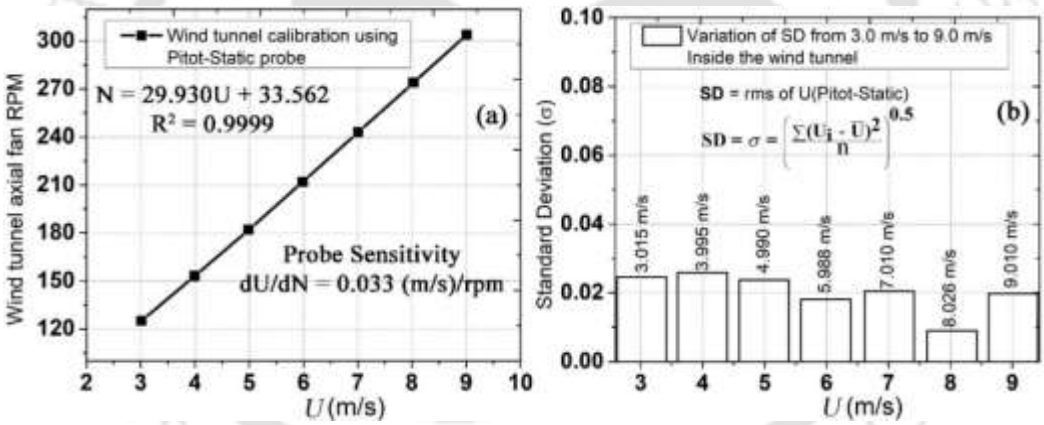

Fig. 3.4 (a) Calibration of Pitot-Static probe with respect to revolution of axial fan; (b) standard deviation in Pitot-Static probe velocity response

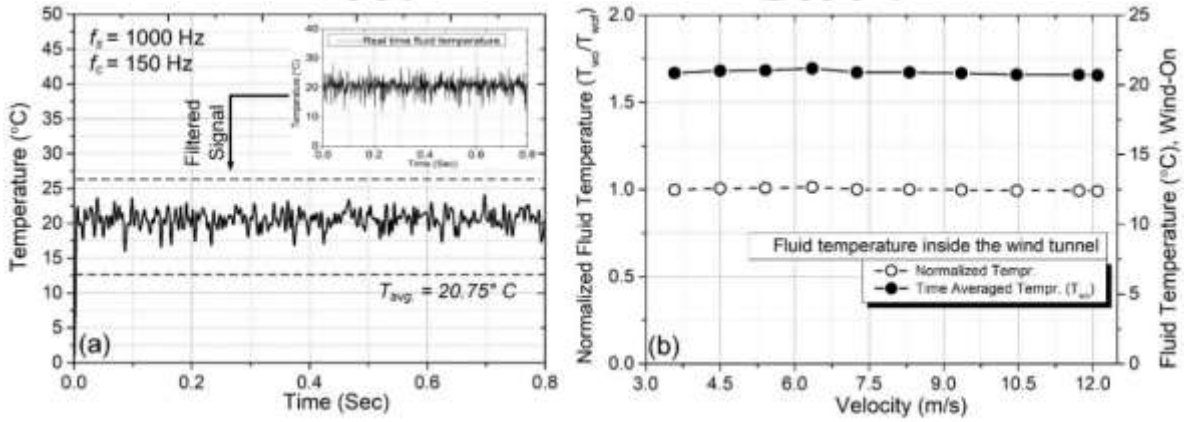

Figure 3.5 Fluid (air) temperature inside the test section: (a) Typical raw temperature response; (b) Normalized fluid temperature at varying wind velocity

3.1.2.2 Hot-wire Anemometry Characterization

A single wire/channel constant temperature hot-wire anemometry (HWA) probe has been mounted inside the tunnel test section at a distance of 500 mm from the inlet of the test section. The separation between the tunnel wall and the probe is kept at 300 mm to avoid boundary layer effects at the surface of the walls. The HWA probe wire is made from tungsten wire coated with platinum having a length of 3 mm and diameter of 10 µm. The HWA system produces instantaneous and fluctuation signals acquired through a national instrument (NI-USB 6363) data acquisition (DAQ) system with a maximum sampling frequency of 2 MHz. The acquired signal is further processed through the national instrument user interface LabVIEW2017 tool. The schematic of the data acquisition layout has been shown in Fig. 3.2(b).

The HWA is a thermal compensating device based on the principle of convective heat transfer from the surface of a heated cylindrical body. The governing relation of the heated wire is derived from the change in the surface temperature subjected to forced or natural flow fields. King (King, 1914) gave the simplified principal analytical relation correlating the effect of the cooling of an electrically heated hot-wire with respect to the surrounding fluid flow (Eq. 2).

$$E^2 = A + BU^n \tag{3.2}$$

where E is the voltage across the hot-wire, A and B are the calibration constant, and n is the velocity power index of the hot-wire. The working fluid being air and within the speed range of 3 to 20 m/s (low Reynolds number), the velocity power index is taken as 0.5 as reported in literatures (Siddal and Davies, 1972; Bishop and Yarusevych, 2011). A CTA probe is employed for the present study because it is easier to use and has a relatively better response at moderate wind flow (Simpson et al. 1979). The hot-wire is often kept with its axis normal to the mean flow direction such that there is uniform heat transfer. It has been observed that a well-aligned single wire CTA probe produces less deviation in its response to fluid flow (Yavuzkurt, 1984). In fact, it governs the working principle of HWA. The cylindrical sensor is usually welded or soldered to the stainless steel prongs, which is connected to the wheat stone bridge where the sensor's resistance acts as one of its variable resistance units (Fig. 3.6). The corresponding change in heat transfer from the wire is balanced through the variable resistance of the wheat stone bridge.

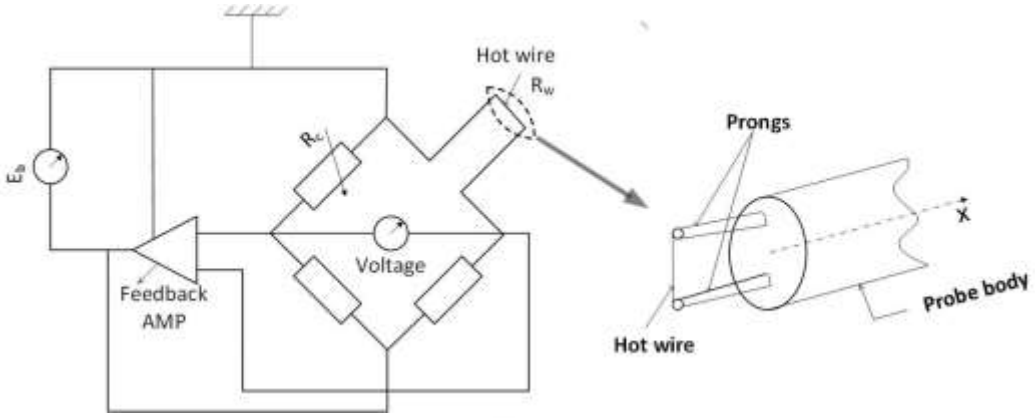

Fig. 3.6. Schematic diagram of hot-wire anemometer circuit

In order to ensure that the acquisition signal from the HWA through DAQ has meaningful interpretations, both pre and post-calibrations of HWA are suggested to check for any voltage lags (Swaminathan et al. 1986; Bishop et al. 2011; Yavuzkurt, 1984). To perform the calibration of HWA, one may follow the in-house or off-house calibration method where the latter is being made through some additional calibration system support as reported in articles (Swaminathan et al. 1986; Lee and Kauh, 1997). The in-house calibration is made possible through velocity measurement of the tunnel with a Pitot-Static probe. The corresponding velocity is used to find the relation between the voltage change in HWA, where it is expected to have the evaluated correlation R-square value close to unity. Equation (3.2) represents a linear relation for dependent variable E^2 as a function of independent variable $\sqrt{U}$ (considering n = 0.5). Therefore, differentiating Eq. (3.2) will give the sensitivity (S) of the CTA probe (Swaminathan et al. 1986; Stainback and Nagabushana, 1997).

$$S = \frac{dE}{dU} = \frac{B}{4E\sqrt{U}} \tag{3.3}$$

Figure 3.7(a) represents the HWA voltage response with respect to changes in inlet velocity. The corresponding linearity curve between E^2 and $\sqrt{U}$ is shown in Fig. 3.7(b). This relation is obtained through the time-average assessment of the time-lapse HWA signal. Here, the time-lapse indicates the acquisition of HWA data in millisecond response over a duration of 30 s. The data points in the plot (Fig. 3.7) are extracted from 30000 samples that are acquired at a sampling rate of 1 kHz. The measurement is repeated several times until the "mean square error" between the averaged value is less than 0.005 for each flow condition. Now, from the evaluated equation of curve (Fig. 3.7b), it is possible to estimate any arbitrary velocity for its corresponding voltage. However, one has to ensure that the predicted values lies within the calibration range, and in the present scenario, it is 2.5 m/s < U < 10 m/s. From the plot shown in Fig. 3.7(a), one can also evaluate the value of S from the polynomial curve.

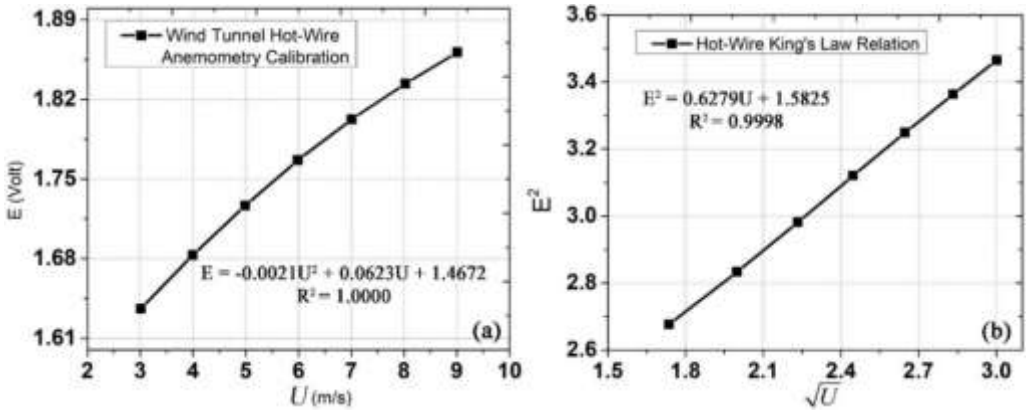

Fig. 3.7. Calibration chart of present HWA probe: (a) mean voltage variation with respect to Pitot-static probe velocity; (b) King's law relation between HWA voltage and velocity

It should also be noted that the variation of *S* is inevitable with the change in freestream velocity, type of probe, geometric configuration, mode of operation, and orientation (Swaminathan et al. 1986; Stainback and Nagabushana, 1997; Farsad et al. 2019). Figure 3.8(a) represents the typical attenuation of *S* with the type of CTA and mode of operation (CVA). Comparing these data with respect to the present probe make it quite apparent that *S* has a similar attenuation pattern with its value less than 0.10 V/(m/s) for velocities above 3 m/s. While investigating the diverse sets of flow conditions, it is recommended to have proper sensitivity curve relation prior to experimental utilization. In this aspect, the curve fitting for *S* has been carried out as shown in Fig. 3.8(b), where the power curve correlation is identified to be the best fitting with R^2 = 0.9999. The calculated sensitivities from the two approaches do not seem to differ significantly. For example, at 3.02 m/s, the difference in sensitivity from Eq. (3.3) with that of the polynomial relation (Fig. 3.8b) is found to be around 0.005.

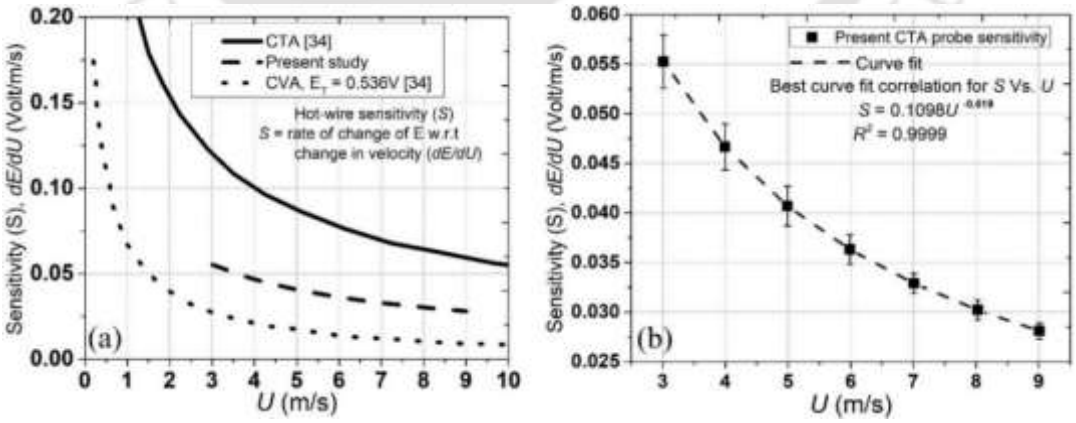

Fig. 3.8 Variation of probe sensitivity with velocity \

A well-calibrated probe helps ascertain less variability of the voltage response with regards to changing freestream velocity ((Swaminathan et al. 1986; Stainback and Nagabushana, 1997; Farsad et al. 2019).). There are several pre and post calibration has been taken into account

prior to its implication as a flow filed mapping tool. The detailed discussion on CTA signal acquisition with dedicated post-processing strategies to extracted the low and high pass signals have been briefly discussed in APPENDIX A.

3.2 Wind Turbine Blade Design and Fabrication Methodology

The blade design of SWT model rotors has been achieved through BEMT and fabrication of the model rotors has been carried out using the fuse deposition modelling (FDM) 3D printer. The design procedure of the rotor begins with the choice of airfoil and rotor parameters, as shown in Table 3.1. Assuming wake rotation for the optimum blade shape, an initial blade shape is determined. Here, the blade design under wake rotation considers the axial and tangential induction factors, it is also assumed that there is no flow interaction between the sectional elements. The optimum condition implies the state when the rotor can produce the maximum power efficiently. Under this assumption, the optimum angle of attack (α) occurs at the maximum value of C_l/C_d (Dehouck et al. 2018; Song and Luitz et al. 2014), and accordingly, the corresponding chord length, pitch and twist distribution can be calculated. The twist in the blade ensures that α is either equal or close to the design α at each section.

Table 3.1 Input parameters for blade shape design

Sl. No	Parameters	Notations
1	Tip speed ratio	λ
2	Number of blades	B
3	Blade span	b
4	Number of blade element	N
5	Radius	R
6	Design lift coefficient @ max C_l/C_d	$C_{l,design}$
7	Design angle of attack @ max C_l/C_d	α_{design}

The foremost step is to define the required geometric parameters such as rotor radius (R), blade span length (b), and the number of blades (B). This is followed by selection of operational limit of λ, optimum value of λ and number of blade element (N). The empirical relation for the rotor λ and the power output (P_{out}) can be express by relation as Eq. (3.4).

$$\lambda = \frac{R\omega}{U}; \quad and \quad P_{out} = C_p 0.5 \rho_{air} \pi R^2 U^3 \tag{3.4}$$

where, P_{out} is turbine output power (W), C_p is power coefficient, ρ_{air} is density of air (kg/m^3), R is radius of the rotor (m) and U is upstream wind speed (m/s). The governing equations for determining the design parameters are expressed in Eqns. (3.5) through (3.9) (Manwell et al. 2009).

$$\lambda_{r,i} = \lambda\left(\frac{r_i}{R}\right) \tag{3.5}$$

$$\varphi_i = \frac{2}{3}tan^{-1}\left(\frac{1}{\lambda_{r,i}}\right) \tag{3.6}$$

$$c_i = \frac{8\pi r_i}{BC_{l,design}}(1-cos(\varphi)) \tag{3.7}$$

$$\theta_{p,i} = \varphi_i - \alpha_{design} \tag{3.8}$$

$$\theta_{t,i} = \theta_{p,i} - \theta_{p,o} \tag{3.9}$$

The procedure needed to define the blade shape is explained in Fig. 3.9 and the necessary input parameters required are listed in Table 3.1. Once the blade chord length and twist are acquired at each section by following the stated blade shape design procedure, the performance analysis is carried out.

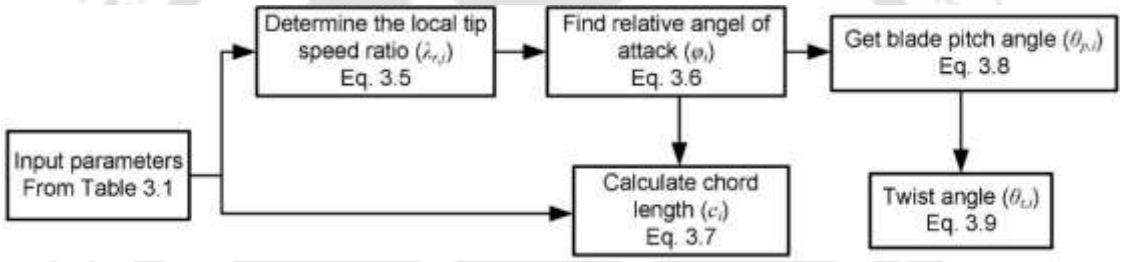

Fig. 3.9 Block diagram for design of blade

3.2.1 Performance Analysis Using BEMT

The performance analysis is carried out to estimate the actual α and lift coefficient (C_l) at the centre of each blade element, and then the C_p of the rotor is calculated. The C_p is determined iteratively considering the drag coefficient and tip losses at each section of the blade. The tip loss factor (F) lies between 0 and 1, and it corresponds to a loss of power production near the blade tip when the air tends to flow around the tip's lower surface to the upper surface. The relation for determining the actual α and C_l through BEMT is obtained from Eqns. (3.10) through (3.20).

$$\sigma_i^{'} = \frac{Bc_i}{2\pi r_i} \tag{3.10}$$

$$\varphi_{i,1} = \frac{2}{3}tan^{-1}\left(\frac{1}{\lambda_{r,i}}\right) \tag{311}$$

$$\varphi_{i,j} = tan^{-1}\left(\frac{1-a_{i,j}}{(1+a'_{i,j})\lambda_{r,i}}\right) \tag{3.12}$$

$$\alpha_{i,j} = \varphi_{i,j} - \theta_{p,i} \tag{3.13}$$

$$a_{i,j+1} = \frac{1}{\frac{4F_{i,j}\,sin^2(\varphi_{i,j})}{C_{l,i,j}\sigma'_{i,j}\,cos(\varphi_{i,j})}+1} \tag{3.14}$$

$$a'_{i,j+1} = \frac{1}{\frac{4F_{i,j}\,cos(\varphi_{i,j})}{C_{l,i,j}\sigma'_{i,j}}-1} \tag{3.15}$$

$$F_{i,j} = \frac{2}{\pi}cos^{-1}\left[exp\left(-\left\{\frac{0.5B[1-\frac{r_i}{R}]}{\left(\frac{r_i}{R}\right)sin(\varphi_{i,j})}\right\}\right)\right] \tag{3.16}$$

$$a_{i,1} = \frac{1}{\left(\frac{4\,sin^2(\varphi_{i,1})}{\sigma'_i C_{l,design}\,cos(\varphi_{i,1})}+1\right)} \tag{3.17}$$

$$a'_{i,1} = \frac{1-3a_{i,1}}{4a_{i,1}-1} \tag{3.18}$$

$$a_{i,j+1} = \left(\frac{1}{F_{i,j}}\right)\left[0.143+\sqrt{0.0203-0.6427(0.889-C_{T,i,j})}\right] \tag{3.19}$$

$$C_{T,i,j} = \frac{\sigma'_i(1-a_{i,j})^2(C_{l,i,j}\,cos(\varphi_{i,j})+C_{d,i,j}\,sin(\varphi_{i,j}))}{sin^2(\varphi_{i,j})} \tag{3.20}$$

For the blade geometry obtained at the chosen operating conditions, the analysis starts by assuming the initial values of a and a'. In this work, both are assumed to be zero initially. To find the starting F_i (first section tip loss factor), an estimated φ is calculated using Eq. (3.11). The step-by-step process required to carry out the numerical analysis of the blade using BEMT is compiled in a block diagram as shown in Fig. 3.10. As the performance and actual relative angle of wind at each blade elements are found, the C_p of the rotor is determined by Eq. (3.21) (Manwell et al. 2009).

$$C_p = \frac{8}{\lambda Z}\sum_{i=1}^{N}(F_i\,sin^2(\varphi_i)(cos(\varphi_i)-\lambda_{r,i}\,sin(\varphi_i))(sin(\varphi_i)+\lambda_{r,i}\,cos(\varphi_i))[1-\left(\frac{C_{d,i}}{C_{l,i}}\right)cot(\varphi_i)]\lambda_{r,i}^2) \tag{3.21}$$

where, *Z* refers to the sum of the number of blade elements and number of elements between the rotor centre and the starting blade section.

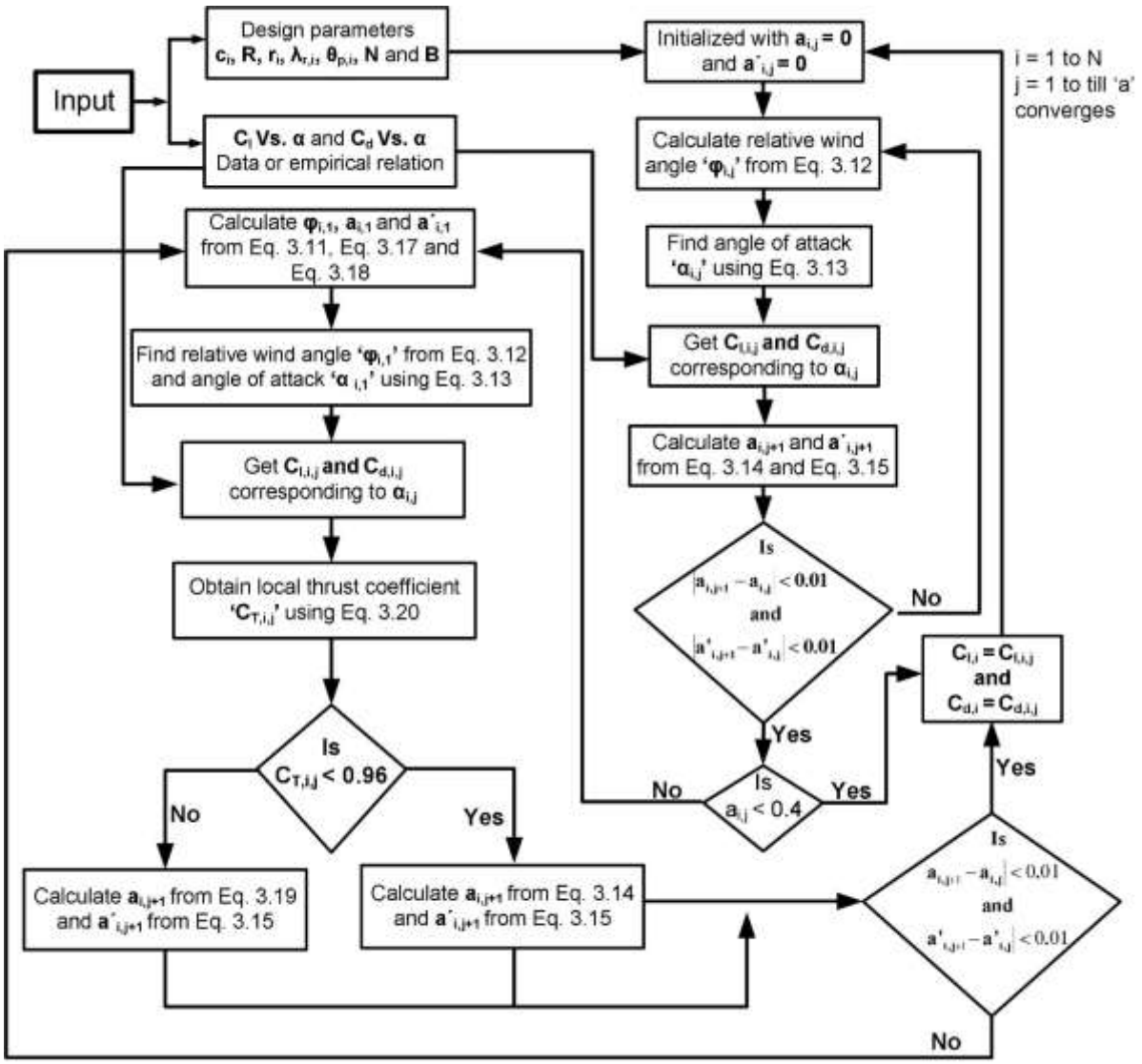

Fig. 3.10. Block diagram for the analysis of blade

3.2.2 Airfoil Selection Methodology

While designing a turbine rotor blade, the foremost task is to select an appropriate airfoil for the desired aerodynamic characteristics. Although, there are many classes/series of airfoils, still, a handful of airfoils are available that find their application in SHAWT under low *Re* and λ conditions (Tummala et al. 2016; Treuren, 2015; McTavish et al. 2013; Liu et al. 2013). Having conducted a brief review on various classes/series of low *Re* airfoils that are often studied and/or used in SWTs or SHAWTs (section 2.0), a total of twelve low *Re* airfoils has been selected, as shown in Fig. 3.11. Thereafter, the aerodynamic performance (C_l/C_d) of these selected airfoils has been carried out to find the most appropriate airfoils at the required *Re*.

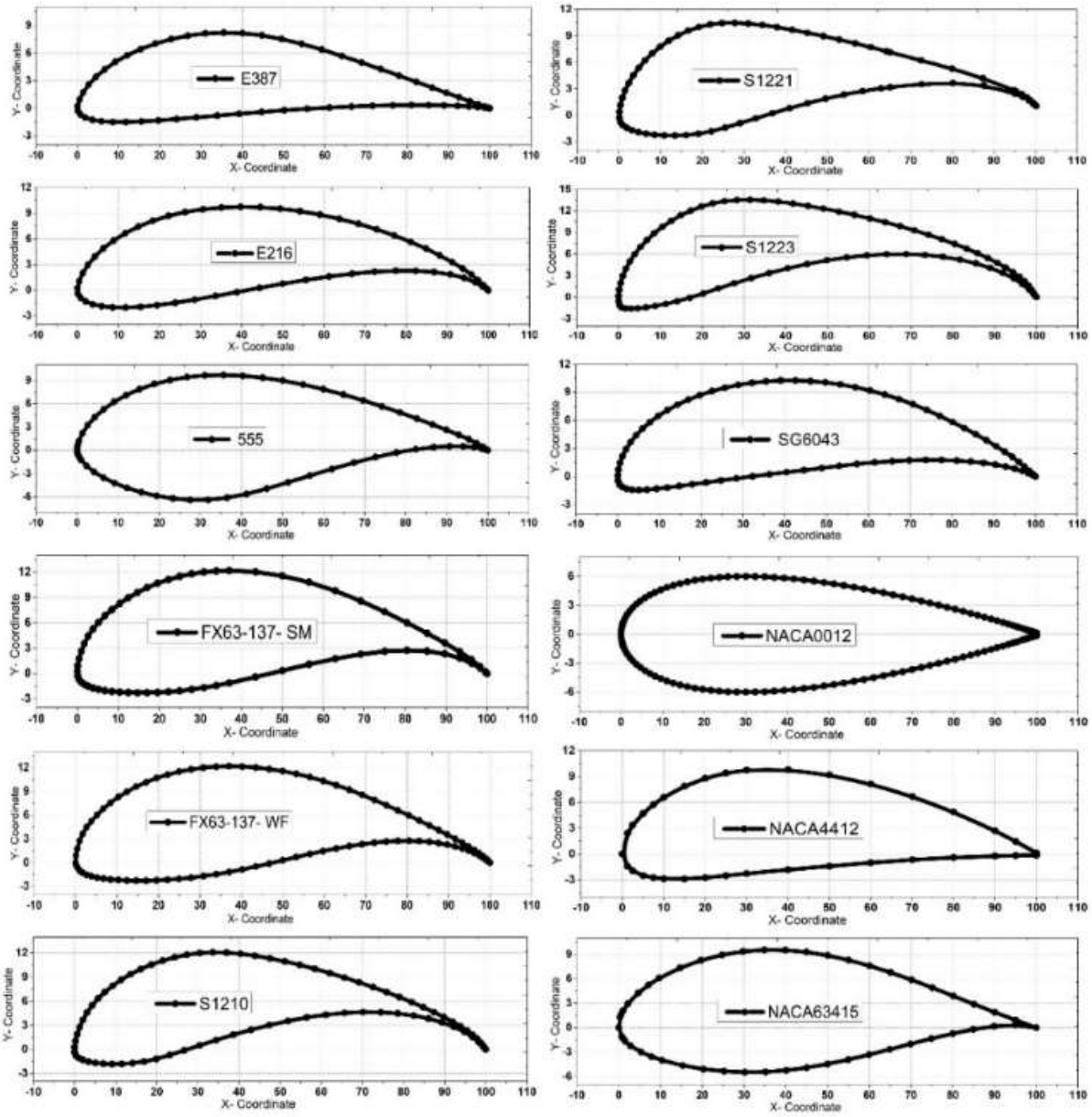

Fig. 3.11 Selected airfoils

The airfoils selected (Table 3.2) are often considered to be suitable for low *Re* applications (Tummala et al. 2016; Treuren, 2015; McTavish et al. 2013; Liu et al. 2013). In the present study, $Re = 0.5 \times 10^5$ is considered for their aerodynamic characterization. Although, the *Re* adopted is not the optimum, however, this value of *Re* is good enough for the SHAWT rotors (McTavish et al. 2013; Liu et al. 2013). The aerodynamic performance of these airfoils has been predicted through the Xfoil and Qblade tools, and for each case, the maximum C_l/C_d corresponding to optimum α is shown in Table 3.2 together with thickness-to-chord (t/c) ratio and camber.

Table 3.2 Selected airfoils geometric and aerodynamic characteristics

Airfoil Name	Thickness (t/c) %	Camber (%)	Max C_l/C_d (Re ~ 0.5 x 10^5)	'α' at max C_l/C_d (Re ~ 0.5 x 10^5)
E387	9.10	3.20	38.088	8.50
S1210	12.00	6.70	14.879	2.50
S1221	12.10	4.90	27.070	3.25
S1223	12.10	8.10	33.055	2.00
FX63137-SM	13.70	6.00	25.946	11.75
FX63137-WF	13.70	5.80	26.818	11.00
SG6043	10.00	5.10	39.710	8.75
NACA0012	12.00	0.00	25.669	5.00
E216	10.40	4.70	40.730	8.00
E555	16.00	2.60	27.828	10.50
NACA4412	12.00	4.00	33.450	9.75
NACA63415	15.00	2.20	29.958	9.50

As evident from Fig. 3.12, the two airfoils E216 and SG6043 have shown relatively higher C_l/C_d than the rest of the airfoils. This is why these two airfoils have been considered for the present design and testing of SHAWT. The third airfoil, NACA63415 is chosen to examine the effect of t/c on the rotor performance. Upon comparison, NACA63415 shows a lower t/c and higher C_l/C_d as compared to E555 with higher t/c and lower C_l/C_d. The fourth airfoil NACA0012 is chosen because of its use in earlier designs of SHAWTs (Kishore et al. 2013; McTavish et al. 2013; Ismail et al. 2022), and also to make a comparative analysis.

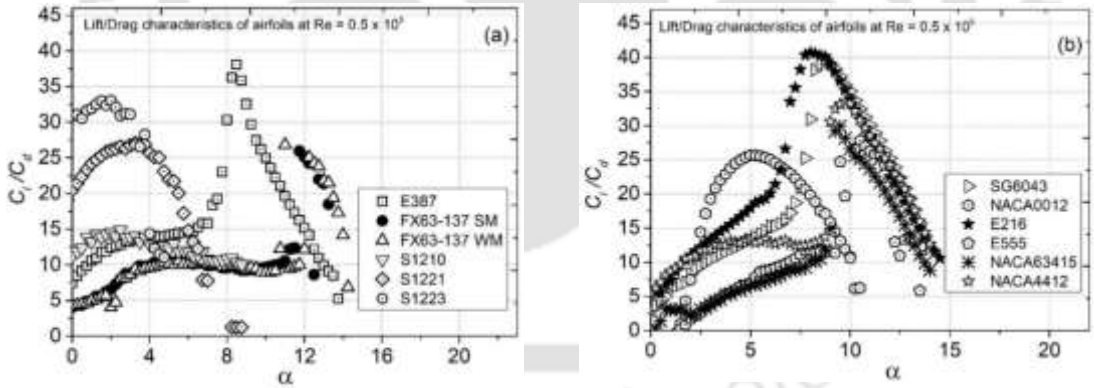

Fig. 3.12. Variation of lift/drag coefficient with angle of attack

The wind turbine blade design consists of the distribution of c, φ, θ_p and θ_t at each section. The algorithm for the rotor design using BEMT is shown by the block diagram (Fig. 3.10). To obtain the geometric parameters, a C-program is developed that uses the BEMT correlations to calculate the values of all the geometric parameters at each cross-section. Upon finding the geometric parameters, the same program is again used for analysing the sectional C_l, C_d, α, λ and the induction factors (a and a') before arriving at the rotor C_p. The input parameters (Table 3.1) for the algorithm (Fig. 3.10) consist of R, b, B, λ, $C_{l,design}$, and α_{design}. The required steps for the analysis of each blade section are shown in Fig. 6. Since the primary objective of the

present study is to evaluate the feasibility of designing a rotor at low *Re* and low λ, the rotor optimum λ is set at 2.5. The blade analysis is carried out by considering a total of 10 divisions where the portion near to the root becomes the first (Manwell et al. 2009; Dehouck et al. 2018). The output of the program provides the c, φ, θ_p and θ_t, and these are calculated as per Eqs. (3.5) through (3.9). The c and θ_p obtained for all the four turbine models at each blade section are presented in Tables 3.3 and 3.4.

Table 3.3 BEMT design chord length of the blade element sections

Section	Airfoil	E216	SG6043	NACA63415	NACA0012
	r/R	Chord length (c) in cm			
1	0.23	4.12	4.19	5.56	8.12
2	0.29	4.1	4.17	5.54	7.78
3	0.36	3.94	4	5.31	7.25
4	0.42	3.71	3.77	5.01	6.67
5	0.49	3.47	3.53	4.68	6.13
6	0.55	3.23	3.29	4.36	5.64
7	0.61	3.01	3.06	4.06	5.2
8	0.68	2.81	2.86	3.79	4.81
9	0.74	2.63	2.67	3.55	4.47
10	0.81	2.46	2.51	3.33	4.17
11	1.00	2.39	2.43	3.22	4.03

Table 3.4 BEMT design pitch angle of the blade element sections

Section	Airfoil	E216	SG6043	NACA63415	NACA0012
	r/R	Section pitch angle (θ_p) in degree			
1	0.23	29.38	28.63	27.88	29.05
2	0.29	24.76	24.01	23.26	24.28
3	0.36	20.93	20.18	19.43	20.49
4	0.42	17.78	17.03	16.28	17.47
5	0.49	15.16	14.41	13.66	15.02
6	0.55	12.98	12.23	11.48	13.01
7	0.61	11.13	10.38	9.63	11.35
8	0.68	9.57	8.82	8.07	9.96
9	0.74	8.23	7.48	6.73	8.77
10	0.81	7.06	6.31	5.55	29.05
11	1	6.53	5.78	5.03	7.28

3.2.3 Blade Fabrication Methodology

The geometric parameters viz., c, θ_p and θ_t distributions obtained using BEMT are imported to the SolidWork for the final design. The sectional view of the designed rotor is shown in Fig. 3.13. The modelled rotors are fabricated by means of a fused deposition modelling (FDM) 3D printer using Polylactic acid (PLA) material that is biodegradable and eco-friendly. The printing process requires a nozzle temperature of 210- 235°C and a bed temperature of 60-70°C. The printing infill density of 60 - 80% is maintained, and this is found to be good enough to ensure the structural stability of the rotor at 3200 rpm. The four SHAWTs, composed of airfoils E216, SG6043, NACA63415, and NACA0012, are named as models M1, M2, M3, and

M4, respectively, and are displayed in Fig. 3.14. Some of the vital parameters that need to be taken care of during the printing process are listed in Table 3.5. The procedure that needs to be followed for the fabrication purpose is shown in Fig. 3.15. The IdeaMaker tool shown in the third step (Fig. 3.15) is a slicing software program that converts the computer aided 3D model into a printable design.

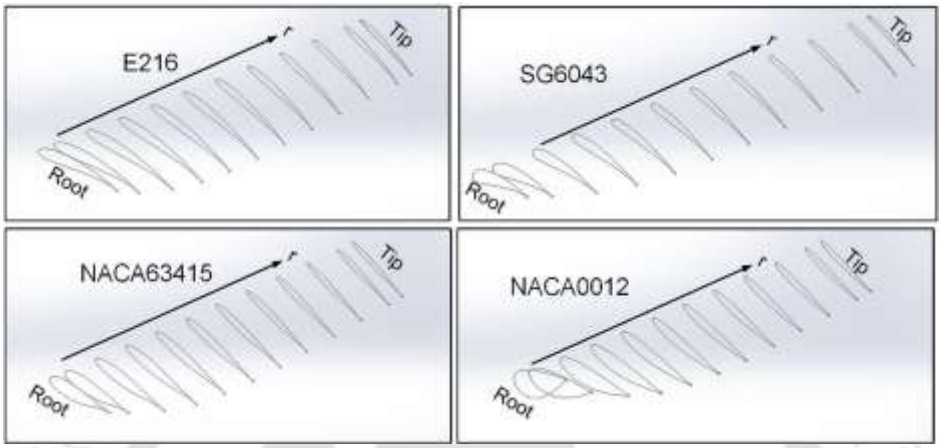

Fig. 3.13 Depiction of airfoil sections of the designed blade

Fig. 3.14. The prototype models of the SHAWT

Fig. 3.15. Blade fabrication procedure

Table 3.5 Vital printing parameters

Parameters	Description
Layer height	Range- 0.08- 0.12 mm for better surface finish.
Infill ratio	Provides stiffness (60-80) %.
No. of shells	Improves blade strength.
First shell speed	Usually low (20-25 mm/s) to ensure a better surface finish.
Infill Ratio of Support	Should be low (12-15%) with maximum overhang angle of 60°.
Platform support	Avoids detachment (especially for thin sections) from the printing bed.

3.2.4 Straight and Linearly Tapered (SLT) Rotors

To make a comparative assessment of the BEMT designed SWT rotors, a set of non-BEMT rotors have been designed and fabricated. The non-BEMT rotors adopted are straight and linearly tapered (SLT) rotors. The SLT rotors opted have NACA0012 as their sectional profile. Being smaller in dimension, the corresponding *Re* for the model rotors is close to 0.5×10^5. Although the WT general aerodynamic properties may vary for low to high *Re*, their behavior is considerable with other thin plate airfoils (Hancock and Pascheke, 2014). The model rotors opted for the study are scaled down with respect to conventional commercial turbines by 800 times with the intention of exploring the SLT rotor blade performance characteristics. The adopted models have the most straightforward dimensional configuration, which could be easily mounted in the wind tunnel test section. The opted three models have C_r/C_t as 1:1(M1), 5:3(M2), and 5:2(M3). These SLT rotors are three-bladed with a rotor diameter of 240 mm, hub height (H_b) of 300 mm, blade span length (L) of 100 mm, and varying chord length. All the SLT model rotors have been fabricated using a fuse deposition modelling (FDM) 3D printer using Polyactic acid (PLA) material. At any location of the span of each turbine, the blade has a NACA0012 sectional profile (Fig. 3. 16a), and the corresponding geometric parameters are shown in Fig. 3.16(b).

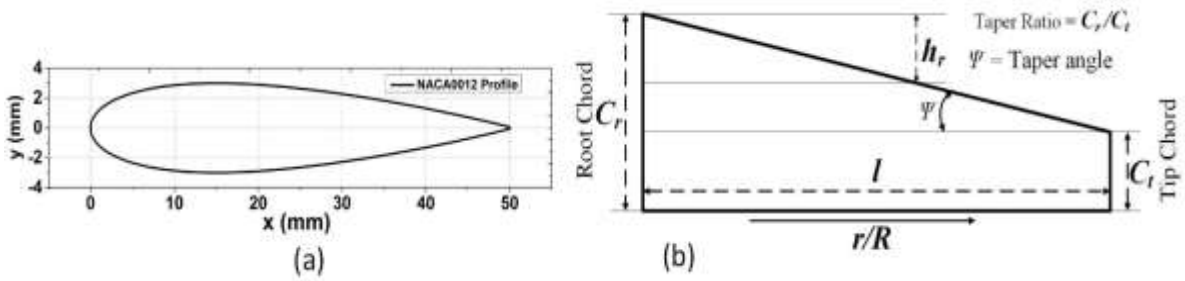

Fig. 3.16. (a)Sectional profile (NACA0012) of HAWT blade; (b) depicting geometric parameters of straight blade.

The three blades of model rotor are linked onto the rotor hub, which then can be installed inside the wind tunnel using a base frame where the vertical turbine support can be mounted quite comfortably (Fig. 3.17b-c). Table 3.6 gives the detailed geometric configuration of the three model rotors. The sectional chord length (C_r), sectional taper height (h_r), and sectional solidity (σ_r) of model turbines have been calculated as per Eqs. (3.22) through (3.26). Figure 3.18(a) shows the varying rotor blade chord length with respect to *r/R*. The values have been evaluated for the sectional radial interval of 0.05 (*r/R*). Figure 3.18(b) represents the varying σ_r of the model rotors, the σ_r of a turbine (σ_r), is defined as the ratio of the area of the blade with respect to the swept area of the rotor (Burton et al., 2001).

Fig. 3.17. (a) BEMT M0 model; (b) SLT M1 model with C_r/C_t = 1:1; (c) SLT M2 model with C_r/C_t = 5:3; (d) SLT M3 model with C_r/C_t = 5:2

$$\tan\psi = \frac{(C_r - C_t)}{l}; \qquad Or,\ \psi = \tan^{-1}\left[\frac{(C_r - C_t)}{l}\right] \tag{3.22}$$

$$C_r(r/R) = C_r(root) - h_r(r/R) \tag{3.23}$$

$$\text{Also, } \tan\psi = \frac{h_r}{r} \tag{3.24}$$

$$\therefore\ h_r\big|_{(r/R)} = \left(\frac{r}{R}\right) R\tan\psi \quad ;or \quad h_r\big|_{\mu} = \mu R\tan\psi;\ \ \mu = r/R \tag{3.25}$$

$$\sigma_r = \frac{BC_r}{2\pi r} = \frac{BC_r}{2\pi\mu.R} \tag{3.26}$$

Table 3.6 Geometric configuration of model M1, M2 and M3

M1	M2	M3
Tip Chord (C_t): 50 mm C_r/C_t = 1:1	Tip Chord (C_t): 30 mm C_r/C_t = 5:2	Tip Chord (C_t): 20 mm C_r/C_t = 5:3

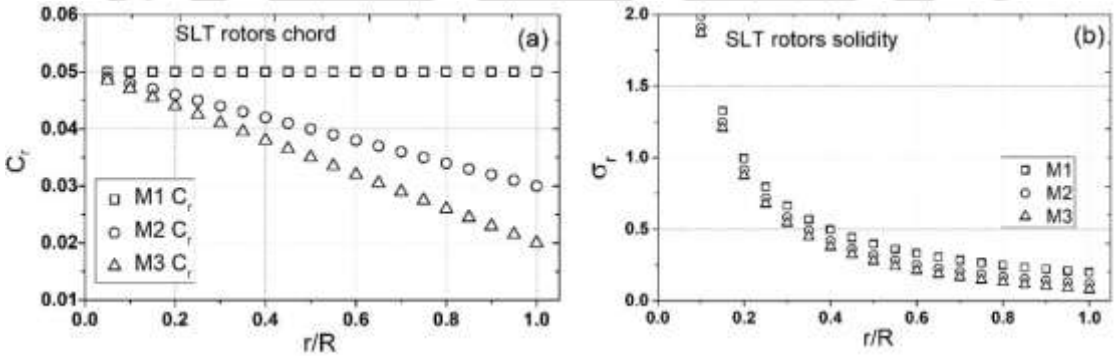

Fig. 3.18. (a) Variation of sectional cord length (C_r) with r/R; (b) variation for sectional solidity (σ_r) with r/R, of SLT model rotors.

The size of model rotor is such that, the rotor blades will be exposed to the core flow inside the tunnel, and the wall boundary layer interference is minimal. For the present study, both BEMT and SLT rotors have the same radius (R = 120 mm). Therefore, the blockage ratio (BR) offered by these rotors is about 12.5%, though, the favorable BR limit suggested by Treuren, 2015; Howell et al., 2010 is 10%, slightly more than the suggested limit, during the experiment, it was

noted that the tunnel boundary layer effect is minimal. Nevertheless, the data presented in this study have been processed with the inclusion of the blockage factor (BF). The blockage correction employed here is taken from Chen and Liou (2011) approach, where the BF is expressed as the ratio of inlet velocity at the test section with and without the model, as per Eq. (3.27). The corrected tip speed ratio (λ_c) and corrected power coefficient ($C_{p,c}$) are expressed as per Eqs. (3.28).

$$BF = \frac{U_m}{U} \tag{3.27}$$

$$\lambda_c = \frac{\lambda}{BF}; \quad and \; C_{p,c} = \frac{C_p}{BF^3} \tag{3.28}$$

3.3 Flow Field Assessment Using Constant Temperature Hot-wire Anemometry

The wind turbines placed in array/cluster or in multirotor configuration are often subjective to unsteady turbulence flow due to the wake dissipation from the neighbouring turbines. Thus, it is essential to understand the underlying flow dynamic of wind turbine wake and its behaviour in array/cluster formation. To carry out this objective, a systematic flow field assessment has been carried out using the constant temperature hot-wire anemometry (CTHWA). The main benefit of using CTHWA is that such probes can give a precise point-wise valuation of the velocity fluctuation and close to the boundary layer. The CTHWA used in the present study is a single and x-probe type, which can produce x-velocity, and x - y-velocity components, respectively. The signal acquisition, pre and post processing analogies has been briefly discussed in Appendix B. The point-wise mapping of the wind turbine wake has been carried out with the help of a 3D traverse system, as shown in Fig. 3.19.

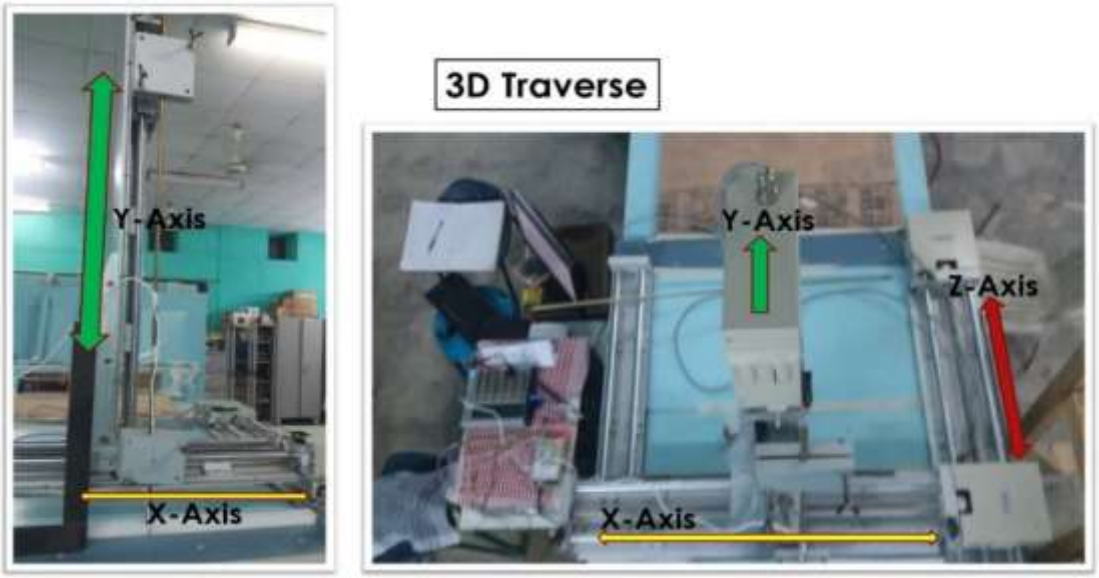

Fig. 3.19. 3D Traverse system mounted on the top of wind tunnel test section

The signals acquisition from CTHWA system are acquired using LabVIEW 2017 graphical user interface (GUI) program, as shown in Fig. 3.20. The probe is intrusive type, producing voltage output with maximum DC off-set of +10 V to -10V; a typical example is shown in Fig. 3.21. The downstream wind turbine wake propagation and flow field mapping has been carried out for single and array of two rotors at multiple downstream locations (*x/R*). However, most of the mapping has been performed within the proximity of the helical vortex core (-1.5 < *y/R* < 1.5). The upstream and downstream turbines have been indicated as UsT and DsT, respectively. All the measurements were performed with respect to the UsT rotor plane, as indicated in Fig. 3.22.

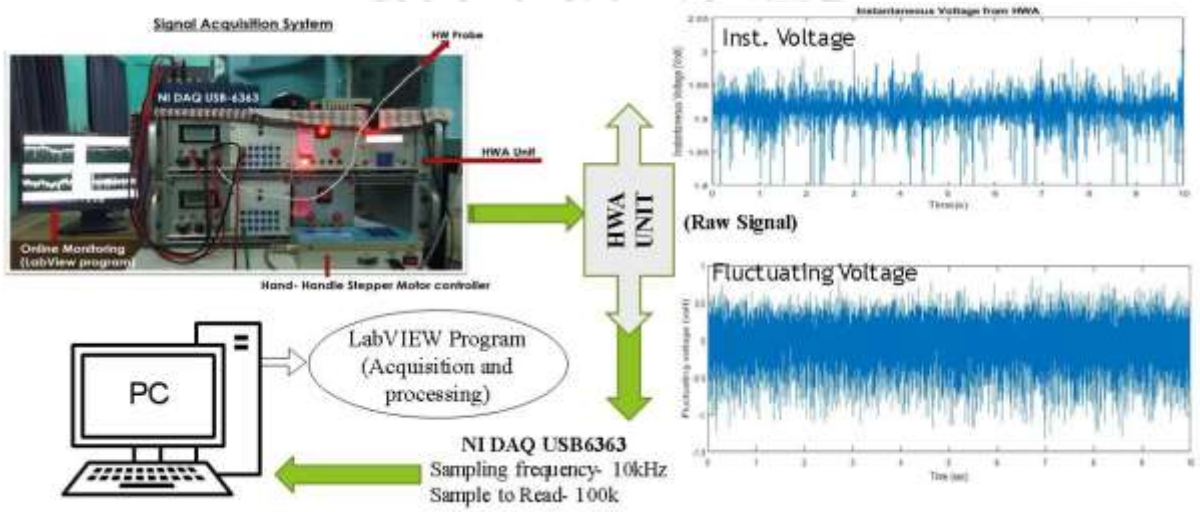

Fig. 3.20. CTHWA signal acquisition and processing layout.

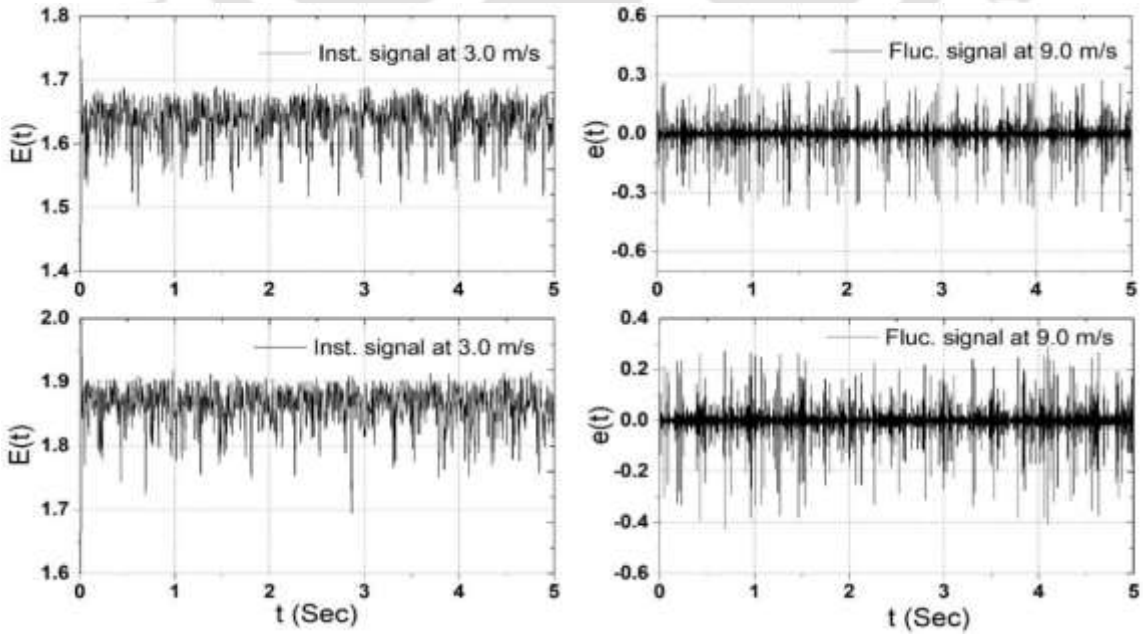

Fig. 3.21. Typical CTHWA instantaneous and fluctuation output signal at wind speed of 3.0 m/s and 9.0 m/s

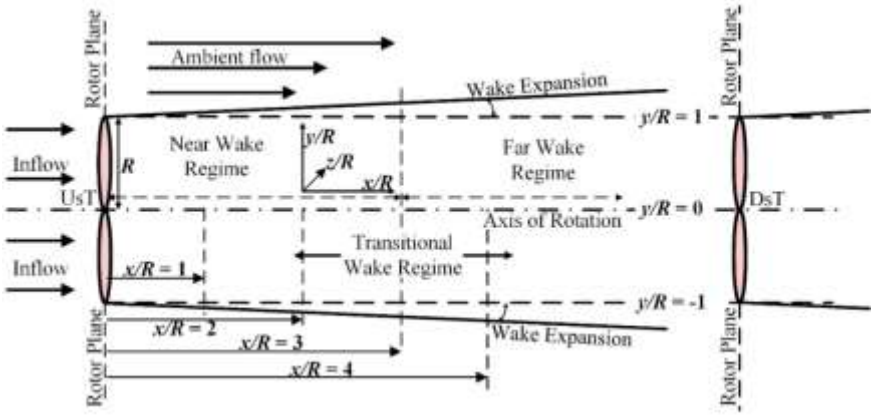

Fig. 3.22. Schematic of turbines in array

The two turbine models have the same design configuration and dimension, with similar hub height (Fig. 3.23a). The models are suitably mounted inside the test section as shown in Fig. 3.23(b). The rotors are aligned with each other; and the height of the rotor hub is 300 mm that is located at a distance of 300 mm from the tunnel sidewall. The models are kept in array with their hub axis parallel and about 300 mm from the wall. At this position, the boundary layer effect is negligible and to reduce the effect of the diffuser section, the positioning of downstream rotor at extreme exit has been avoided and so is for the inlet section. In this study, the effect on DsT is examined at different downstream locations (x/R), where the R is the radius of the rotor that is 120 mm. The corresponding blockage ratio (BR) is calculated to be about 12.5%, and as per reported literatures (Treuren, 2015; Werle, 2010) this range of BR is reasonable enough to avoid any blockage correction. For rotors in the array, they are installed collinear to each other and the rotor spacing is such that it is well under the dimensional constraints of the test section.

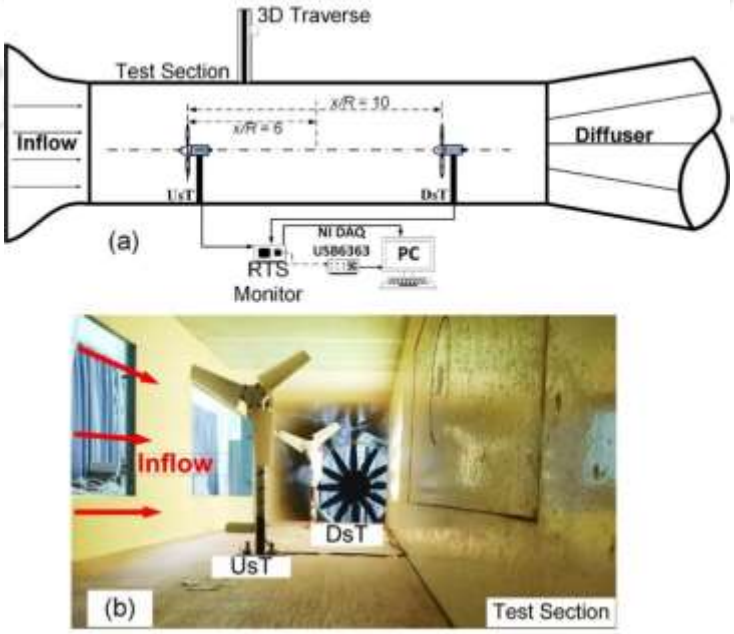

Fig. 3.23. Wind tunnel (a) schematic of tunnel, turbines and acquisition, and (b) sectional view of tunnel and array of rotors

3.4 Flow Field Assessment Using Particle Image Velocimetry (PIV)

The wind turbine flow field assessment using classical probes like the pitot, pitot-static tubes, or using CTHWA can produce point-wise data. However, when it comes to instantaneous flow field analysis to abstract the coherent structures, the implication of CTHWA or pitot probes are not reliable. For instant, a CTHWA can give a precise fluctuating velocity at a location; but having that data will not be able to dictate the overall pattern of the vortex shedding, though one can assess the average velocity distribution for a given field of view (FOV) using the 3D traverse system. And to achieve this, a systematic measurement is needed, resulting in data acquisition with substantialy time lag. To overcome this issue, a particle image velocimetry system (PIV) has been used. The PIV system captures the movement of particles (seeding particle), thereby, calculate the velocity of the particle or velocity distribution within the FOV. More detail on the type and methodology of PIV has been discussed in the subsequent sections.

3.4.1 Stereo PIV Theory

A stereoscopic-PIV system make use of two cameras as shown in Fig. 3.24(a) to view the flow field from two perspectives so that the out-of-plane velocity components can be measured. The arrangement provides two-dimensional projected flow field with three velocity components (2D-3C). Here, the nominally perpendicular angle from the laser sheet to the camera optical axis are evaluated from the individual camera viewpoint. On the other hand, the two-dimensional two components (2D-2C) of velocities is obtained by keeping the camera optical axis perpendicular to the laser sheet (Fig. 3.24a). Figure 3.24(b) shows the typical arrangement of the stereo-PIV for the present study.

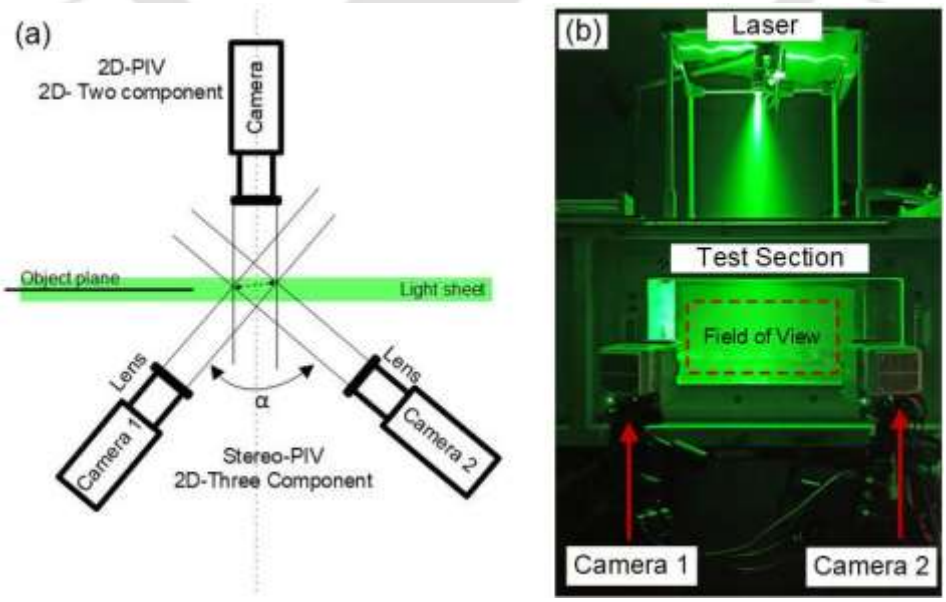

Fig. 3.24. Illustration of (a) 2D and 3D-PIV arrangement, and (b) stereo PIV setup at wind tunnel laboratory, IITG.

In the stereo arrangement, the pair of 2D velocity vectors for a point in the flow field using the two different image is then synchronized to produce the 3D velocity vector. Therefore, the combination of the vector fields from the two cameras is subsequently used to generate the three-dimensional velocity field for the plane in the fluid. In stereo-PIV arrangement as shown in Fig. 3.24, one can expect that due to the oblique configuration of the cameras, the object plane and image plane may not be aligned parallel. As a result, the plane of focus is also not aligned parallel, rather the subject plane will be in focus only along a line where it intersects the plane of focus, as shown in Fig. 3.25(a). To solve this problem, a Scheimpflug adapter is used which ensures that the image plane, lens plane, and object plane interest at a common point often expressed as the Scheimpflug intersection (Fig. 3.25b). This is achieved by tilting the lens principle plane and image sensor plane; subsequently, the best focus is obtained which is also aligned with the laser light sheet.

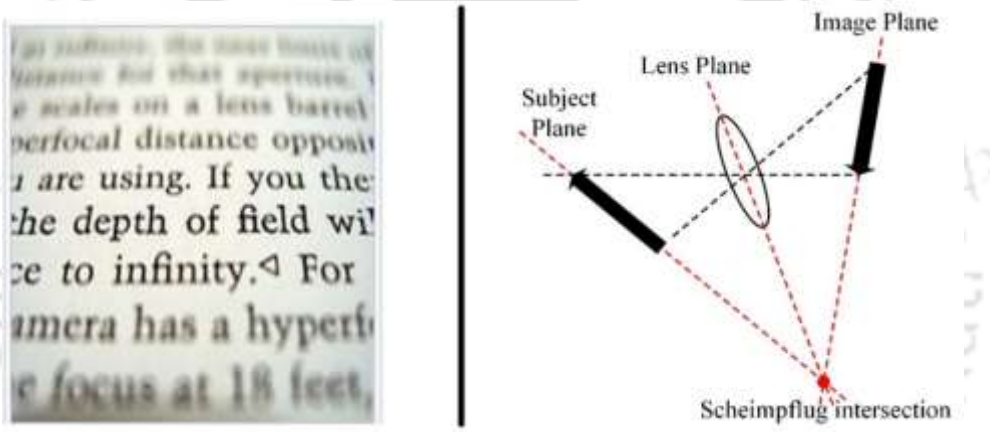

Fig. 3.25. Illustration of (a) focus along a line, and (b) Scheimpflug ratification

Furthermore, the Scheimpflüg configuration presents an angled distortion (Fig. 3.25), a calibration method is adopted to remove the distortion from the vector fields. The calibration measure ensures that correct angled/perspective distortion due to the camera tilt and any other image distortions in the optical system is obtained. A calibration mark with indicator points at the known positions is line up to the laser light-sheet. Thereafter, images from the camera are taken and analyzed; a mapping functions is generated using a third-order calibration polynomial equations for individual camera. The functions also excuse the need of two cameras be precisely aligned with respect to object plane because the function accurate the center of the fields of view (FoV) for each camera.

3.4.2 Particle Image Velocimetry System and Methodology

The PIV system employed in the present study has been procured from LaVision Pvt. Ltd., Germany. The system includes (1) image capture components, (2) lighting components, (3) a

synchronizer (programming timing unit- PTU), (3) a seeding particle generator, and (4) analysis components (image processing- DaVis 10.0 software). The image capturing components is equipped with a Schimpflug adapter which is very useful for the stereo-PIV measurement. The lighting components are primarily composed of a laser generator and light-sheet optics. Additionally, the optical arm of the laser system is equipped with an adjustable laser light-sheet optical lens that helps control the sheet thickness manually. A thicker light-sheet is preferable in the case of flow visualization, whereas a thin light-sheet is essential where the investigation is more of quantitative nature. The present system uses two continuous-wave (CW) pumped Q-switched Nd:YLF (Neodymium-doped yttrium lithium fluoride) DPSS laser resonators generating infrared laser light at 1053 nm, which is converted to 527 nm laser light by an intra-cavity Harmonic generation assembly (HGA). The harmonic generators yield a laser output at 527 nm of green colour. Further, to ensure that both laser outputs can be used with a single set of external optics, the 527 nm laser beams are combined and allowed to exit through a single port of the laser head. The use of two independently pulsed and controlled resonators allows the generation of a double pulse output with inter-pulse separation times of less than ten nanoseconds. This ultra-short inter-pulse separation cannot be achieved using a single resonator laser fitted with an electronic double pulse option.

The whole operation would be simply expressed into three segments (1) laser initiation and adjustment, (2) calibration of cameras' field of view (FoV) using calibration plate, and (3) recording and processing. The former two condition needs a great deal of care particular to avoid any human error because the outcome of later results depends on the accuracy of alignment and setting of both camera and laser. Though unlike other flow measurement systems like hot-wire anemometry, pressure scanner and others, the PIV system doesn't require pre and post-experiment calibration apart from its extrusive nature. Figure 3.26 represents the schematic of the experimental setup and the PIV arrangement. The system configuration of the PIV unit has been taken in reliance with the wind tunnel working space (600 mm × 600 mm × 2000 mm), so that the laser-sheet, FOV, and seeding particle are precisely recognized. Detailed technical specification of PIV system has been mentioned in APPENDIX D.

The PIV image acquisition and image processing methodology can be divided primarily into four steps:

1. PIV acquisition or sampling of the image frame
2. Recording and processing
3. Processing of captured images into interpretable data
4. Extraction and post-analysis of the sampled data

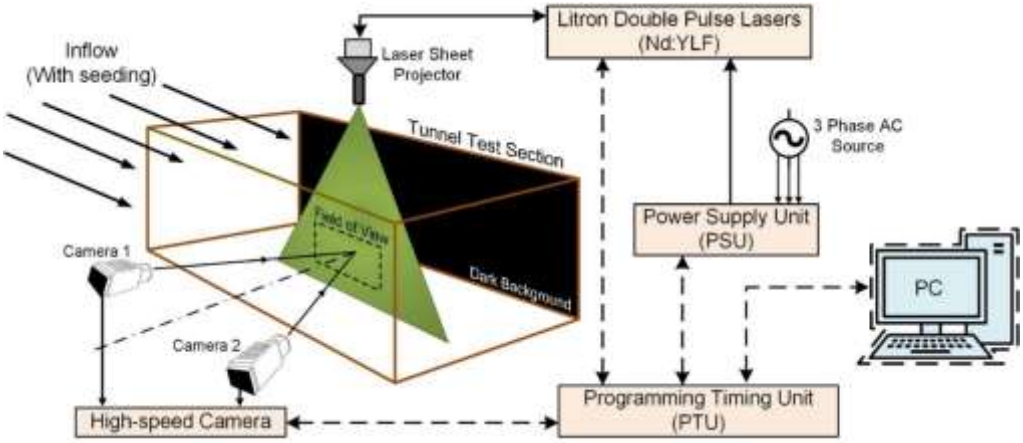

Fig. 3.26. Schematic of experimental PIV arrangement

The point to be noted here is that every captured image will produce instantaneous data for the given FOV; thus, if it is required to generate the instantaneous flow response at any particular position, one has to extract the same from all the individual frames. Furthermore, the framework of PIV analogies is such that it is highly dependent on the spatial resolution, interrogation window/grid, timeframe, field of view (FOV), and, most notably, the measure and distribution of the seeding particle. The acquisition/sampling or frame per second (fps) of the PIV should be such that the assigned rate will capture all the essential vortex field, which generally features low-frequency dominating shading and high-frequency eddies. The significance of the latter is that high-frequency response often dictates the nature of fluctuating parameters like turbulent intensity, Reynold stress, and others. The data extracted from the whole domain/FOV or within the masked regime (cropped section) can be expressed further to preview the contour field, including a frame-wise assessment of the concerned parameter. Since PIV assessment conjugates the particle movement into a single or double frame thus, it is possible to trace the vector field. Subsequently, one can easily generate the flow vector within the concerned FOV or masked region.

3.4.2.1 Calibration of PIV

The calibration of PIV basically means the calibration of the camera with respect to a default calibration plate. The calibration plate is a standard plate usually provided by the manufacturer along with the camera, though one can create their own grid plate. These plates have specific sets of marking in the form of a square or circular dots evenly distributed on the plate. The calibration plate employed in the present study is a 2D/3D plate of model ID: 309 – 15; that is, the area of the plate is 309 × 309 mm^2, and the spacing between the dot is 15 mm. The size of each dots is about 3 mm, circular in shape. An illustration of calibration plate 309-15 is shown in Fig. 3.27. Prior to the calibration, one has to ensure that the proper optical lens is employed, FOV is properly set, the laser light-sheet and surface of the plate are almost collinear, and the

camera is properly focused. The calibration of 2D-PIV measurement will produce the pixel grid based on the marking of the captured image; a typical illustration is shown in Fig. 3.27(b). Whereas, for the stereo-PIV image to be taken from both the cameras and subsequently, the inbuilt algorithm (beyond the scope of the present study) will produce two sets of perspective pixel grids for the left and right cameras as shown in Figs. 3.27(a) and 3.27(c). Once calibrated for either case, one can see and calculate the approximate data points, focal length, pixel sizes, and others. Among the various parameters, Fit error is an important parameter, defining the accuracy of calibration; it is the average difference between the generated pixel grid to the actual grid of the calibration plate. The fit error should be less than one pixel, though, for best correlation, it is recommended to have the fit error less than 0.5 pixels.

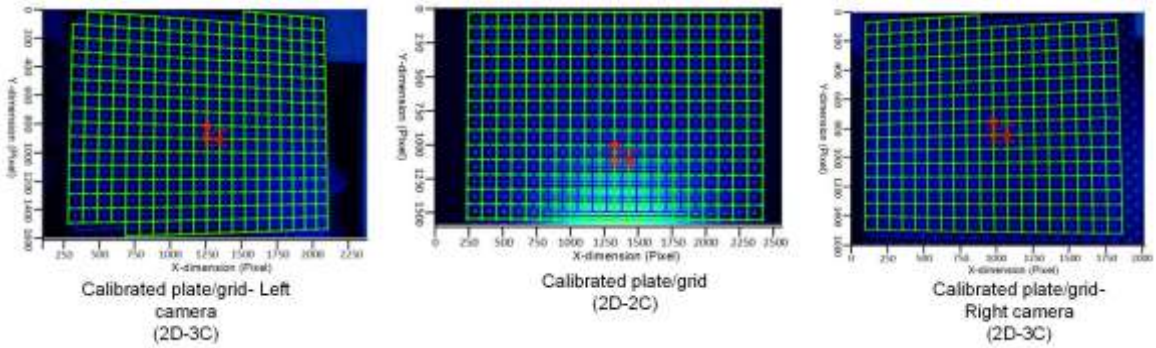

Fig. 3.27. Illustration of calibrated plate (309-15) and grid generation where (a, c) represents the left and right camera perspective for stereo-PIV, and (b) represents the perspective of 2D-PIV.

3.5 Blockage Correction

One of the significant issues with the wind tunnel study is the blockage caused by the model being tested. A high blockage could result in several anomalies on the measured data and can mitigate to other related parameters (Treuren, 2015). The blockage caused by the model is often expressed in terms of blockage ratio (BR), which is defined as the ratio of the projected or frontal area of the model to the wind tunnel test section area (Treuren, 2015; Howell et al. 2010). In the present investigation, the BR is found to be 12.5%. Though it is about 2.5% slightly more than the suggested limit, during the experiment, it was noted that the tunnel boundary layer effect is minimal. Although this value is insignificant, however, the effect of BR on C_p have been examined by two different methods of blockage correction as discussed below.

Chen and Liou, (2011) suggested the blockage correction for small wind turbines and expressed the measured parameters in terms of blockage factor (*BF*). This *BF* is defined as the ratio of inlet velocity with and without the model in the wind tunnel, i.e., U_m/U as expressed by Eq. (3.29). The corrected λ and C_p can be expressed by Eqs. (3.31) and (3.33) respectively.

$$BF = \frac{U_m}{U} \tag{3.29}$$

$$\lambda_m = \frac{R\omega}{U_m} \tag{3.30}$$

$$\therefore \quad \lambda = \lambda_m \times BF = \frac{R\omega}{U} \tag{3.31}$$

$$C_{p,m} = \frac{\tau\omega}{0.5\rho\pi R^2 U_m^3} \tag{3.32}$$

$$\therefore \quad C_p = C_{p,m} \times BF^3 = \frac{\tau\omega}{0.5\rho\pi R^2 U^3} \tag{3.33}$$

where, the subscript *m* represents the condition with the model. According to Chen and Lio (2011), the corrected parameters must consider the inlet velocity without the inclusion of the model, and this is what is followed in the present wind tunnel experiments. Thus, the fan rpm of the tunnel is kept the same irrespective of the inclusion of model. This is done to maintain a similar suction pressure. Figure 3.28 shows the variation of inlet velocity with and without the model. The error measured in each case is expressed in terms of SD, the average deviation in either case is found to be around 2.3% for velocity < 5 m/s and close to 1% for velocity > 5 m/s. In this study of blockage correction, two wind speeds are considered, and accordingly, the corrected λ and C_p are calculated using Eqs. (3.31) and (3.33).

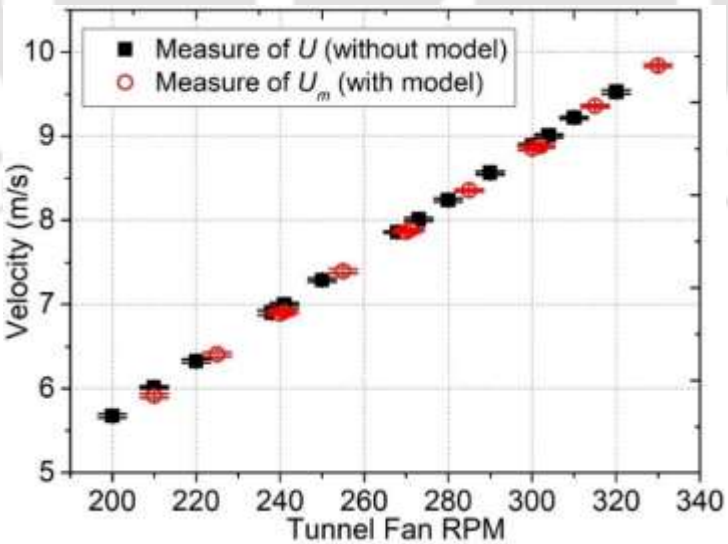

Fig. 3.2 8. Variation of inlet wind velocity inside the wind tunnel test section

Pope and Harper blockage correction is the other popular wind tunnel correction approach used in the wind turbine studies (Pope and Harper, 1966). They have expressed the corrected velocity (U_c) in terms of the correction factor (ε_t) as per Eqs. (3.34).

$$U_c = U(1+\varepsilon_t); \qquad \text{where, } \varepsilon_t = 0.25\left(\frac{\text{Model frontal area}}{\text{test section area}}\right) \tag{3.34}$$

The corrected power coefficient ($C_{p,c}$) and the corrected tip speed ratio (λ_c) can be expressed by Eqs. (3.35) and (3.36). In this method, considering ε_t = 0.0314 and U = 8.01 and 9.00 m/s, the corresponding U_c are found to be 8.26 and 9.29 m/s, respectively.

$$C_{p,c} = \frac{\tau\omega}{0.5\rho\pi R^2 U_c^3}; \qquad \text{and} \quad \lambda_c = \frac{R\omega}{U_c} \tag{3.35}$$

$$\Rightarrow \qquad C_{p,c} = \frac{C_p}{(1+\varepsilon_t)^3}; \qquad \text{and} \quad \lambda_c = \frac{\lambda}{(1+\varepsilon_t)} \tag{3.36}$$

Based on the above two methods (Chen and Liou, 2011; Pope and Harper, 1966), the performance estimation of the model rotors is carried. A typical case study on the rotor performance due to the effect of blockage has been depicted in Table 3.8, for U = 8.01 m/s and 9.0 m/s. Table 3.7 shows the percentage deviation in each case. In all the cases, the percentage deviation indicates the decrement in the value of C_{pmax}. Similar analogy has been adopted for all the case studies, further result on the implication of blockage has been addressed in subsequent chapters.

Table 3.7 C_{pmax} estimation without and with blockage correction

$U \rightarrow$		U = 8.01 m/s				U = 9.00 m/s			
	Methods ↓	M1	M2	M3	M4	M1	M2	M3	M4
C_{pmax}	Chen and Liou, (2011)	0.299	0.229	0.258	0.140	0.344	0.300	0.281	0.152
	Pope and Harper, (1966)	0.273	0.208	0.235	0.124	0.314	0.274	0.256	0.139
	U_m (Without blockage correction)	0.313	0.239	0.270	0.146	0.359	0.313	0.293	0.159
% deviation of Chen and Lio method w.r.t U_m		4.50 %	4.50%	4.50%	4.50%	4.10%	4.10%	4.10%	4.10%
% deviation of Pope and Harper method w.r.t U_m		12.94 %	12.94%	12.94%	15.38%	12.57%	12.57%	12.57%	12.57%

CHAPTER 4
WIND TUNNEL TESTS OF SMALL HORIZONTAL-AXIS WIND TURBINES FOR LOW TIP SPEED RATIO APPLICATIONS

4.1 Introduction

In this study, potential SHAWT has been examined through dedicated experimental and numerical analysis. In doing so, at first, extensive literature review has been undertaken, a detailed review on small wind turbines has been outlined in Chapter 2 (section 2.3). The main intention of this study is to examine the applicability of the model turbines for low *Re* and low λ conditions. The rotor blades were designed using the concept of blade element momentum theory (BEMT), which were then fabricated and tested in the wind tunnel. The details of airfoil selection, blade design criteria of the SHAWT has been outlined in Chapter 3 (3.2); whereas the wind tunnel experimental investigation methodology has been enumerated in Chapter 3 (section 3.1). Apart from the BEMT rotors, series of non-BEMT rotors were also tested. These rotors have the straight forward configuration, name straight and linearly tapered (SLT) rotors. The detailed performance characteristics of the modelled rotors are discussed in the following subsections.

4.2 Blade Design and Analysis Using BEMT

A total of twelve airfoils (E387, FX63-137SM, FX63-137 WM, S1210, S1221, S1223, SG6043, NACA0012, E216, E555, NACA63415, NACA4412) has been selected based on the applicability of these airfoils for SHAWTs or under low Re flow. The aerodynamic lift and drag characteristics of these airfoils obtained through XFOIL and QBlade tools at Re = 0.5 x 10^5 (Fig. 3.12). Thereafter, the rotor blade design and performance evaluation has been carried out using BEMT. Subsequently, the rotor blade having the highest estimated C_{pmax} is fabricated by a fuse deposition modelling 3D printer. The model fabricated from polylactic acid (PLA) material is then tested in the low-speed wind tunnel at different inflow conditions. After analysing the aerodynamic behavior of 12 airfoils through XFOIL and QBlade tools, it is seen that E216 has the highest C_l/C_d ratio at low *Re* of 0.5 x 10^5, followed by SG6043 (Fig. 4.1). Accordingly, these two airfoils viz., E216 and SG6043 along with two other airfoils NACA0012 and NACA63415 have been selected for the BEMT design and analysis. The NACA0012 being the simplest symmetrical airfoil of the NACA family has been quite extensively studied (Singh and Ahmad, 2013; Kishore and Priya, 2013; McTavish et al. 2013; Ismail et al. 2022). Because of this reason, NACA0012 airfoil is selected as a baseline airfoil for the rotor models. All the 12 airfoils selected has different thickness to chord (t/c) ratio as shown in Fig. 4.1. To understand the effect of airfoil thickness, a NACA63415 airfoil having

t/c of 13% has also been selected. From Fig. 4.1, it is seen that the E555 airfoil has a larger t/c ratio (16%) but has a relatively lesser $(C_l/C_d)_{max}$ at Re = 0.5 x 10^5, and therefore, NACA63415 is chosen in the present study for a comparative analysis.

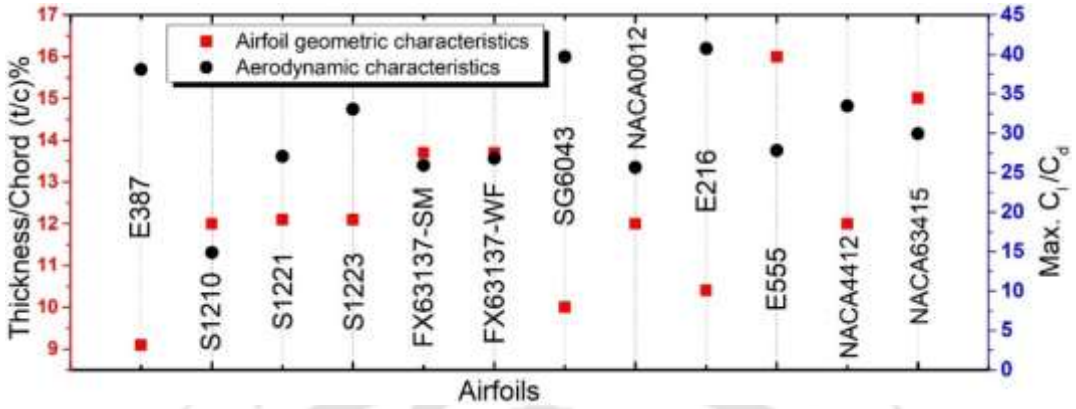

Fig. 4.1. Test Airfoils with their t/c and Maximum C_l/C_d at Re = 0.5 x 10^5

Subsequently, using the BEMT concept, the rotor design has been performed for the airfoils E216, SG6043, NACA0012, and NACA63415. The input parameters of the rotor design through BEMT is shown in Table 4.1. The input values of the rotor models are dictated by the constraints of the wind tunnel facility. The design and analysis of the rotor blades have been achieved using the in-house developed C++ program of BEMT (Fig. 3.10). The geometric configuration of the proposed four models of SHAWT is shown in Fig. 4.2. It depicts the non-linear distribution of rotor chord length and the sectional pitch angle obtained through BEMT.

Table 4.1. Rotor Design Input Parameters through BEMT

Airfoils	Optimum λ	Rotor radius	Blade length	No. of blades	No. of elements
E216, SG6043, NACA0012, and NACA63415	2.5	120 mm	100 mm	3	10

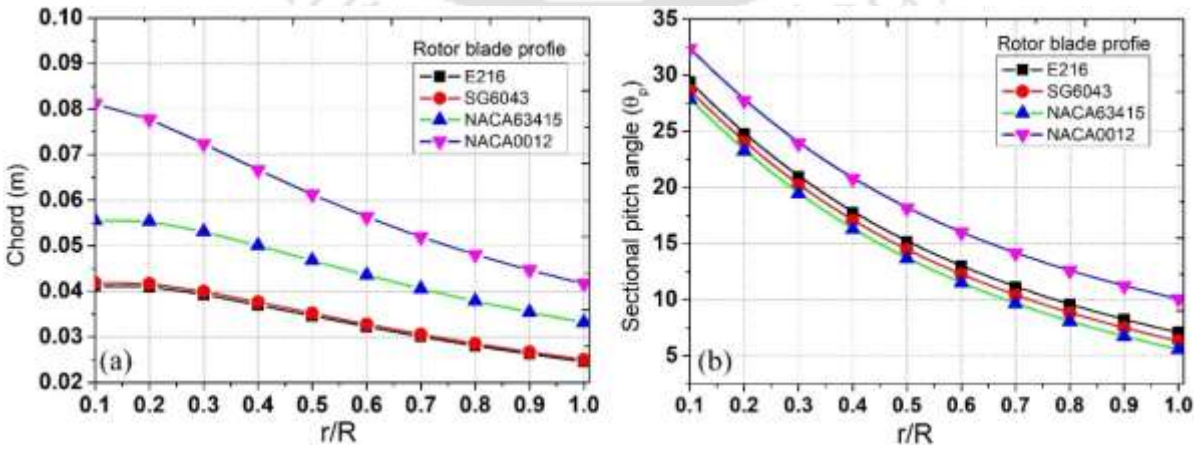

Fig. 4.2. Geometric distribution of the test models from BEMT analysis (a) variation of chord length, and (b) variation of blade sectional pitch angle

The rotor designs of the selected airfoils are followed by their sectional aerodynamic analysis and the performance characteristics at the design λ. The typical representation of the lift and drag coefficients (C_l and C_d) distribution over 10 sections along the blade span at the design condition is shown in Fig. 4.3, and their corresponding C_l/C_d is shown in Fig. 4.4. On the basis of aerodynamic characteristics, it is quite clear that E216 airfoil has a relatively better performance than the rest of the airfoils, whereas NACA0012 airfoil has the least C_l/C_d (Figs. 4.3 and 4.4). This suggests that symmetrical airfoil usage in SHAWT models may not be very promising. Another important observation from this analysis is that the root section has lesser C_l/C_d characteristics as compared to tip section suggesting that tip section is more accountable to the power extraction.

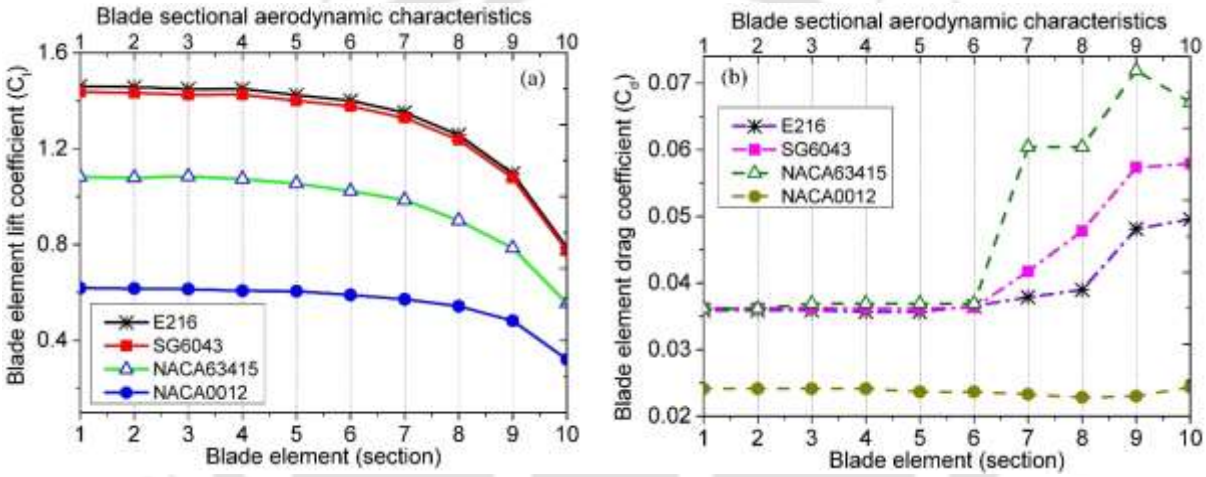

Fig. 4.3. Representation of rotor blade sectional characteristics (a) lift coefficient and (b) drag coefficients of the designed rotor blades

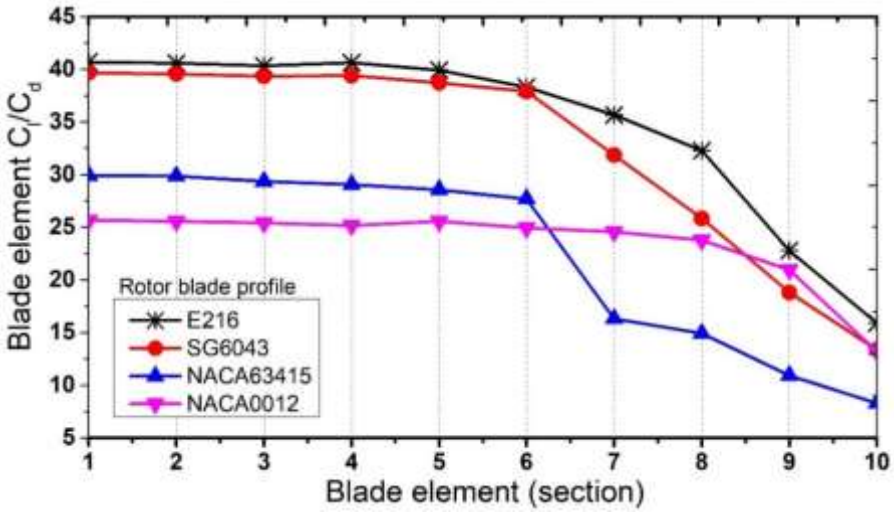

Fig. 4.4. Sectional Lift/Drag ratio of the designed rotor blade

Thereafter, with the help of Eqs. (4.1) and (4.2), the C_p of all the four models is estimated under the prescribed condition (Table 4.1) using BEMT analysis. The performance estimation presented in Fig. 4.5 shows that the SHAWT model having E216 profile has the highest C_p of 0.37 at λ = 2.5. This predicted C_p is about 62.39% of Betz's limit. This estimation through BEMT for low Re and low λ application is very much suitable for the SHAWT. Other observation through BEMT analysis is the reduction in C_p while selecting a thicker blade. From Fig. 4.5, it can be seen that NACA63415 having t/c of about 13% (compared to 10.4% of E216) produces a lesser C_p by 8%. This particular observation on the dependence of t/c on the performance of SHAWT models can be an interesting topic for future research. The experimental investigation is then performed for the model having E216 profile, which is discussed in the following subsections.

$$F = \left(\frac{2}{\pi}\right)\cos^{-1}\left[\exp\left(-\left\{\frac{(B/2)\left[1-(r/R\right]}{(r/R)\sin\phi}\right\}\right)\right] \tag{4.1}$$

$$C_p = \left(\frac{8}{\lambda M}\right)\sum_{i=k}^{M} F_i \sin^2\phi_i(\cos\phi_i - \lambda_{ri}\sin\phi_i)(\sin\phi_i + \lambda_{ri}\cos\phi_i)\left[1-\left(\frac{C_d}{C_l}\right)\cot\phi_i\right]\lambda_{ri}^2 \tag{4.2}$$

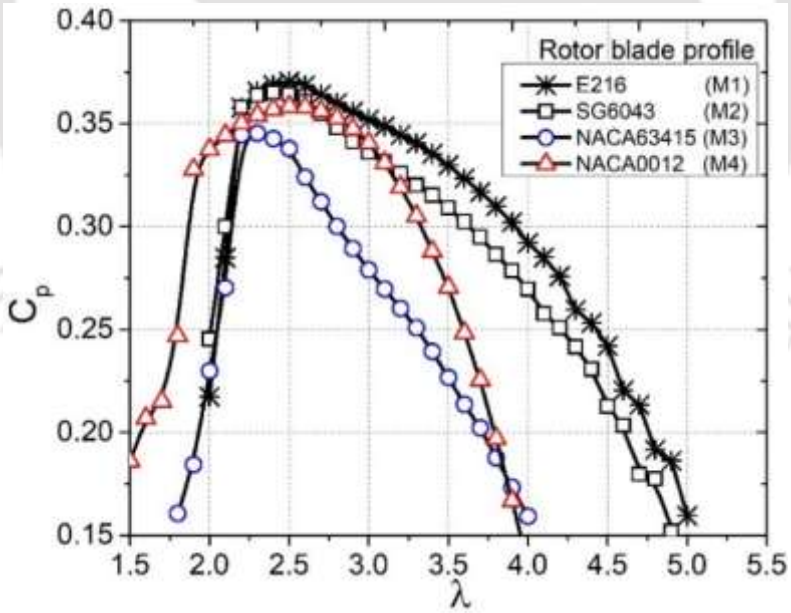

Fig. 4.5. Performance characteristics of test models using BEMT analysis

4.2.1 Performance Assessment of BEMT Rotors.

The prediction by BEMT is only useful in estimating the expected output, however, it is the experimental outcome that determines the feasibility of the designed rotor. It is therefore required to examine the overall rotor performance meticulously. The geometric and wind flow conditions for the performance estimation of rotors is given in Table 4.2.

Table 4.2 Model turbines and corresponding experimental constraints

SHAWT models	Blade profile	Wind Velocity, U (m/s)	Pitch angle, θ_p (°)	Evaluated Parameters
M1	E216	7 m/s, 8 m/s, and 9 m/s	$\theta_p = \theta_{p,design}$ and, $\theta_p = \theta_{p,design} \pm 5^o$	τ, ω, P, C_p
M2	SG6043			
M3	NACA63416			
M4	NACA0012			

4.2.1.1 Rotational Characteristics at Design Pitch Angle

To start with, the rotational characteristics of test rotors have been examined at their respective $\theta_p = \theta_{p,design}$. Through BEMT, the values of $\theta_{p,design}$ of M1, M2, M3, and M4 are found to be 25.47˚, 25.48˚, 25.47˚, and 24.57˚, respectively. Because of their smaller sizes, the θ_p deviation of the rotor is assumed to be within $\theta_p = \theta_{p,design} \pm 0.5^\circ$ for all the cases. Figure 4.6 represents the averaged rpm at U = 7 m/s, 8 m/s, and 9 m/s of the rotors. From Fig. 4.6(a), it can be seen that the rotor M1 could reach up to ~3400 rpm at 9 m/s. However, there is a substantial drop of about 35% when tested at 7 m/s. Similar behaviour is also seen for M2, where the drop in rpm is ~33.5% (Fig. 4.6b); while for M3, the drop in rpm is found to be about 35.3% (Fig. 4.6c), and for M4, this is about 36.4% (Fig. 4.6d). One of the noticeable features of rotational characteristics is the unique display of rpm vs. λ at different flow conditions, and this is also reported in previous studies (Song and Luitz, 2014). Figure 4.7 shows the rotational behaviour of the model rotors at U = 9.0 m/s, where the rotors show different magnitude of rpm with a closely related slope. The observation also suggests that for every unique flow condition, these rotors would display a unique operational limit of λ.

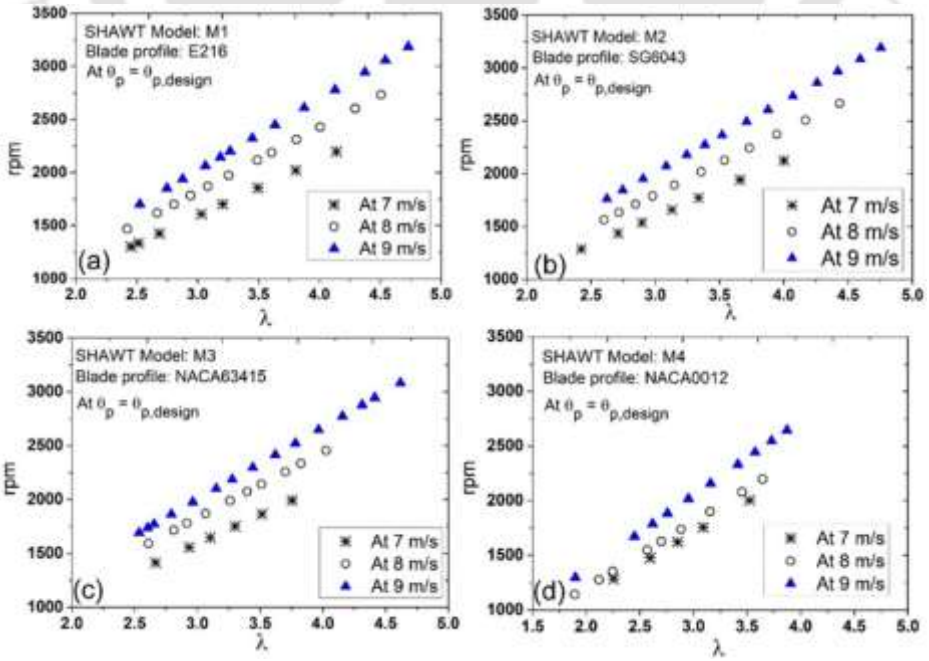

Fig. 4.6 Rotational characteristics of SHAWT models (a) M1, (b) M2, (c) M3, and (b) M4 at $\theta_p = \theta_{p,design}$

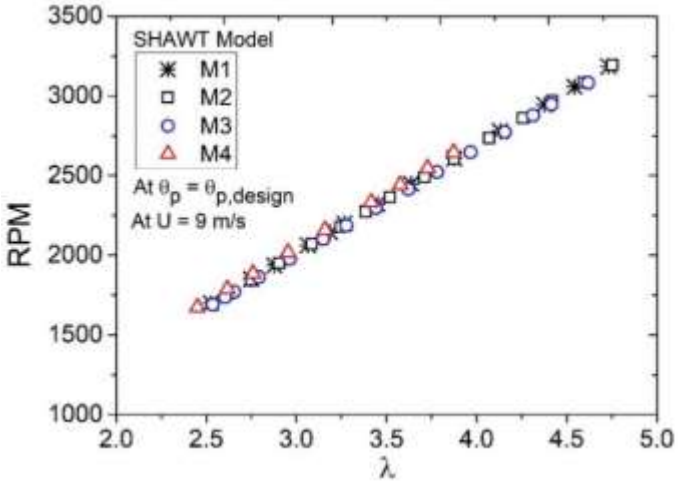

Fig. 4.7. The rotational characteristics of four model rotors at U = 9 m/s under design condition

4.2.1.2 Power Extraction Characteristics at Design Pitch Angle

The power extraction characteristics of the rotors are shown in Fig. 4.8. It can be seen that with the change of wind speed, the operational range of λ changes. Figure 4.8(a) depicts the power extraction of M1 at $\theta_{p,design}$ = 25.47˚, where it can be observed that from the available wind power of ~20.2 W (at 9 m/s), the M1 is capable of extracting 7.4 W at λ = 2.52. It is interesting to note that a sharp fall in performance is observed beyond λ_{opt} condition indicating the initiation of stalling effect. A significant drop in power extraction is observed at 7 m/s, where M1 is able to capture only ~2.4 W from the available instant power of 9.5 W (Fig. 4.8b). The M2 rotor is able to capture ~6.4 W at λ = 3.0, suggesting that its performance is relatively lesser than M1 at 9 m/s. Similarly, at 9 m/s, the M3 rotor is able to capture ~5.8 W at λ = 2.5 (Fig. 4.8c), while M4 captures ~3.5 W at λ = 2.46 (Fig. 4.8d). Furthermore, while changing the wind speed, there is a change in the optimum power extraction with a new operational range of λ, although the rotor tries to capture the optimum power close to $\lambda_{opt} = \lambda_{design} \pm 0.5$. It can thus be summarized that at the same wind speed and at their respective $\theta_{p,design}$, the power produced by M1 > M2 > M3 > M4 as can be seen from Fig. 4.9.

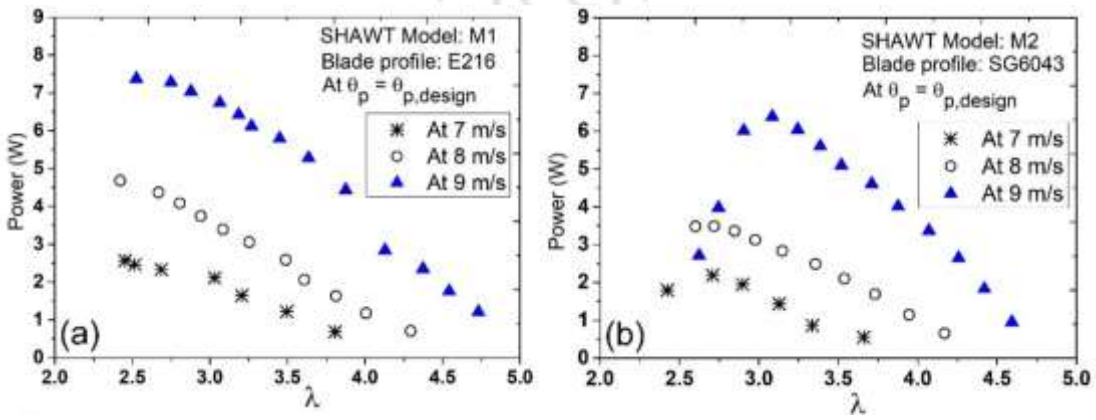

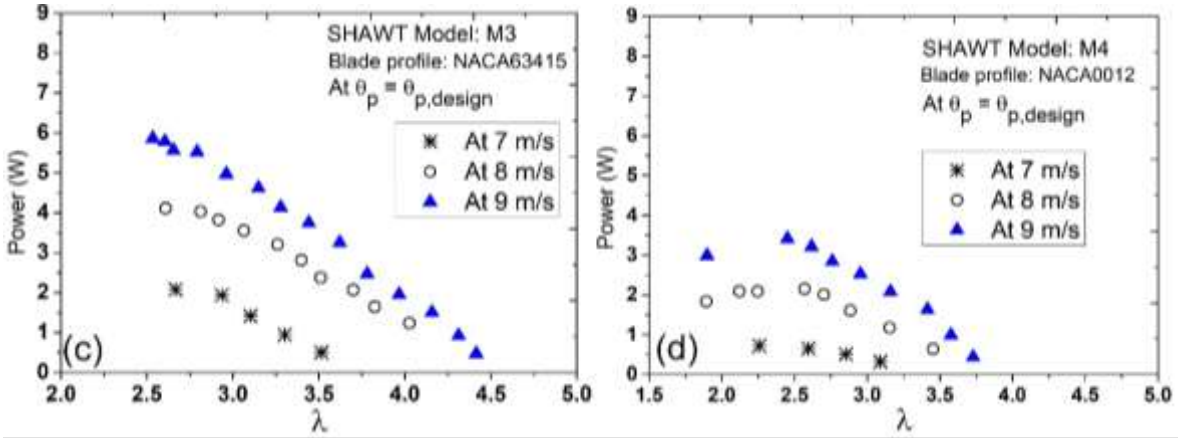

Fig. 4.8. Power extraction characteristics of model SHAWT (a) M1, (b) M2, (c) M3, and (b) M4 at $\theta_p = \theta_{p,design}$

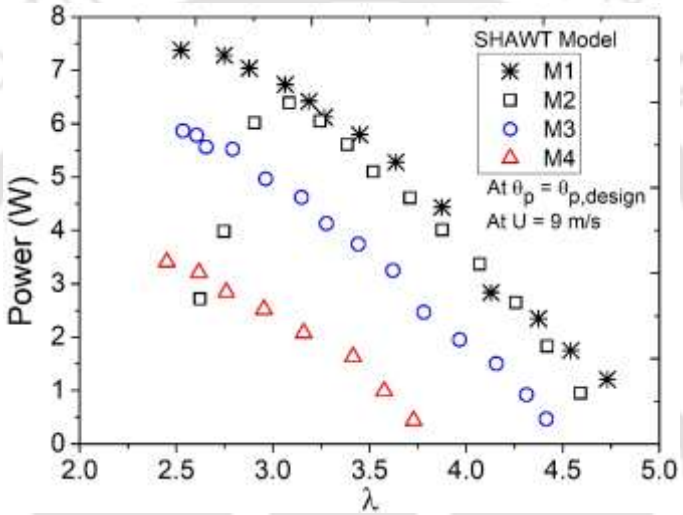

Fig. 4.9. Power extraction characteristics of the tested models at 9 m/s under design condition

To further understand the extent of power extraction by the model rotors, the individual rotor is subjected to different wind speeds at a fixed load. Figure 4.10 shows the power extraction potential of the model rotors with the change of *U*. At no-load condition, the cut-in wind speed of the rotors is found to be in the range of 2 – 2.5 m/s, whereas, at the load condition, it lies in the range of 3.5 – 5 m/s. The cut-out wind speed of the test rotors is found to be in the range of 11–14 m/s. It is to be noted that the rotors have not been tested at higher wind speed to avoid structural failure. However, in reality whole swept area does not contribute to power generation due the presence of the Hub (about 15-25% of R). Furthermore, the spanwise movement of flow is inevitable, thus reducing the performance of rotor and as a result, a reduction Cp from predicted value is observed. Following the standard procedures reported, the errors associated with torque and rpm are calculated in terms of standard deviation (SD), which are found to be about 1.0% and 2%, respectively. The corresponding uncertainty of power is found to be about 2.2%.

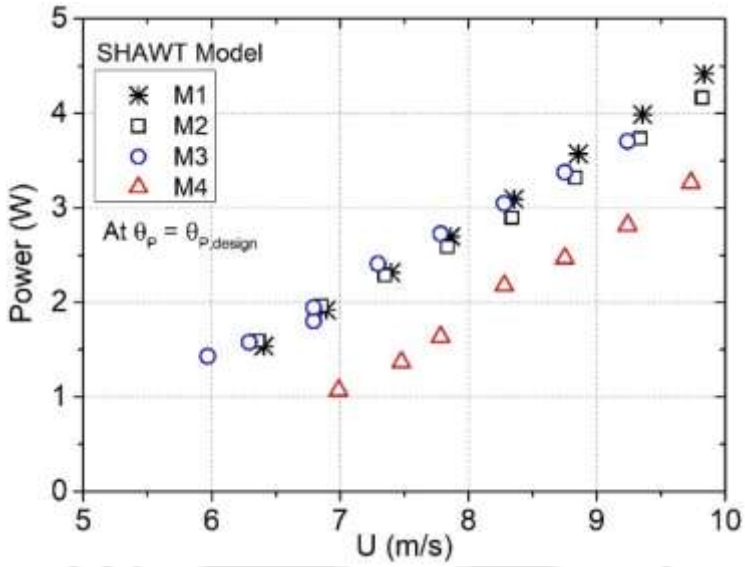

Fig. 4.10. Variation of power with wind speed

4.2.1.3 Power Coefficients at Design Pitch Angle

Having analysed the rpm and power extraction characteristics, the C_p of each rotor is evaluated. Figure 4.11(a) shows the performance of M1 at $\theta_{p,design} = 25.47^{\circ}$. At U = 7, 8, and 9 m/s, the optimum C_p of M1 is found to be 0.24, 0.30, and 0.34, respectively, which is about 41.2%, 50.4%, and 58.01% of Betz's limit. It is evident that any change of U leads to a change of C_{pmax} and the operational range of λ, some typical characteristics of SHAWTs (Treuren, 2015; McTavish et al. 2013). The predicted C_{pmax} of the M1 (by BEMT) is found to be 0.37 at λ = 2.5, whereas the closest value of C_{pmax} (by experiments) is 0.34 at λ = 2.46. Thus, there is a deviation of about 8% between the theoretical and the experimental analyses. This is mainly caused by the hub losses, frictional losses, tip losses, and others. Notwithstanding, the performance of M1 is found to be promising despite being a SHAWT with its low *Re* condition. Similarly, the performance of M2 is evaluate at $\theta_{p,design} = 25.48^{\circ}$, where the C_{pmax} is found to be 0.22, 0.24, and 0.30 at U = 7, 8, and 9 m/s, respectively (Fig. 4.11b), which is about 37.1%, 40.5%, and 50.6% of Betz's limit. In this case also, the operational limit of λ changes with higher λ_{opt} than the design condition. At U = 9 m/s, there is a decrease of C_{pmax} by 11.7% as compared to M1, suggesting that M2 is inferior in terms of performance than M1. At U = 7, 8, and 9 m/s, the C_{pmax} of M3 is found to be 0.19, 0.26, and 0.28, respectively, when $\theta_{p,design} = 25.47^{\circ}$ (Fig. 4.11c), which is about 32%, 43.8%, and 47.2% of Betz's limit. Finally, at $\theta_{p,design} = 24.57^{\circ}$, the C_{pmax} of M4 is found to be 0.06, 0.13, and 0.16 at U = 7, 8 and 9 m/s respectively (Fig. 4.11d), which is about 9.8%, 22%, and 26.3% of Betz's limit. From BEMT, the M4 shows a C_{pmax} = 0.36 (at 9 m/s), however, the experimental data gives the C_{pmax} = 0.16, indicating a higher amount of loss than the other models. Table 4.3 shows the C_{pmax} and the corresponding optimum λ of all the test rotors.

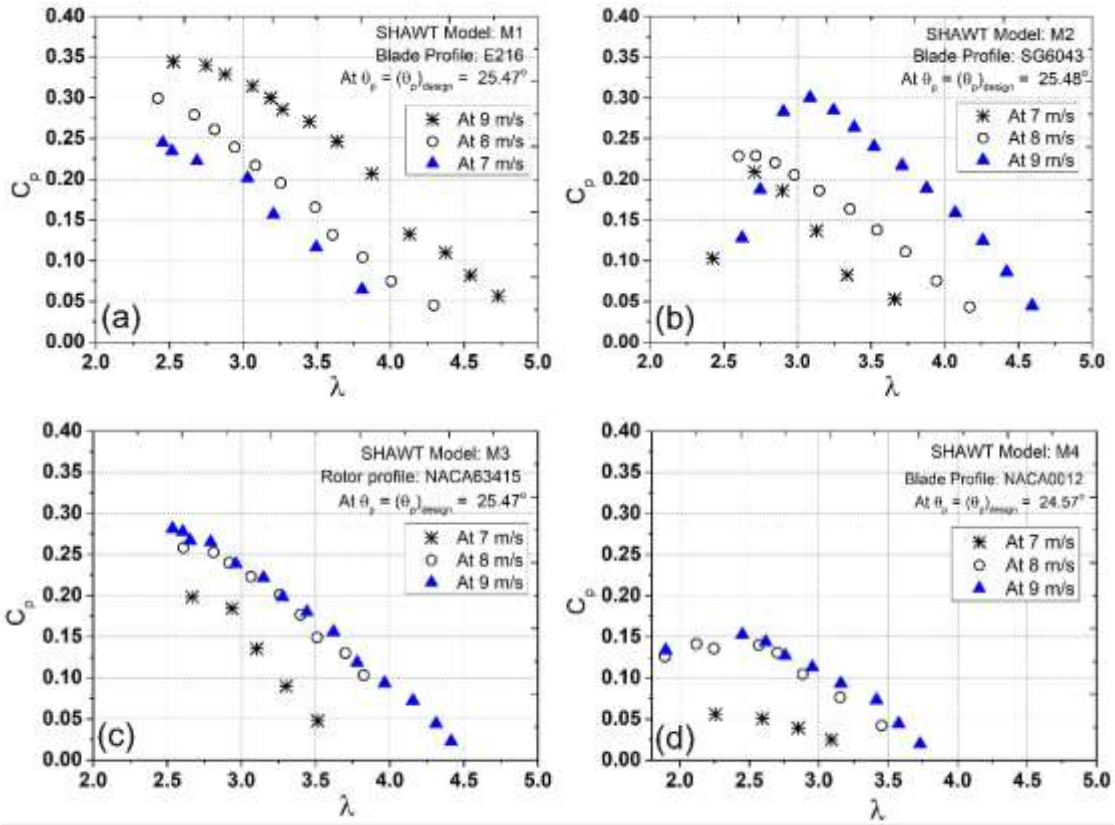

Fig. 4.11. Performance characteristics of SHAWT models (a) M1, (b) M2, (c) M3, and (d) M4 at $\theta_p = \theta_{p,design}$

Table 4.3 Experimental values of maximum C_p at design pitch angle and optimum rotor λ.

SHAWT models	M1			M2			M3			M4		
BEMT C_{pmax} at λ = 2.5	0.37			0.36			0.33			0.35		
U (m/s)	7	8	9	7	8	9	7	8	9	7	8	9
Maximum C_p	0.24	0.30	0.34	0.20	0.23	0.30	0.20	0.26	0.28	0.05	0.14	0.16
Optimum λ	2.45	2.42	2.52	3.0	2.6	2.7	2.66	2.60	2.53	2.25	2.12	2.45

The comparative analysis of all the test rotors is shown in Fig. 4.12 at their respective $\theta_{p,design}$. The performance drop in C_p is found to be analogous to its aerodynamic behavior. Figure 4.12(a) shows the performance curve of the rotors at 8 m/s, where the C_{pmax} of M1, M2, M3, and M4 are found to be 0.30, 0.23, 0.26, and 0.14, respectively. As expected, the C_{pmax} of each model rotor increases at 9 m/s. For M4, this enhancement is found to be 54.12%, 48%, and 47.22% for M1, M2 and M3, respectively (Fig. 4.12b). It can be stated that under the design θ_p condition, M1 performs better than the rest of the rotors. Further, the experimental C_{pmax} of M4 shows a reduced value as opposed to its BEMT predicted value. This reduction of C_{pmax} could be attributed to its relativley higher starting torque and higher solidity. Though the earlier studies on the use of NACA0012 (Singh and Ahmad, 2013; Kishore and Priya, 2013; McTavish et al. 2013; Ismail et al. 2022) had shown promising results, however, the rotors used by them

were proportionately larger than the present test cases. At this point, it can be stated that operating a high solidity SHAWT could deterioate the overall rotor performance. Thus, there is a need to study the effect of solidity on SHAWTs at low *Re* and low λ conditions, especially for different turbine configurations. The C_{pmax} of M1 and M4 at 9 m/s is found to be around ~0.34 and ~0.16 at λ = 2.45 and 2.52, respectively. Hence, the BEMT prediction and the wind tunnel experiments demonstrate the suitability of M1 rotor for low *Re* and low λ applications.

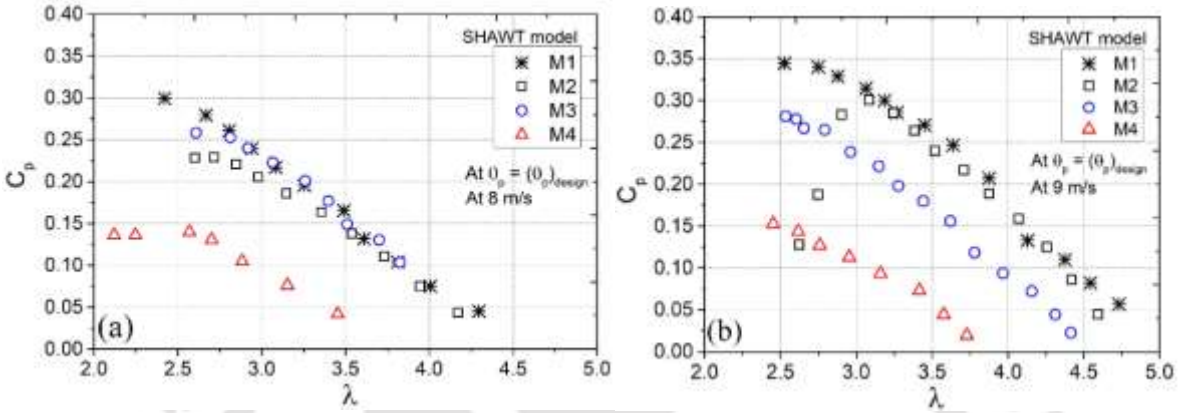

Fig. 4.12. Performance characteristic of SHAWT models at (a) 8 m/s and (b) 9 m/s under $\theta_p = \theta_{p,design}$ condition

4.2.1.4 Rotational Characteristics at Offset Pitch Angle

From the above analysis, it can be stated that the model rotors produce the maximum C_p close to BEMT predicted value at $\theta_{p,design}$. Now, to ensure that this $\theta_{p,design}$ is the optimum condition, an experimental study on the rotor performance is also carried out at off-set pitch angles. This off-set angle is not associated with the BEMT program, and rather it is simply the off-set angle with respect to the $\theta_{p,design}$ that is manually adjusted during the experiments. A past study (Song and Luitz, 2014) on the effect of off-set θ_p has indeed shown some promising results. In view of this, the performance of the model rotors is carried out at $\theta_p = \theta_{p,design} \pm 5^{\circ}$. Figure 4.13 shows the rotational characteristics of the model rotors at different off-set pitch angles. The rotor M1 could reach up to ~3200 rpm at $\theta_{p,design}$, but as expected, when θ_p is varied, a fall in rpm with respect to λ is observed (Fig. 4.13a). Under the same wind speed, M2 can reach to about 2700 rpm (Fig. 4.13b). The rpm of M3 slightly decreases by about 8% with respect to M2 (Fig. 4.13c). On the other hand, the M4 rotor shows a further decrease in rpm, reaching up to about 2200 rpm (Fig. 4.13d). For M1 and M2, the rpm is found to be maximum at $\theta_{p,design}$, and $\theta_{p,design}$-5˚; whereas for M3 and M4, the rpm is found to be maximum in the order of $\theta_{p,design}$, $\theta_{p,design}$-5˚, and $\theta_{p,design}$+5˚. At $\theta_p = \theta_{p,design}$-10˚, the acquired rpm data for all the model rotors are relatively insignificant as compared to other θ_p conditions, and hence, these data are not presented. The implication of off-set θ_p from $\theta_{p,design}$ is also found to be promising in an array of turbines (Hasan et al. 2019; Ossmann et al. 2021).

It is quite clear from Fig. 4.13 that there is drop in rpm of the rotors upon changing the θ_p from its design value. In all the cases, the rpm at off-set angle is relatively lesser than the $\theta_{p,design}$ suggesting a degradation in the rotor performance. It is to be noted that the model rotors have different sensitivity towards off-set θ_p, and this is mainly due to their varying geometric configurations.

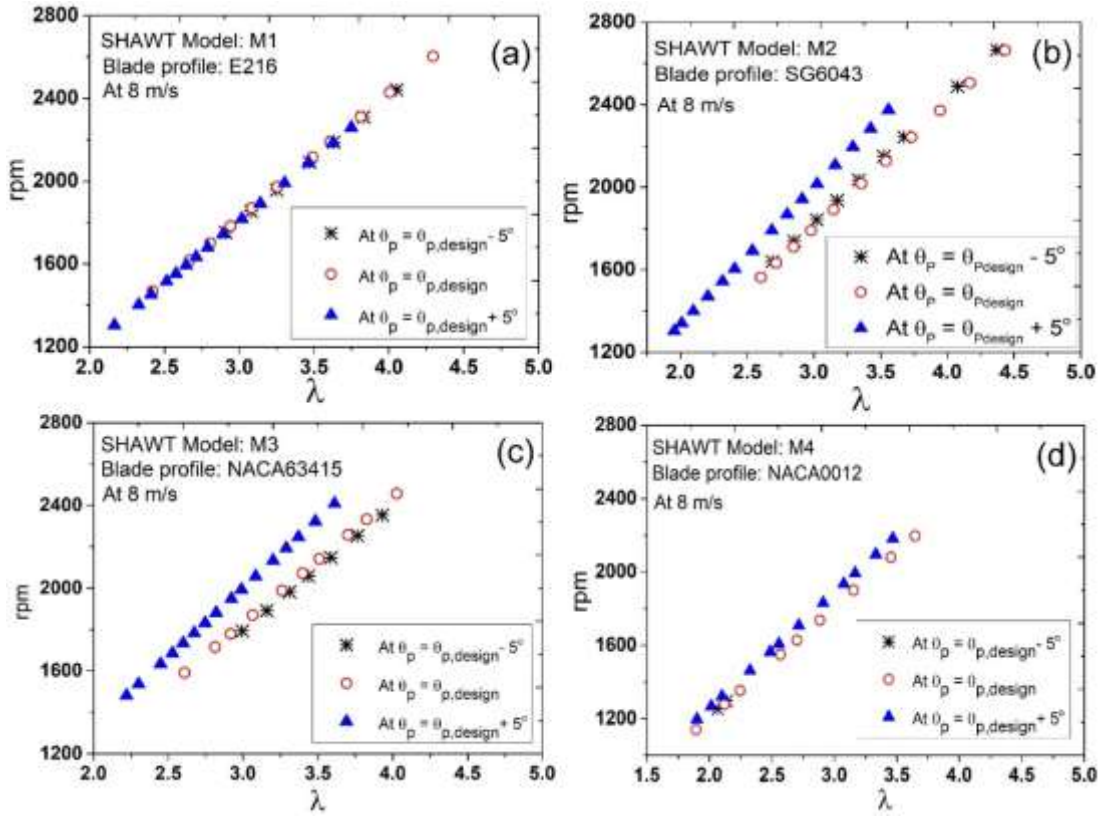

Fig. 4.13. Rotational characteristics of SHAWT models (a) M1, (b) M2, (c) M3, and (b) M4 at off-set θ_p conditions

4.2.1.5 Power Extraction Characteristics at Off-Set Pitch Angle

The power extraction characteristics of the test rotors at different θ_p are presented in Fig. 4.14. From the available wind power of ~14.2 W (at U=8 m/s), the M1 can capture P_{max} of ~4.7 W and ~4.3 W at $\theta_{p,design}$ and $\theta_{p,design}$ + 5˚, respectively as compared to ~3.2 W at $\theta_{p,design}$ - 5˚ (Fig. 4.14a). In the case of M2, the rotor can produce P_{max} of ~3.5 W and ~5.4 W at $\theta_{p,design}$ and $\theta_{p,design}$ + 5˚, respectively (Fig. 4.14b). The power extraction by M2 at $\theta_{p,design}$ + 5˚ is found to be higher as compared to $\theta_{p,design}$, however, its corresponding C_{pmax} is lesser. A considerable drop in the power extraction potential of M3 is recorded at $\theta_{p,design}$ - 5˚ (Fig. 4.14c), where P_{max} of ~4.1 W is obtained at the design condition. Finally, the baseline rotor M4 produces the maximum power at $\theta_{p,design}$ (~ 2.2 W) and $\theta_{p,design}$ + 5˚ (~ 3.55 W) as seen in Fig. 4.14(d). The M4 rotor power extraction at θ_p (< $\theta_{p,design}$) is noticed to be negligible and insignificant, and therefore, the data are not presented. While operating at $\theta_{p,design}$, the P_{max} value of M4 is found

to be lesser than at $\theta_{p,design}$ + 5˚. This anomaly is due to relatively higher solidity and the associated drag of M4 at higher θ_p. This impact is also seen in the C_p characteristics with respect to the BEMT predicted value. Furthermore, the performance degradation of the model rotors is found to be significant, and the corresponding measured parameters are negligible when $(\theta_{p,design}$ - 10°) < θ_p > $(\theta_{p,design}$ + 10°).

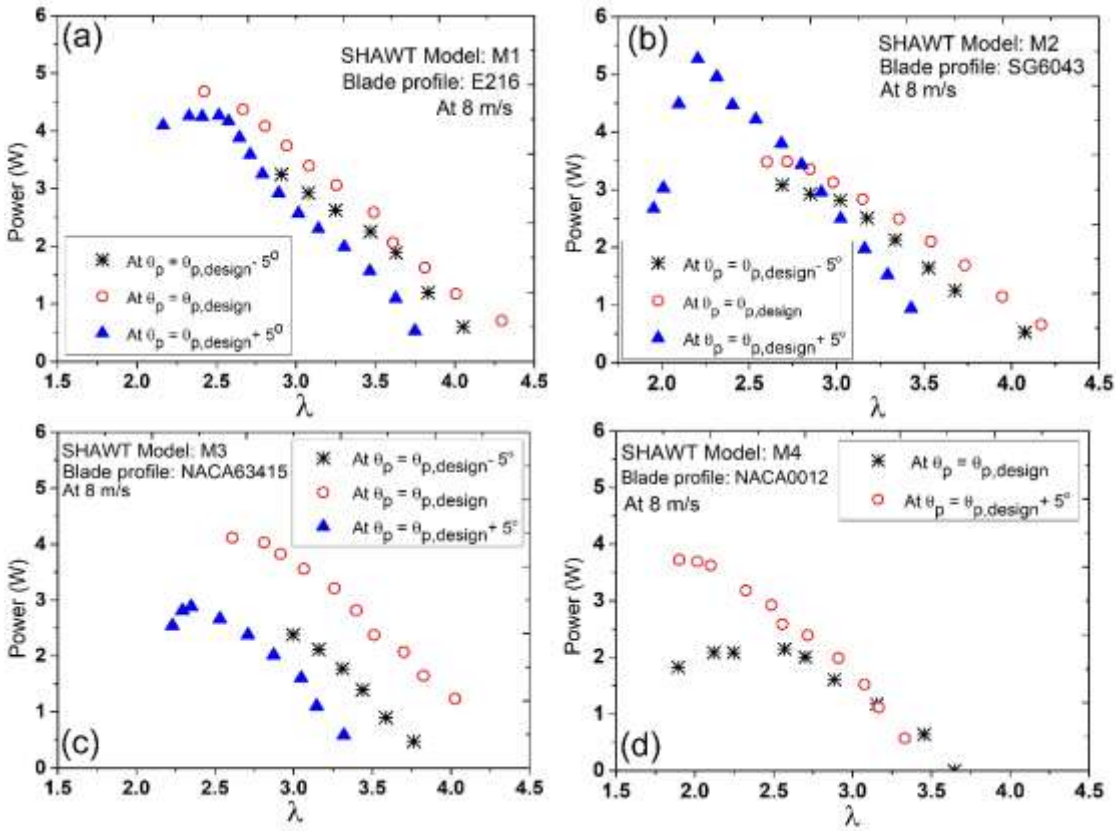

Fig. 4.14. Power extraction characteristics of model SHAWT (a) M1, (b) M2, (c) M3, and (b) M4 at off-set θ_p conditions

4.2.1.6 Power coefficients at offset pitch angle

Finally, the variation of C_p with λ at different θ_p is evaluated and presented in Fig. 4.15. The C_{pmax} of rotor M1 is obtained at $\theta_{p,design}$ followed by $\theta_{p,design}$ + 5˚ (Fig. 4.15a), however, a substantial drop in C_p is observed at $\theta_p = \theta_{p,design}$ - 5˚. The concurrent results obtained during the power extraction study have also shown that the test rotors give a potential power output closer to $\theta_{p,design}$. For M2, a decrease of C_{pmax} by about ~11.4% is observed upon changing the $\theta_{p,design}$ to $\theta_{p,design}$ + 5˚ (Fig. 4.15b). While M3 shows C_{pmax} of 0.26 and 0.24 at $\theta_{p,design}$ and $\theta_{p,design}$ + 5˚, respectively at U = 8 m/s (Fig. 4.15c). Further, there is a drop in C_{pmax} by about 30% while operating at $\theta_p = \theta_{p,design}$ - 5˚. For M4, the change of C_{pmax} is about 29% with respect to C_{pmax} at $\theta_{p,design}$ condition (Fig. 4.15d). Here, a reduction in the operational limit of M4 in terms of λ is observed. The decreasing order of C_{pmax} of the test rotors are found to be M1, M2, M3, and M4. These experimental C_{pmax} values of the test rotors are relatively lesser than the BEMT prediction though they show a nearly identical behavior.

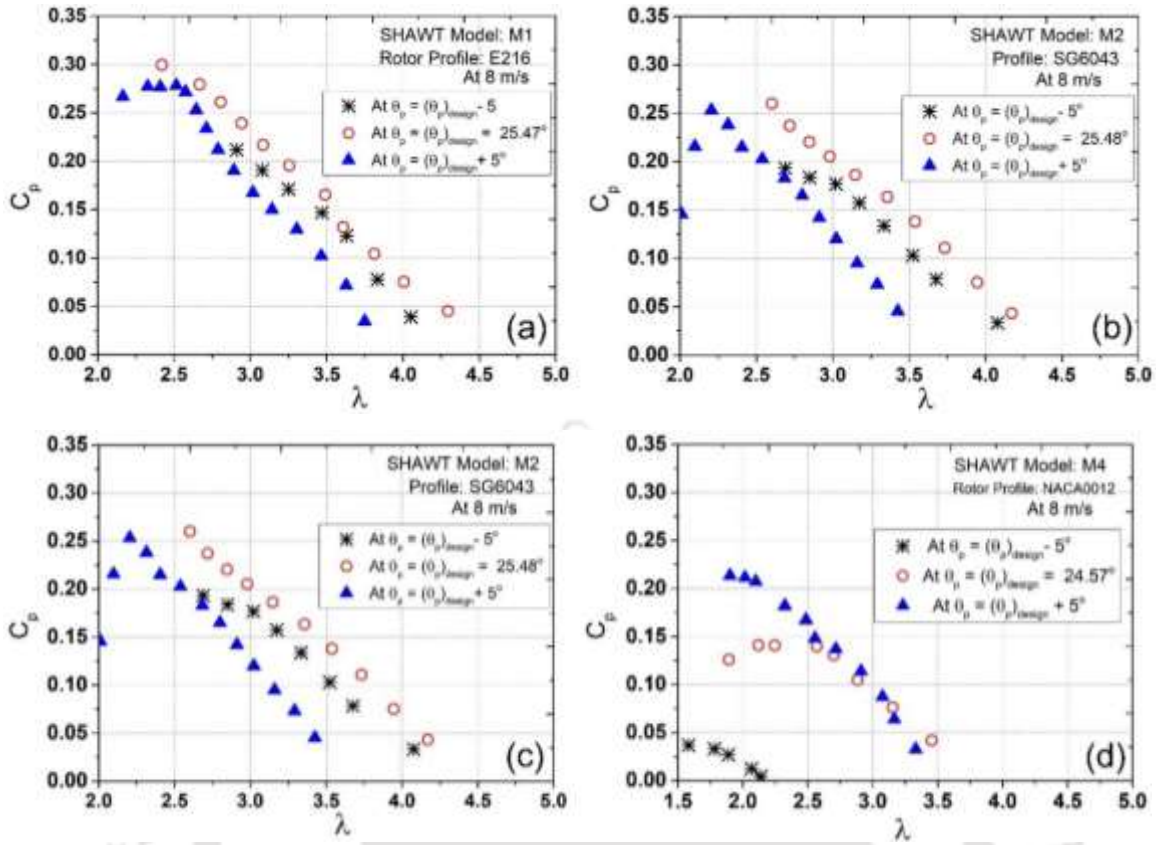

Fig. 4.15. Performance characteristics of SHAWT models (a) M1, (b) M2, (c) M3, and (d) M4 at off-set θ_p conditions

From the above analysis, it can be suggested that upon varying the θ_p from its design condition, it is very unlikely for a BEMT rotor to outperform from its design condition. The other key observation of this study is the change in the operational limit of λ with θ_p, and this is found to be consistent with the previous studies (Song and Luitz, 2014; McTavish et al. 2013; Ismail et al. 2022). The reduction in the experimental C_p is primarily due to hub losses, tip losses, frictional losses, pitch angle misalignment, and others.

The present study demonstrates the capability of the model rotors at low *Re* and low λ conditions. The rotors M1 (E216 profile) and M2 (SG6043 profile) show promising results. The effect of *t/c* in M3 (NACA63415) is not found to be very influential in improving its performance. On the other hand, the use of thinner airfoil like E216 (M1) sounds optimistic for the rotor blade. Though with the use of thicker airfoil, an additional advantage could be gained in terms of structural strength and extended operational limit. From the present study, it is to be noted that at low *Re* and low λ, the performance of SHAWT model rotors degrades with an increase of solidity. The present model rotors could potentially be employed on taller structures, seashores, moving boats, and at high altitudes where the wind velocity is significant.

4.3 Design and Testing of Mixed Airfoil SHAWT

The large wind turbines (LWTs) are often designed considering different airfoils across the section of the blade. The adoption of such methodology comes from the fact that, for an LWT blades, they are often subjected to extreme aerodynamic load, thus requires not only the structural integrity but also geometric/aerodynamic refinement (Bilgli et al. 2021). The implication of multiple airfoil has its own advantage over the uniform airfoil, to maintain and enhance the overall performance as well as to focus the section of need. It is quite understood because the root section of the blade will be subjected to major stress as a consequence of the centrifugal force, thus, it is necessary to have a thicker airfoil at the root section and in most LWTs. Likewise, the SHAWT will also require a thicker airfoil at the root section, as such rotors are often noted for their high rpm to attain the high tip seed ratio. On the other hand, the tip section of the SHAWT is required to have thinner airfoil to maintain optimum performance (Tummala et al. 2016; Abdelsalam et al. 2021). With this analogy, a case study has been performed to examine the effect of mixed airfoil on SHAWT performance.

In this study, the mixed airfoil blade for the SHAWT has been chosen on the basis of t/c and max. C_l/C_d ratio. From the class of airfoils examined in the literature survey (Table 2.3), a total of six low *Re* airfoil has been opted (Table 4.4) for the root section, as shown in Fig. 4.16. Accordingly, upon reviewing their aerodynamic characteristics at *Re* = 0.5 x 10^5, and considering the t/c, airfoil E555 and LS (1)-0421 has been considered for the root section.

Table 4.4 Root airfoils geometry and aerodynamic characteristic

Airfoil	Thickness (*t/c* %)	Chamber (%)	Max. C_l/C_d	'α' at max. C_l/C_d
SG6040	16	2.3	26.065	11.5
NACA63418	17.9	2.2	20.774	11
S835	21	2.4	23.68	11
S823	21.4	2.4	20.94	11.5
LS (1)-0421	20.9	2.4	23.79	10.25
E555	16	2.6	27.828	10.5

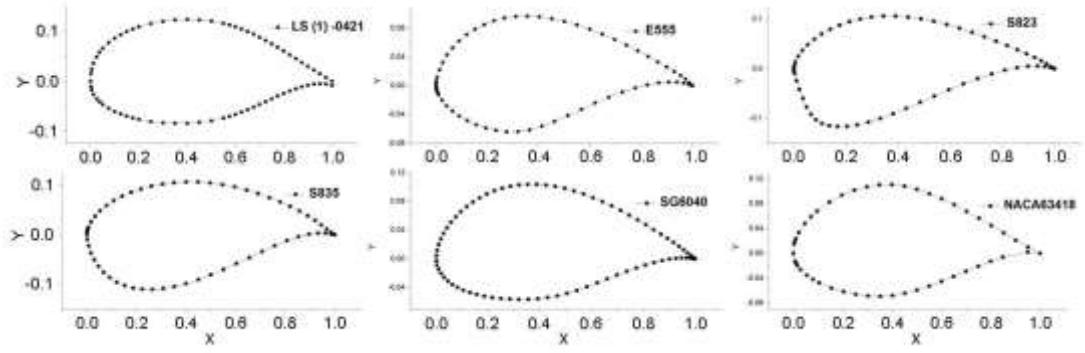

Fig. 4.16. Thick airfoils of mixed profile SHAWT blade

The design and performance analysis procedures adopted for the mixed airfoil blade is similar to the case study presented in section 4.3. In this case also, a total of 10 blade elements where considered; the first two elements from the root section are taken as airfoil having the higher t/c, which is in line with the general approach (Manwell et al. 2015). Whereas, the remaining eight elements are taken for the airfoil having lesser t/c; this is to ensure that maximum segment of the blade is contributing towards the power generation. The case study presented in section 4.3 shows that E216 airfoil has a promising implication in SHAWT, thus, the first combination of mixed airfoil is LS (1)-0421 – E216 and the second combination taken is E555 – E387, which has been indicated as MX1 and MX2, respectively. The geometric parameters of the mixed airfoil have been obtained through BEMT as per the methodology described in Fig. 3.5. Table 4.5 represents the geometric parameters of the two rotors. The sectional and modelled illustration of mixed airfoil SHAWT is shown in Fig. 4.17, and Fig. 4.18 represents the fabricated model.

Table 4.5 BEMT designed chord length and pitch angle of the blade element sections

Airfoil	**LS (1)0421 – E216 (MX1)**	**E555 – E387 (MX2)**	**LS (1)0421 – E216 (MX1)**	**E555 – E387 (MX2)**
r/R	Chord length (c) in cm		Section pitch angle (θ_p) in degree	
0.23	5.46	4.72	27.13	26.88
0.29	5.43	4.69	22.51	22.26
0.36	3.94	4.84	20.93	20.43
0.42	3.71	4.56	17.78	17.28
0.49	3.47	4.26	15.16	14.66
0.55	3.23	3.97	12.98	12.48
0.61	3.01	3.7	11.13	10.63
0.68	2.81	3.45	9.57	9.07
0.74	2.63	3.23	8.23	7.73
0.81	2.46	3.03	7.06	6.56
1	2.39	2.61	6.53	6.03

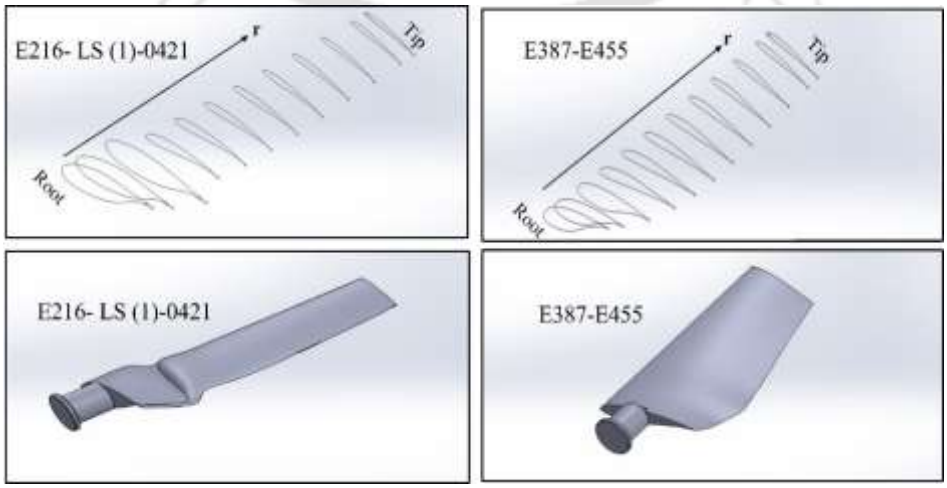

Fig. 4.17 Depicting the airfoil sections and solid models for the mixed airfoils blade

Fig. 4.18. Illustration of mixed airfoil SHAWT (a) MX1 (LS(1)042-E216), and (b) MX2 (E555-E387)

4.3 Performance Characteristics of Mixed Airfoil SHAWT

The modelled rotor blade was tested in the subsonic wind tunnel. The operational limit and conditions were kept similar to the case study presented in section 4.2. Figure 4.19 shows the C_p vs λ relation of MX1 and MX2, predicted through BEMT. The maximum value of *Cp* for MX1 and MX2 at design λ (=2.5) and $\theta_{p,design}$ are 0.37 and 0.36, respectively; this value of C_{pmax} is about 62.4 % and 60.7 % of Betz's or Betz-Joukowsky limit. The $\theta_{p,design}$ for the MX1 and MX2 rotor are 23.48º, respectively. The predicted performance curve shows that C_p vs λ characteristics curves for the two rotors have relatively similar trend, this is presumably due closely related $\theta_{p,design}$. However, unlike single airfoil bladed rotors (section 4.3), the experimental investigation of MX1 and MX2 shows lesser performance than the BEMT prediction, as shown in Figs. 4.20(a) and 4.20(b).

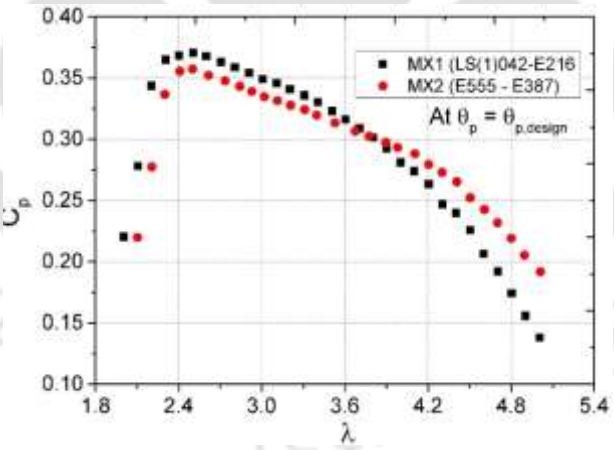

Fig. 4.19. BEMT prediction of rotor MX1 and MX2

The rotor MX2 (E555-E387) has E555 as its root profile and has a max. Cl/Cd of 27.8, whereas MX1 having LS(1)-0421as its root profile has a max. Cl/Cd of 23.8 (Table 4.4). As explained by Tummala et al. 2016, the root profile plays an important role in providing initial torque to the rotor, and the tip profile contributes towards power generation. Therefore, MX2 depicts a slightly higher value at the beginning of turbine operation; however, as the operation progress, the effect of tip profile comes into play, and we see that MX1 having E216 outplays MX2. Figure 4.20(a) shows that under the design condition, the MX1 C_{pmax} at U = 7, 8 and 9m/s are

about 64%, 69% and 74%, respectively of the performance obtained numerically (Fig. 4.19). On the other hand, Fig. 4.20(b) depicts the rotor performance of MX2, its C_{pmax} at the same velocity conditions produces about 65%, 73%, and 78%, respectively, of the BEMT predicted value.

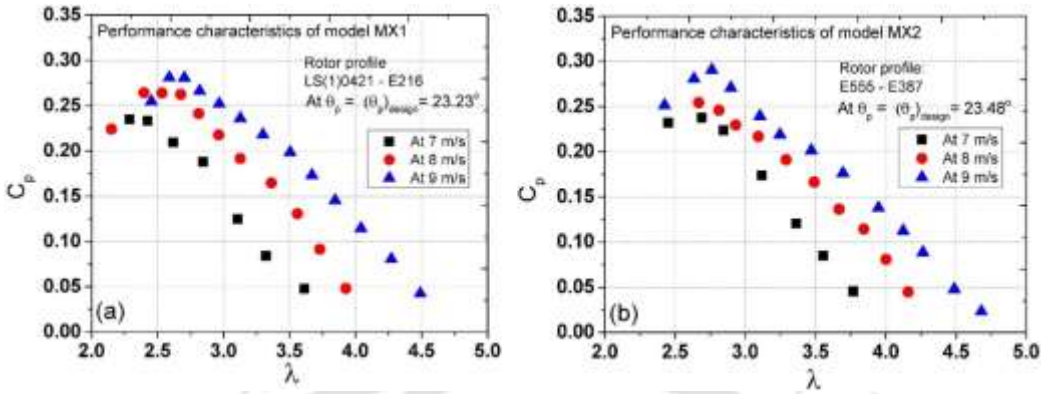

Fig. 4.20. Performance characteristics of (a) MX1, and (b) MX2 at $\theta_{p,design}$

Among the two mixed airfoils rotors, MX1 has relatively higher performance than MX2; though the difference is not significant. It is also observed that MX rotors undergoes about 22% reduction in its C_{pmax} value from its BEMT prediction, compared to about 8% in single airfoil rotor (E216). Thus, suggesting, not so favourable outcome of MX rotor; however, at lower wind speed and blade pitch angle (Fig. 4.21), the MX rotors shows stable performance than the single airfoil rotor. This favourable outcome at lower U and θ_p could be attributed to the contribution of the thicker airfoil at the root, which are known for maintaining the necessary torque apart from structural stability (Karthikeyan et al. 2015). Detailed values of C_{pmax} for MX1 and MX2 at different blow conditions is shown in Table. 4.6.

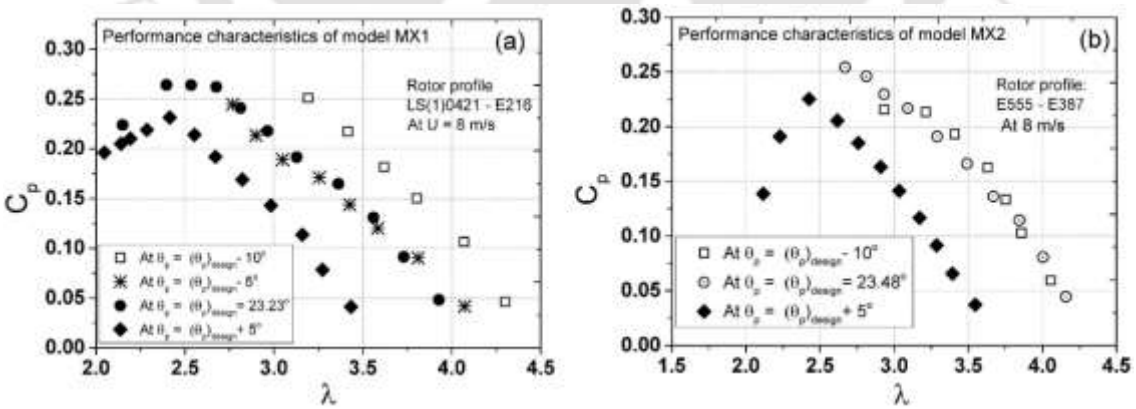

Fig. 4.21. Performance characteristics of (a) MX1, and (b) MX2 at different θ_p

Table 4.6 Analytical and experimental performance characteristics of the rotors

Rotor	**MX1**			**MX2**		
BEMT predicted	C_{pmax} = 0.37 (**at, λ = 2.5**)			C_{pmax} = 0.36 (**at, λ = 2.5**)		
Wind speed (m/s)	9	8	7	9	8	7
Experimental C_{pmax}	0.29	0.25	0.23	0.28	0.26	0.23
λ	2.76	2.66	2.68	2.58	2.39	2.28

4.4 Summary of the Study

This study aims at the design, development and testing of SHAWT model rotors meant for low *Re* and low λ conditions. On the basis of literature survey, airfoil E216, SG6043, NACA63415, and NACA0012 have been chosen for developing the model rotors viz., M1, M2, M3, and M4. Furthermore, testing on mixed airfoil SHAWT has also been performed. The modelled rotors are designed and analyzed using BEMT. Subsequently, they were fabricated and tested in a low-speed subsonic wind tunnel. The key findings of the study are summarized below:

- From BEMT analysis, the C_{pmax} of M1, M2, M3, and M4 at $\lambda = 2.5$ is found to be around 0.37, 0.35, 0.34, and 0.36, respectively, which is about 62.4%, 59.02%, 57.33%, and 60.7% of Betz's limit.
- From wind tunnel studies, the C_{pmax} of M1 at $\theta_{p,design}$ is found to be 0.34 at U = 9 m/s, and this is about 58.01% of Betz's limit. At the same U, the M2 at $\theta_{p,design}$ is capable to produce a C_{pmax} of 0.30 which is about 50.6% of Betz's limit. With a thicker airfoil, the M3 at $\theta_{p,design}$ shows a C_{pmax} of 0.28 at the same U, which is about 47.2% of Betz's limit.
- The M4 (baseline rotor) at $\theta_{p,design}$ reveals a C_{pmax} of 0.16 at U = 9 m/s, which is about 26.3% of Betz's limit. The anomaly in the experimental C_{pmax} of M4 with respect to the predicted value of 0.36 could be attributed to relatively higher solidity and lesser aerodynamic characteristics at low *Re*.
- The effect of θ_p variation on C_p is examined at $\theta_p = \theta_{p,design} \pm 5^\circ$. For all the model rotors, the C_{pmax} is found to be optimum at $\theta_p = \theta_{p,design}$ with the exception of M4 where a C_{pmax} = 0.21 is obtained at $\theta_p = \theta_{p,design} + 5^\circ$. This could be credited to high solidity of M4 as compared to M1, M2 and M3.
- The testing on mixed airfoil SHAWT suggest that the combination has a favorable performance at lower U and θ_p.

The present investigation demonstrates the superior performance of the M1 rotor (with E216 profile) in terms of rotational speed, power extraction, and power coefficient. And also show promising result when used in mixed airfoil blade. The model rotor could be used as a standalone off-grid power generating unit for the individual households, small wind farm, and places requiring minimal energy demand. The know-how of the present investigation could be used in the design and development of other small wind turbines having rotor diameters less than 5 m.

CHAPTER 5
PERFORMANCE ASSESSMENT OF STRAIGHT AND LINEARLY TAPERED (SLT) ROTORS FOR OFF-GRID APPLICATIONS

5.1 Introduction

The objective of this study is to enable the applicability of SLT rotors as a means of standalone off-grid power generation unit, for which a series of experimental investigations have been performed. The motivation for this study comes from the fact that, the BEMT designed rotor involves complex design and fabrication process, as described in Chapter 3 (section 3.2). It is indeed necessary to consider much cheaper and easy to fabricate sets of potential SHAWT blades for off-grid applications. An extensive review has been performed on the scope of non-BEMT rotors; the detailed literature survey has been presented in Chapter 2(section 2.3). The non-BEMT rotors opted for the study are straight and linearly tapered (SLT) rotors; its operational and geometric characteristics are such that it falls in the category of SWTs. The performance of SLT model rotors has been carried out under low *Re* and low λ conditions. Based on the literature review on SWTs (chapter 2), the opted *Re* is 0.5×10^5 and the operational limit of λ is in the range of $0 < \lambda < 6$ (McTavish et al., 2013; MacPhee et al., 2019). Four small HAWT were designed and tested (Fig. 5.1). The first model rotor (indicated at M0) has been designed through the BEMT concept (Chapter 2), while the rest of the three model rotors (indicated as M1, M2, and M3) were designed through linear expansion of a tapered blade based on root chord to tip chord. All the four model rotors have NACA0012 as their sectional profile, the selection of this airfoil has been made based on simplest configuration, available aerodynamic characteristics, and its usage in small HAWTS (Eleni et al., 2012; Kishore et al., 2013; McTavish et al., 2013; Ismail et al., 2022). The model rotors were fabricated using a fuse deposition modelling 3D printer. Afterwards, they were tested in a low turbulence subsonic wind tunnel facility at the Indian Institute of Technology Guwahati (IITG) under different geometric and flow conditions.

Fig. 5.1. (a) BEMT M0 model; (b) SLT M1 model with C_r/C_t = 1:1; (c) SLT M2 model with C_r/C_t = 5:3; (d) SLT M3 model with C_r/C_t = 5:2

5.2 Part-I: Design and Testing of BEMT Rotor

In order to compare the performance characteristics of the SLT rotors, a SHAWT model is developed using BEMT. The design procedures adopted are such that the model would operate at low λ and low *Re* conditions. In this study, the range of λ is between 0.5 – 6 and Re = 0.5 × 10^5. The value of Re is within the scope of SWT applicability as reported in the literature (McTavish et al., 2013). The design procedure using BEMT has been briefly elaborated in chapter 3(section 3.2.3). Figure 5.2(a) represents the variation of chord length (c) and pitch angle (θ_p) along the blade span. The rotor modelled using BEMT is indicated as M0. The corresponding C_p of the M0 rotor is evaluated as per Eq. (4.2), as shown in Fig 5.2(b). The predicted C_{pmax} of M0 is about 0.35 at λ = 2.5, about 59% of the Betz-Joukowsky limit (0.593). In order to ascertain that the M0 rotor is capable of capturing the predicted value, the experimental study on M0 is also carried out. The design parameters obtained through BEMT analysis are fed into the FDM 3D printer, and to ensure that the surface roughness of the blade is well maintained, some vital printing parameters (Table 3.5) are closely monitored.

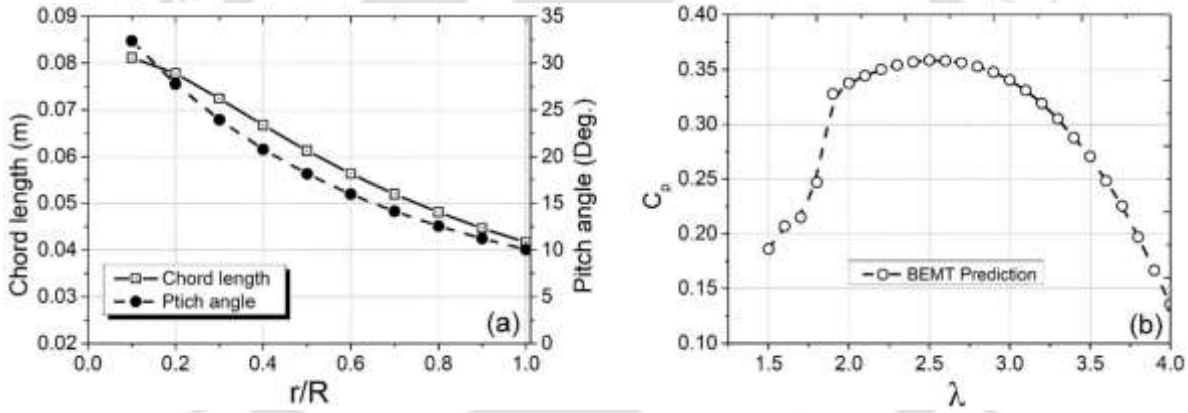

Fig. 5.2. BEMT analysis of M0 rotor: (a) geometric configuration; and (b) performance prediction.

The in-house fabricated rotor model is tested in the wind tunnel under various flow conditions, as shown in Fig. 5.3(a). The investigation is carried out at the design pitch angle (β_{design} = 24.57°) of the rotor. The inlet velocity is varied between 6 to 9 m/s ensuring that the range of λ is within the design limit. It can be observed that the experimentally obtained C_{pmax} value is significantly lower than the predicted value. The maximum C_p value recorded is about 0.15 at λ = 2.8; this is about 58% lesser than the predicted value. Therefore, it can be stated that the BEMT model rotor having a NACA0012 profile produces significantly less C_p compared to the theoretical prediction. This reduction in the rotor performance could be attributed to its relatively higher starting torque and higher solidity, apart from highly transitional and weak aerodynamic performance of NACA0012 at low *Re* (=0.5 × 10^5) as reported (Winslow et al., 2018; Istvan and Yarusevych S, 2018; Lee and Han, 2019). Though the earlier studies on the

use of NACA0012 (Kishore et al., 2013; Eleni et al., 2012; McTavish et al., 2013; Ismail et al., 2022) have shown promising results, however, the rotors used by them was proportionately larger than the present test model. Moreover, the BEMT prediction does not consider the spanwise flow, and for an large wind turbine, it is reasonable. For an small wind turbine, its effect cannot be totally ignored. At this point, it can be acknowledged that operating a higher solidity SHAWT could deteriorate the overall performance of the rotor. Though, there is a need for a detailed study on solidity's effect on the HAWT at low *Re* and low λ. A past study by Song and Luitz, 2014, has shown some promising outcomes while performing the rotor test at offset β. Therefore, it will be interesting to note such behavior for the present rotor. Here, the offset angle is the condition when $\beta \neq \beta_{design}$. This offset angle is not associated with the program, and instead, it is simply the offset angle with respect to the β_{design} that is manually adjusted during experiments. The offset angle is kept at $\beta = \beta_{design} \pm 5^{\circ}$. At β_{design} condition, the M0 rotor can reach up to about 2200 rpm; however, at $\beta_{design} + 5^{\circ}$, the rpm increase and thus the performance of the rotor. As seen from Fig. 5.3(b), the C_{pmax} of M0 rotor increased at $\beta_{design} + 5^{\circ}$, and the corresponding C_{pmax} is about 0.213, which is about 47% increment from the BEMT prediction. At $\beta = \beta_{design} - 10^{\circ}$, the acquired rpm data are relatively insignificant, and thus the data are not presented. The implication of offset β from β_{design} is found to be promising in an array of turbines (Hasan et al., 2019; Ossmann et al., 2021).

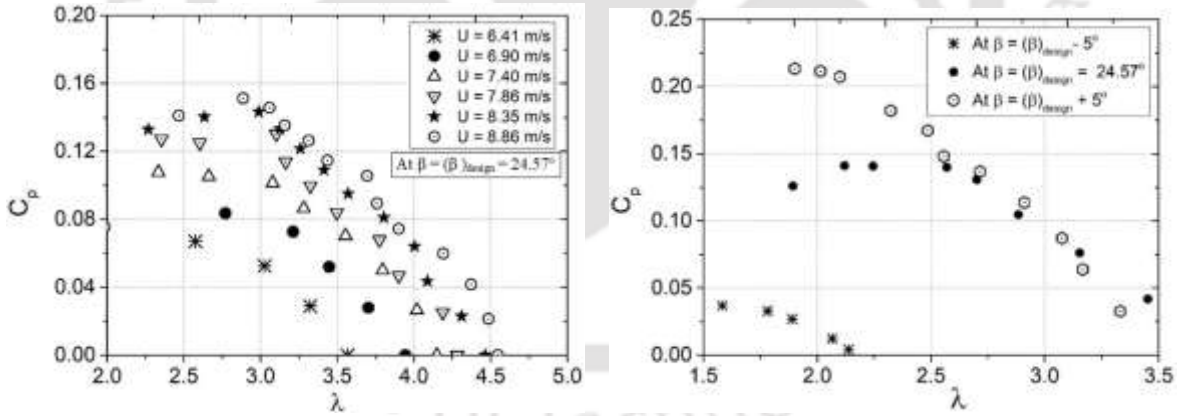

Fig. 5.3. Performance of M0 model rotor (a) at different U and $\beta = \beta_{design}$ (b) performance of M0 rotor at different β under U = 7.95 m/s

5.2 Part-II: Performance Characteristics of SLT Rotors

This section presents the experimental study involving SLT model rotors' performance characterization. Three SLT rotors are adopted, indicated as M1, M2, and M3 (Table 5.1). These model rotors are not developed through BEMT; therefore, the design pitch angle is unknown for this case. To trace the optimum configuration of β for the SLT rotors, the rotor β is gradually varied with respect to the rotor plane, and the corresponding C_p is recorded for all the cases. Usually, the β of the rotor can be fixed or variable depending upon the control system,

where the latter is comprised solution of a well-calibrated mechanism widely used in large WTs (Jauch et al., 2007; Nagai et al., 2009). Such systems are meant for regulating the optimum power when the wind gust is not uniform (Nagai et al., 2009; Smida and Sakly, 2016). By controlling the value of β, it is possible to reduce the thrust force, and the root mean square of torque by about 96% compared to fixed β (Roch et al., 2018). The dependence of β on C_p of the SHAWT has been observed for its practical implementation in the urban region under extreme turbulence (Jauch et al., 2007). So far, the investigation on SLT rotors' performance concerning β is minimal.

Table 5.1 Geometric configuration of model M1, M2 and M3

Rotor Blade Configuration		
Section profile: NACA0012 Rotor Radius (R): 120 mm Span length(L): 100 mm Root Chord (C_r): 50 mm Material: PLA		
M1	M2	M3
Tip Chord (C_t): 50 mm C_r/C_t = 1:1	Tip Chord (C_t): 30 mm C_r/C_t = 5:2	Tip Chord (C_t): 20 mm C_r/C_t = 5:3

In order to have a much better picture of the effect of β, it is varied between 0° and 90° with a step size of 10°. The corresponding performance characteristic at different β of M1 is shown in Fig. 5.4(a), and one can see that C_{pmax} = 0.22 is obtained at $\beta = 20^o$; this is about 37% of the Betz-Joukowsky limit, whereas the minimum value could reach as much as 0.002. Having a distinct optimum performance for a defined β is the general characteristic of many turbines (Jauch et al., 2007). It is also quite intriguing to note the sudden rise and fall of C_p with respect to β. When $20^o < \beta < 50^o$, the M1 model is capable of capturing 15-18% of the Betz-Joukowsky limit. Such behavior could be inferred from the aerodynamic characteristics of NACA0012 for high α where the airfoil performance degrades. It can be noted that there is an abrupt fall in the rotor performance at high α. In the present case, this fall is found to be beyond $\beta > 50^o$, and when $50^o < \beta < 80^o$, the M1 rotor could hardly capture 3% to 6% of the Betz-Joukowsky limit. The detailed optimum value of C_{pmax} at its corresponding λ is shown in Table. 5.2.

The M1 model rotor has a larger projected surface area due to its rectangular blade shape. So, in the subsequent examination, the model adopted is of lesser blade area (M2). The model M2, as shown in Fig. 5.4(b), is an SLT rotor having C_r/C_t = 5:3. The rotor blade configuration of M2 is defined in Table 5.1. The model frontal surface area (at $\beta = 0^o$) is about 80% of M1 and 10% more than M3. The model is tested under the same flow condition, and it is observed that

the M2 model rotor produces lesser power than M1 (Fig. 5.4). The value of C_{pmax} = 0.14 (24% of the Betz-Joukowsky limit) is achieved at β = 20° that is about 36% less than the C_{pmax} of M1. Also, similar to the model M1, there is only one optimal β, as distinctly visible through Figs. 5.4(a) and 5.4(b). For this model, due to decreased surface area, the effect of initial drag-driven power generation will be less than in M1. Also, a taper rotor blade could reduce the sectional induced torque. It is the leading cause for the rotational motion of HAWT and is the function of the product of C_l, airfoil section, chord length, and radius (Burton et al., 2001). Furthermore, due to the rectangular shape of M1, the influence of drag is strong, whereas the M2 model rotor having a tapered shape will be subjected to lesser drag, particularly towards the tip of the blade. While altering β from 10° to 20°, the increase in C_p is only about 32.5% of the Betz-Joukowsky limit. Although this value is relatively less, but, considering the low range of λ, the result obtained is reasonable. Beyond $\beta > 30^o$, a significant decrease in the rotor performance is observed where most of the evaluated $C_p < 0.026$. The value of C_{pmax} at different β with its corresponding λ is shown in Table 5.2.

The findings on the M2 model rotor have paved the way for a clearer perspective on the performance characteristics of model M3. Table 5.1 expresses the geometric configuration of M3. The frontal area of M3 (at $\beta = 0^{\circ}$) is 70% of M1 and 87.5% of M2. Figure 5.4(c) represents the performance of M3 for a varying range of β. Due to further reduction in the frontal area, a substantial drop in C_p is noted in this case also. Upon reducing the C_t by 60% with respect to the C_r, the corresponding optimal C_p has decreased by about 56.4% to that of M2. One of the intriguing observations with this case is that, unlike models M1 and M2, M3 tends to produce better C_p towards the higher β. From Figure 15, the optimum performance is captured when 55° < β < 65°, details of which are shown in Table 5. It can be observed that the C_{pmax} value is close to 10.1% of the Betz-Joukowsky limit for this model.

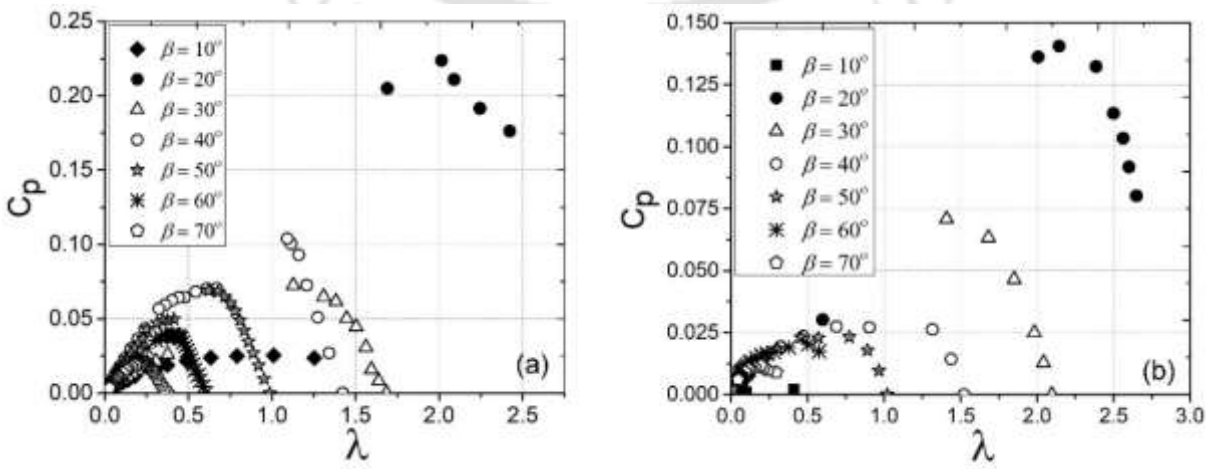

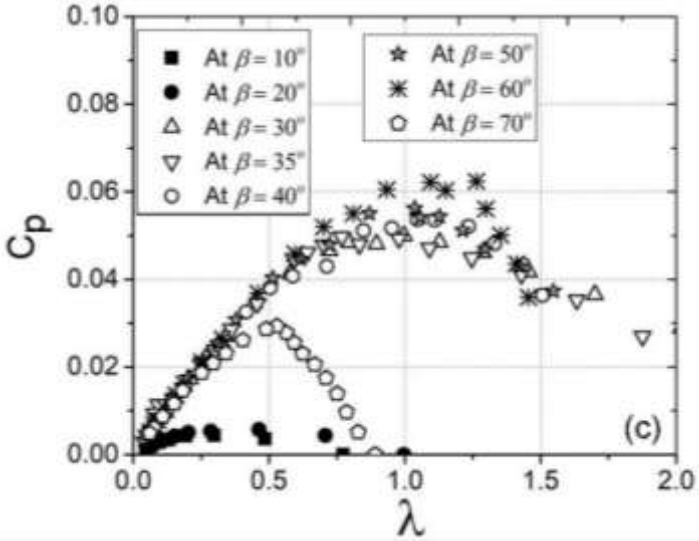

Fig. 5.4. Performance characteristics of (a) M1, (b) M2, and (3) M3 SLT rotor

Table 5.2 Values of optimum C_{pmax} and λ at corresponding β

NBEMT Model	Performance parametrs	β						
		10°	20°	30°	40°	50°	60°	70°
M1	C_{Pmax}	0.02	0.22	0.07	0.10	0.07	0.04	0.02
	λ	1.01	2.02	1.13	1.09	0.62	0.40	0.23
M2	C_{Pmax}	0.002	0.14	0.07	0.03	0.02	0.02	0.01
	λ	0.41	2.14	1.41	0.69	0.77	0.05	0.19
M3	C_{Pmax}	0.004	0.006	0.05	0.05	0.06	0.06	0.03
	λ	0.30	0.46	1.00	1.05	1.04	1.26	0.53

From Figs. 5.4(b) and 5.4(c), it is quite apparent that M2 and M3 have lesser performance and seem to have a unique C_p trend in contrast to M1 (Fig. 5.4a). The M3 performance characteristics show a relatively smooth increment in C_p with a gradual increase in β value. So, it can be stated that for an SLT rotor, the regime of maximum performance increases or shift towards higher β as the taper ratio increases. From Fig. 5.5, one can specify that for the present SLT rotors C_p (M1) > C_p (M2) > C_p (M3). A systematic twist across the blade section is often required to enhance the performance of straight bladed rotor, such as for the BEMT rotors (Schubel and Crossley, 2012). Furthermore, even if the rotor blade is not modelled as per BEMT, a combination of a linear and non-linear twist on the blade is found to be promising (Rahgozar et al. 2020). The techniques presented by Rahgozar et al. (2020) are unique and appreciable; however, their calculated C_{pmax} values predicted numerically are relatively high (C_p > 0.45). Such an outcome is infrequent for a small wind turbine due to several losses; therefore, such analysis will need further experimental validation.

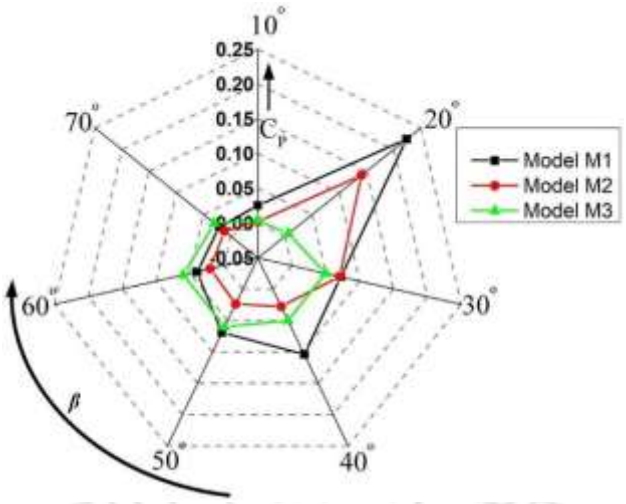

Fig. 5.5. Variation of optimum C_p with change in β for model M1, M2, and M3.

5.3 Comparative Analysis and Operational Characteristics of BEMT and SLT Rotors

From the above discussions, it is apparent that the applicability of NACA0012 for the BEMT rotor is not very promising. The performance of NACA0012 is found to be very poor for the SHAWTs operating at low *Re* and λ conditions. Although, the BEMT prediction shows strong performance characteristics of M0 mainly because the analysis does not account for the airfoil weak aerodynamic characteristics at low *Re* ($=0.5 \times 10^5$), where it is known for depicting transitional behavior (Winslow et al., 2018; Istvan and Yarusevych, 2018). Moreover, the analysis does not consider the span wise movement of flow. However, such an effect cannot be totally ignored for a small wind turbine like the present case. The experimental observation on the M0 rotor shows that the model rotor is able to capture about C_p of 0.15, a substantial drop from its BEMT prediction of 0.35 (Fig. 5.2b). Although when the same rotor is tested in offset condition ($\beta = \beta_{design} + 5°$), the M0 produces C_{pmax} of 0.213 (Fig. 5.4). The SLT rotors, on the other hand, show better performance with M1 that is able to capture C_{pmax} of 0.22 at $\beta = 20°$. However, as the taper ratio is increased, their performance degrades, as shown in Fig. 5.6. Among the three SLT rotors, M1 shows the potential characteristics for rotors of such kind while operating at low *Re* and low λ conditions.

While examining the C_p of SLT rotors, one fascinating phenomenon that has been recorded is the way C_p falls. The observation has been particularly seen for models M1 and M2 at $\beta \leq 40^o$. For ease of understanding, the C_p *vs.* λ curves for these rotors have been discussed into three different regimes. Under defined sets of rotor's geometric alignment and upstream flow condition, gradual loading and performance characterization is carried out. During the initial stage of the no-load condition, the model rotors operate at their maximum rotational speed, but with gradual loading, as expected, a decrease in rpm is recorded due to increasing resistive force. At some point during loading, the optimum value of C_p is successfully logged for models

M1 and M2, at around the initial 30-50% loading stage. Figure 5.7(a) shows the performance characteristics of M1 and M2, and it can be observed that after reaching the aerodynamic stall, instead of a gradual drop in the rotor rpm, an abrupt sink in the rotational speed is recorded. This phenomenon is only recorded for M1 and M2 when $\beta \leq 40^{o}$, as shown in Fig. 5.7(a). This behavior is further acknowledged by varying the upstream velocity. It is observed that the behavior still exists; a typical case study of this scenario is shown in Fig. 5.8. One may infer that because of the stalling effect, non-uniform loading across the blade section, and load applied approach close or equal to the load developed due to the pressure field across the rotor blade.

In order to properly define the performance curve of the SLT rotor and its unique behavior than its counterpart BEMT rotor, three distinct regimes, namely potential phase, sinking phase, and damping phase, have been considered, as depicted in Fig. 5.7(b). The potential phase (I) of the curve is the regime of potential power extraction of the SLT rotor. The sinking phase (II) is that segment of the curve where one could see a sudden fall in the performance and rotational speed of the rotor. Finally, the damping phase (III) is the last regime of the curve where the rotor finally falls into a non-generative mode, and the self-stabilization process initially marks this segment after a sudden fall in the rpm (sinking effect) followed by the damping of rpm. This unique quality behavior can be quantitatively represented by changing rotational speed of the rotor. It is recorded using a proximity sensor with a rate of 100 samples/sec and simultaneously analyzed as shown in Fig. 5.8. The observation shows the unique quality of the SLT rotor (Fig. 5.8); here, the step size represents the moment of loading situations. The rotor is initially allowed to rotate in no-load condition followed by gradual loading (L), which results in a fall of the rotor rpm. Apart from this, the cut-in speed for the SLT rotors were also examined, and it is observed that their cut-in speed occurs in the range of 3.0 – 4.5 m/s in no-load condition.

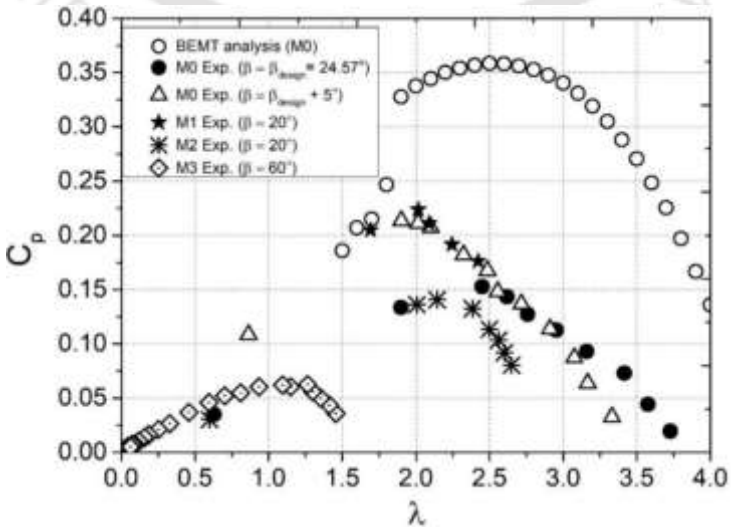

Fig. 5.6. Comparative analysis of SLT rotors and BEMT rotor at different β

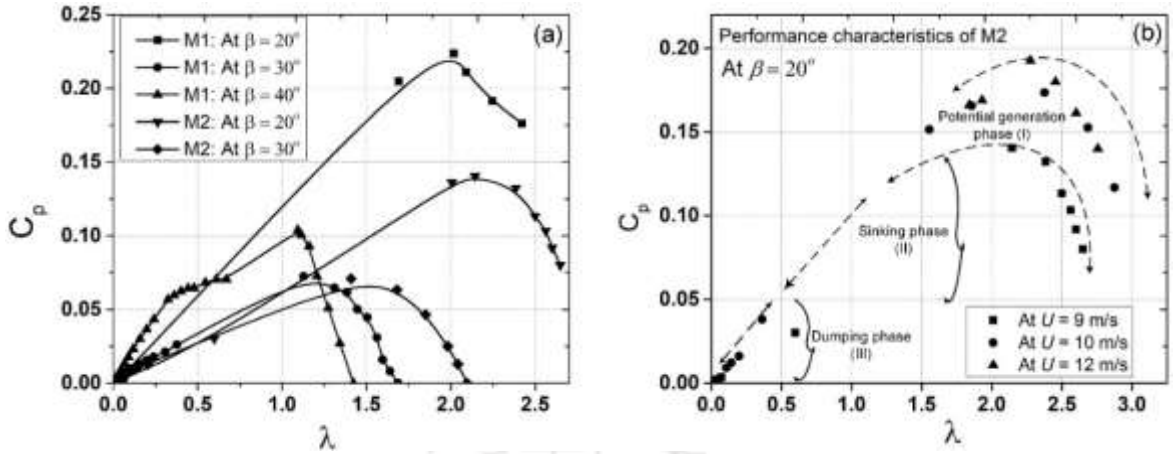

Fig. 5.7. (a) Sinking effect of model M1 and M2; (b) variation of C_p with change in freestream velocity.

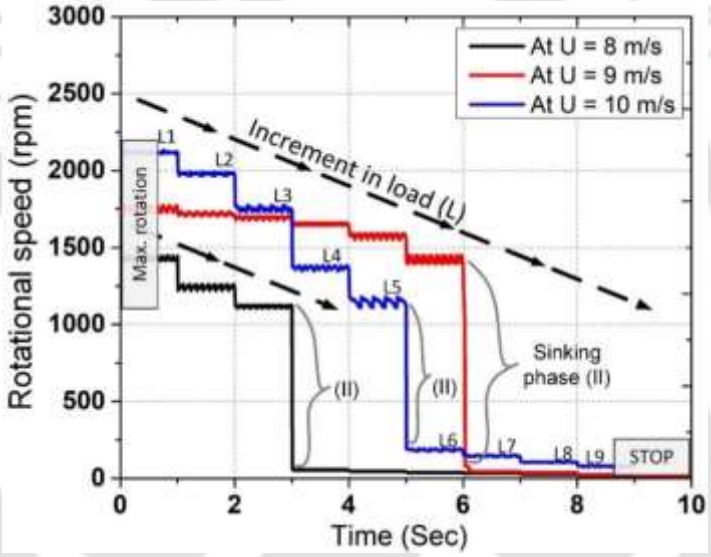

Fig. 5.8. The typical fall in the rotational speed of SLT rotor at different *U*

A better insight into such peculiar operational behavior (Fig. 5.8) exhibited by the SLT rotor would undoubtedly constrain their operative limit. From the above observations, it is suggested to operate the SLT rotors in the potential generation phase (I) to extract the available wind power. On the other hand, prior knowledge of the sinking phase (II) and dumping phase (III) shall be helpful in restraining the SLT rotors in case of high wind gusts that could potentially damage the rotor. Thence, upon employing the necessary load or pitch control, it would ensure that the rotor rotates at its nominal angular velocity without causing any damage or operating in non-generative mode.

These SLT model rotors can be potentially used as a standalone off-grid application, especially where there is the least energy demand for rural communities, regions of minimal energy usage, and conventional turbines procurement is not necessary or feasible. The adopted model rotors

have relatively lesser C_p than large WTs, but it has shown promising results for its application under low *Re* and λ conditions. Nevertheless, the objective of the study is to ascertain the implication of SLT rotors to be used as standalone alone generating units, which have been substantially understood.

5.4 Summary of the Study

The study presents the experimental investigation performed on SLT rotors as standalone off-grid power generating units. Three models of SHAWT having NACA0012 airfoil have been considered for the study. All rotors depict a unique performance characteristic, typically governed by the range of λ and β. The SLT model rotors are differentiated based on the ratio of the root chord by tip chord as M1 (1:1), M2 (5:3), and M3 (5:2). A BEMT rotor is also developed for comparative analysis, having NACA0012 as its section profile considering *Re* = 0.5×10^5. The overall observation and findings from the present study have been summarised below:

- The BEMT prediction of model rotor M0 shows C_{pmax} of 0.35 at λ = 2.5. However, experimental observation on the M0 rotor shows C_{pmax} of 0.15. Thus, the applicability of NACA0012 as a BEMT rotor profile at low *Re* and λ does not seem to be promising due to its highly transitional behavior at low *Re* conditions.
- The real-time performance assessment of the three SLT rotors using the RTS reveals the dependence of C_p on β.
- The wind tunnel experiments on the SLT models reveal that λ changes with change in β. The C_{pmax} of M1, M2, and M3 is found to be about 0.22, 0.14, and 0.06 when β is kept at 20^o, 20^o, and 55-65^o, respectively.
- The favourable models, M1 and M2, can capture 37% and 24% of the Betz-Joukowsky limit while operating at $\beta = 20^o$.
- It is suggested to operate SLT rotors at lower β.
- With an increase in the taper ratio (C_r/C_t), the optimum value of C_{pmax} shifts towards the higher β.
- While examining the operational features of SLT rotors, particularly in the case of M1 and M2, a sudden drop in the rotational speed is observed after stall, instead of gradual decrement. The effect is observed to be very much prevailing when β is less than 40^o. Therefore, it is suggested to operate such rotors in the potential generation phase of the power characteristics curve.

CHAPTER 6
WIND TUNNEL PROBE INTO AN ARRAY OF SMALL-SCALE HORIZONTAL-AXIS WIND TURBINES OPERATING AT LOW TIP SPEED RATIO CONDITIONS

6.1 Introduction

In the context of energy supplement through renewable energy sources, the contribution of wind energy over the past few decades have increased significantly. No wonder the prospect of wind energy throughout the globe seems to be very promising. The major share of wind power comes mainly from the large wind farms (LWFs) that encompass large wind turbines (LWTs) and medium wind turbines (MWTs). These LWTs and MWTs are mostly installed in large offshore or onshore wind farms that could occupy as much as 100 - 200 km^2 of area (Sadorsky, 2021; Lienard et al. 2020). To fulfil the rising energy demand, the role of LWFs is worth noting, though, they have some drawbacks with respect to land acquisition, ecological impact, noise pollution, impact on birds, and others (Wang and Prinn, 2010; Marini et al. 2017; Hernandez et al. 2021). One of the major concerns is that they occupy vast areas, especially when whole world is facing population growth issues. However, the benefit of wind energy in comparison to fossil fuel plants is obviously appreciable and acceptable, and hence, replacing the existing LWFs with other sources is not reasonable looking at the future concerns. In such a dilemma, the implication of small wind farm (SWF) or small wind turbine integrated system (SWTIS) could bear some segment of renewable energy demand, as depicted in Fig. 6.1.

Fig. 6.1. Cluster/multirotor arrangement of small wind turbine

Although there is no global standard for SWF or SWTIS; however, they usually consist of small wind turbines (SWTs) (Abderrazzaq, 2004; Becerra et al. 2017). The SWTs could be further classified into small horizontal axis wind turbines (SHAWTs) and small vertical-axis wind turbines (SVAWTs) (Benedict et al. 2016; Tummala et al. 2016). Generally, the rotor diameter of SWTs is less than 5 m and could produce power in the range of few kilowatts (kWs). Further, the range of tip speed ratio (λ) is expected to lie between 0.5 and 7 and the blade tip Reynolds number (*Re*) in the range of 0.3 x 10^5 - 3.0 x 10^5. These ranges of low *Re* and low λ are also the basic features of SHAWTs (Refan and Hangan, 2012; Singh and Ahmad, 2013); the blades of such rotor are usually design through blade element momentum theory (BEMT). The corresponding C_{pmax} of these rotors are mostly found in the range of 0.10 – 0.45 (Refan and Hangan, 2012). With the inclusion of a duct as an augmentation technique, the C_p value of a SHAWT can be enhanced (Venters and Helenbrook, 2016). The SVAWTs, on the other hand, are characterized by their smaller size and usually show C_{pmax} in the range of 0.05 – 0.35 (Mohammed et al. 2020; Keisar et al. 2020). Furthermore, form the economic point of view, the SWTs have benefits over the LWTs due to their ease of operation, lower capital and maintenance costs. More detail on the implication of wind farm and the effect of array/cluster configuration has been addressed in the literature review Chapter 2(section 3.3).

6.1.1 Testing of Rotors in Array

In this investigation, a wind tunnel study on the array of two identical SHAWTs has been carried out. The study is primarily focused on giving an insight into the performance characteristics of the individual turbine rotors and the wake flow characteristics between the rotors, both operating at low λ. The experimental assessment was carried out using CTHWA. The upstream and the downstream rotors are indicated as UsT and DsT, respectively. The schematic diagram of the setup and methodology has been described in Chapter 3(section 3.3). The separation between the rotors is defined by *x/R*, where *R* is radius of the rotor and *x* is the distance from the rotor in streamwise direction. Both UsT and DsT models are developed through blade element momentum theory (BEMT), as described in Chapter 3. The rotor blade is of constant profile having E216 airfoil, and this profile is adopted on the basis of its promising aerodynamic and performance characteristics, particularly for its implication in SHAWTs (Gupta et al. 2017; Abdelsalam et al. 2021). The design and performance analysis through BEMT has been considered for low λ, and in the present study, the optimum λ is kept at 2.5 with a corresponding *Re* of 0.5 x 10^5. A comparative study has also been performed and presented in Chapter 4.

6.2 Performance Estimation of Stand-alone Rotor

The rotor performance is tested at U = 7 m/s, 8 m/s and 9 m/s by keeping the rotor blade pitch angle (θ_p) at design value ($\theta_p = \theta_{p,design}$ = 25.47º) that is evaluated through BEMT. All the rotor characteristics in the present study are drawn for the design angle θ_p. At different flow conditions, the variation of rotor operational characteristics of UsT under loading condition is presented in Fig. 6.2. The increment in rotational frequency of the rotor with respect to λ at U = 7, 8 and 9 m/s is shown in Fig. 6.2(a). It is seen that the UsT could reached up to ~2550 rpm and ~3400 rpm at 8 and 9 m/s respectively. The rotational speed is found to be minimum at 7 m/s and maximum at 9 m/s, and at the same time, there is an increase in operational limit of λ with U which is also the basic characteristics of SHAWTs (Mohammed et al. 2020; Treuren, 2015). The corresponding potential power extraction by the UsT is presented in Fig. 6.2(b). At U = 9 m/s, the UsT is capable of capturing ~7.3 W from the available 21 W ($0.5\rho AU^3$), and this gives a $C_p \approx 0.34$ at $\lambda \sim 2.5$, as shown in Fig. 6.2(c). The UsT produces C_{pmax} of about 0.24, 0.30, and 0.34 at U = 7, 8, and 9 m/s. It is evident all the values of C_{pmax} obtained are within low λ range, and therefore, it can be suggested that the UsT model having E216 profile is applicable for SHAWTs.

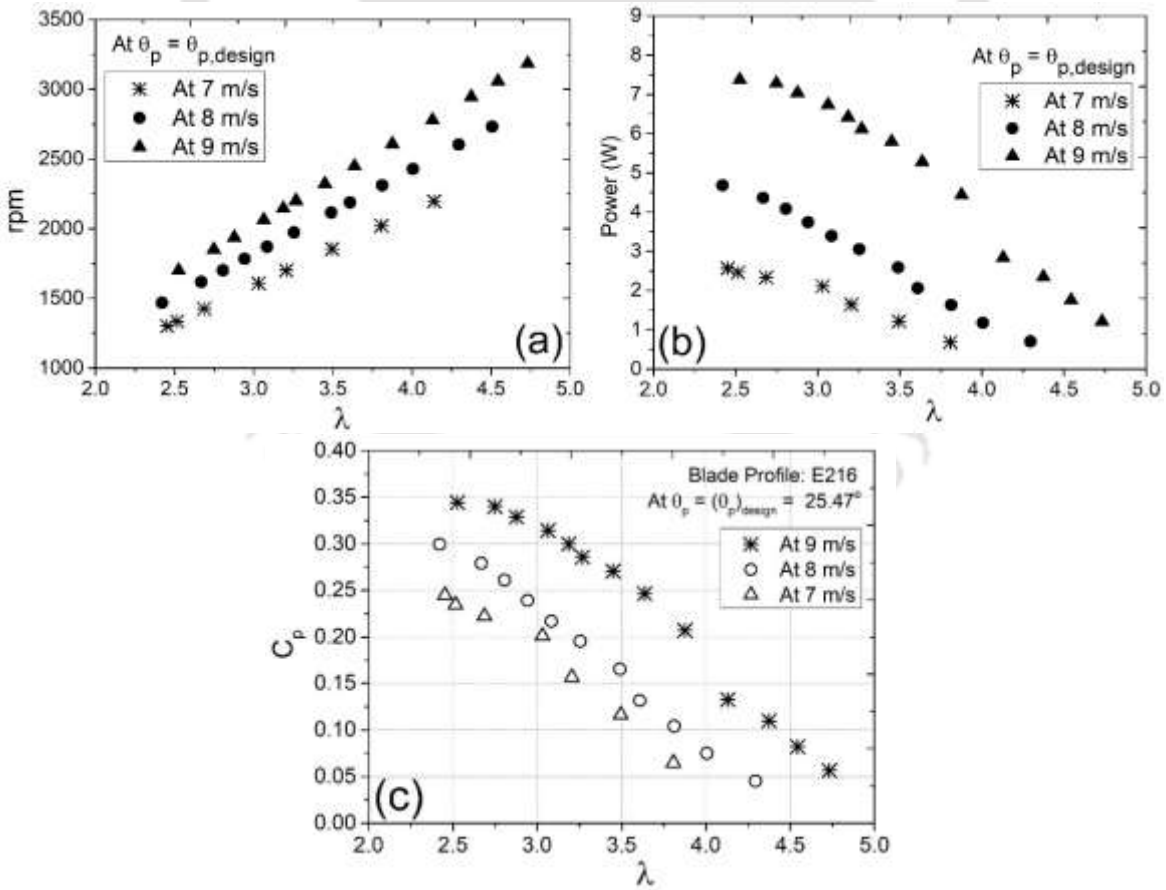

Fig. 6.2. Operational characteristics of UsT (a) averaged rotational behavior, (b) averaged power extraction, and (c) power coefficient at U = 7 m/s, 8 m/s and 9 m/s

The above observation has been made at $\theta_{p,design}$ that is the optimum angle at which the rotor designed through BEMT can produce an optimum C_p (Manwell et al. 2009). However, as reported the optimum value of C_p can be slightly different from expected while observed at different pitch value (Treuren, 2015; Rocha et al. 2018). In view of this, a change in C_p is also recorded by varying θ_p, where the deviation in θ_p is kept at $\theta_{p,design}$ ± 5º and ±10º. The observation is conducted at 8 m/s with a pitch angle tolerance of ±0.5º, and the corresponding performance characteristics is shown in Fig. 6.3(a). It can be seen that the UsT produces the maximum performance at its design condition, $\theta_p = \theta_{p,design}$ = 25.47º, whereas there is a significant reduction in its performance when $\theta_p < \theta_{p,design}$. There is a decrease in C_p value at $\theta_p > \theta_{p,design}$ but the level of decrement rate is relatively lesser as compared to the case when $\theta_p < \theta_{p,design}$ as seen in Fig. 6.3(a). The C_p data at $\theta_p = \theta_{p,design}$ -10º are found to be insignificantly lesser, and hence, they are not presented. The evaluated C_{pmax} is about 0.21, 0.30, 0.28, and 0.22 when $\theta_p = \theta_{p,design}$ - 5º, $\theta_{p,design}$, $\theta_{p,design}$ + 5º, and $\theta_{p,design}$ + 10º, respectively. It can thus be stated that the SHAWT rotors designed through BEMT and operating at offset pitch angle ($\theta_p \neq \theta_{p,design}$), are highly unlikely to produce more than at the design condition. The value of C_{pmax} at the design condition can also be evaluated through BEMT approach where the variation of C_p with λ value is calculated numerically for each blade element and finally summed up using Eqns. 6.1 and 6.2 (Manwell et al. 2009) to get the C_p of rotor.

$$C_p = \left(\frac{8}{\lambda N}\right)\sum_{i=k}^{N} F_i \sin^2\phi_i(\cos\phi_i - \lambda_{ri}\sin\phi_i)(\sin\phi_i + \lambda_{ri}\cos\phi_i)\left[1-\left(\frac{C_d}{C_l}\right)\cot\phi_i\right]\lambda_{ri}^2 \tag{6.1}$$

$$F = \left(\frac{2}{\pi}\right)\cos^{-1}\left[\exp\left(-\left\{\frac{(B/2)[1-(r/R]}{(r/R)\sin\phi}\right\}\right)\right] \tag{6.2}$$

In Eqns. 6.1 and 6.2, N is number of elements, ϕ is relative angle, λ_r is local tip speed ratio, B is number of blades, r is radial distance from centre of the rotor, C_d is coefficient of drag, C_l is coefficient of lift, i is the blade element and F is the Prandtl's tip loss factor.

The designed optimum tip speed ratio (λ_{opt}) of the UsT is set at 2.5 and the corresponding C_{pmax} is found to be 0.37 as shown in Fig. 6.3(b). From experimental analysis, UsT produces closest C_{pmax} of 0.34 at 9 m/s for the same λ_{opt} as seen through Fig. 6.3(b). This reduction in performance could be attributed to the losses near the hub, tip and due to friction. The UsT model is designed to operate at low λ and low Re condition, and therefore, C_p = 0.34 obtained

by the UsT model is good enough to justify its low C_p extraction with respect to to Betz's limit. The C_p obtained is relatively favorable and optimistic as compared to SVAWTs, since their C_p value is generally found between 0.10 – 0.25 at low λ and low *Re* (Jain and Saha, 2019; Rathod et al. 2019). It is also observed that as the upstream velocity is reduced, there is a reduction of power extraction. This declining nature of C_p with the decrease of U can be viewed from the *Re* perspective. With the reduction of U, there is also a reduction of *Re* as seen from linear relation (Eq. 7). The UsT model used is designed using BEMT for low *Re* and λ application and in the present case $Re = 0.5 \times 10^5$. Therefore, it is expected that with the reduction of *Re* (or U), a fall in aerodynamic characteristics of the UsT is inevitable. The ultimate impact is the overall reduction in C_p of the rotor at lower upstream flow conditions as shown in Fig. 6.3(b).

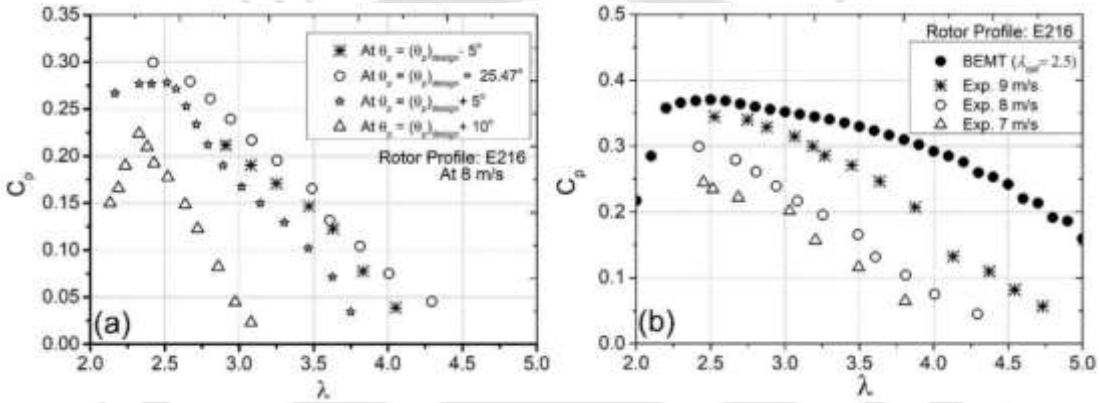

Fig. 6.3. (a) Performance characteristics of UsT at different blade pitch angle, and (b) comparison of experimental outcome with BEMT analysis

6.3 Performance Estimation of Rotors in Array

In this section, the performance of the rotors (UsT and DsT) in the array is examined for their implication in the development of small-scale wind farm. The upstream and downstream turbines have the similar design, geometry and aerodynamic configuration, so that the output data can directly be related. This is ensured by keeping the rotor geometric dimension and θ_p at similar conditions and are placed collinear to each other, at the centre of section. The operational and performance characteristics of UsT as a stand-alone system or without the influence of DsT have been presented and discussed in previous section, where the UsT is found capable to extract ~50.6% and 57% of Betz's limit while operating at U = 8 m/s and 9 m/s, respectively. In the performance estimation of DsT, it is indeed expected that there would be some level of degradation of C_p due to the mitigating wake from the UsT. The two rotors in the array are separated by downstream distance as expressed by *x/R*. The points of measurements (POMs) are evaluated with respect to the rotor plane of UsT which is also considered here as the frame of reference. The four downstream locations are *x/R* = 6, 8, 10, and 12 of the rotor planes of UsT with respect to the rotor plane of DsT.

At first, the rotational characteristics of DsT with respect to UsT is observed under no-load condition, as shown in Fig. 6.4. The normalized mean rpm (*Ω2/Ω1*) of DsT with respect to UsT under different flow condition is shown in Fig. 6.4(a). It is seen that the value of *Ω2/Ω1* is found to be lesser at low velocity and vice-versa. The observation suggests that DsT is unable to capture the available kinetic energy at low *U*, and this is observed to be quite consistent at all the four *x/R* locations. However, the recovery rate at *x/R* = 12 is relatively higher as compared to *x/R* = 3 due to larger separation effects. Moreover, it is interesting to note that with the increase of *U*, a decrease in the rotational deficit (1- *Ω2/Ω1*) is observed in Fig. 6.4(b). This unique observation is also noticed at all the four *x/R* locations. For example, at *x/R* = 6, the rotational deficit of DsT rotor is about 30% and it decreases to about 22% while changing *U* from 3.8 m/s to 7.6 m/s (Fig. 6.4b). The major cause of this behavior could be attributed to the sudden rise in wake TI at higher rpm of UsT leading to an additional thrust on DsT. Furthermore, the rotational deficit at different *x/R* locations when *U* > 5 m/s relatively gradual as compared to low freestream condition (Fig.6.4b) can also be seen.

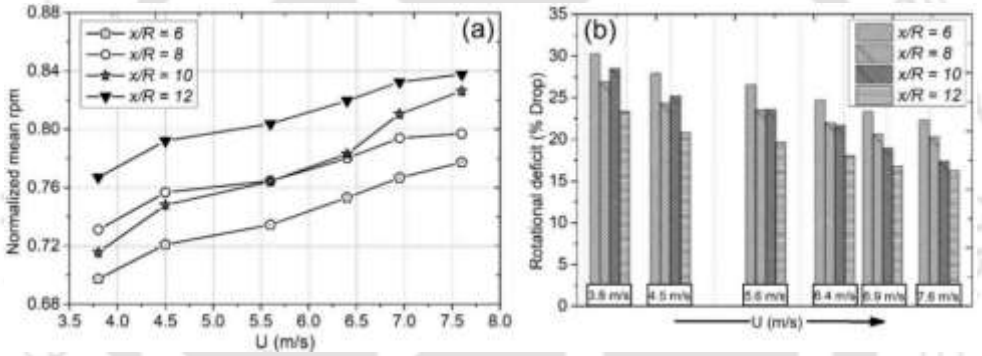

Fig. 6.4. Rotational characteristic of DsT with respect to UsT (a) normalized mean rpm, and (b) rotational deficit in %, at different downstream position under no-load condition

The no-load characteristics of rotors in the array are only helpful in mitigating the rotational attenuation of rotors particularly for DsTs under different flow conditions. However, the major concern of rotors in the array occurs when they are under loading condition where the overall power generation or wind farm efficiency is of outmost importance. In this aspect, the normalized rotational speed of DsT with respect to UsT under loading is also evaluated at two wind speeds as shown in Fig. 6.5. In both the cases, it is seen that with an increase of *x/R*, the normalized value increases suggesting a recovery in the angular velocity of DsT as a consequence of recovery in flow momentum. The observation is analogous to the study carried out under no-load condition (Fig. 6.4). However, the rotational recovery rate is relatively lesser due to induced load on the DsT rotor. For example, at *U* = 7 m/s, the normalized value is ~0.59 at load condition as compared to ~0.81 at no-load condition when the DsT is installed at *x/R* = 10. From Fig. 6.5, it is indeed interesting to note that irrespective of *x/R* location, the slope of normalized rotational speed with respect to λ is unique and uniform.

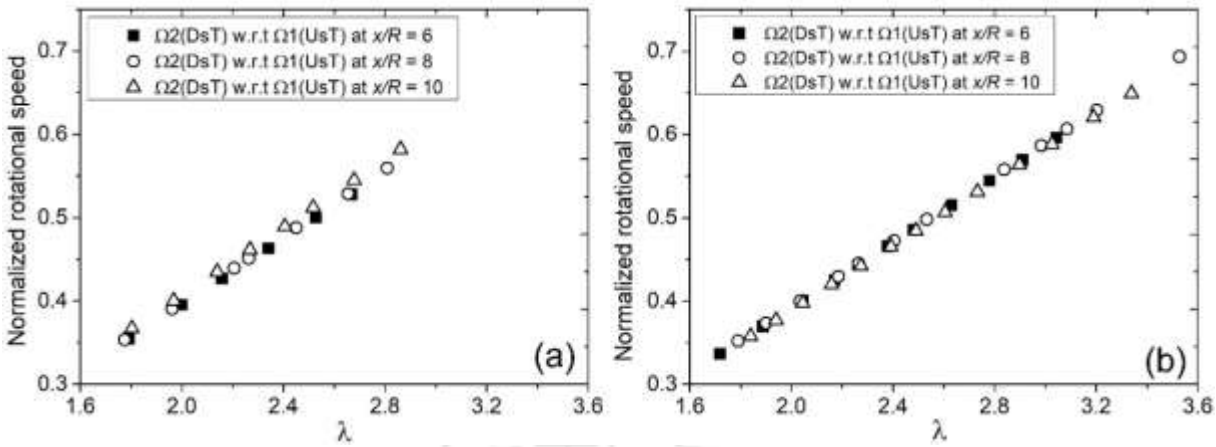

Fig. 6.5. Normalized rotational speed of DsT with respect to UsT (a) at U = 7 m/s, and (b) at U = 8 m/s, under loading condition

At U = 8 m/s, the DsT can reach up to ~1900 rpm when installed at x/R = 6 which is about 27% lesser than UsT as shown in Fig. 6.6(a). This reduction in rpm also leads to a drop in power extraction potential of the DsT by about ~60% with respect to UsT. This suggests that there is a substantial drop in the performance of DsT when it is placed close to UsT (x/R = 6). But with an increase of rotor spacing, the recovery in performance of DsT occurs, which is evident from of Fig. 6.6(b). It is quite apparent from Fig. 6.6 that because of flow recovery at x/R = 10, there is an increase in rotational characteristics of DsT by about ~10% and the power recovery by about ~25%. It is also observed that as x/R is increased, the rpm of DsT also increases and so is the operational limit of λ. Figure 6.6(c) represents the corresponding C_p of DsT when installed at different x/R locations subjected to an upstream flow (upstream of UsT) of U = 8 m/s. As expected, the performance of DsT upgrades as it is installed far away from the UsT. The evaluated C_{pmax} is about 0.12, 0.13, and 0.15 at x/R = 6, 8 and 10, respectively that is about 20.2%, 22.0%, and 25.3% of Betz's limit. Further, it is observed that C_{pmax} of DsT drops by about ~56% and ~59.5% with respect to UsT and BEMT prediction, respectively. Although, the values are relatively lesser while the rotor is operating as a stand-alone system but with substantial knowledge on the rotational and power deficit of downstream rotors at different x/R locations, one can judiciously frame the layout for a small-scale wind farm. The drop in the performance characteristics have also been expressed as a ratio of C_p of DsT to the C_{pmax} of UsT while operating as a stand-alone system (no wake effect) as shown in Fig. 6.7. It is seen that when DsT is installed at x/R = 10, it is able to produce ~50% C_{pmax} of the stand-alone system (UsT). With an increase in the separation distance, the increment in performance of the DsT is also noticed in the work of Adaramola and Krogstad, (2011).

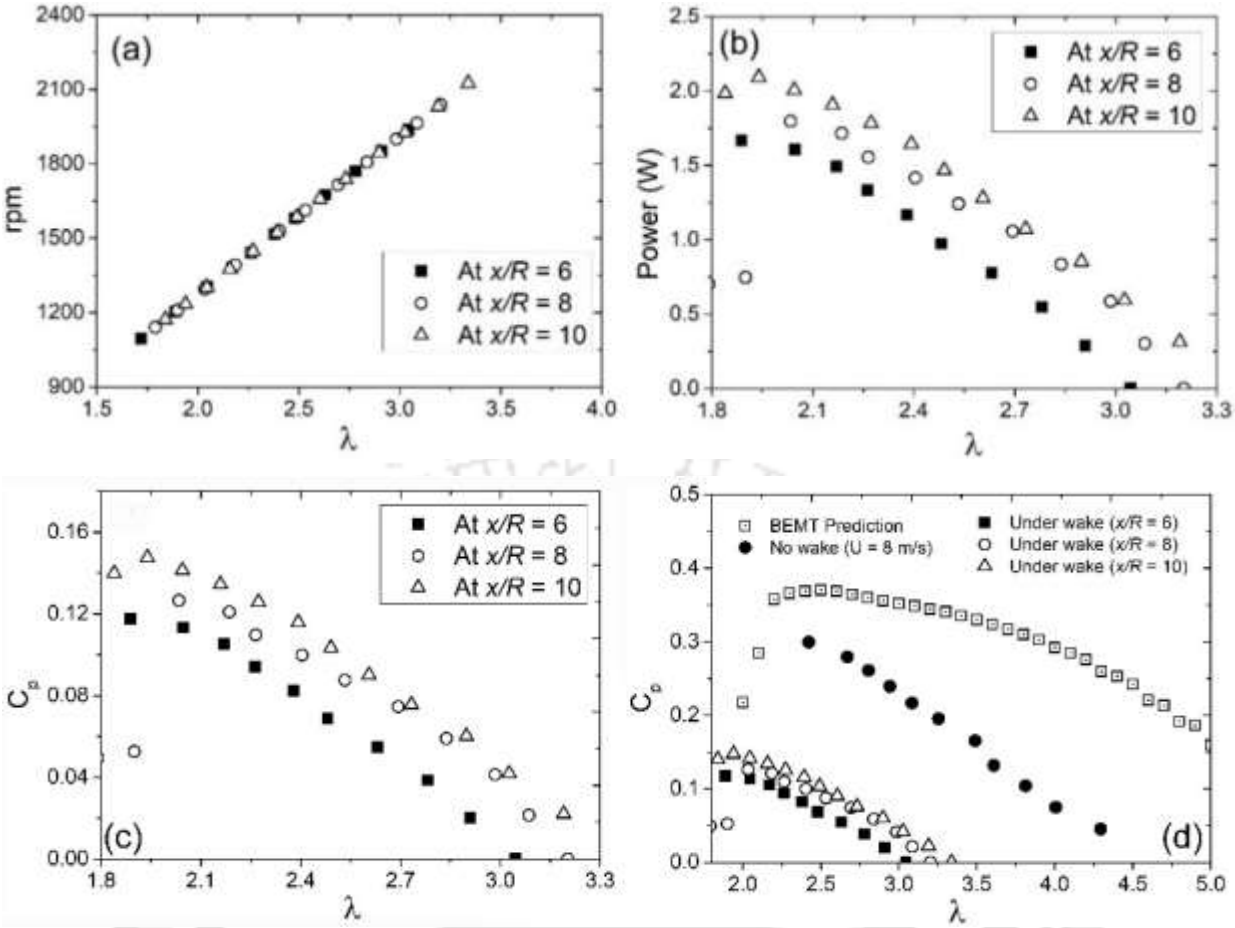

Fig. 6.6. Operational characteristics of DsT (a) rpm vs λ, (b) power vs λ, and (c) C_p vs λ, and (d) comparison with standalone no wake influence rotor and BEMT prediction, at different downstream locations at U = 8 m/s

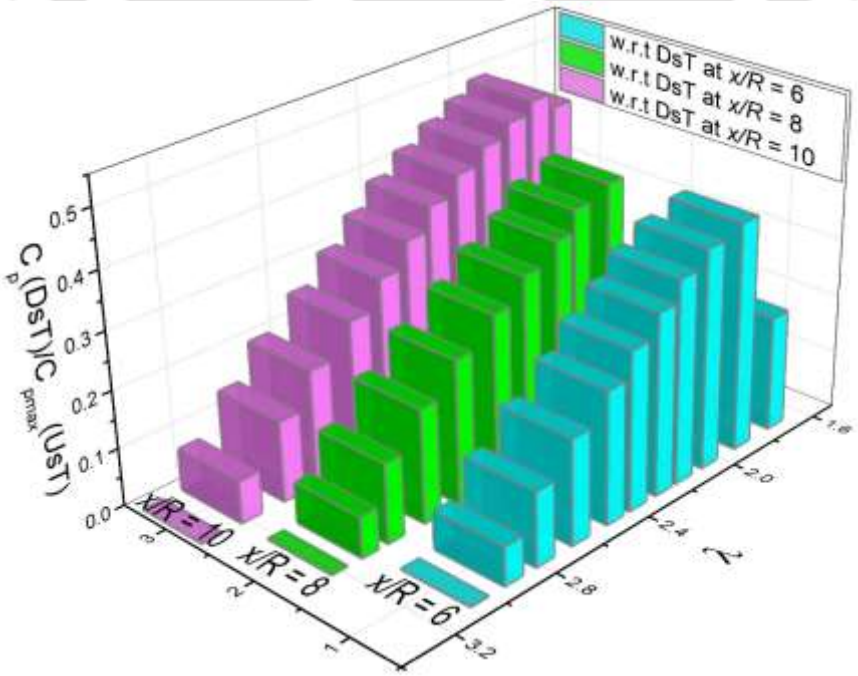

Fig. 6.7. Normalized power coefficient of DsT at different downstream location

6.4 Downstream Flow Field Assessment

The nature of performance degradation of DsT with respect to UsT can further be investigated through velocity flow field assessment of the UsT rotor wake. With regards to SHAWTs, because of their relatively lesser hub height, it is quite obvious that such rotors would be subjected to not only upstream wake but also from the surface (ground) boundary layer. The inflow gradient due to the SBL and the ABL varies with height and depends on several factors (Adhikari et al. 2018). The variation of velocity profile with height can be obtained through wind profile power law and extension of Monin-Obukhov similarity theory known as log wind profile (Adhikari et al. 2018; Tieleman, 1992). Since the present study is carried out inside the wind tunnel, the vertical streamwise velocity gradient is minimum. To confirm the uniformity and minimum surface boundary layer gradient, a hot-wire anemometry (HWA) measurement of streamwise velocity is carried out along vertical direction (y/H). Here, the nominal height (H) taken is 300 mm which also represents the hub height of the present rotors. In this study, the POMs are taken with respect to tunnel inlet at 300 mm. Subsequently the time averaged streamwise velocity is evaluated and normalized with Pitot-static probe streamwise velocity at the hub height, as shown in Fig. 6.8. It can be observed that the normalized percentage velocity reaches close to ~0.99 at $y/H < 0.1$, and this suggest that the SBL of present wind tunnel is less than 30 mm. Thus, the experimental scenario could be considered with a flow under stable ABL (Hancock et al. 2014). With this consideration, the experimental investigation on the downstream flow field is carried out at POMs x/R = 2.67, 4.83, 8.33, and 12.5. The POMs are selected in such a way that the flow measurement would depict the probable flow profile just upstream of DsT.

The streamwise velocity at different downstream and vertical locations is conducted through 3D-traverse mechanism mounted on the top of wind tunnel test section. A step size of 10 mm is kept while mapping along y/R. The time averaged streamwise velocity distribution at different downstream (x/R) and at vertical direction (y/R) is evaluated and presented in Fig. 6.9. One could see that the normalized velocity U_x/U has an unsymmetrical distribution at different x/R and U condition. It can be seen that between $0.7 < y/R < 1.2$, a sudden dip in U_x/U is noted, which is also observed towards the lower half of rotor wake between $-1.2 < y/R < -0.7$. This is also observed when $x/R < 12$ and is found to be consistent with increase of inflow velocity. The major cause of such a dip in velocity is attributed to the reduction of streamwise velocity

towards the tip region of rotor blade and the formation of helical vortex shedding as reported in literatures (Jackson and Amano, 2017; Medici and Alfredson, 2006; Krogstad and Eriksen, 2013). Furthermore, among the different segments of the rotor blade (from root to tip), it is often discussed that the blade section towards the tip region is mainly responsible for the power extraction in running condition. One can thus presume that this sudden dip in the streamwise velocity is due to loss in flow momentum or kinetic energy capture by UsT blade mostly towards the last 30-40% of blade segment. This observation is also confirmed by the fact that towards the hub region ($-0.3 < y/R < 0.3$) the energy extraction is negligible; and the flow recovery is relatively higher as compared to tip region. Although it is seen that behind the rotor and close to the rotor hub the streamwise velocity reaches to about $0.7U$. This could be attributed to flow acceleration by central core vortices evolving from the hub and the nacelle. From Fig. 6.9(i) through Fig. 6.9(l), a gradual increase in normalized velocity is noted until at $x/R = 12.5$ where the profile has transitioned from the W-shape to a slightly U-shape. This shape transition could be further understood from the observation of Zhang et al. 2012, where they have also found an asymmetric. More details on the shape transition are discussed below.

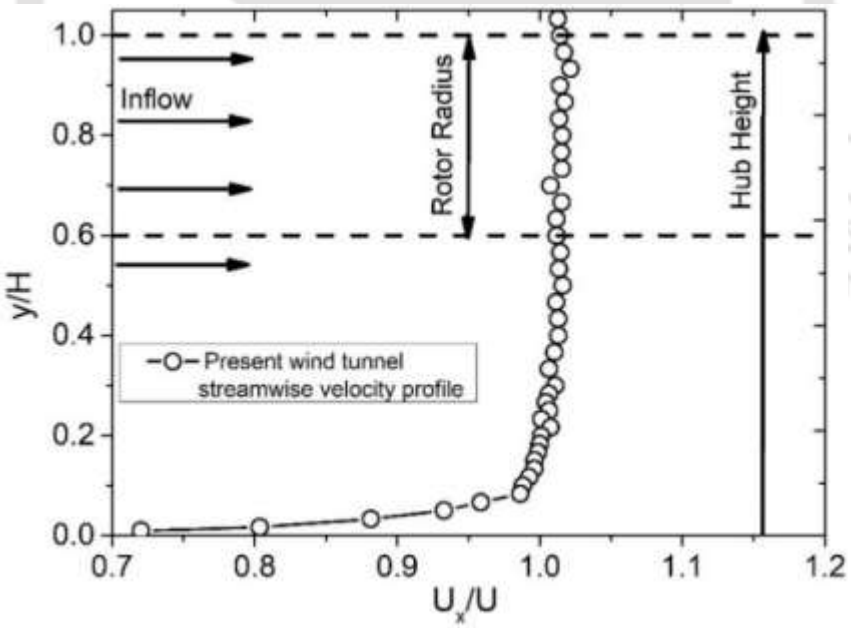

Fig. 6.8. Variation of normalized streamwise velocity profile with tunnel height of present wind tunnel (without rotor)

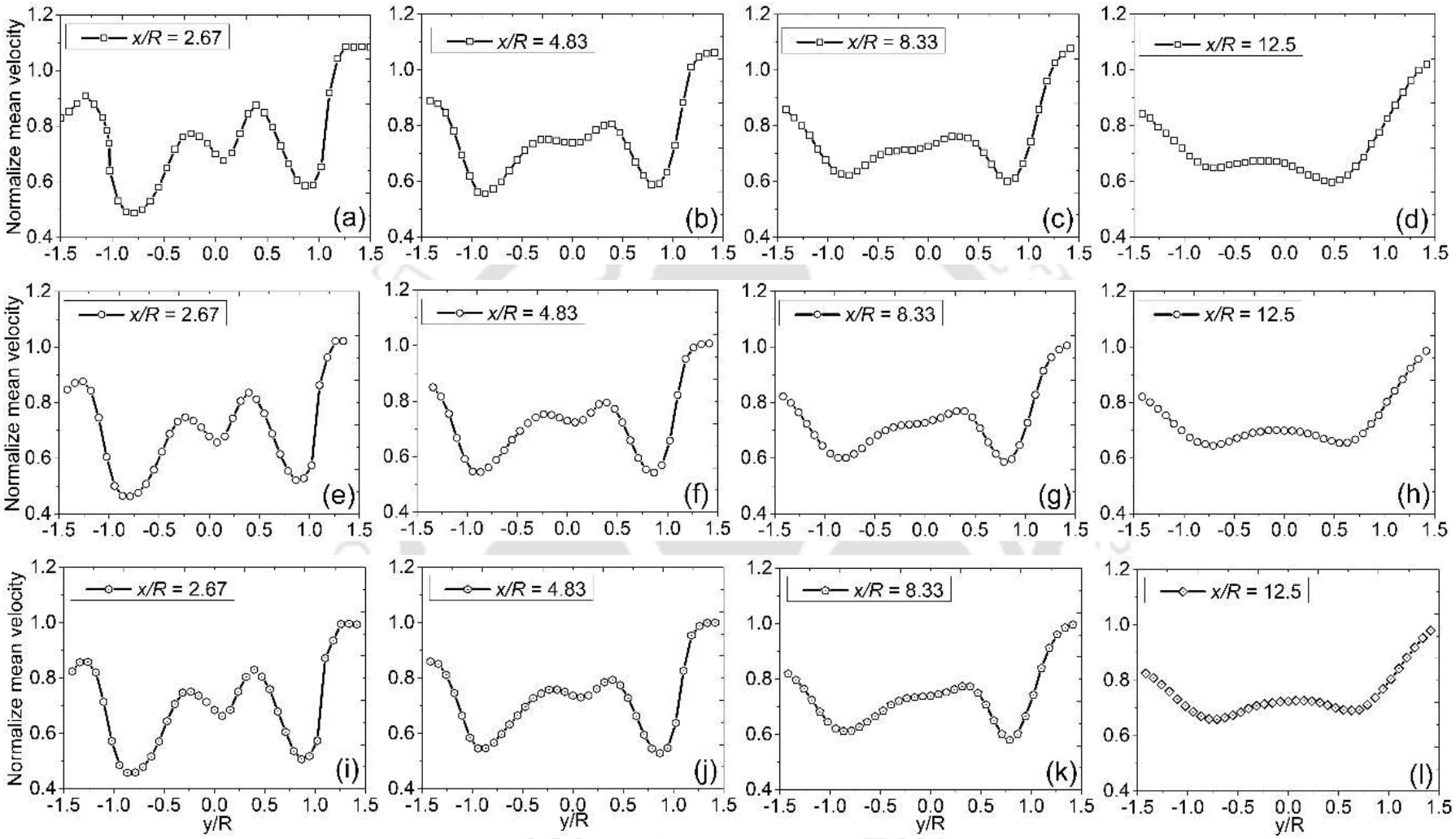

Fig. 6.9. Variation of normalized mean velocity at different *x/R* and flow conditions (a, b, c and d) at U = 3.8 m/s, (e, f, g, and h) at U = 5.6 m/s, and (i, j, k, and l) at U = 6.95 m/s

Using the velocity deficit expression (Eq. 6.3), the shape transition of streamwise velocity profile is analysed at x/R = 2.67, 4.83, 8.33, and 12.5 at different flow conditions as shown in Fig. 6.10.

$$Vel\_def = \left(1 - \frac{U_x}{U}\right) \tag{6.3}$$

where U_x is the time averaged streamwise velocity

$$U_x = \frac{1}{T}\int_0^T U(t)dt \qquad ; T = Sampling\ time$$

The velocity deficit at x/R = 2.67 is found to be quite prominent where the deficit is found to be maximum towards the rotor tip and at this region the drop with respect to the upstream velocity is ~55% (Fig. 6.10a). This deficit is observed towards both upper and lower halves of the wake field, although the profile of deficit is asymmetrical in nature. The asymmetrical velocity field distribution is the general downstream flow characteristics of any rotor when the flow mapping is performed along the vertical direction (Medici and Alfredson, 2009; Hasan et al. 2019) In most of the cases, such an asymmetry is due to the presence of vertical tower and nacelle. However, this may not be the case when POMs are along the lateral direction (z/R) (Hancock et al. 2014). It can also be noted that even with change in U, there is not much significant alteration in the profile of velocity deficit (Fig. 6.10a to 6.10c), except for a slight deviation at x/R = 12.5 (Fig. 6.10d). With an increase of x/R, the shape transformation is specifically visible between $-1.0 < y/R < 1.0$. Looking at this segment, the profile is more like a W-shape particularly for x/R = 2.667 and 4.83, suggesting a significant drop in U_x. Based on a past study (Jackson and Amano, 2017), the regime $x/R < 6$ is considered as the near wake regime, and in the present study, it is marked by the formation of W-shape velocity deficit profile. However, as POMs $x/R > 8$, the W-shape starts disappearing until its form is slightly U-shaped, as seen in Fig. 6.10(c) and Fig. 6.10(d). Similar observation has also been found in a past numerical investigation (Sedaghatizadeh et al. 2019).

From the perspective of velocity deficit at different downstream locations, (Fig. 6.11), it is seen that at all the x/R locations, there is an average 10-20% deficit difference between the upper and the lower halves of the wake profile. A very interesting observation has been encountered when POMs are outside the rotor swept domain. For $y/R > 1.2$, the recorded velocity deficit is found to be negative and this suggests that there is an increase in fluid velocity towards the edge of rotor wake. This negative behaviour of velocity deficit outside the rotor swept area is also reported in literature (Hancock et al. 2014). Medici and Alfredson, (2006, 2008) have also noted this behaviour towards the outer part of the tip vortex, where they obtained a relatively

higher velocity peak for every vortex passage. Whereas towards the inner part, they observed a periodic velocity dip. However, in the present study, the reason of velocity enhancement could be attributed to the resultant velocity which is the confluence of tangential velocity, helical vortex, and ambient turbulence (T_a). The effect of T_a on flow recovery has also been reported in literature (Talavera and Shu, 2017; Kecskemety and McNamara et al. 2011), where it is argued that an increase in T_a would decrease the velocity deficit. This is further confirmed from Fig. 6.11(c) where a negative velocity deficit is found to be comparatively lesser. Furthermore, close to x/R = 12, the flow recovery has reached ~70% of U or ~30% velocity deficit within the rotor swept region -1.0 ≤ y/R ≤ 1.0 (Fig. 6.11c), suggesting the potential inclusion of DsT afterwards.

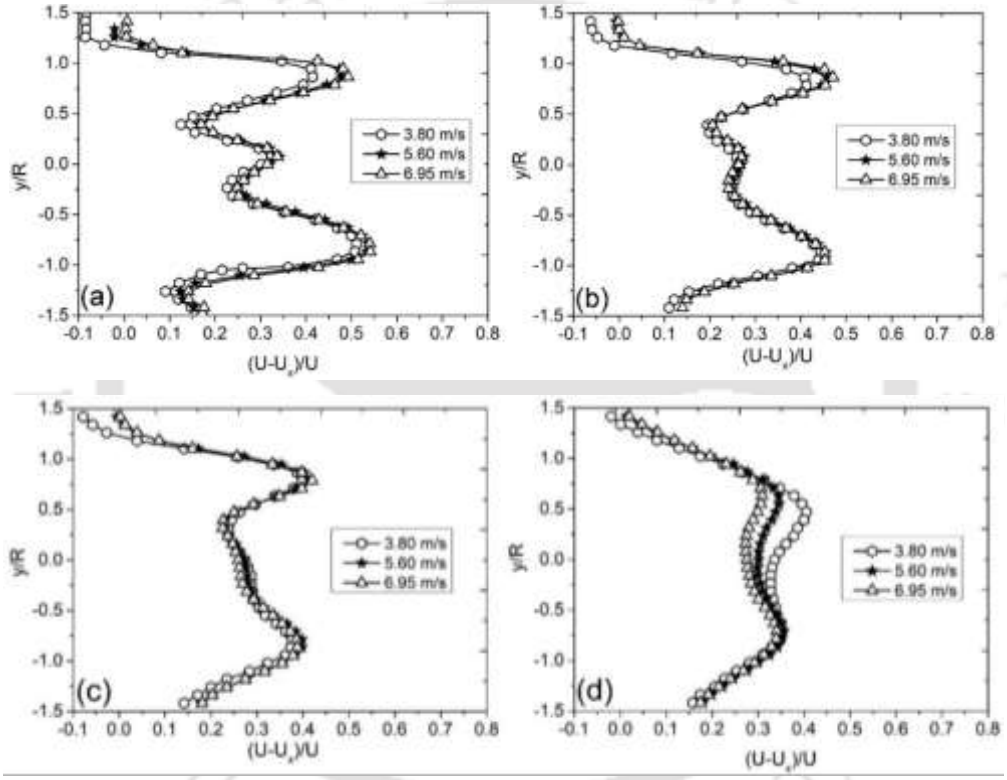

Fig. 6.10. Variation of velocity deficit at different x/R (a) x/R = 2.67, (b) x/R = 4.83, (c) x/R = 8.33, and (d) x/R = 12.5

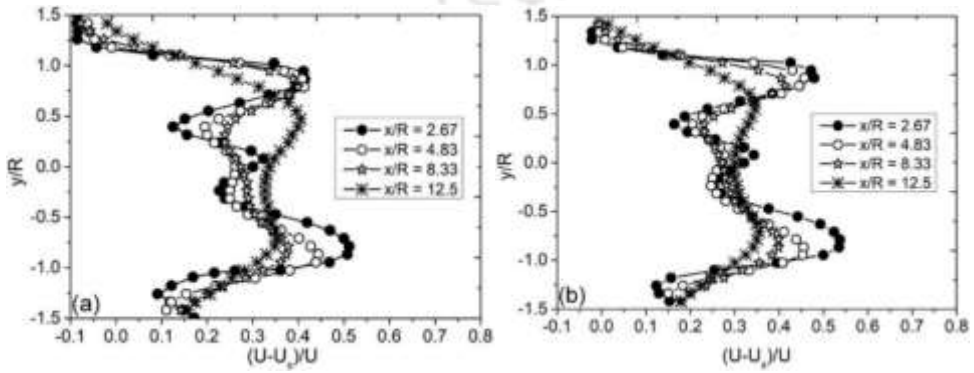

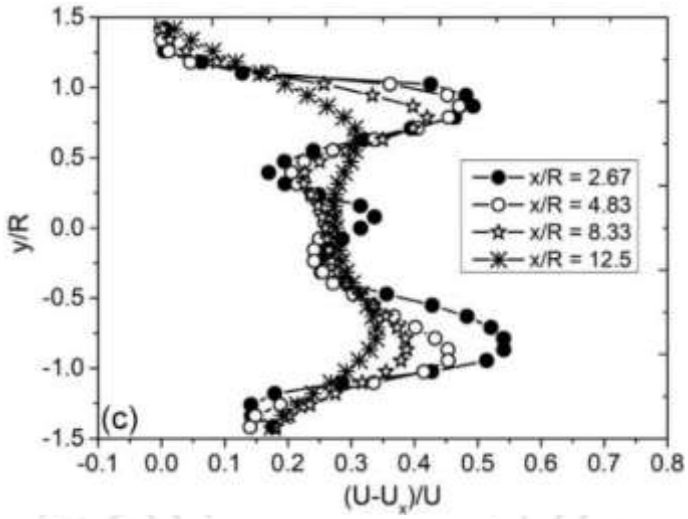

Fig. 6.11. Variation of velocity deficit at different *x/R* and flow conditions (a) *U* = 3.8 m/s, (b) *U* = 5.6 m/s, and (c) *U* = 6.95 m/s

The placement of turbines in the array is very important in order to maintain the overall performance of the wind farm. They should be placed such that it is neither too far nor too close as can be deduced from Figs. 6.10 and 6.11. Installing the DsT very far from the UsT could result in an unaccounted economic burden for the plant. The present study primarily meant for the SWF development, undoubtedly suggests a substantial drop in C_p of DsT and increase of velocity deficit when $x/R \leq 8$. The results of this study may be useful for the development of SWF composed of SHAWTs having rotor diameter < 5 m.

6.4 Effect of Yawing

Apart from the inline wind farm layouts, the study of yaw effect on the overall wind farm configuration has also gained much interest among the wind energy research community in recent times (Grant and Parkin, 2000; Medici and Alfredsson, 2008; Uemura et al. 2017). Figure 6.12(a) represents the typical inline configuration of the two turbines, where both the upstream turbine (UsT) and the downstream turbine (DsT) are kept at zero yaw (γ) angle, and has the clockwise rotation. Figure 6.12(b) shows the typical yaw arrangement of inline rotor configuration; here, the DsT is kept at $\gamma = 0°$ and the UsT is kept in yaw condition ($\gamma \neq 0°$). The implication of such configuration will be encounter when the wind direction is varying, thus would require realignment of the rotor axis. In most of the LWTs, the provision of yawing is often not available, which is compensated by the pitching motion of the blade but for SWTs, such provisions can be made. In recent times, the importance of γ on the overall wind farm performance has been studied (Grant and Parkin, 2000; Medici and Alfredsson, 2008). The significance of γ on the HAWT rotor performance has been presented by Bahaj et al. (2007);

their examination involves simultaneous incorporation of γ and β. They observed that the rotor performance decreases with increases of γ, and this decrease in power is observed to be approximately a function of the cosine of γ^2 and the corresponding thrust as the cosine of γ. Furthermore, it is observed that an increase of β degrades the overall rotor performance, a similar analogy is noted in the present work also (section 6.4). In both Figs. 6.12(a) and 6.12(b), the UsT and DsT rotates in clockwise direction. There could be a yaw arrangement cases where the rotation of the inline turbines is opposite to each other or counter rotating. The implication of counter rotating arrangement comes from the fact that under the omnidirectional wind gust, the effect would help in counter balancing the aerodynamic load on the DsT, thus maintaining the rotor performance. A typical arrangement of yaw and counter rotating inline turbine arrangement is shown in Fig. 6.13. The implication of such arrangement is acknowledged in the reported article (Rocha et al. 2018), the combination of counter-rotating turbines seems to enhanced the power extraction. Therefore, along with the benefit of yaw configuration (Hasan et al. 2017), it will be an exciting and challenging task to model the wake propagation for such configuration. However, for the present study, the arrangement shown in Figs. 6.12(a) and 6.13(a) has been examined.

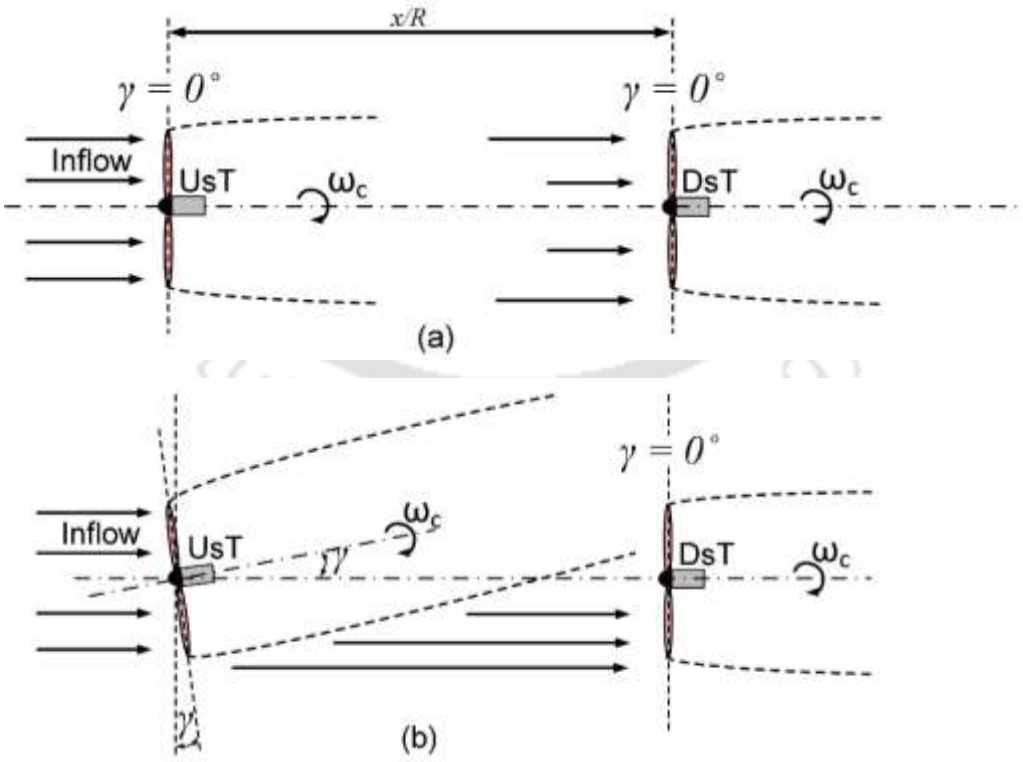

Fig. 6.12. Inline top view arrangement of two turbines (a) $\gamma = 0°$, and (b) $\gamma \neq 0°$ (UsT)

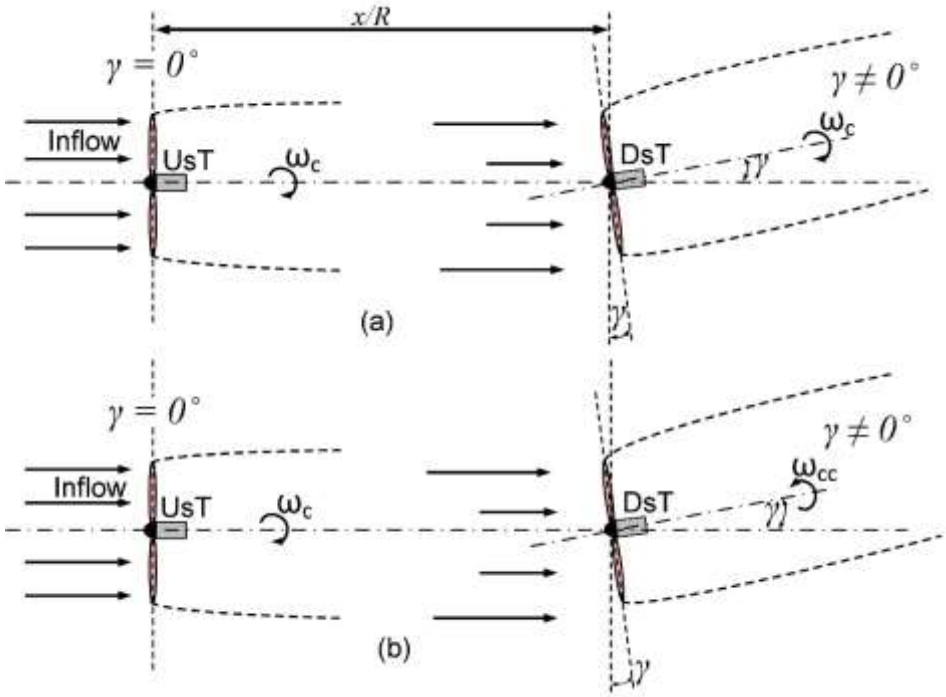

Fig. 6.13. Inline top view arrangement of two turbines in yaw configuration with (a) clockwise, and (b) counterclockwise rotation.

In present study, the configuration illustrated in Fig. 6.12(a), an inline arrangement with $\gamma = 0°$ has been compared with an arrangement shown in Fig. 6.13(a). The separation between the two turbines were kept at x/R = 6 and 10, the rotor configuration opted for the case study is a SLT type that produces C_{pmax} of 0.14 at $\lambda = 2$. The study is mainly intended to seek the information on SHAWT performance when kept under yaw configuration, operating at low λ and low *Re*. It is observed that the DsT performance decreases not only in inline configuration but also in yaw condition, as shown in Fig. 6.14. It is interested to note that with increase of yaw angle, DsT performance further decrease, also the operational range of the rotor (λ) also decreases. The averaged C_{pmax} and percentage decrease in either cases have been tabulated in Table 6.1.

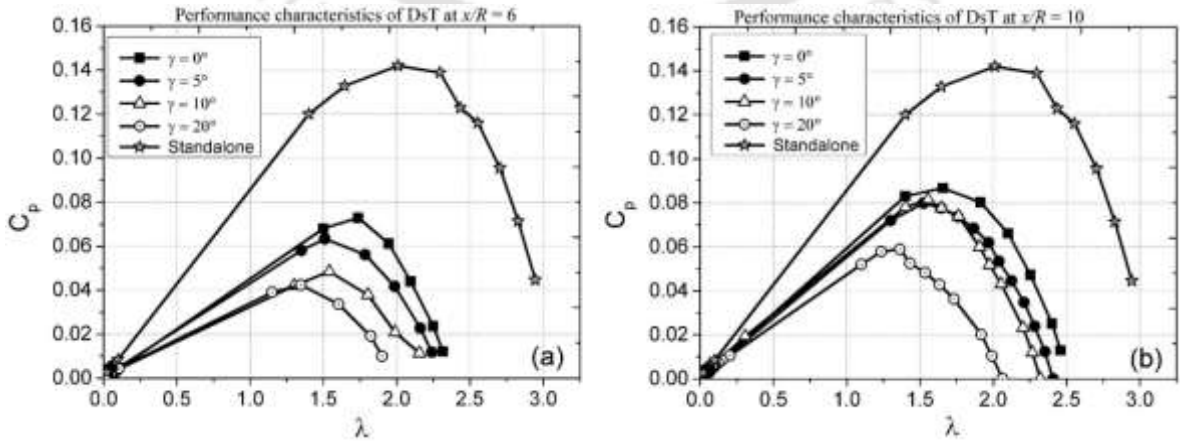

Fig. 6.14. Performance characteristics of DsT under yaw configuration (a) x/R = 6, and (b) x/R = 10

Table 6.1 Inline performance characteristics of DsT under yaw condition

DsT position		**Yaw angle (γ)**				
		Standalone	0º	5º	10º	20º
x/R = 6	C_{pmax}	0.142	0.0728	0.063	0.048	0.042
% decrease w.r.t UsT			48.71	55.42	65.91	70.20
x/R = 10	C_{pmax}	0.142	0.087	0.080	0.081	0.059
% decrease w.r.t UsT			38.91	43.78	42.61	58.52

6.5 Summary of the Study

The study is primarily intended to find the performance characteristics of stand-alone rotor (UsT), followed by combined rotors (UsT + DsT) and the downstream wake flow characterization of UsT while operating at low λ. Following are some of the key findings.

- The BEMT predicted C_{pmax} of the model rotor is about 0.37 at λ = 2.5, which is about 62.39% of Betz's limit.
- The experimentally obtained C_{pmax} of the stand-alone model rotor is found to be 0.30 and 0.34 at 8 m/s and 9 m/s, respectively.
- With the inclusion of DsT, a substantial drop in both the rotational frequency and the performance is observed. At x/R = 6, the DsT undergoes about ~27% decrease in rpm and a reduction in power extraction by ~60% with respect to UsT at 8 m/s.
- Although there is an increase of rpm in both the rotors with respect to an increase in U; however, there is a decrease of rotational deficit.
- At x/R = 6, the C_{pmax} of DsT is obtained to be ~0.13, which shows a drop of about 78.08% and 61.8% from Betz's limit and C_{pmax} of UsT, respectively. The performance of DsT rotor increases by about 46.1% when installed at x/R = 10 as compared to the one kept at x/R = 6. Other notable observation is the change in the operational limit of λ of DsT due to the influence of wake generated by UsT.
- The wake flow study suggests that within the near wake regime (x/R < 6), the velocity deficit profile is marked by the formation of W-shape. However, when POMs are taken at x/R > 8, the W-shape starts disappearing until it resemblances a U-shape. Furthermore, close to x/R = 12, the downstream flow recovers by about ~70% of upstream velocity, suggesting the possible inclusion of DsT afterwards for potential power extraction.
- The effect of yaw on the rotor performance has been investigated. It is observed that DsT performance decreases with increase in γ; however, with increase in separation distance from x/R = 6R to 10R, about 1 0 – 15% recovery in C_{pmax} is noted. Furthermore, a distinct operation range of λ is noted when γ is varied.

CHAPTER 7
STUDY OF WIND TURBINE WAKE CHARACTERISTICS USING STEREO PARTICLE IMAGE VELOCIMETRY (PIV)

7.1 Introduction

A precise assessment of the wind turbine wake is an essential aspect in dictating the flow dynamic of the wake and thus helps in modeling of the wake propagation. The flow physics of wind turbine though seems complex and stochastic due to its 3-dimensional flow behavior, however, due to its unique helical motion (Vermeer et al. 2003; Porté-Agel et al. 2021), one may express the physical interpretation of the wake into a sequence of events. This will require an in-depth understand of the flow field dynamic both in terms of qualitative and quantitative analogy. The case study on downstream flow deficit presented in Chapter 6 using the CTHWA gave the fundamental understanding; however, the investigation does not highlight the underlying flow physics and also no information on helical motion of the wake can be extracted from those results. Essentially, the probe (CTHWA) is not favorable in describing the complex 3-dimensional helical motion of the wind turbine due to limited mobility, field of mapping, variability, and its intrusive nature (Bruun, 1995). Though prove to be useful for two-dimensional modeling (Steven and Meneveau, 2017).

In line with the prospect of acknowledging the 3-dimensional nature of the wind turbine wake, a Stereo Particle Image Velocimetry (PIV) instrument has been employed in this study. Being extrusive in nature the instruments has a wide range of application in the fluid mechanic studies in recent times (Yoon and Lee, 2004; Yang et al. 2020; Scharnowski and Kähler, 2020). The fundamental and experimental methodology of PIV system has been described in Chapter 3 (section 3.4). A stereo PIV instrument make use of two cameras to extract the out-of-the plane movement of the particles thus helps in determining the third component (z-component) of the velocity field. A brief representation on the method of acquisition, processing, and data extraction of PIV system has been highlighted in Fig. 7.1. For the present study, to assess the flow dynamic of the rotor wake, the field of view (FOV) has been keep at 2560 pixel x 1650 pixel with a maximum sampling rate or frame per second (fps) of 1400 Hz. However, the fps has been kept at 748 Hz, and a camera expose time (t_{exp}) of 1000 µs, as per the condition $1/t_{exp}$ < fps(S). The time period between the subsequent frame is $1/\Delta t$, where $\Delta t = 1/\text{fps}$. The image acquisition rate selected is such that most of the low and high-frequencies of vortex shedding are captured. A total of 2000 images were taken for a sample duration of 2.67 seconds; however, while processing, only those sequences of frames displaying proper seeding and vortex shedding are considered. The present study intends to examine the in-depth flow behaviour of the wind turbine wake using Stereo PIV. At high velocity (> 5 m/s), the seeding particle density drastically decreases, perhaps due to over-stretching under the high suction

pressure of the tunnel fan. Therefore, the study has been performed at 1.5 m/s < U < 4 m/s; this range of velocity produces a uniform/distinct wake field downstream of the model turbine. The downstream distance (*x/R*) has been taken from the rotor plane to the mid-point of FOV. Furthermore, to examine the flow characteristic at specific *x/R* location, a masking domain of 100 mm x 200 mm has taken, as shown in Fig. 7.2. The selected mask region is further processed to reduce the background noise, thereby, PIV correlation has been carried out to evaluate the corresponding field characteristics like velocity, turbulence, vorticity, and other. The step is repeated for all the frames, afterward at any location, one can extract the instantaneous flow field parameters.

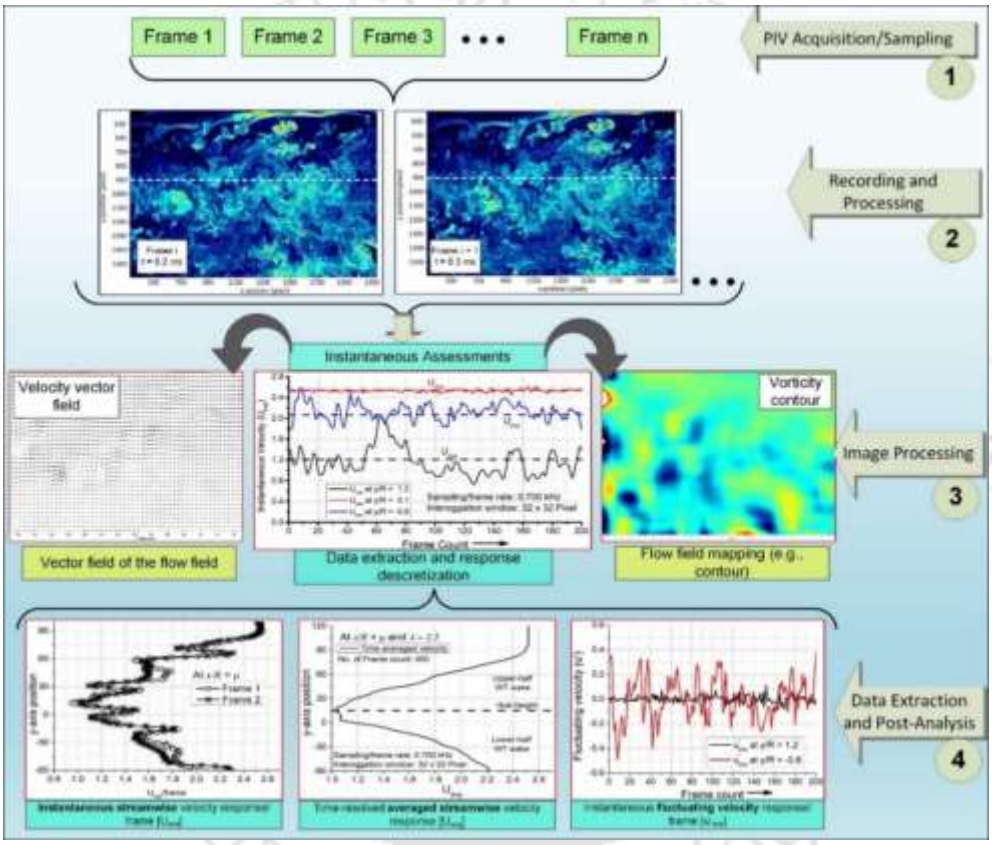

Fig. 7.1. Illustration of PIV acquisition, processing, and data extraction

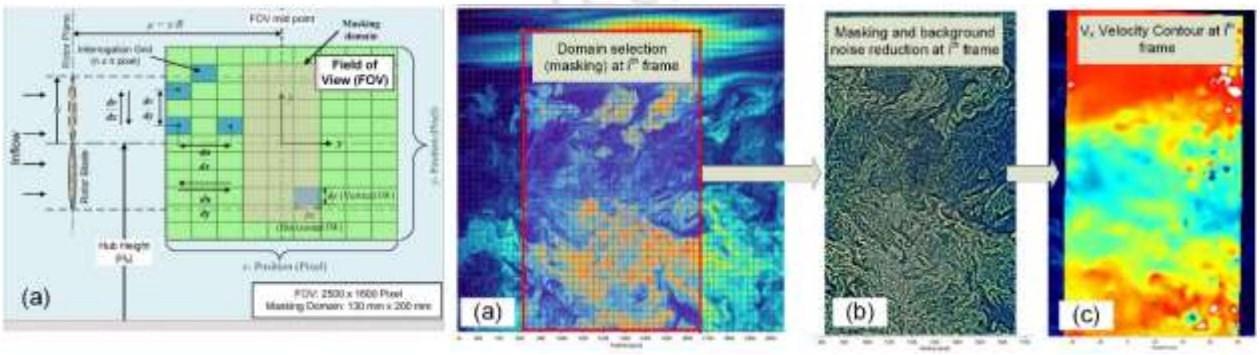

Fig. 7.2. Illustration of PIV processing (a) schematic FOV layout, (b) domain selection –masking, (c) background noise reduction, and (d) flow field characterization

The intent of the present study is to abstract the downstream flow field characteristic of wake dissipating from a small wind turbine (SWT). In this regard, a small HAWT having E216 profile with a rotor diameter (D) of 65 mm, known for producing potential power at low tip speed ratio (λ) has been selected. Details on the rotor blade design and operational characteristics can be excess from Chapter 3. The optimum λ of the rotor is close to 2.5, thus all the investigation in the present study has been carried out between $2 < \lambda < 3$, detaied result is presented in Chapter 4. The PIV assessment has been carried out to determine the velocity fluctuation, time-averaged velocity, turbulence intensity, vorticity development and others, at different *x/R*, *y/R*, and λ conditions. The wake information from this study will certainly be helpful in modeling of small wind farm and for the small wind turbine integrated systems.

7.2 Scatter and Average Data Estimation

The primary objective of the present is to determine and define the downstream flow field characteristic of the wind turbine wake operating at low λ and low freestream velocity (U). A total of four downstream locations, x/R = 6, 10, 14, and 18 has been opted w.r.t the rotor plane. The selection of these x/R position are such that the regime of study falls under the far wake regime (Steven and Meneveau, 2017), and which is about six times of the rotor diameter ($6D$) after the near wake regime. This regime of interest is also important from the fact that most of the wake models are based on the extent of far wake regime (Vermeer et al. 2003; Larsen et al. 2009).

For the present study, the value of U taken are 1.8, 2.5, 3.0, and 3.6 m/s to meet the intended range of λ for the model rotor, which is 2.11, 2.50, 2.60, and 2.61, respectively. At first, the nature of flow behavior at stream wise (x) and along vertical direction (y) has been examined to see the scatter distribution of the flow parameter. Figure 7.3(a) shows the scatter distribution of V_x at x/R = 6, 10, 14, and 18 for U = 1.8 m/s. Similarly, the V_x distribution at U = 2.5, 3.0, and 3.6 is presented in Figs. 7.3(b), (c), and (d), respectively. The scatter distribution shows the concentration of the data point thus able to represent the averaged profile into a meaning pattern. It is interesting to note that even at x/R = 6, the time-averaged velocity profile has a Gaussian type distribution which is in-line with the analytical proposition of Larsen et al. 2009, Frandsen et al. 2006, and Bastankhan and Porté-Agel, 2014. However, when the downstream mapping point is increased, as expected the slope of the averaged V_x profile becomes stepper. This strongly suggest the flow recovery, at the same time the standard deviation or the level of fluctuation also decreases. The scatter distribution also depicts asymmetric nature of the

velocity profile, which is not as per the classical description of the wind turbine wake (Vermeer et al. 2003; Jensen, 1983). The asymmetric nature of the flow profile is due to the presence of the nacelle and the vertical support structure; thus, it is expected that the lower half of the wake will have lesser velocity and will take more to recover. The other two components of the flow field, V_y and V_z at the same x/R location and under same the inflow conditions are depicted in Figs. 7.4 and 7.5, respectively. In these cases, also, close to the rotor plane (x/R = 6) the level of fluctuation is quite strong compared to far wake (x/R = 18). One of the key observations in Fig. 7.5, it is interesting to note the distinct pattern of V_z profile close to the rotor plane; representing two opposite crests. These two opposite crests are the consequence of helical motion of the wake, further detail on this feature has been mentioned in the next subsection. Similar to the observation made on the level of data scattering at x/R = 6 for V_y component, the level of scattering also reduces for the V_z component as the downstream distance increases. One can also note that the level of fluctuation in V_z at any downstream location is relatively larger than the V_y component, this mainly due to the helical motion of the wind turbine wake.

Furthermore, it is to be note that though V_x, V_y, and V_z component individual represents unique features and have distinct characteristics but one cannot ignore the fact that all the three flow field parameters are interrelated. Therefore, it is essentially that the resultant value is also evaluated, as per Eq. (7.1), the result of is presented in Fig. 7.6.

$$Resultant\ Velocity\ (V_R) = \sqrt{V_x^2 + V_y^2 + V_z^2} \tag{7.1}$$

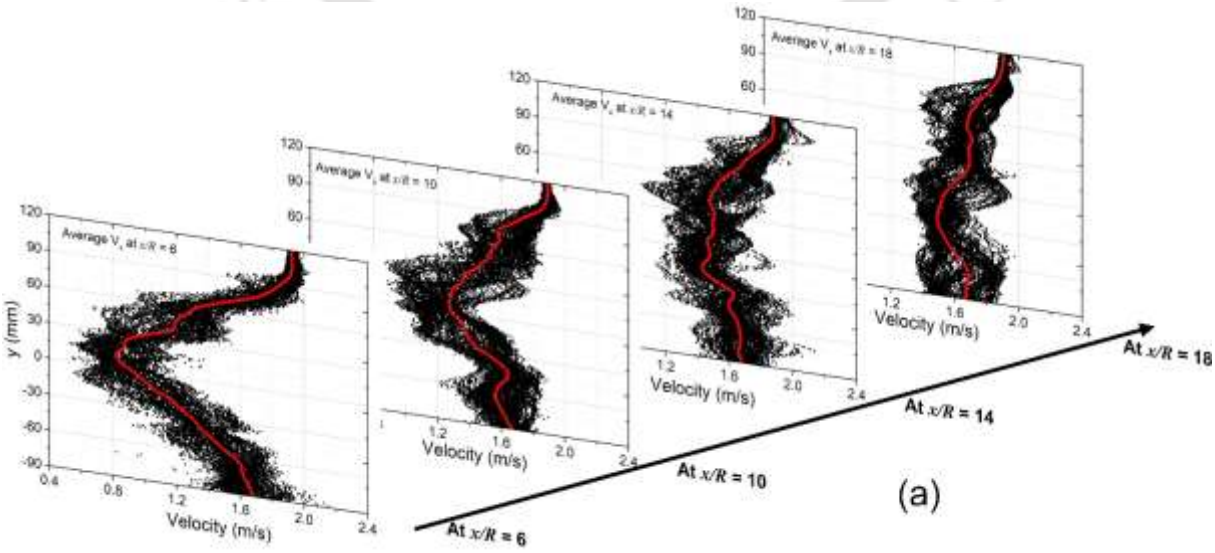

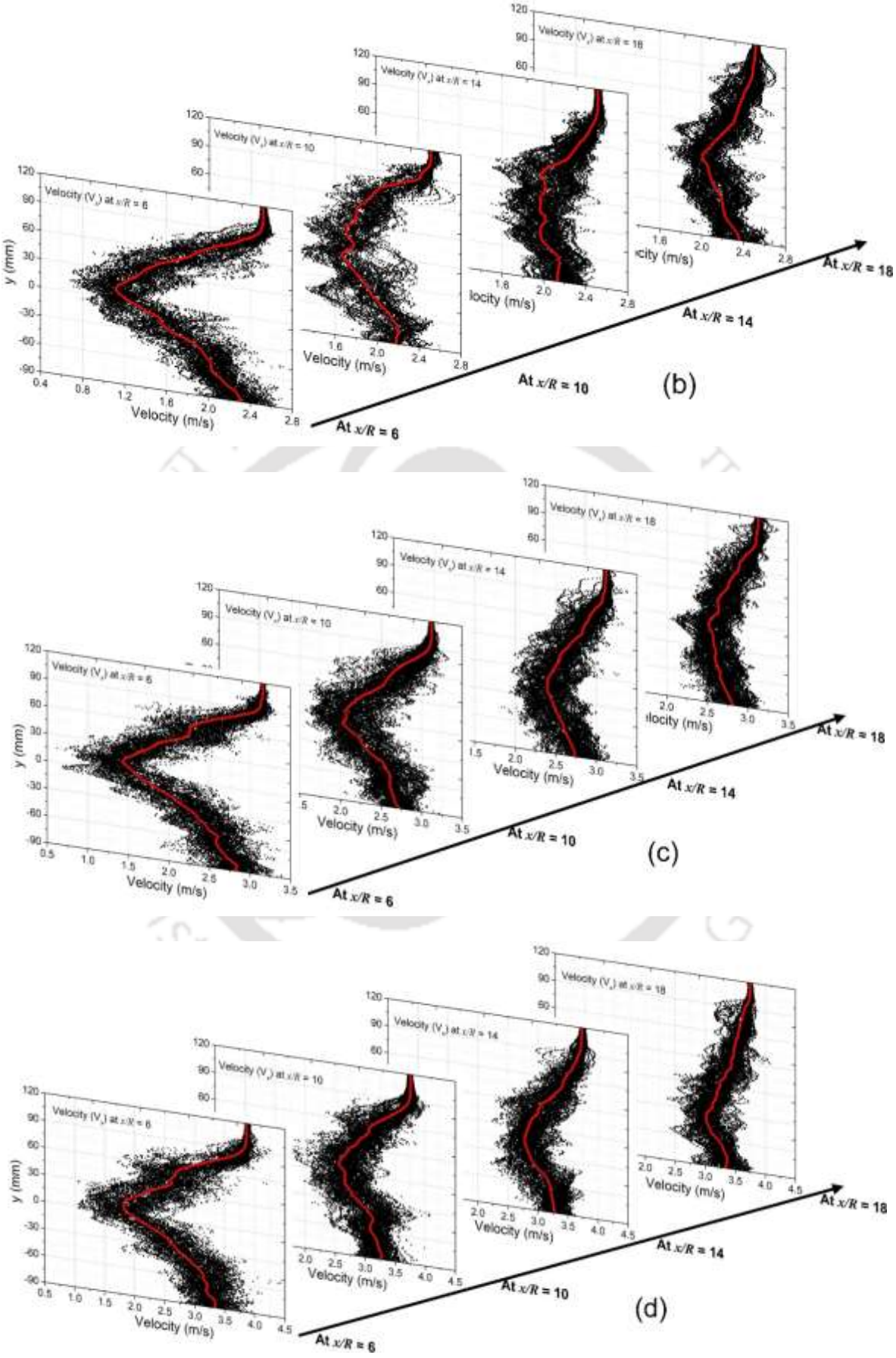

Fig. 7.3. Downstream V_x velocity at (a) 1.8 m/s, (b) 2.5 m/s, (c) 3.0 m/s, and (d) 3.6 m/s

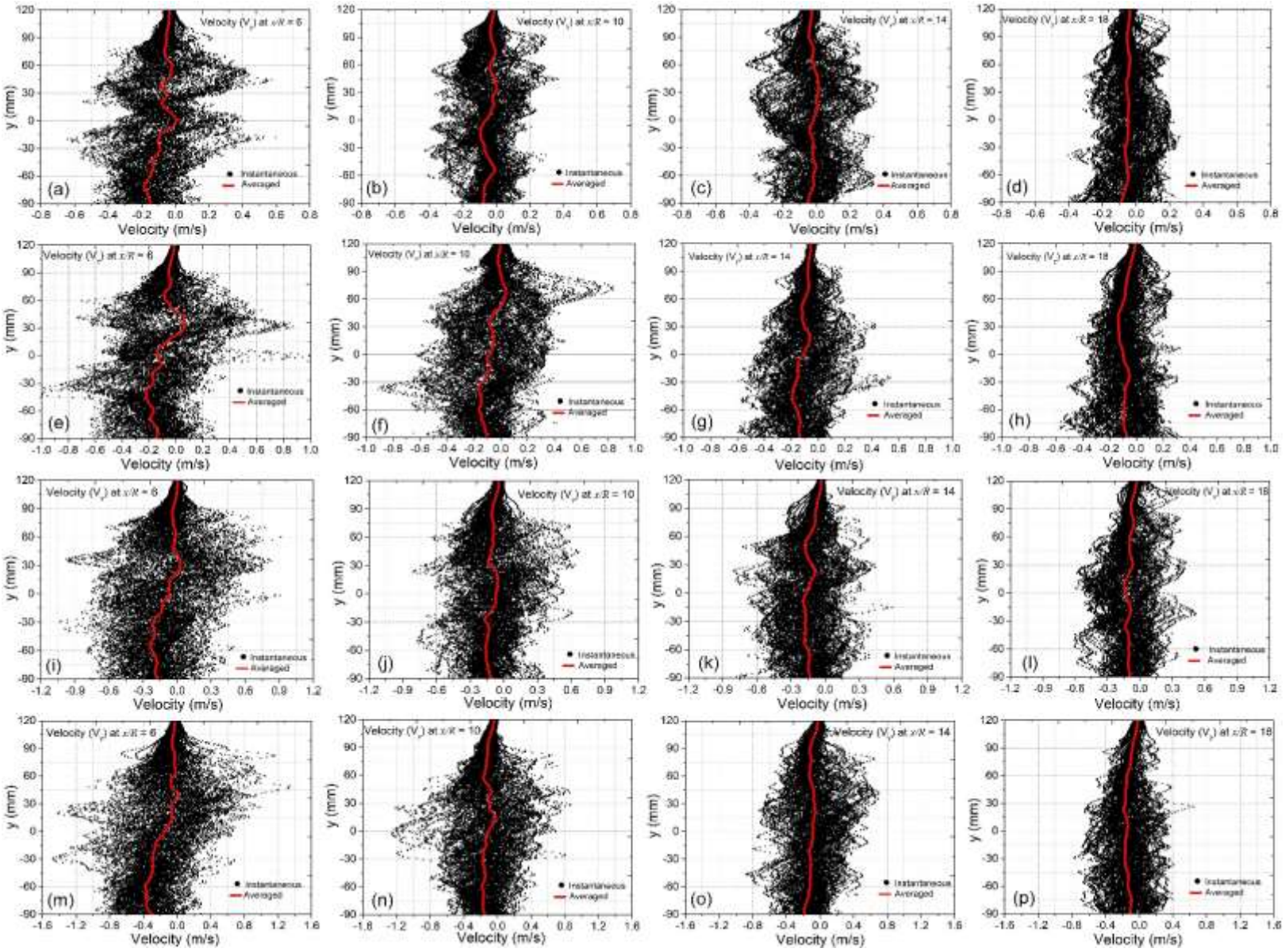

Fig. 7.4. Downstream V_y velocity at (a-d) 1.8 m/s, (e-h) 2.5 m/s, (i-l) 3.0 m/s, and (m-p) 3.6 m/s

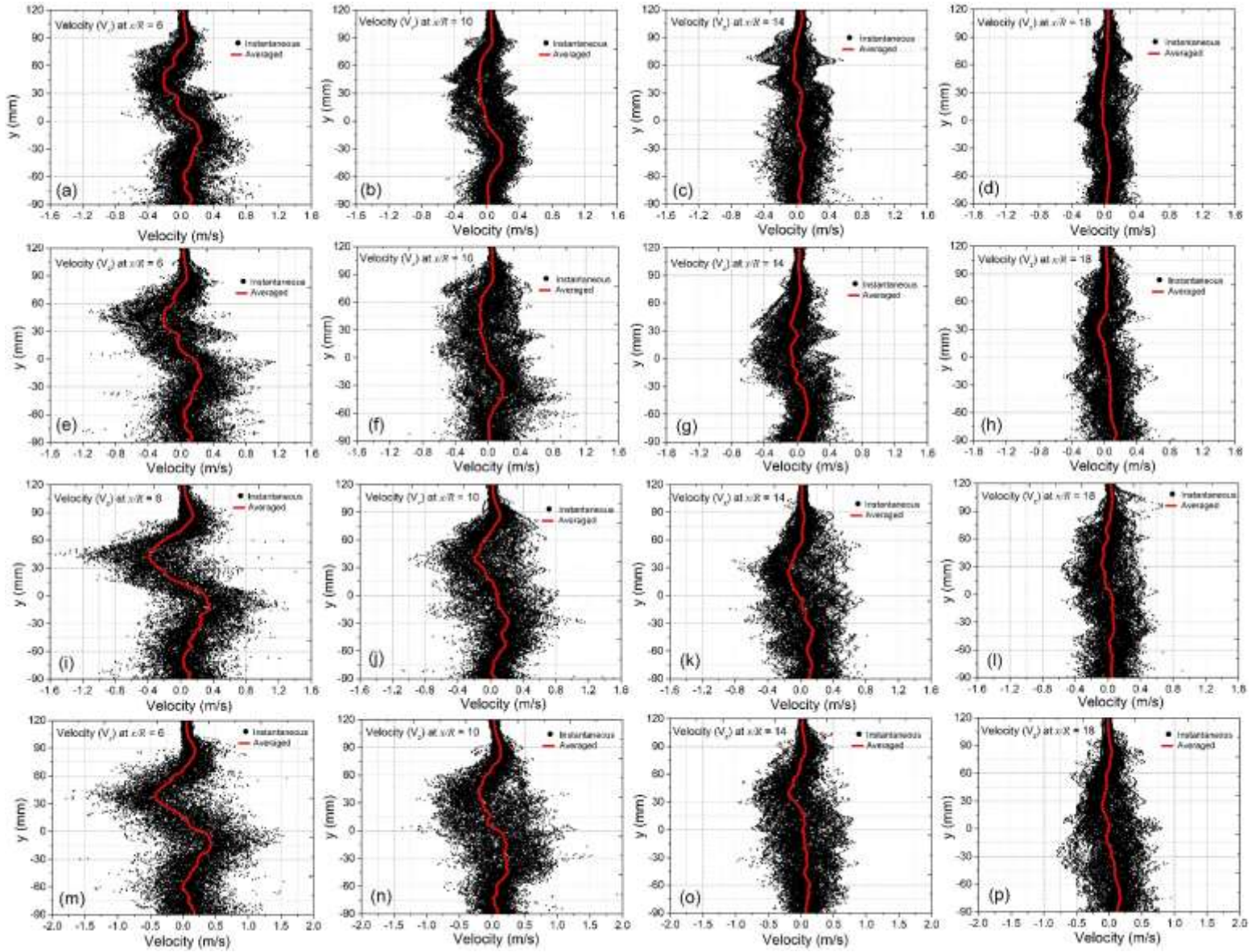

Fig. 7.5. Downstream V_z velocity at (a-d) 1.8 m/s, (e-h) 2.5 m/s, (i-l) 3.0 m/s, and (m-p) 3.6 m/s

The instantaneous velocity component can be obtained by considering all the sampled PIV image frame where each data point represents the instantaneous value per frame with a time difference of 1/fps. Once the instantaneous velocity fluctuation at a point is known, the time-average velocities (V_{avg}) can be calculated, as per Eqs. (7.2) through Eq. (7.5). And the respective standard deviation (σ) can be obtained as per Eqs. (7.6) through Eq. (7.8), implication σ is to find the turbulence intensity of the flow field. The uncertainty assessment has been presented in Appendix E.

$$V_{avg.x} = \left(\sum_{i=f_o}^{f_n} (V_x)_i \right) / n; \qquad \textit{where, n is the number of frame count} \tag{7.2}$$

f_o = *Refrence frame, &* f_n *is the* n^{th} *frame*

$$V_{avg.y} = \left(\sum_{i=f_o}^{f_n} (V_y)_i \right) / n \tag{7.3}$$

$$V_{avg.z} = \left(\sum_{i=f_o}^{f_n} (V_z)_i \right) / n \tag{7.4}$$

$$\textit{Therefore, } V_{avg.R} = \left(\sum_{i=f_o}^{f_n} (V_R)_i \right) / n = \left(\sum_{i=f_o}^{f_n} \left(\sqrt{\left(V_x^2 + V_y^2 + V_z^2 \right)} \right)_i \right) / n \tag{7.5}$$

$$\textit{Standared deviation } (\sigma_x) = \left(\sum_{i=f_o}^{f_n} \left((V_x)_i - V_{avg.x} \right)^2 / n \right)^{0.5} \tag{7.6}$$

$$\textit{Similarly, } \sigma_y = \left(\sum_{i=f_o}^{f_n} \left((V_y)_i - V_{avg.y} \right)^2 / n \right)^{0.5} \tag{7.7}$$

$$\textit{Similarly, } \sigma_z = \left(\sum_{i=f_o}^{f_n} \left((V_z)_i - V_{avg.z} \right)^2 / n \right)^{0.5} \tag{7.8}$$

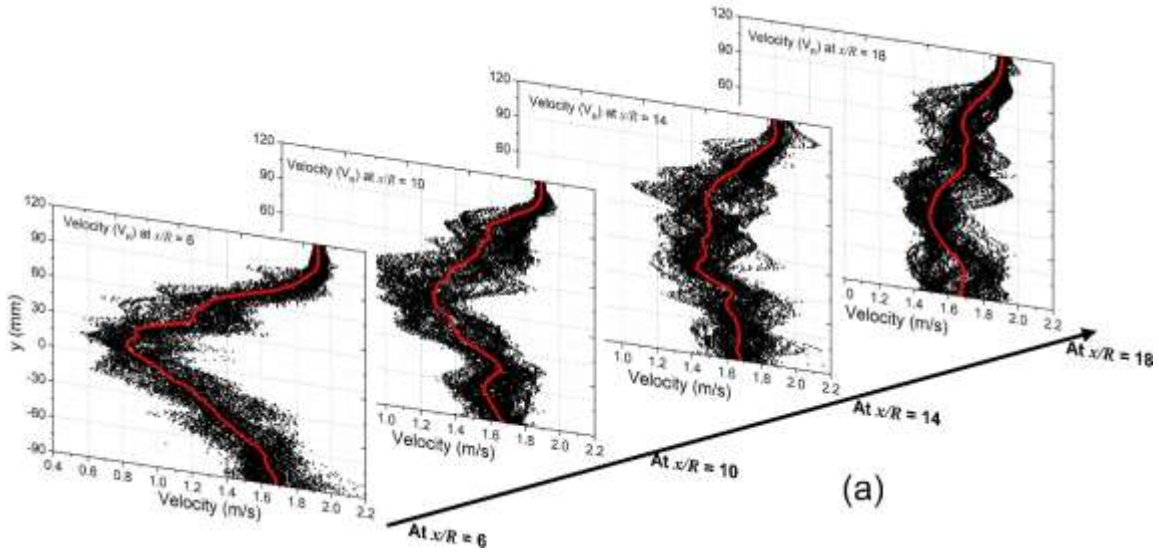

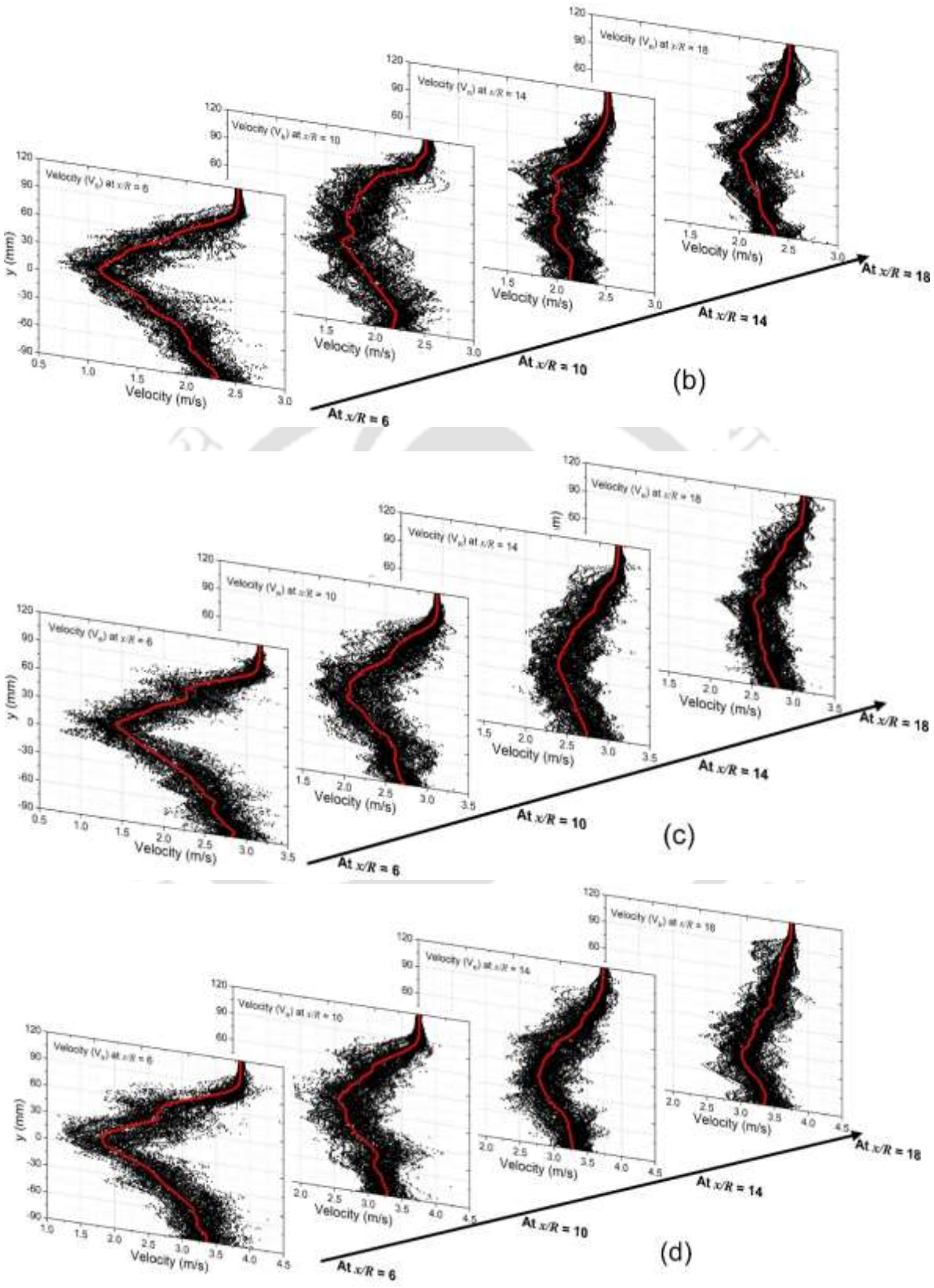

Fig. 7.6. Downstream resultant velocity (V_R) at (a) 1.8 m/s, (b) 2.5 m/s, (c) 3.0 m/s, and (d) 3.6 m/s

7.3 Downstream Flow Field Characteristics

The nature of downstream flow field of any model in the fluid mechanic study is often expressed in non-dimensional form, basically to mitigate the scaling effect. This adoption ensures that the underlying flow physics is retained even after model scaling is carried out, since the laboratory scale model may be subjected to geometric enhancement. Therefore, in the present investigation, all the flow parametric assessment has been analyzed as non-dimensional variability like velocity deficit, normalized velocity, turbulence intensity, and others.

The downstream velocity is mostly dominated by V_x, and in most of the analytical models only V_x component is considered (Bastankhan and Porté-Agel, 2014); this is to simplify the wake model description. In this regard, the downstream velocity deficit in term of V_x, as per Eq. 7.9 has been evaluated, as shown in Fig. 7.7. The results presented in Figs. 7.7(a) through 7.7(d) shows the variation of time-averaged V_x at different x/R along y/R for λ = 2.11, 2.50, 2.60, and 2.61. It is interesting to note that velocity deficits are relatively low at higher λ, and maximum close at λ = 2.5, which apparently is also the optimal condition of the model rotor (Chapter 4). This leads to an analogy that perhaps; one can expect the maximum deficit when the rotor is operating at the or close to the rotor design condition.

$$\textit{Velocity deficit (Vel. def.)} = \left(U\text{-}V_{avg.x}\right)/U; \qquad \textit{(deficit w.r.t to } V_x\textit{)} \tag{7.8}$$

$$\textit{and,} \qquad \textit{Vel. def.} = \left(U\text{-}V_{avg.R}\right)/U; \qquad \textit{(deficit w.r.t to } V_R\textit{)} \tag{7.9}$$

The wind turbine wake being three-dimensional in nature will be influence by both y and z-components also, thus velocity deficit with respect to V_R is also evaluated, result of which is shown in Figs. 7.7(e) through 7.7(h). One can clearly see that overall variation in the profile pattern is relatively less (1-6%), but still, it is not wise to totally ignore the influence of y and z-components, especially, when the interest is more towards flow physics intuition. In line with the case study, the variation of velocity deficit at a given x/R for different λ has also been carried out, results of which is shown in Figs. 7.8(a) through 7.8(b). The results show that, the maximum deficit is between 0.45 - 0.55, 0.27 - 0.35, 0.17 - 0.24, and 0.12 - 0.20, at x/R = 6, 10, 14, and 18, respectively. The observation indicates that at about 9D and beyond, one can expect about 70 – 80% flow recovery, which close to the approximation of Porté-Agel et al. (2015) and Bastankhan and Porté-Agel, (2018) estimation.

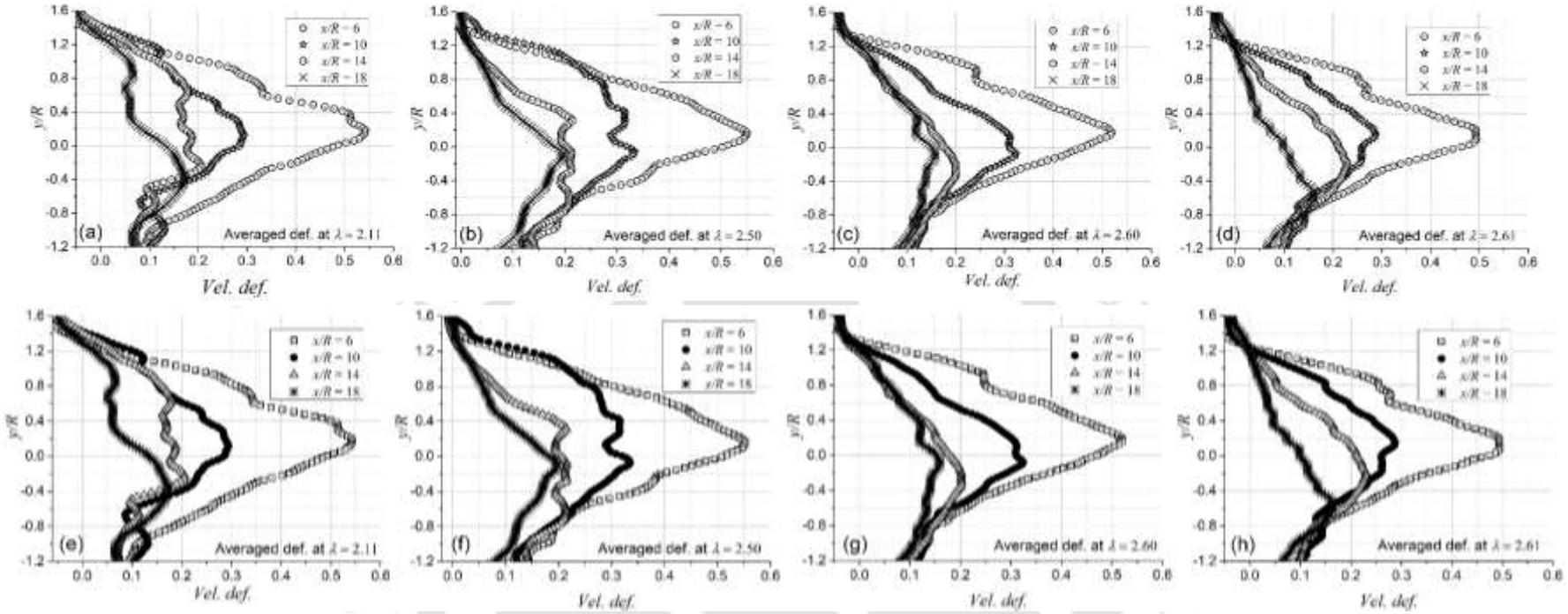

Fig. 7.7. Variation of velocity deficit (a-d) averaged V_x, and (e-h) averaged resultant velocity (V_R)

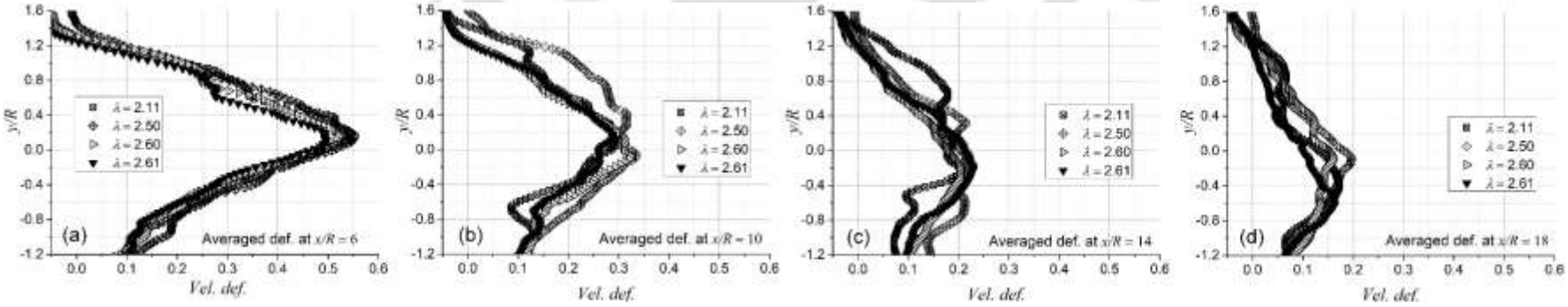

Fig. 7.8. Variation of V_x deficit at (a) x/R = 6, (b) x/R = 10, (c) x/R = 14, and (d) x/R = 18

The observations mentioned above are helpful in describing the characteristics of V_x; however, it does not shade light on the behaviour of V_y and V_z components. In this regard, the best way to address the share of y and z-components in the wake field is through normalized velocity (η) description, expressed by Eq. (7.10) through Eq. (7.12). The idea behind adopting η as a decisive parameter comes from the fact that the freestream velocity (U) is apparently the contribution of x-component, thus addressing the share of y and z component with respect to U will help understand the extend of momentum transfer analogy. The result of η_x as a function of x/R at different λ is shown in Figs. 7.9(a) through 7.9(d). It can be seen that beyond $y/R > 1.2$, the velocity of η_x is slightly higher, suggesting that there is increase in the V_x. As addressed by Medici and Alfredsson, (2008), Krogstad et al. 2014, towards the tip of the blade or at the brink of wind turbine helical vortex core, there is influence of ambient flow on the stream wise flow apart from the helical motion influence. Thus, one may see increased stream wise velocity toward the brink of helical vortex core, the effect of which is also felt on the helical blade tip vortex (Eriksen and Krogstad, 2017). Figures 7.9(a) through 7.9(h) shows the share of V_y component, the findings indicate that the influence of V_y is minimal. The only key feature to be note here is that towards the lower half of the turbine wake, the share of wake along y-direction is more towards –ve y-direction, mainly due to the confluence of the vortex shedding dissipating from the vertical support structure. Figures 7.9 (i) through Fig. 7.9(l) shows the flow characteristic of the wake along z-component, the results on η_z with respect to y/R indicates some interesting flow features particularly close to the rotor plane. At $x/R = 6$, one can see two distinct opposite crests towards the upper and lower half of the wake field. The extent of these crests is bout 10-15% of U, thus suggesting that the momentum transfer on V_z is relatively high compared to V_y. Upon carefully exploring the behaviour of the rotor wake in frame-by-frame mode and through in-depth visual interpretation, it is understood that these two opposite patterns are the consequence of helical vortex. The value of η_z is +ve toward the lower half whereas, it is –ve towards the upper half, suggesting that there is out-of-the plane movement in the lower half and into-the plane movement in the upper half of the rotor wake. The physical interpretation of such analogy come from the fact that the direction of wake rotation is opposite to the direction of the rotor blade (Vermeer et al. 2003; Sorensen et al. 2014). And for the present case, the rotor rotation is clockwise, thus the wake rotation is counter clockwise, which in fact is the cause of two opposite crest formation (Figs. 7.9(i)-(l)).

$$Normalized\ Velocity\ (\eta_x) = V_{avg.x} / U; \qquad (x-component) \tag{7.10}$$

$$Normalized\ Velocity\ (\eta_y) = V_{avg.y} / U; \qquad (y-component) \tag{7.11}$$

$$Normalized\ Velocity\ (\eta_z) = V_{avg.z} / U; \qquad (z-component) \tag{7.12}$$

Now, to estimate the wake propagation, one can generate the equation of the curve from the data point, which in classical approach is achieved through linear regression analysis. Considering the case study of normalized velocity at x/R = 6, for λ = 2.11, 2.50, 2.60, and 2.61. It is observed that the fifth order polynomial equation express by Eq. 7.13 produces reasonable curve fit for y/R vs. η_x. The coefficient of polynomial for all the four curves are mentioned in Table 7.13. Similar, assessment can be obtained for the y and z-components, accordingly one can estimate the probable velocity deficit and flow strength at x/R = 6. Thus, this regression analogy can be made for other x/R locations.

$$Y = A_0 + A_1 X + A_2 X^2 + A_3 X^3 + A_4 X^4 + A_5 X^5 \tag{7.13}$$

Table 7.13 Coefficient of polynomial between Y (= y/R) and X (= η_x)

λ	A_0	A_1	A_2	A_3	A_4	A_5	R^2
2.11	0.519	- 0.210	0.458	0.2065	- 0.126	-0.032	0.9831
2.50	0.515	-0.218	0.439	0.235	-0.129	-0.043	0.9849
2.60	0.554	-0.199	0.457	0.165	-0.153	-0.003	0.9711
2.61	0.570	-0.164	0.482	0.133	-0.170	0.010	0.9693

The observations indicated above are the time-averaged parameters, which does not provide much information on the level of flow fluctuation at the considered downstream locations. Therefore, it is indeed required to assess the turbulence intensity (TI) of the flow field. The TI is expressed as the square root of turbulent velocity (Cengel and Cimbala, 2009). As acknowledged from Figs. 7.8 and 7.9, the contribution from x-component is prominent, hence variation in TI_x has been evaluated as per Eq. 7.14, and the result in shown in Fig. 7.10 for different x/R and λ conditions. The result shows that TI_x is maximum close to the rotor plane and decreases with increase in x/R and λ. The level of TI_x at x/R = 6 is between 6 – 18%, which decreases to 4 – 8% at x/R = 18. However, upon considering all the three components of fluctuations (u_x, u_y, and u_z), as per Eq. 7.14, it is observed that the value of net TI is about 1.2 – 2 times of TI_x (Fig. 7.11). This observation would not have been possible even with other conventional probes like single or x-probe CTHWA. Therefore, contrary to TI_x assessment, it is observed that at high λ, the net TI is quite significant and greatly influence by y and z-fluctuating components, which in fact is the result of wind turbine helical wake motion.

$$\textit{Turbulence Intensity (TI)} = \left(\overline{u_x^2}\right)^{0.5} / U = TI_x; \qquad \textit{where, } u_x = V_x - V_{avg.x} \tag{7.13}$$

$$\textit{Net TI} = \left(\left(\overline{u_x^2} + \overline{u_y^2} + \overline{u_z^2}\right)/3\right)^{0.5} / U; \qquad \textit{where, } u_y = V_y - V_{avg.y} \;\&\; u_z = V_z - V_{avg.z} \tag{7.14}$$

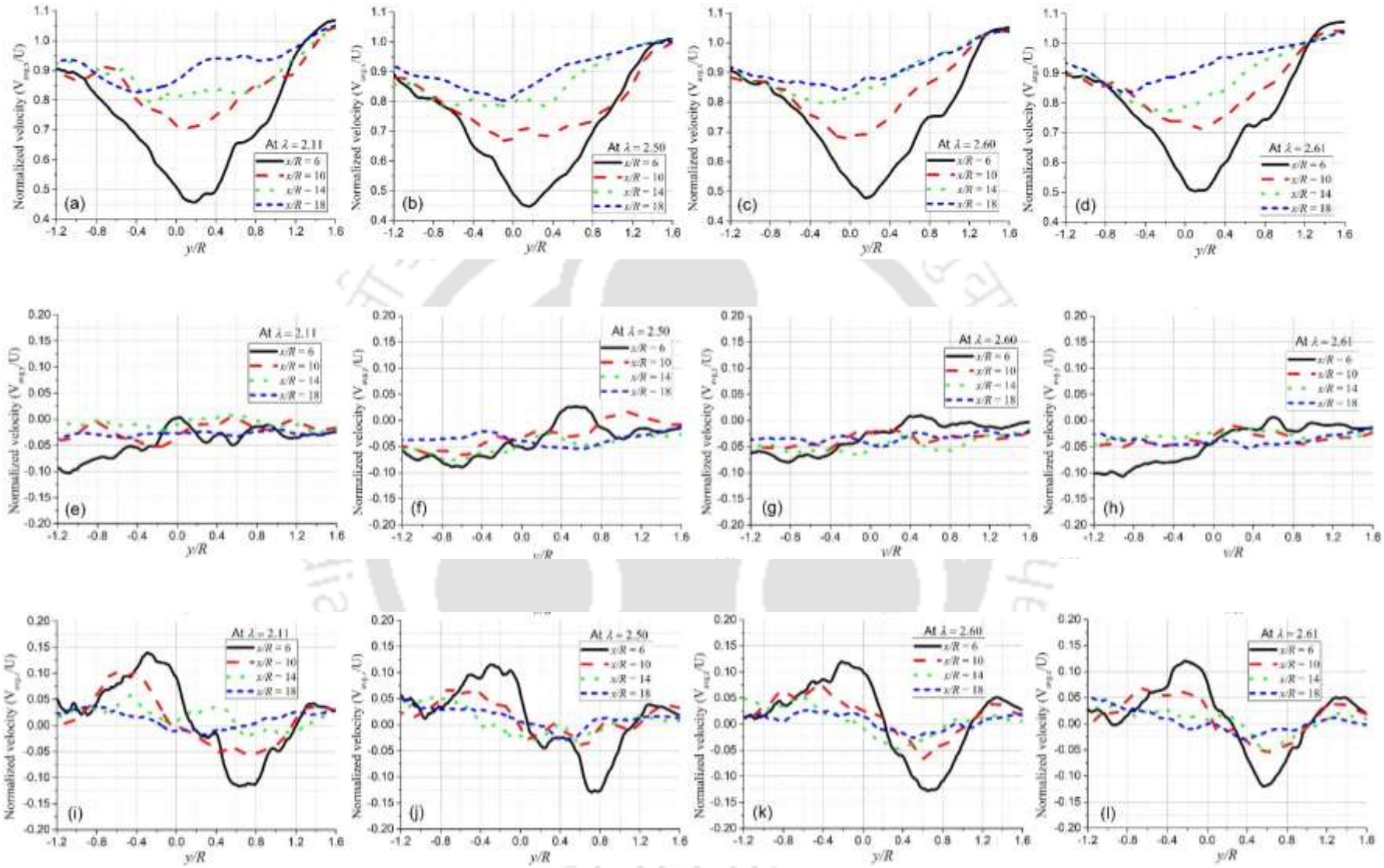

Fig. 7.9. Variation of time-averaged normalized velocity of (a-d) V_x- component, (e-h) V_y- component, and (e-i) V_z- component at different x/R and λ conditions

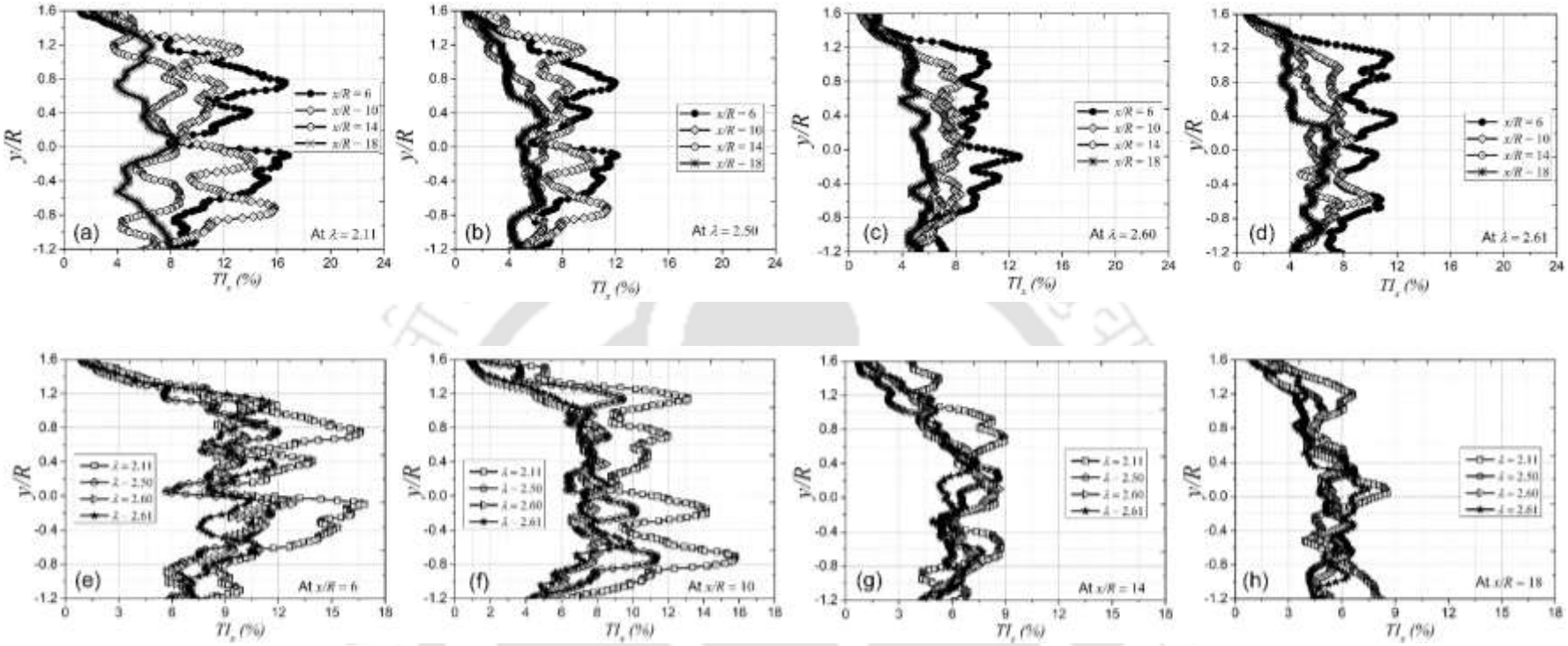

Fig. 7.10. Variation of turbulent intensity at (a-d) different *x/R*, and (e-i) different λ

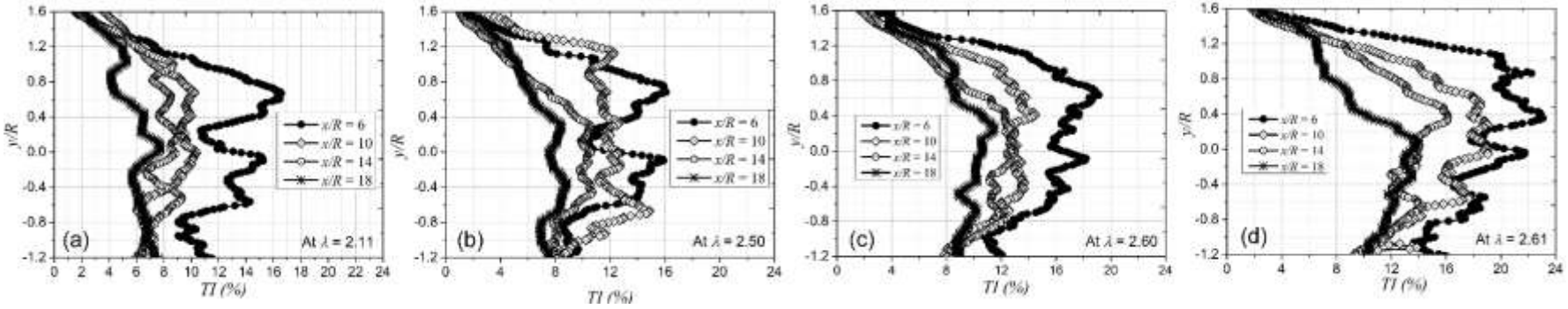

Fig. 7.11. Variation of net turbulent intensity at (a) λ = 2.11, (b) λ = 2.50, (c) λ = 2.60, and (b) λ = 2.61

7.4 Downstream Description Using Contour Field

The time-averaged assessment carried out and presented in the above discussion help understand the flow behavior at specific downstream location (x/R). Based on such analysis, most of the classical analytical wake models has been propounded (Vermeer et al. 2003); however, the results do not provide sufficient information on the overall two or three-dimensional flow field. In this regard, full flow field assessment has been carried out using PIV but this time the masking domain has been increased to about 300 mm x 200 mm, with an interrogation window of 24 × 24 pixel. The processing has been carried out for all the 800 images, and the corresponding velocity and vorticity contour field are generated. Since it is not possible to present the contour field for all the frames, therefore, focus has been made on the time-averaged contour field. A typical demonstration of V_x velocity contour field at λ = 2.11, 2.50, 2.60, and 2.61 has been shown in Fig. 7.12. The point to be note here is that though it represents instantaneous flow field, one can distinctly notice relatively higher velocity field towards the upper half of the wake; the central core has reduced field and the lower half has relatively enhanced field but lesser then upper half wake.

For the same reference distance (x/R = 6), the vorticity field (ω_z) has been evaluted as per the relation $dV/dx - dU/dy$, the result is shown in Fig. 7.13. In this case also, the instantenous vorticity contour field indicate that there is presence of strong vorticity field toward the upper half of the rotor wake. This assessment is supported by the fact that the vorticies encounter above $y/R > 0$ are mostly dissipating from the blade tip (tip vortices) and blade span (bound vortices), where the contribution of latter becomes negligible at far wake. The blade tip vortex in particular though decays with x/R but maintain regular pattern towards the upper half of the rotor wake, more detail on will be discussed in the next subsection. On contrary, the lower half of the vorticity field does not represents or maintains uniformity due to the confluence of vortex shadding from the vertical support structure.

The averaged velocity contour field of V_x is shown in Fig. 7.14, the case studies presented are for λ = 2.11, 2.50, 2.60, and 2.61 with reference to x/R = 6. The three-dimensional depiction of V_x contour indeed compliment the assessment made at x/R = 6 (Figs. 7.3 and 7.7), here we could see that towards the brink of wind turbine vortex core, enhancement in velocity occurs, whereas substantial reduction in the velocity field is noted within the central core ($-0.5 < y/R < 0.5$). Similar analogy can be made from V_y contour field (Fig. 15), it is noted that level of fluctuation is quite intensive in both upper and lower half of the wake. However, the lower half

of the wake is mostly dominated by –ve V_y, suggesting downstream motion, which is the consequence of centrifugal motion impart by the helical motion of wake and due to the confluence of vortex shedding dissipating from vertical support.

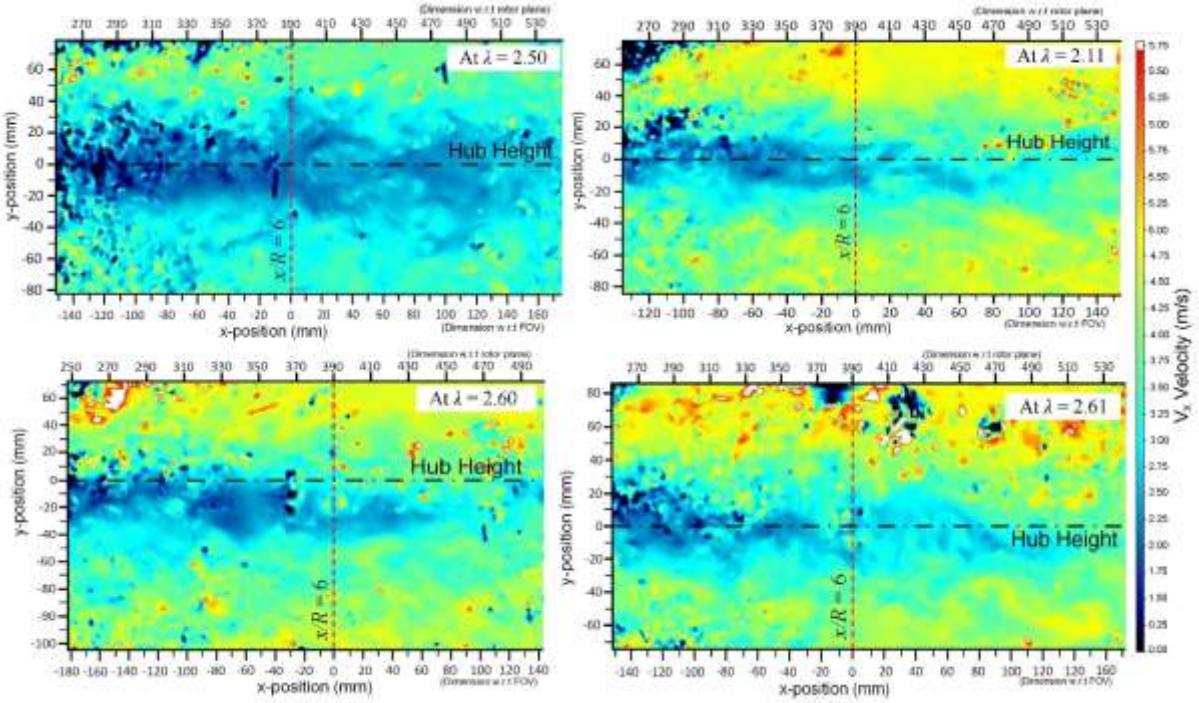

Fig. 7.12. Illustration of instantaneous V_x velocity contour at λ (a) 2.11, (b) 2.50, (c) 2.60, and (d) 2.61

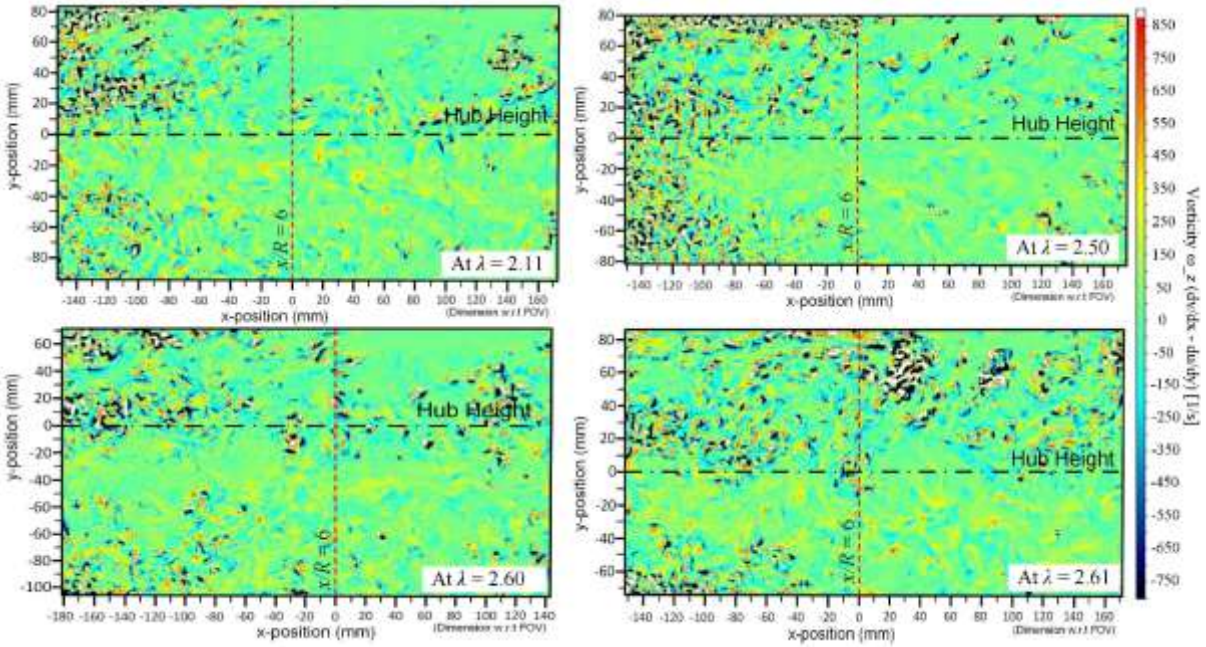

Fig. 7.13. Illustration of instantaneous vorticity contour at (a) 2.11, (b) 2.50, (c) 2.60, and (d) 2.61

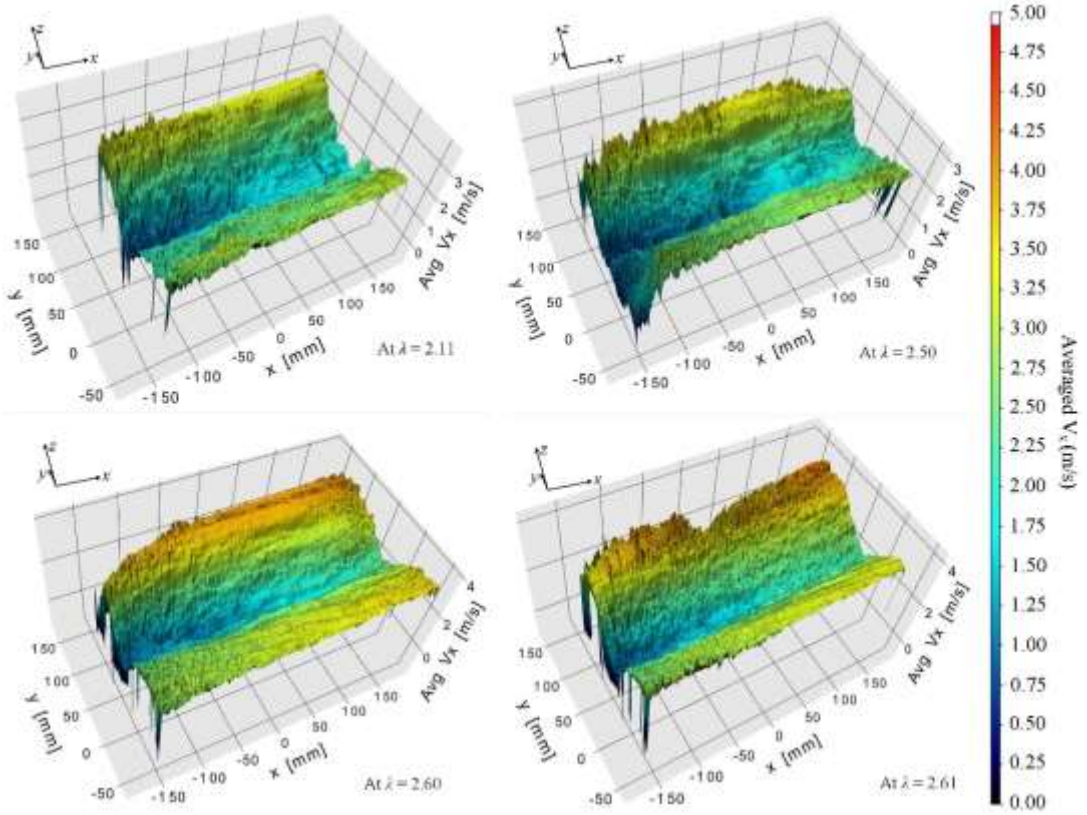

Fig. 7.14. Illustration of time averaged V_x velocity contour at λ (a) 2.11, (b) 2.50, (c) 2.60, and (d) 2.61

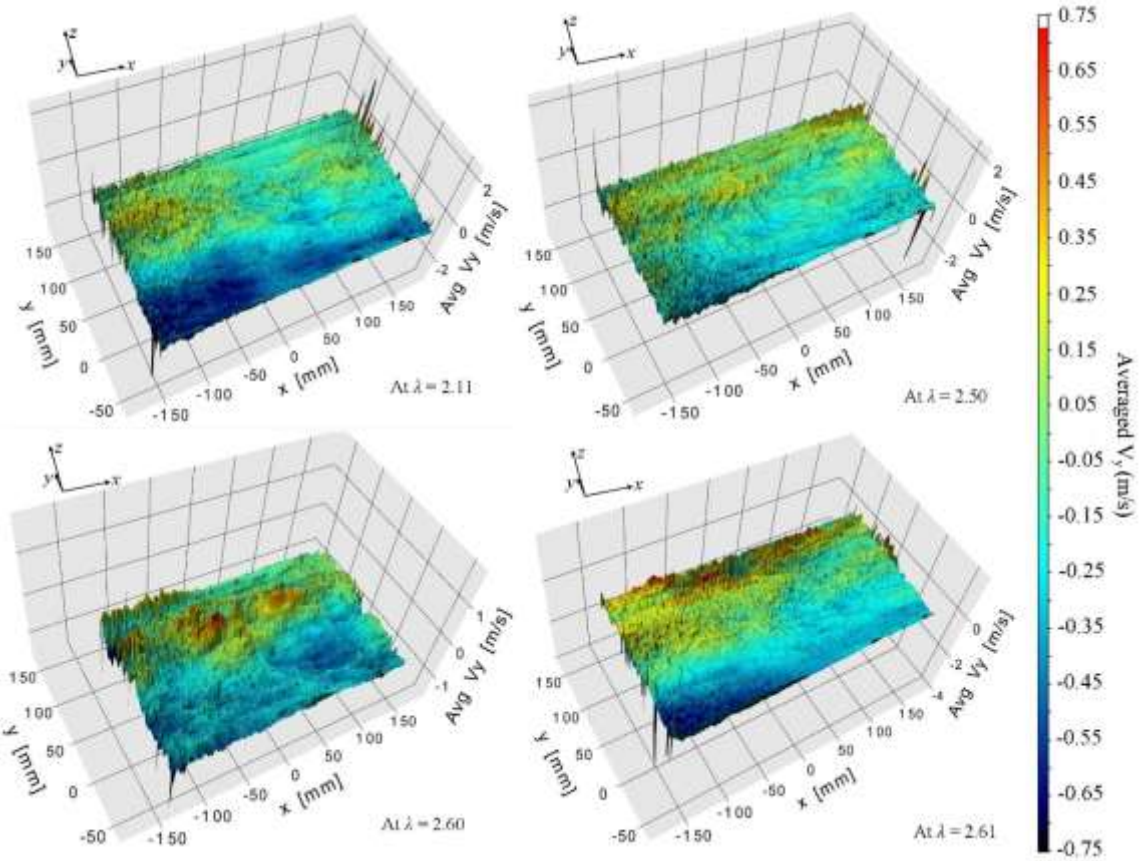

Fig. 7.15. Illustration of time averaged V_y velocity contour at λ (a) 2.11, (b) 2.50, (c) 2.60, and (d) 2.61

7.5 Study on the Nature of Helical Tip Vortex

This segment of the PIV study is focused on the assessment of the nature of helical tip vortex. In the making of wind turbine wake models, it often so happened that the models do not consider the characteristic of the blade tip vortex (Vermeer et al. 2003; Larsen et al. 2009; Steven and Meneveau, 2017). However, the physical reality is that, it is the blade tip vortex that defines the core regime of the wind turbine wake. The main reason for not adopting the helical features of wind turbine wake is to reduce the complexity of the wake model, furthermore, even the data-driven wake model do not invoke the helical vortex characteristics (Sun et al. 2020; Ti et al. 2020). Thus, the underlying features of the wake are often forgotten, which after all, are the driving force in the formation of complex three-dimensional helical vortex field.

In this aspect, a systematic PIV assessment has been made mainly through time-resolve flow visualization to witness the sequence of events that eventually dictates the nature of stochastic wind turbine wake. To carry out the objective, the acquisition and processing analogies adopted for the above discussion are kept same, that is, a total of 800 images are processed. However, in this process only those sequence of frames where considered that clearly demonstrate the tip vortex signatures. The captured and considered frames are then discretized into number of equal pixel grids to map and trace the movement of vortices. The images captured were mapped with 32 × 32 pixels grid (1 pixel ~ 0.26 mm), thus shift in the vortex pattern is calculated as a factor of 32 times the number of grids. If the fps of the PIV study is 's', then time period at i^{th} frame will be t_i = i/s, therefore, the time period after four frames will be $t_{i+4} = t_i + 4/s$. Accordingly, frame-by-frame shift in the vortex structure has been mapped. Since in the modelling of wind turbine wake, generally, the velocity at the outer core are examined to express the expansion and contraction of the wake. Therefore, the present case study is mainly focused on the mapping of the blade tip vortex. To understand the nature of the blade tip vortex, a case study at λ = 2.11 and 2.50 has been considered, since these two operating conditions are close to the optimum condition of the model rotor of low tip speed ratio (Chapter 4). Figure 7.16(a), 7.16(b), 7.16(c), and 7.16(d) represents the flow visualization of wake at $t = t_i$ = i/s, t_i + 15/s, t_i + 30/s, and t_i + 46/s, respectively. Information on shift in the tip vortices are made possible by visualizing the particle concentration in different frame, a typical illustration of particle concentration is shown in Fig. 7.17. The corresponding ensemble visualization field as per Figure 7.18 shows the tracking of tip vortex for a total of 46 frames, the acquisition reference is x/R = 6 from the rotor plane, at λ = 2.11.

It is observed that, the rotation of tip vortex is same as the direction of rotation of the rotor blade, and in the present case, it is clockwise. However, the direction of helical vortex ring (anti-clockwise) is opposite to the direction of blade (clockwise). The flow visualization

indicates that there is a strong movement or diffusion of inner wake toward the tip vortex, which as a result provides radial momentum to already translating wake. And perhaps this is one of the essential reasons, why normalized velocity (η_x) has the value $\eta_x > 1$, when $y/R > +1$, as seen in Fig. 7.9. The visualization has been carried out under highly seeded condition thus, helped in recognizing some minute details of wake. Such as the relative motion between the central vortex core and the viscous sub-layer close to the blade tip. Similar assessment has been made at $\lambda = 2.50$, as shown in Fig. 7.19, at this case also, the behaviour of the tip vortex is almost identical, except, it is observed that the time-lag and subsequent distance between the tip vortex are reduced.

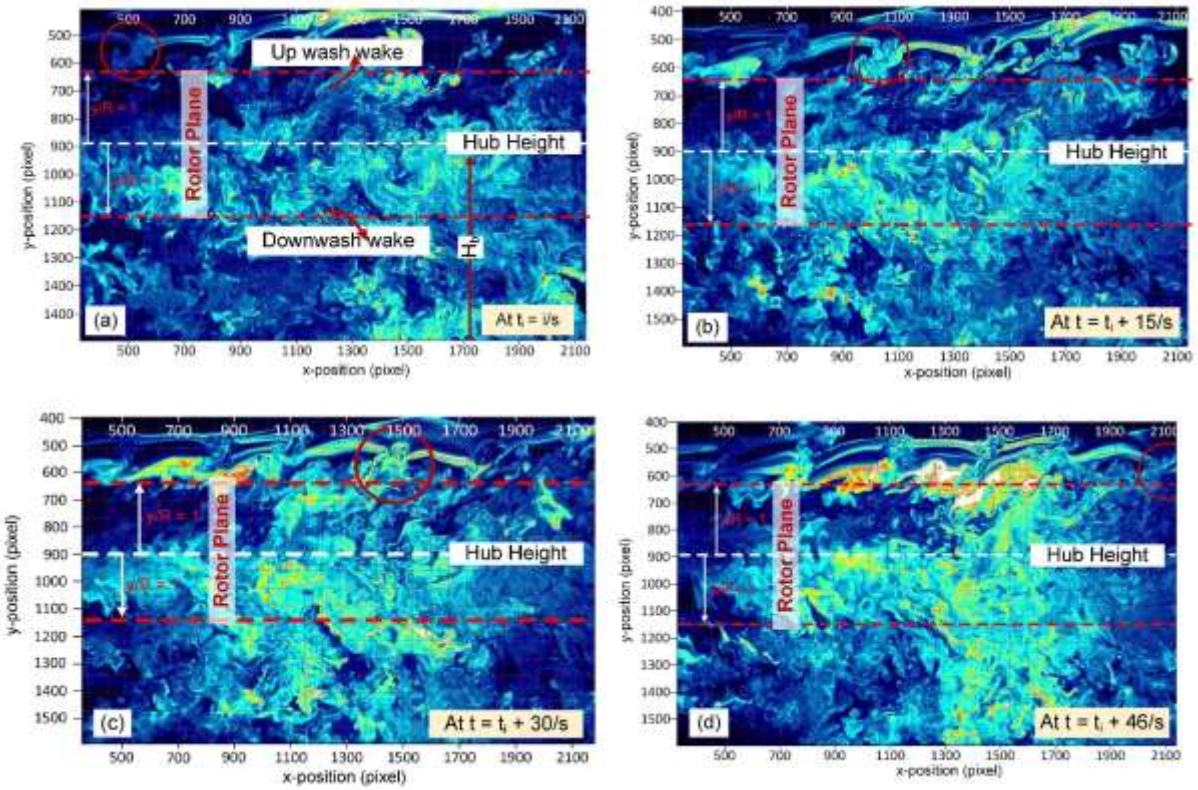

Figure 7.16 Represents the flow visualization of wake at (a) t = t_i = i/s, (b) t_i + 15/s, (c) t_i + 30/s, and (d) t_i + 45/s

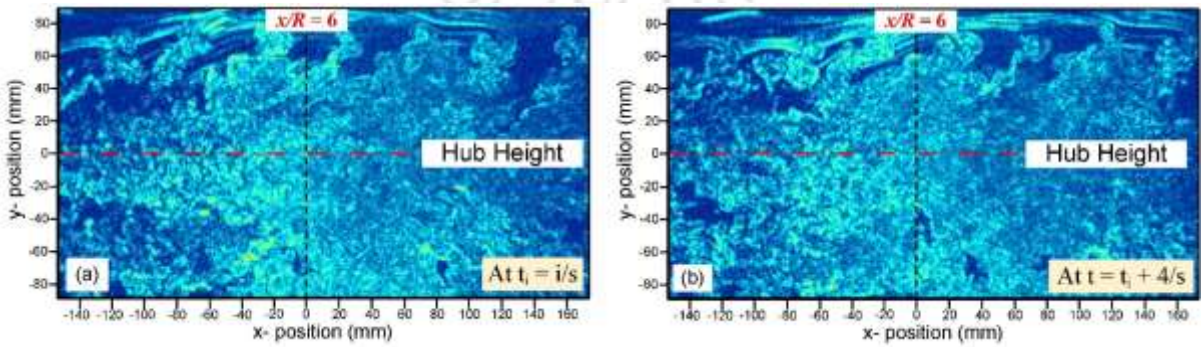

Figure 7.17 Illustration of particle concentration at (a) t = t_i = i/s, and (b) t_i + 4/s

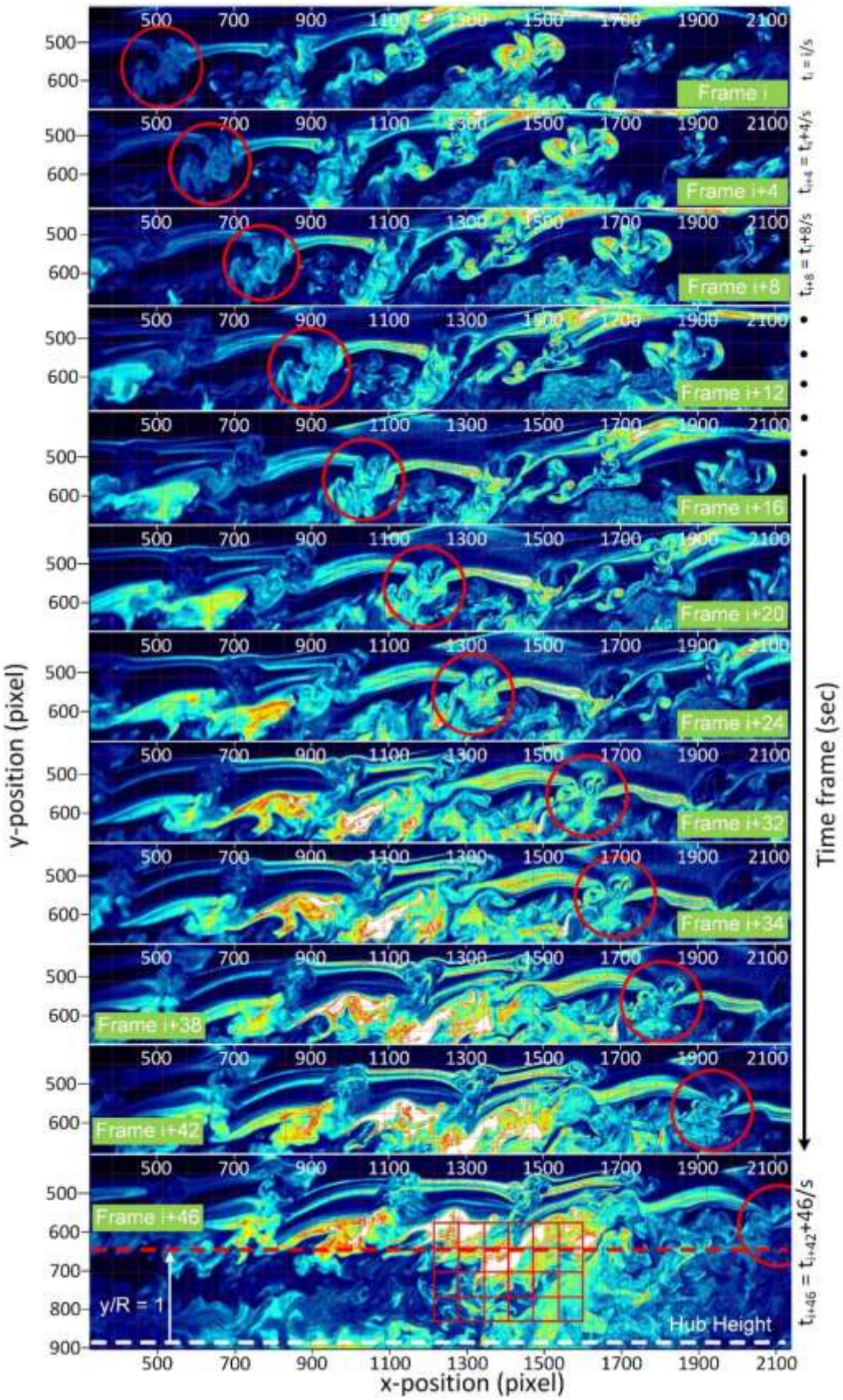

Fig. 7.18. Illustration of tip vortex mapping and tracking at λ = 2.11

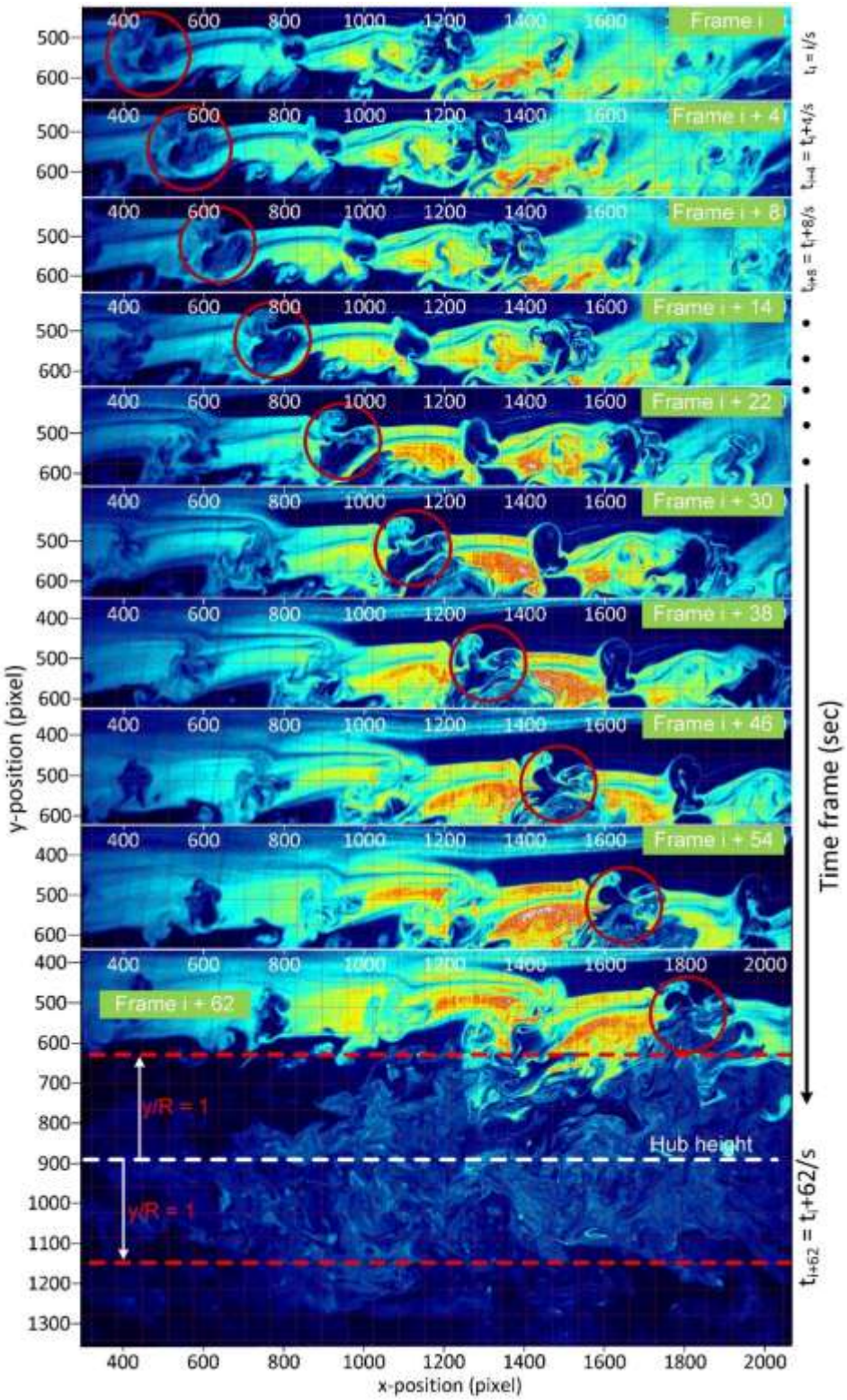

Fig. 7.19. Illustration of tip vortex mapping and tracking at $\lambda = 2.50$

Although the tip vortex signature can be synchronized with the rotational characteristics of the rotor blade, its precise contribution to understanding the flow movement is not soo certain. Thus, it is necessary to find a unique signature field from the respective component to address the moment of wake in a time-varying response at any position. This, along with the relative

velocity (V_{rel}), can be employed to signify the relative motion between the sublayers of the wind turbine. Based on stereo PIV assessment, the downstream wake can be discussed into different sublayers with their relative field (Fig. 7.20a). And, with the help of the velocity vector field, characteristics of the sublayer can be expressed as per Fig. 7.20(b).

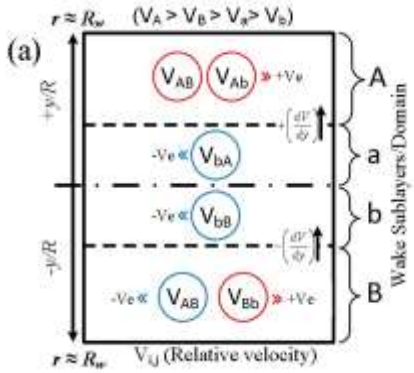

(b) Vector field analogy of velocity components

V_x	V_y	V_z	Flow Analogy
+	+	+	Into-the-plane streamwise flow & Upwash
+	+	-	Out-of-the-plane streamwise flow & Upwash
+	-	-	Out-of-the plane streamwise flow & Downwash
+	-	+	Into-the-plane streamwise flow & Downwash
-	-	-	Out-of-the-plane streamwise reverse flow & Downwash
-	+	+	Into-the-plane streamwise reverse flow & Upwash
-	-	+	Into-the-plane streamwise reverse flow & Downwash
-	+	-	Out-of-the-plane streamwise reverse flow & Upwash

Fig. 7.20. Illustration of (a) downstream wake sublayer, and (b) flow field analogy

10.2.4 Summary of the Study

The intent of this study is to extract the downstream flow field characteristic of wake dissipating from a small wind turbine (SWT). To determine the underlying flow characteristics of the wind turbine wake at different downstream locations (x/R), a dedicated stereo PIV mapping at low λ conditions has been carried out. Thereupon, wake analysis has been performed to triangulate the three velocity components (V_x, V_y, and V_z) with the velocity deficit and the helical vortex analogy. Following are some of the key findings.

- At x/R = 6, the time-resolved scatter distribution and the time-averaged velocity profile (V_x) has a Gaussian-like distribution. However, profile becomes much stepper at high at x/R > 14.
- Time-averaged velocity profile (V_x) is asymmetric in nature due to the presence of nacelle and the vertical support structure.
- It is noted that velocity deficits are relatively low at higher λ, and maximum close to λ = 2.5, which apparently, is also the optimal condition of the model rotor. This leads to an analogy that perhaps; one can expect the maximum deficit when the rotor is operating at or close to the rotor design condition.
- The observation indicates that at about 9D and beyond, one can expect about 70 – 80% flow recovery.
- Beyond y/R > 1.2, the value of η_x is slightly higher, suggesting increment in V_x, which is due to the influence of ambient flow, apart from the helical motion influence.
- At x/R = 6, the assessment of V_z velocity reveals two distinct opposite crests towards the upper and lower half of the wake field. And the stereo vector field study suggests such pattern is due to the out-of-the-plane and into-the-plane movement of wake.

CHAPTER 8

SPIRAL POLAR PLOT ANALOGY TO DICTATE THE TWO-DIMENSIONAL DEPICTION OF HELICAL VORTEX LINES (HVLS)

8.1 Introduction

The characteristics of wake propagation from any rotating blade or propeller have unique characteristics when examined under different fields of view and flow conditions. The generic representation of any rotating rotor and its wake propagation is expressed and perceived as the wake dissipating from the blade tip, often known as the rotor blade tip vortex (Vermeer et al. 2003). Such representations are three-dimensional and have a uniform and symmetric configuration unless there are some obstructions. In general, the downstream flow field of the rotor wake is distinguished into the near wake and far wake regimes, which are differentiated based on their stability and integrity of the helical vortex ring (Steven and Meneveau, 2017). The most common analogy of such description is associated with the wind turbine wakes, where the near wake regimes are described as the regime of a stable helical pattern. The infield flow behaviour can be associated with the rotor's geometric and aerodynamic characteristics (Whale et al. 2000; Grant and Parkin, 2000). The extent of the near wake regime is often discussed till $x/R < 6$. On the other hand, the far regime is the field of instability, and at these regimes, the helical vortex structure starts dissipating, and the confluence of the vortex core with the ambient flow is highly encountered (Massouh and Dobrev, 2007). The near wake flow behaviour is also associated with the turbine's performance characterization and its relation with the aerodynamic behaviour of the blade (Sørensen et al. 2014; Zhang et al. 2019). Thus, there is a need to make a quantitative as well as a qualitative narrative of the near wake geometry. The near wake identification can be made through visual interpretation, such as through flow visualization of the stable helical vortex ring and from the flow field mapping. The latter is helpful in acknowledging the velocity deficit and the momentum loss due to the rotor. In any case, it is imperative to relate the nature of the vortex pattern with the geometric configuration. The depiction of the helical vortex is often carried out by the flow visualization approach, such as through PIV using the seeding particles under highly seeded conditions. The laser sheet is fired on the section of interest to examine the content. The temporal and spatial depiction of the captured images from the PIV presented in Chapter 7 can be ensembled to generalize the full 2D or 3D structure of the propagating wake. Furthermore, since the PIV output is temporal based, it is quite handy to extrapolate the subsequent pattern of recognition. Thereby, one will be able to dictate the unique nature of the wind turbine wake. However, in the 2D PIV assessment, the capture images do not produce or represent the full 3D helical structure of the wind turbine wake, and thus, it is not easy to perceive or recognize the

subsequent pattern. Figure 8.1(a) illustrate the 3D depiction of helical vortex ring. A full 2D depiction of the helical vortex ring can be intuited from the helical vortex lines (HVLs), when the laser is fired close to the rotor blade tip. The HVLs are the pattern of vortex shedding from individual blades, as shown in Fig. 8.1(b). But, the actual pattern of the helical vortex ring cannot be directly interpreted merely with the 2D depiction of HVLs, which in fact, as discussed, are the sequence of vortex shedding from the individual rotor blade. Thus, for some, it may seem difficult to interpret exactly the helical cycle of wind turbine wake just from the 2D PIV images of HVL. To overcome this issue, an illustrative method has been adopted, which is the combination of HVLs sequence, spiral analogy, and polar co-ordinates, named spiral polar plot (SPP).

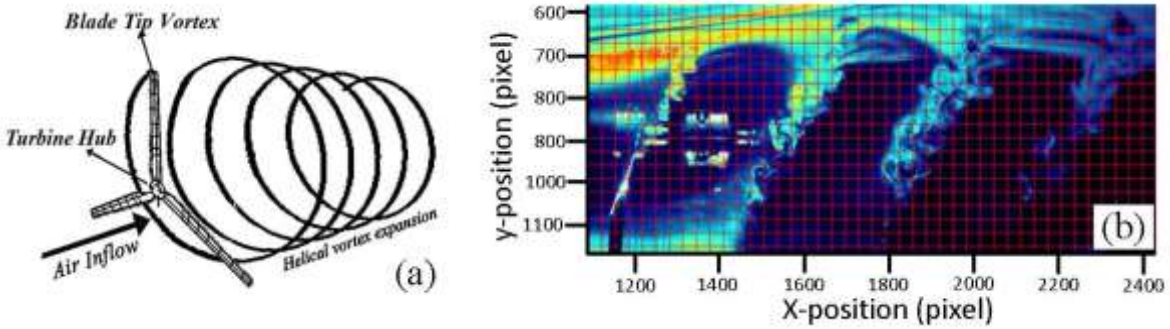

Fig. 8.1 Illustration of (a) helical vortex ring, and (b) 2D depiction of helical vortex lines (HVLs).

8.1.1 Background of The Analogy

The background of the present study is associated with the flow field assessment and flow visualization of the wind turbine wake close to and within the vicinity of the helical vortex core. The precise knowledge of such a study has a significant implication in the wind turbine blade design and wind farm modelling. Although initially, the investigation was indented for an in-depth flow field mapping of the turbine wake under different inflow, geometric, and tip-speed ratio conditions, the output of the flow surrounding the subsequent blade passage depicted a sequence of HVLs. These HVLs, as discussed, are 2D in nature and have an intrinsic relationship with the helical vortex pattern and the estimation of the wake propagation. It has been noted that the sequence of HVLs is repetitive after every revolution and, therefore, shows a distinct identity within the near wake regime. It can thus be triangulated with the HVL sequence, helical cycle, and the position of the HVLs, where the latter can be expressed in terms of the azimuthal angles.

A unique approach is needed to represent the HVL sequence, and its relation with the rotor wake dynamic, as the two events do not fit under the classical approach. The illustration of the HVLs using the PIV system is an indirect 2D description of the 3D helical vortex ring. In this

study, the PIV visualization data presented in Chapter 7 has been used to associate the cyclic nature of the wake, as well as with the sequence of the HVL, the position of HVL, and its period/shift. Thus, the first thing required is a spiral pattern to represent the expanding wake; here, the concept of a nautilus shell comes into the picture. The nautilus is a sea creature that can create a geometrically impeccable shell to shelter itself inside, as shown in Fig. 8.2(a). As the nautilus matures, it leaves behind vacated chamber with a new septum, and in the process (Tinello, et al. 2016; Liang et al. 2021), it creates a spiral geometry which can be expressed as a logarithmic spiral (Fig. 8.2b). The circle of the nautilus shell is not uniform in nature, as its periphery increases with the radial position and with every cycle; thus, it can be intuited as evolving helical wake. However, as per our requirement, there is also a need for sequence and repeated events, such as the metamorphosis of the butterfly (Truman, 2019), as shown in Fig. 8.2(c). The life cycle events of butterflies and moths can be associated with the nautilus spiral or logarithmic spiral as a sequential omnidirectional event, as shown in Fig. 8.3(a). However, it is required that all the events are closely related; so that they all can be arranged and associated with a single spiral (Fig. 8.3b). Thus, after any number of cycles or time periods, or phases, one can triangulate the number of events happened so far and sequence of events that have occurred. More details of the analogy have been discussed in section 3.

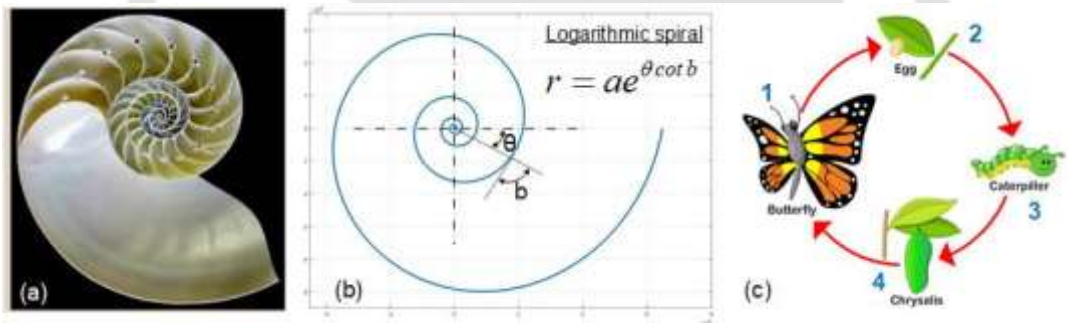

Fig. 8.2. Illustration of (a) Nautilus shell, (b) 2D geometry of Nautilus shell, and (c) metamorphosis/life cycle of butterfly (Tinello, et al. 2016; Liang et al. 2021)

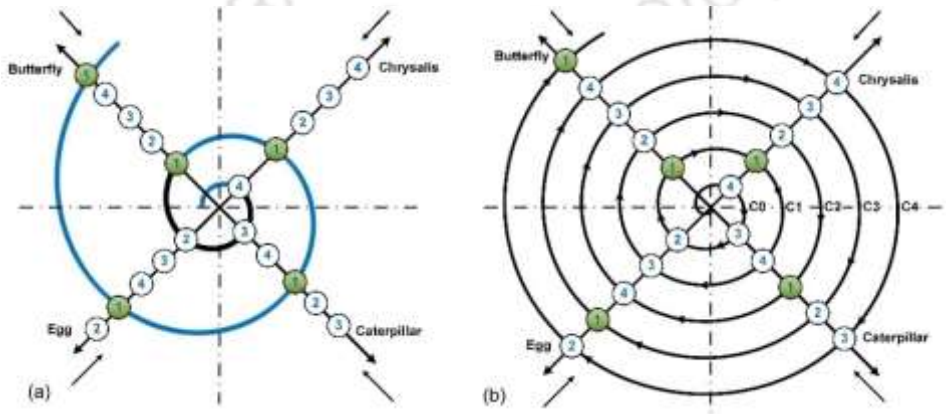

Fig. 8.3. Illustration of (a) four phases of metamorphosis in nautilus spiral, and (b) combined representation of metamorphosis in continuous polar spiral and nautilus spiral.

The concept of the spiral model or related analogy has also found its applications in the field of academics (Veladat and Mohammadi, 2011; Harden and Stamper, 1999), economics (Ashby et al. 2019), biomedical/healthcare research (Thomson, 2018), and others. Most of such concepts are simple and unique in the approach, and these techniques rely on the sequence of events, such as the spiral model, which is often used in academic curriculums to adjust or arrange specific events related to time, objectives, process, and others. However simple, the models describe are not favourable for adjusting the sequence of events which carries variability and uniqueness with reference to the spatial and temporal field. The spiral patterns are helpful in generalizing the events and expressing the same in involute forms, such as in the case of machine design, architectural mapping, and navigation (Liu and Huang, 2011; Sellamuthu et al. 2020).

In light of the analogy adopted to predict and dictate the sequence of events from the wake propagation and its relation with the rotor geometry and wake characteristics. This work proposes a method to estimate the characteristics of HVLs through pixel discretization of the sample images obtained through PIV system and, thereby, sequence recognition of the HVLs with respect to the temporal and spatial field can be carried out.

8.2. Representation of HVLs Sequence Using Spiral Polar Plot (SPP)

The HVLs captured by the PIV are basically a 2D description of the helical vortex ring dissipating from the blade tip. But, the actual pattern of the helical vortex ring cannot be directly interpreted merely with a 2D depiction of HVL, which in fact, as discussed, is the sequence of vortex shedding from the individual rotor blade. Thus, for some, it may seem difficult to interpret the helical cycle of wind turbine wake from the 2D PIV images of HVL.

To overcome this issue, an illustrative method has been developed, which is the combination of HVLs sequence, spiral analogy, and polar coordinates, named spiral polar plot (SPP). The HVLs generated by the individual blades are represented through coloured spheres as B1, B2, B3, … and so on for the blade 1, blade 2, blade 3, … and so on, respectively. These coloured spheres are arranged along the reference position of individual blades (P1, P2, P3, … and so on) with respect to the reference cycle (C0). The helical vortex ring of the rotor wake is presented as a combination of spirals, where any individual spiral marks the beginning of HVL sequence from their respective blade. A typical representation of three spirals from three rotor blades (B1, B2, and B3) is shown in Fig. 8.4. It is to be noted here that, in every spiral cycle, as the spiral say moves from one polar position to another, so does the HVL spheres but the prior HVL sphere will be moved to the next cycle. A typical replica of HVLs replacement sequence for a three-bladed rotor in an SPP is illustrated in Fig. 8.5. The analogy of the

subsequent cycle sphere's replacement can be further understood from Table 8.1; the sequence shown in the table is with respect to the three, four, and six-bladed rotors. Furthermore, it can be observed from Fig. 8.4 that for all the three blades, even if separate spirals are created, a similar sequence is obtained, as seen for P1, P2, and P3, thus in our proposed methodology, only a single spiral is considered for all the cases. And finally, the polar coordinate (in deg.) dictates the angular position or azimuthal angle of the target blade tip vortex with respect to the first blade. Thus, the position of the polar coordinate of all the three cases will be different, as seen through Fig. 8.6 and Fig. 8.7, where DoW (direction of wake) represents the forward sequence of HVLs and FOV represent the field of view in which HVL formation is observed. The cycle C1, C2, C3, … indicates the spiral cycle, and C0 represents the initial reference cycle. It is important to note that the spiral cycle sequence should not be confused with the cycle of the helical vortex. However, one can note that a total of six spiral cycles will give one helical cycle, which can be represented as an involute (Fig. 8.7b). In general, the number of the spiral for a unit revolution will be equivalent to the number of blades.

Table 8.1. Represents the sequence of HVLs at different polar positions and rotor blades.

HVL sequence for **Three-bladed rotor**				
	Ref. cycle	Cycle		
Position	C0	C1	C2	C3
P1	B1	B2C1	B3C2	B1C3
P2	B2	B3C1	B1C2	B2C3
P3	B3	B1C1	B2C2	B3C3

Position of HVL for **Four-bladed rotor**					
Position	Ref. cycle	Cycle			
	C0	C1	C2	C3	C4
P1	B1	B2C1	B3C2	B4C3	B1C4
P2	B2	B3C1	B4C2	B1C3	B2C4
P3	B3	B4C1	B1C2	B2C3	B3C4
P4	B4	B1C1	B2C2	B3C3	B4C4

HVL sequence for **Six-bladed rotor**							
	Ref. cycle	Cycle					
Position	C0	C1	C2	C3	C4	C5	C6
P1	B1	B2C1	B3C2	B4C3	B5C4	B6C5	B1C6
P2	B2	B3C1	B4C2	B5C3	B6C4	B1C5	B2C6
P3	B3	B4C1	B5C2	B6C3	B1C4	B2C5	B3C6
P4	B4	B5C1	B6C2	B1C3	B2C4	B3C5	B4C6
P5	B5	B6C1	B1C2	B2C3	B3C4	B4C5	B5C6
P6	B6	B1C1	B2C2	B3C3	B4C4	B5C5	B6C6

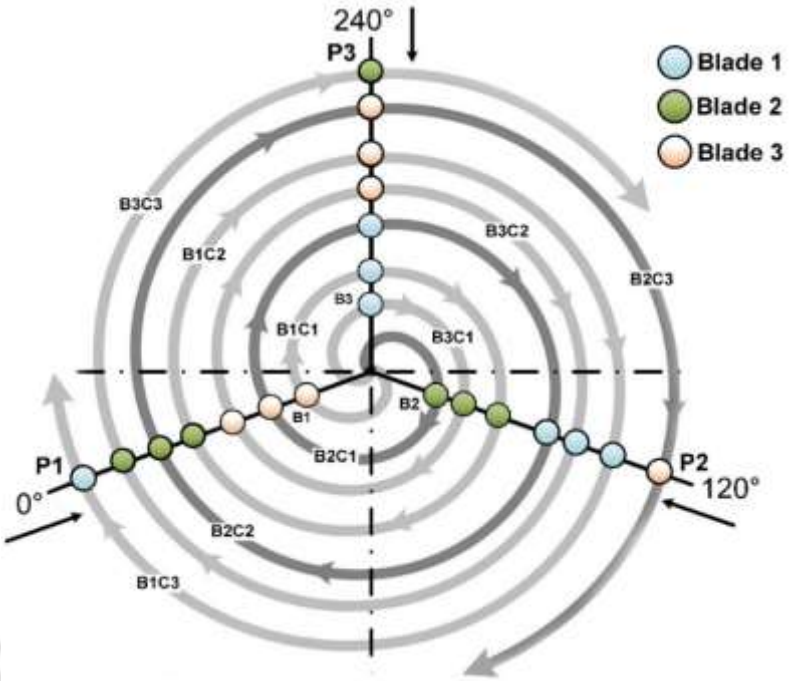

Fig. 8.4. Helical polar plot presentation of 2D helical vortex line of three-bladed rotor with individual rotor blade spiral.

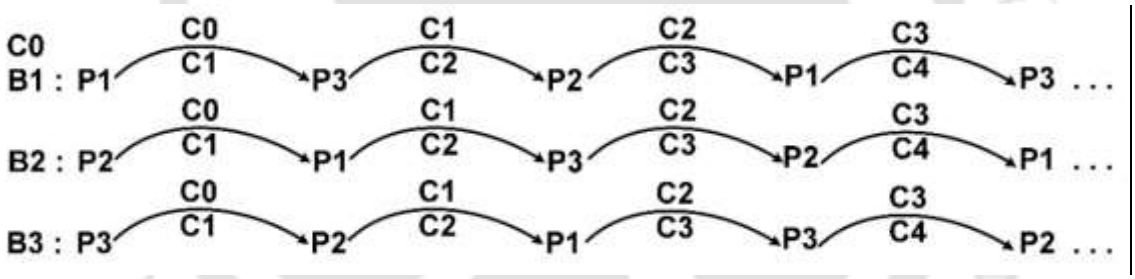

Fig. 8.5. Illustration of replacement sequence in SPP for three bladed rotors

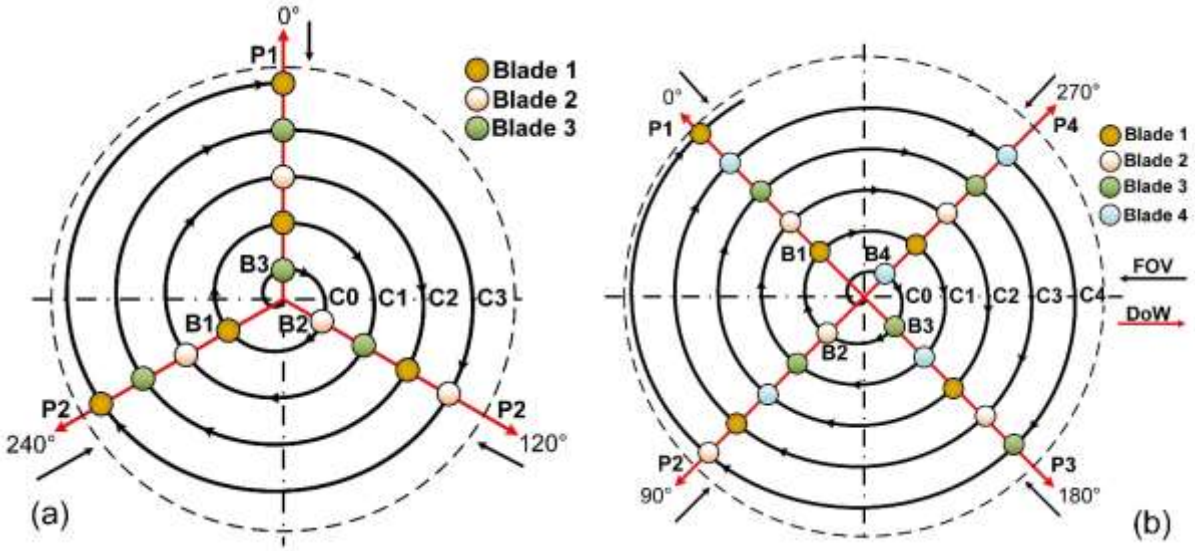

Fig. 8.6. Helical polar plot presentation of 2D HVL (a) three-bladed rotor, and (b) four-blade rotor with first rotor blade spiral.

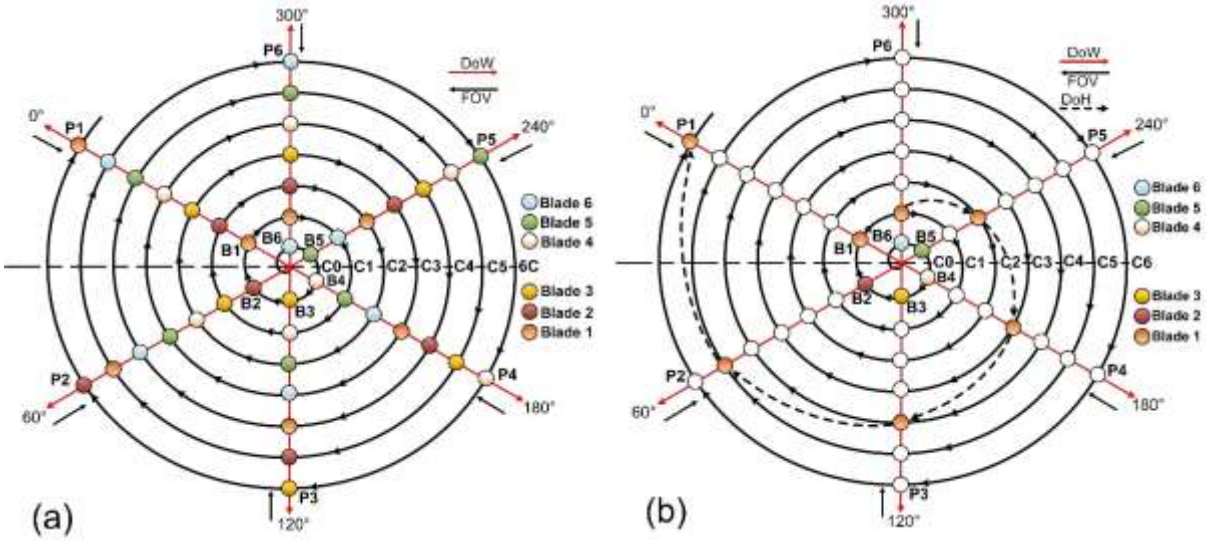

Fig. 8.7. Helical polar plot presentation of 2D HVL of (a) six-bladed rotor with first rotor blade spiral, and (b) comparison of spiral cycle and helical cycle.

The sequence of 2D HVLs obtained from PIV imaging thus can be expressed as a coloured spherical pattern for each polar-coordinates, which will repeat after every helical cycle. An example of HVL sequence for the three, four, and six-bladed rotor is shown in Table 8.2. It is interesting to note that, as the number of blades increases, a diagonally distinct coloured pattern is obtained. A further distinct cyclic pattern is obtained when a higher number of the helical cycle or revolution is considered, as indicated in Table 8.3. Thus, with reference to any polar coordinate or azimuthal angle (Eriksen and Krogstad, 2017), and under a specific time period, one can easily express the sequence of HVLs that will propagate along the streamwise direction using the spiral polar plot (SPP). The methodology proposed here can have numerous applications as long as there is a sequence of events involving dependability, functionality, and consistency. It can be utilized in the biological cycle interpretation (e.g., life cycle, food chain, and others), object prioritization (e.g., transportation, construction, and others), economics, and others. The authors do not claim at this point that the methodology would work for any cyclic events; however, certainly, the methodology proposed has its unique nature of sequence interpretation. The general description of HVLs sequence at any polar position and for a unit helical revolution can be expressed as per Eq. (1). The sequence constraint of the expression Eq. (8.1) is $1 \leq K \leq n$; however, if $K > n$ or $K = n + C$, then the sequence to be considered is $K = C$.

$$K_{i,j} = C0_i + (n - Cj) \tag{8.1}$$

where, $C0_i$ is the reference cycle element and Cj is the cycle number

i = Ref. blade number, j = 1,2,3, … n, and n = number of blades

Table 8.2 Representation of 2D HVL sequence for a rotor with different blade number

(a)Three-bladed HAWT HVL sequence	
Position	2D HVL sequence
P3 (240°)	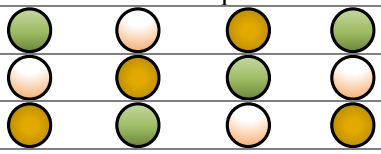
P2 (120°)	
P1 (0°)	

(b) Four-bladed HAWT HVL sequence	
Position	2D HVL sequence
P4 (270°)	
P3 (180°)	
P2 (90°)	
P1 (0°)	

(c) Six-bladed HAWT HVL sequence	
Position	2D HVL sequence
P6 (300°)	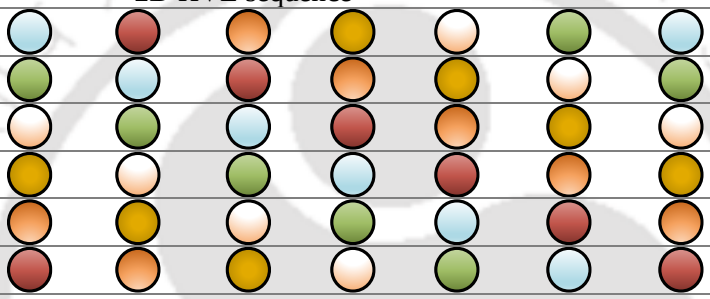
P5 (240°)	
P4 (180°)	
P3 (120°)	
P2 (60°)	
P1 (0°)	

Table 8.3 The identification of HVL sequence along a given polar position and cycle.

Six-bladed HAWT **HVL sequence**																		
Spiral cycle	C0	C1	C2	C3	C4	C5	C6	C7	C8	C9	C4	C5	C6	C1	C2	C3	C4	C5
Position	2D HVL sequence																	
P6 (300°)																		
P5 (240°)																		
P4 (180°)																		
P3 (120°)																		
P2 (60°)																		
P1 (0°)																		
	1st helical cycle/revolution							2nd helical cycle/revolution						3rd helical cycle/revol.				

From the above discussion, it is indeed interesting to acknowledge the beauty of SPP analogy in representing the HVLs into a simpler and intuitive form. Throughout the methodology discussed, it is realized that the SPP will only work if there is some sequence of events. Thus, with regard to the wind turbine wake, the only possible parameters that could possibly be linked with the analogy is the associated parameters of the wind turbine helical vortex ring and in this case, it will be the PIV characteristics of HVLs. The parameters that can be associated with the analogy are the HVL streamwise velocity, pitch, slope of HVL, and others. For example, the

HVLs velocities with respect to different azimuthal angle and cycle for a three-bladed rotor can be presented as per Table 8.4(a); where, the shaded velocity represents the velocity of HVL dissipating from blade B1. And for n-number of rotor blade, the velocity of HVL can be presented as per Table 8.4(b); similar matrix can also be formed for other associated parameters. These parameters in the present study has been obtained with the help of PIV system; such parametric analogy is part of the future work plan. Now, once the values are obtained with respect to different cycle (temporal) and position (spatial), and the corresponding matrix can be generated. Thereby, one can directly link the same with the SPP model; it will be possible to associated the characteristics of the wake at the given λ, U, β, and Re conditions.

Table. 8.4. The identification of HVL velocity and their sequence in SPP.

(a) **Three-bladed** HAWT HVL sequence													
Spiral cycle	C0	C1	C2	C3	C4	C5	C6	C7	C8	C9	C10	C11	C12
Position	Velocity of HVL												
P1	$V_{1,0}$	$V_{1,1}$	$V_{1,2}$	$V_{1,3}$	$V_{1,4}$	$V_{1,5}$	$V_{1,6}$	$V_{1,7}$	$V_{1,8}$	$V_{1,9}$	$V_{1,10}$	$V_{1,11}$	$V_{1,12}$
P2	$V_{2,0}$	$V_{2,1}$	$V_{2,2}$	$V_{2,3}$	$V_{2,4}$	$V_{2,5}$	$V_{2,6}$	$V_{2,7}$	$V_{2,8}$	$V_{2,9}$	$V_{2,10}$	$V_{2,11}$	$V_{2,12}$
P3	$V_{3,0}$	$V_{3,1}$	$V_{3,2}$	$V_{3,3}$	$V_{3,4}$	$V_{3,5}$	$V_{3,6}$	$V_{3,7}$	$V_{3,8}$	$V_{3,9}$	$V_{3,10}$	$V_{3,11}$	$V_{3,12}$
	1^{ST} rev.					2^{nd} rev.				3^{rd} rev.			4^{th} rev.
(b) **n-bladed** HAWT HVL sequence													
Spiral cycle	C0	C1	C2	C3	C4	C5	C6	C7	C8	•	•	•	Cn
Position	Velocity of HVL												
P1	$V_{1,0}$	$V_{1,1}$	$V_{1,2}$	$V_{1,3}$	$V_{1,4}$	$V_{1,5}$	$V_{1,6}$	$V_{1,7}$	$V_{1,8}$	•	•	•	$V_{1,n}$
P2	$V_{2,0}$	$V_{2,1}$	$V_{2,2}$	$V_{2,3}$	$V_{2,4}$	$V_{2,5}$	$V_{2,6}$	$V_{2,7}$	$V_{2,8}$	•	•	•	$V_{2,n}$
•	•	•	•	•	•	•	•	•	•	•	•	•	•
•	•	•	•	•	•	•	•	•	•	•	•	•	•
Pn	$V_{n,0}$	$V_{n,1}$	$V_{n,2}$	$V_{n,3}$	$V_{n,4}$	$V_{n,5}$	$V_{n,6}$	$V_{n,7}$	$V_{n,8}$	•	•	•	$V_{n,n}$
	1^{st} helical cycle/revolution												

8.3 Summary of the Study

In this work, a unique methodology has been introduced that combines the HVL sequence, helical/spiral analogy, and polar co-ordinates reference, thus named as spiral polar plot (SPP). Using SPP, one can easily define the sequence of HVLs at any given polar coordinate position and with respect to blade position. The methodology dictates the nature of HVLs pattern in recognition with the depiction of wake propagation.

Though the work presented in this chapter does not involved quantitative analysis, it does open an opportunity to triangulate the PIV data. In the future work, the SPP analogy will be explored by incorporation the time and spatial distinction of HVLs.

CHAPTER 9
MODELLING AND ESTIMATION OF HORIZONTAL-AXIS WIND TURBINE WAKE THROUGH DATA-DRIVEN APPROACH

9.1 Introduction

Maintaining an optimum wind farm efficiency is one of the critical aspects of wind energy developers, which has gained significant interest among the research communities over the years. The key challenges in the path of wind farm modeling are the stochastic and variability in the wind turbine wake. Different analytical wake models have evolved over the years to comprehend such a wake propagation process.[1,2] Assessment by analytical wake models comes from the fact that the turbines in the array/cluster are subjected to different sources of aerodynamic loadings. These loading can be discretized into the wind turbine wake, atmospheric boundary layer, inflow turbulence, and others. Several wind turbine wake models have been proposed, some of which are the legacy of Jensen, Larsen, Lissaman, Frandsen, and Ainslie's wake models, a detailed review is presented in Chapter 2. Despite their robustness, the analytical formulations of these models are widely explored as research tools for estimating the performance of wind farms. However, these models often overestimate the flow characteristics because of several limitations and assumptions like top-hat shape, Gaussian profile, axisymmetric, negligible atmospheric boundary layer effect, and others (Vermeer et al. 2003; Steven and Meneveau, 2017). In view of this, there is always a scope for developing better correlations to predict the performance of wind farms more accurately.

In recent times, data-driven assessment is finding significant applications to solving complicated problems. In continuation with Chapter 8 that has showcased the SPP analogy using the SPIV flow visualization. In this study, a machine learning (ML) based wake model is developed to estimate the wake propagation using the SPIV time-resolved data presented in Chapter 7. The presented model can reproduce the velocity, velocity deficit, and turbulence fields of the turbine wake using the high-fidelity stereo particle image velocimetry (PIV) data. Driven by a substantial PIV simulation dataset presented in Chapter 7, the inherent relationship between inflows and wake flows is established using the Artificial Neural Networks (ANN) technique based on the back-propagation algorithm. Derived from the concept of the human nervous system, the analogy of ANN uses 'Neurons' as a fundamental building block. These neurons are ensemble as input, hidden layer/layers, and output layers, which are interconnected with the help of weight and biases, and the relationship between the layers is achieved using the transfer function (Haykin, 2009). The ANN techniques can build a wake deficit or power generation model by examining the phenomenon in data instead of integrating information

about the physical conduct of wind turbines (Sun et al. 2020; Ti et al. 2021). Kusiak et al. (2009) established a model to forecast the power of wind farms by applying a data mining approach based on the k-nearest neighbour method and suggested a data-driven approach as a reliable source. After employing the ANN tool, Fischer et al. (2017) pointed out that for a specific wind farm, the method of using actual local wind information input is the best, and the method of using the average data to stimulate meteorological wind forecasting may not be effective. Yan et al. (2019) trained a geometric model-artificial neural network using an offshore wind farm observation dataset. A two-dimensional power curve was presented to estimate the power generation of a wind farm by using wind speeds and wind directions. A recent review article by Zehtabiyan-Rezaie et al. (2022) outlined the fundamental factors that governed the wind-farm flow modelling, which is purely based on a data-driven approach. The study mentioned the complexity, interpretability, and generalization that may constitute power prediction of wind turbines in a wind farm. Wind farm control has recently become an active research area based on wind turbine power modeling. Maximum power point tracking is a commonly used strategy in which each wind turbine continuously adjusts the rotor speed and pitch angle to reach its maximum power coefficient at any wind speed and in any wind direction. To date, studies on wake control are very limited due to the lack of relatively accurate data and effective models to predict the power generations of multiple turbines such as wind farms.

To date, studies on wake control are very limited due to the lack of relatively accurate and effective models to predict the power generations of wind farms. In this study, firstly, the ANN method and the SPIV data measured from a wind tunnel (Chapter 7) are applied to build an ANN-wake model. The case study has been structured as follows. In section 9.2, the ANN methodology adopted to build the wake model has been described, whereas section 9.3 highlight the classical analytical wake model to represent the velocity deficit has been described. Section 9.4 presents the results, which have been described into two parts- the first part presents the wake modelled through ANN methodology. The ANN predicted-results are then compared with the analytical model and low λ studies in the second part.

9.2 Artificial Neural Network Methodology

The ANN makes use of transfer function to map input (X) data with the output (Y) data without any necessary physical assumption relationship between X and Y (Haykin, 2009). However, once a well-trained ANN model is established between X and Y, one can make a conclusive remark between the parameters with prior knowledge of their physical characteristics. The main anticipated objective of the ANN wake deficit model is to estimate the downstream velocity profile of the wind turbine wake at different tip speed ratio (λ) conditions. The

assessment has been carried out for the far wake regime; thus, input data are extracted from the far wake. The model can be deployed by six steps. Fig. 9.1 demonstrates the process of the model development. The input data for the present study are the time-resolved PIV data, and the velocity parameters invoked are averaged with respect to the number of frame (fps) count. Details on PIV assessment methodology and data processing analogy has been comprehensively described in Chapter 3, and related downstream velocity characteristics has been addressed in Chapter 4. Figure 9.1 shows the schematic of the ANN wake deficit model assessment layout for different datasets.

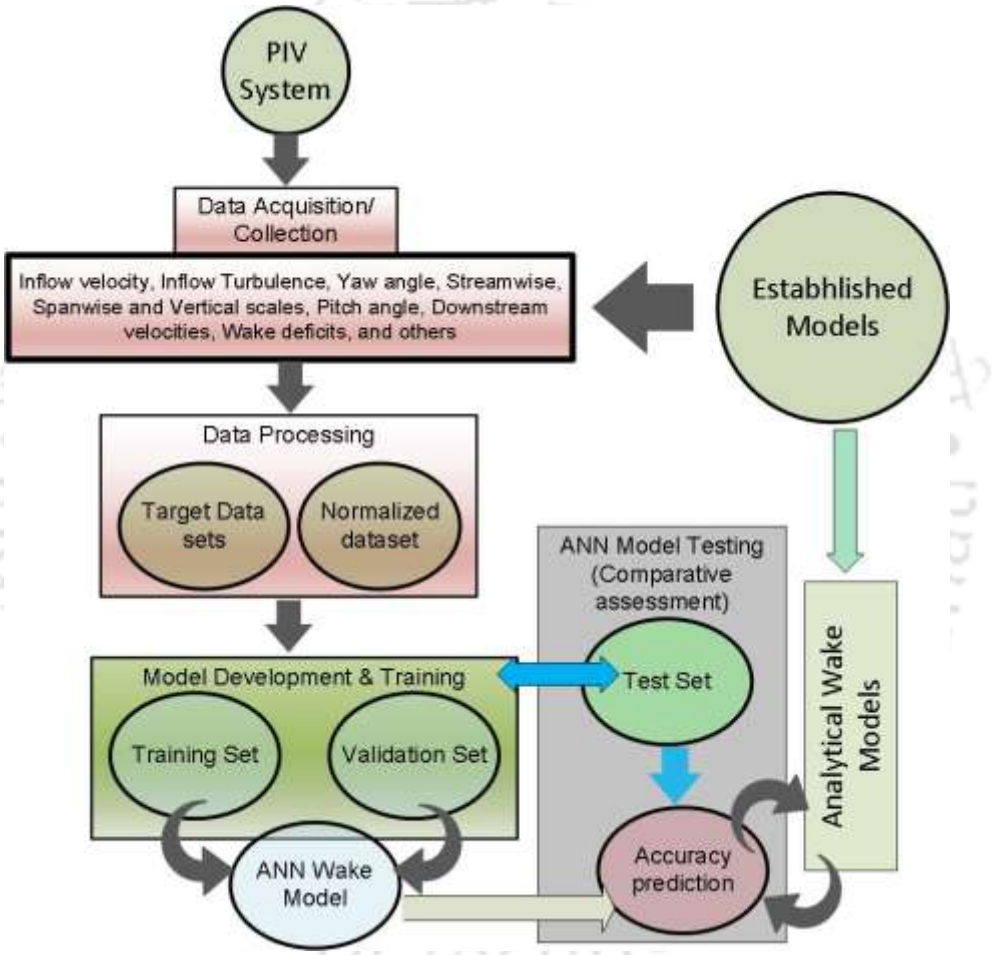

Fig. 9.1 Flow chart of the ANN model development process

Once input data (x/R, y/R, λ, U) and target data (Vel. Def.) are set, the next step involved is the selection of the number of neurons, hidden layers, an output layer, and transfer function. The selection of characteristics of ANN variable is important in laying out of proper ANN network (Haykin, 2009). For the selection of the number of neurons and hidden layer, a statistical approach has been adopted, though one may also use some empirical relation between the hidden layer/neurons with the input/output variable presented in articles (Kavzoglu and Matter, 2003; Blanchard and Samanta, 2020). The relationship mentioned is robust and is not precisely

applicable for all the scenarios. That is why statistical approach has been adopted, which will be explained in the subsequent subsection. To carry out the objective, the MATLAB program-Neural Net Fitting tool has been used to generate the ANN model. Furthermore, using the MATLAB script tool, necessary model variability has been carried out. The input variable includes downstream location (x/R = 6, 10, 14, and 18), vertical mapping (-1.2 < y/R < 1.5), and tip speed ratio (λ = 2.11, 2.50, 2.60, and 2.61). A total of 16 sets with possible output parameters are shown in Table 1. The output variable may include normalized velocity (η), velocity deficit, and turbulent intensity (TI). The input data are divided into 70% of training data, 15% of validation data and 15% of test data, the choice of such data sharing for the training is noted to be favorable in several reported articles. (Kavzoglu and Matther, 2003; Kusiak et al. 2009; Blanchard and Samanta, 2020; Ti et al. 2021).

Table 9.1 Representation of Input and Output variables of wind turbine wake

	Input			*Expected Output*							
Variables	λ	x/R	y/R	η_x	η_y	η_z	η_V	*Vel. Def.* V_x	*Vel. Def.* V	TI_x	*Net TI*
Set 1	2.11	6									
Set 2	2.11	10									
Set 3	2.11	14									
Set 4	2.11	18									
Set 5	2.50	6									
Set 6	2.50	10									
Set 7	2.50	14									
Set 8	2.50	18									
Set 9	2.60	6									
Set 10	2.60	10									
Set 11	2.60	14									
Set 12	2.60	18									
Set 13	2.61	6									
Set 14	2.61	10									
Set 15	2.61	14									
Set 16	2.61	18									

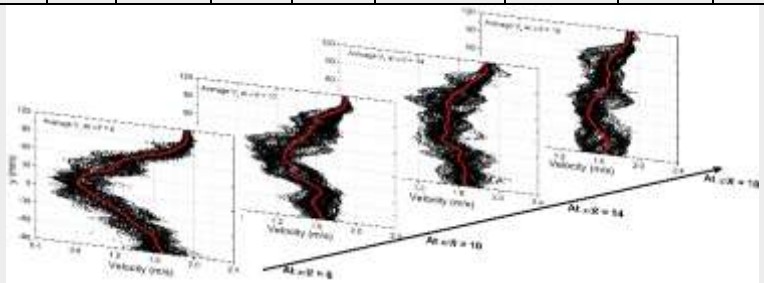

Scatter field data

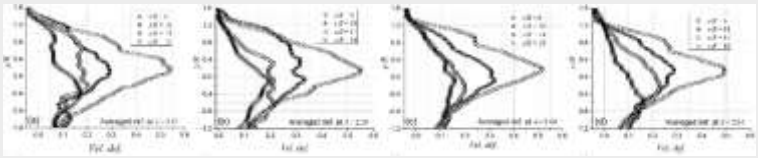

Averaged data

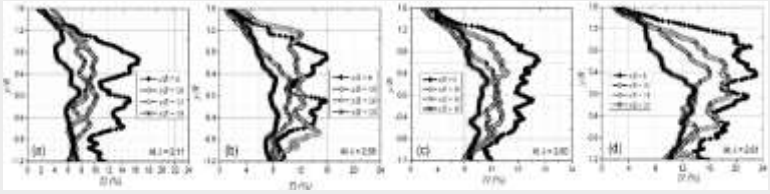

Turbulence intensity data

Since ANN is more of a trial and error approach, several combination of ANN models were formed and tested to arrive at a promising network that would help predict the wake propagation. However, to arrive at the desired network, a combination of single and double hidden layer with the number of neurons varying between 4 to 12 were examined. Although, the mostly used performance metric is the mean square error (MSE), as per Eq. (9.1). In this

study, to make a decisive argument, two more statistical analogies were adopted, this includes- sum squared error (SSE) and mean absolute error (MAE). SSE is expressed as a total deviation of the estimated value (Y_{est}) from the target value (Y_{tar}) as per Eq. (9.2), whereas, MAE is expressed as the average of absolute error in the estimation data, as per Eq. (9.3). It is to be noted that lesser the value of MSE, SSE, and MAE, better be the model response.

$$MSE = \frac{1}{k}\sum_{i=1}^{k}\left(\left(Y_{tgt}\right)_i - \left(Y_{est}\right)_i\right)^2 \tag{9.1}$$

$$SSE = \sum_{i=1}^{k}\left(\left(Y_{tgt}\right)_i - \left(Y_{est}\right)_i\right)^2 \tag{9.2}$$

$$MAE = \frac{\left(\sum_{i=1}^{n}\left|\left(Y_{est}\right)_i - \left(Y_{tgt}\right)_i\right|\right)}{k} \tag{9.3}$$

where, k is the number of estimated data points

Apart from the above-mentioned statistical ANN trend performance analogies, the value of the correlation factor or coefficient of determination (denoted by R^2) is also implemented to assess the ANN performance. A perfect input(target)-output(predicted) relationship is obtained when $R^2 = 1$; thus, one can say that the value of R^2 indicates the strength of the correlation between an independent (X) and a dependent variable (Y). The expression of the coefficient of determination is shown in Eq. (9.4).

$$R^2\left(Y,\hat{Y}\right) = 1 - \frac{\sum_{i=1}^{n}\left(Y_i - \hat{Y}_i\right)^2}{\sum_{i=1}^{n}\left(Y_i - \overline{Y}\right)^2} \tag{9.4}$$

In the equation, n is the number of variables; Y_i is the i^{th} observation of the response variable; $\hat{Y}_i$ is the value estimated by the regression function; $\overline{Y}$ is the mean value of the observation. The ANN training has been carried out with the Levenberg-Marquardt function (Marquardt, 1963), which is a back-propagation algorithm. This function optimizes the ANN model curve by reducing the sum of the squares of the deviation with that of the empirical dependent variable. The back-propagation algorithm follows an iterative adjustment of the weights (W) and biases (B), which is based on the error response between Y_{est} and Y_{tgt}. The stopping criteria in the training process are the number of iteration and error tolerance, which are represented as epochs and goals, respectively. Thus, the training stops when the minimum error or when the optimum

epoch is reached, here, the optimum epoch refers to the iteration at which MSE is the minimum. Different network configurations were constructed, and each configuration differs in the number of hidden layers and neurons. The number of neurons was gradually increased for both single or two-hidden layers, and the corresponding MSE, SSE, and MAE were then compared. Thereupon, the best neural network is selected for further assessment; Fig. 9.2 represents a typical ANN model with three input, a single hidden layer, and a single output. The hidden layer carries the number of assigned neurons. In the present study, various combinations of neurons and hidden layers were tested; however, the hidden layer has been restricted to a maximum of two layers. The associated transfer function for the hidden layer considered is "Tansig", whereas, towards the output layer, 'Purelin' transfer function has been employed, which helps generate a linear relationship. Apart from the transfer function, the activation function (φ) is an essential neural network entity; it helps the network decide which signals/data to pass on. This function also adds non-linearity to the network, which in return, makes complex tasks easier to learn. It works on some predefined offset value, and once that value is crossed, the signal is triggered; on the other hand, the transfer function is used to render the input to output signals. It computes the net weight of the neural network. It is to be noted that the transfer function also associates φ along with providing the output (Haykin, 2009). The detailed working procedure of ANN processing can be discussed in four steps, as mentioned below.

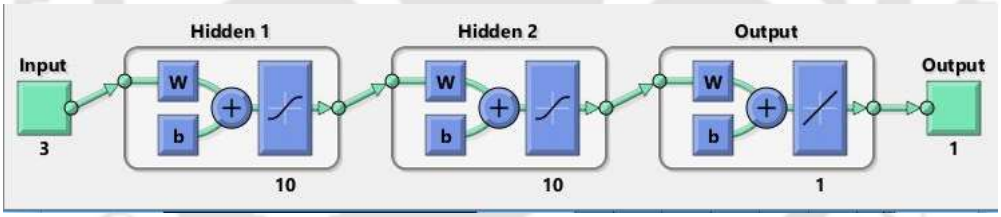

Fig. 9.2 Typical illustration of ANN model with three input, two hidden layer, and single output.

Step 1: Input layer- data normalization

The process is initiated with data normalization, where the scaling of both inputs and targets is kept in the range of 1 (highest) and -1 (lowest). The normalization process is carried out using the 'mapminmax' function, which is expressed as per Eq. (9.5).

$$Y = \frac{\left(Y_{max} - Y_{min}\right) \times \left(X - X_{min}\right)}{\left(X_{max} - X_{min}\right)} + Y_{min} \tag{9.5}$$

where Y is the normalized value of X, 'Y_{max}' is 1, 'Y_{min}' is -1, 'X' is the actual parameter of interest, 'X_{min}' is minimum value of interest, and 'X_{max}' is the maximum value of interest. Thus, the normalized input parameter in the present study are presented as $(x/R)_{nom}$, $(\lambda)_{nom}$, and $(y/R)_{nom}$.

Step 2: Hidden layer weight

The follow-up of input normalization is the ascription of weight (W) and biases (B), which are generated through a neural network. The corresponding relationship between the hidden layer output is a linear equation expressed as Eq. (9.6).

$$f_{l,i,n} = \sum_{i=1}^{j}\left(W_{l,i(x/R)} \times (x/R)_{nom,n} + W_{l,i,\lambda} \times \lambda_{nom,n} + W_{l,i(y/R)} \times (y/R)_{nom,n} + B_{l,i}\right) \quad (9.6)$$

where $W_{l,i(x/R)}$, $W_{l,i,\lambda}$, and $W_{l,i(y/R)}$ are the weights of input variable x/R, λ, and y/R corresponding to neuron (i) for the hidden layer 'l', '$B_{l,i}$' is the bias at hidden layer 'l' assigned to neuron (i), and 'j' to the number of neuron considered. The multiplying factors $(x/R)_{nom,n}$, $(\lambda)_{nom,n}$, and $(y/R)_{nom,n}$, are the nth value of $(x/R)_{nom}$, $(\lambda)_{nom}$, and $(y/R)_{nom}$, respectively. And finally, $f_{l,i,n}$ is the n^{th} sum of the weighted normalized variables associated with the i^{th} neuron for the hidden layer 'l'.

Step 3: Assignment of transferfFunction

The next essential step involves assigning a mathematical operator, and the mostly used is the 'Tansig' transfer function; known as tan sigmoid function, as per Eq. (9.7). For 'z' number of hidden layers, there will be separate 'z' number of transfer function. Furthermore, each hidden layer may or may not be initialized with the same activation function (Haykin, 2009).

$$Tan\,sig(\ for\ f_{l,i,n}) = F_{l,i,n} = \frac{2}{\left(1+exp\left(-2f_{l,i,n}\right)\right)} - 1 \quad (9.7)$$

Step 4: Output layer- weight and transfer function

In this step, towards the outer layer, assignment of W and B are carried out, which are then express through some linear transfer function; the mostly used 'Purelin' transfer function has been employed in the final normalized output (a_o), as per Eq. (9.8).

$$a_o = \sum_{i=1}^{j}\left(W_{lo,i} \times F_{l,i,n}\right) + B_{lo} \quad (9.8)$$

where $W_{o,i}$ is the weight at output layer with respect to neuron 'i', and B_o is the output layer bias.

Step 5: Output/target generation through de-normalization

Finally, the actual estimated output is obtained by the de-normalization of the processed variables. The de-normalization is carried out using Eq. (9.5), where in this case, it will be expressed in term of 'X', instead of 'Y'.

9.3 Analytical Wake Models

The wake models primarily used in the wind farm layout design are based on the analytical wake models, which are mostly governed by momentum conservation analogies. Although it comes with several assumptions and constraints, they were widely explored in the past studies. For the present study, three analytical models are examined and compared with the experimental and ANN predictions.

Jensen Wake Model: Jensen (1983) developed a pioneering turbine-wake model, which has been extensively used in the literature and commercial software (e.g., WAsP, WindPRO, WindSim, Wind-Farmer, and OpenWind). The model assumed a linear variation of the downstream velocity deficit with a top-hat shape velocity profile, defined by Eq. (9.9).

$$Vel.\,def.\left(\frac{\Delta U}{U}\right)=\frac{U-U_d}{U}=\frac{1-\sqrt{1-C_T}}{(1+2k_w x/D)^2};\qquad U_d \text{ is the downstream velocity} \tag{9.9}$$

Where k_w is the wake expansion rate, its value is considered to be 0.075 and 0.04 for the onshore and offshore wind farm, respectively. Further details are mentioned in Chapter 2.

Frandsen Wake Model: It is a single wind turbine wake model proposed by Frandsen et al. (2006) and considers a cylindrical control volume having a cross-sectional area that is equal to the wake area. The velocity deficit (Eq. 9.10) in this model also considers axisymmetric and top-hat profile.

$$Vel.\,def.=\frac{1}{2}\left(1\pm\sqrt{1-2\frac{AC_T}{A_w(x)}}\right) \tag{9.10}$$

where A is the rotor swept area, and A_w is the wake area at downstream distance x. The relation '+' is considered when $0 \le C_T \le 0.75$, and '-' when $C_T \ge 0.75$. Further details are mentioned in Chapter 2

Bastankhah and Porté-Agel (B-P) Wake Model: The B.P wake model is proposed by Bastankhah and Porté-Agel, (2014), derived a Gaussian-like axisymmetric wake model defined by Eq. (9.11).

$$Vel.\,def.=\left(1-\sqrt{1-\frac{C_T}{8(\sigma/D)^2}}\right)\times exp\left(-\frac{1}{2}\left(\frac{D}{\sigma}\right)^2\times\left(\frac{r}{D}\right)^2\right) \tag{9.11}$$

where,

$$\frac{\sigma}{D}=k_w\left(0.5\frac{x}{R}\right)+\varepsilon$$

Thus, the B-P wake model will be defined by the standard deviation (σ) of the Gaussian function, characterized by downstream distance (x/R), wake expansion rate (k_w), and the linear intercept function (ε). It is noted that k_w increases with the inflow turbulence intensity (TI_x), which upon linear regression shows $k_w = 0.35TI_x$ (Bastankhah and Porté-Agel, 2014; Fuertes et al. 2017). Furthermore, using the measurement data, Fuertes et al. (2018) noted that the linear intercept function could be expressed as a function of the wake growth rate, as per Eq. (9.12)

$$\varepsilon = -1.91k_w + 0.34 \tag{9.12}$$

The relation for ε has been further explored by Ishihara and Qian, (2018), and Niayifar and Porté-Agel, (2016). They have also noted the dependence of ε on the inflow conditions, coefficient of thrust, and others; however, the empirical relation in Eq. (9.12) is found to be reasonably acceptable. Further details are mentioned in Chapter 2.

9.4 Results and Discussions

The applicability of ANN in the estimation and mapping of the downstream flow field has been explored in this work. This data-driven modelling is possible due to substantial amount of flow field data extracted using stereo particle image velocimetry (PIV). Input data for the ANN model comprises downstream location (x/R), vertical mapping (y/R), and the corresponding tip speed ratio (λ), whereas, the expected output data includes velocity deficit with respect to V_x, and resultant velocity (V_R). The wind turbine wake being three-dimensional in nature, constitutes V_x, V_y, and V_z components; however, the contribution of y and z-component are very less. Therefore, the dominating component V_x and the resultant velocity (V_R) have been considered for the ANN study. A comprehensive detail on the choice and significance of these parameters have been mentioned in Chapter 7. Finally, the predicted data using the ANN wake model are compared with the experimental and analytical models.

9.4.1 ANN Network Configuration

The intention of this work is to examine the different configurations of ANN models that would efficiently and effectively estimate the downstream flow field behavior of the wind turbine wake. Such examinations are necessary to arrive at a reasonable and reliable neural network since there can be an infinite combination of neurons, hidden layer, and output layer. However, to reduce the computational cost and time, the network combination of the number of hidden

layers and the number of neurons is limited to 2 and < 15, respectively, which produces reasonable and reliable results. The selection of the best network combination has been made based on respective error associated with the predicted output to the expected value, which in the present case is the velocity deficit of V_x and V_R. The three statistical performance criteria, namely MSE, SSE, and MAE, have been considered, the result of which is presented in Figs. 9.3 through Fig. 9.5. While looking at the network combination presented in Fig. 9.3, it can be seen that the MSE of 3-12-1 network combination has the minimum MSE. Furthermore, the value of MSEs is relatively higher with a double hidden layer. The case study is analogous even with separate and different output variables for the same input (Fig. 9.3b), which is close to 2 x 10^{-4}. The same network combination also shows lesser SSE, as shown in Fig. 9.4, and for either case, the value of SSE is close to 4. To further complement the favorable network combination, MAE analysis is also carried out, the result of which is shown in Fig. 9.5. Thus, for the given input and target data conditions, it is noted that a single hidden layer with twelve neurons produces a reasonable and reliable network model. The corresponding network training, validation, and testing result of 3-12-1 perceptron are shown in Fig. 9.6, and the post-training regression relationships between the target and estimated w.r.t deficit of V_x are presented in Fig. 9.7. Its regression result shows that the opted network combination learns better with the number of epochs, and shows relatively linear regression fit at 371 epochs. A similar outcome is noted while predicting the deficit w.r.t V_R (Fig. 9.8). Thus, matching the predicted output with the input target as intended, which is supported by a correlation coefficient (R) of about 0.993 for either case study. With this result, it can be agreed that the proposed ANN network mod performed well and produced a reliable outcome.

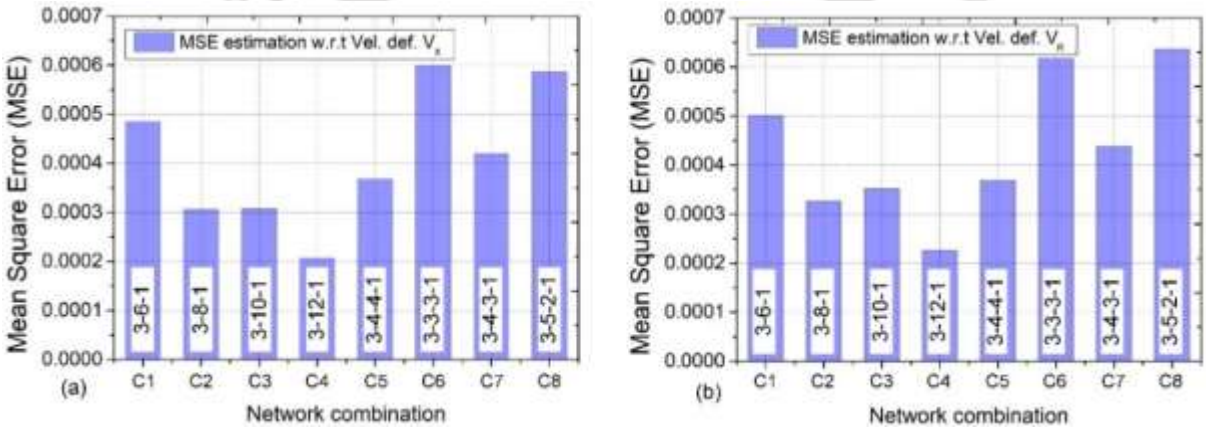

Fig. 9.3. Neural network performance assessment using MSE w.r.t (a) vel. def. V_x, and (b) vel. def. V_R

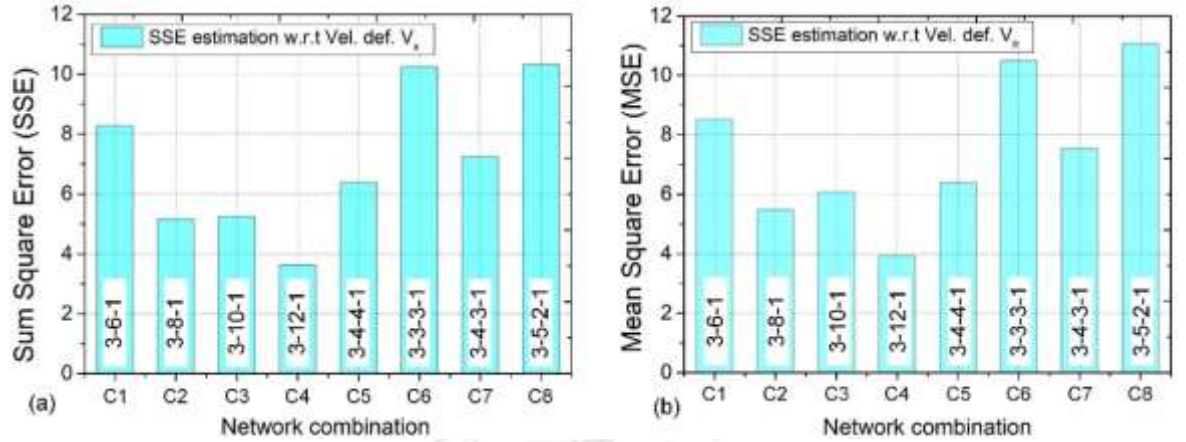

Fig. 9.4. Neural network performance assessment using SSE w.r.t (a) vel. def. V_x, and (b) vel. def. V_R

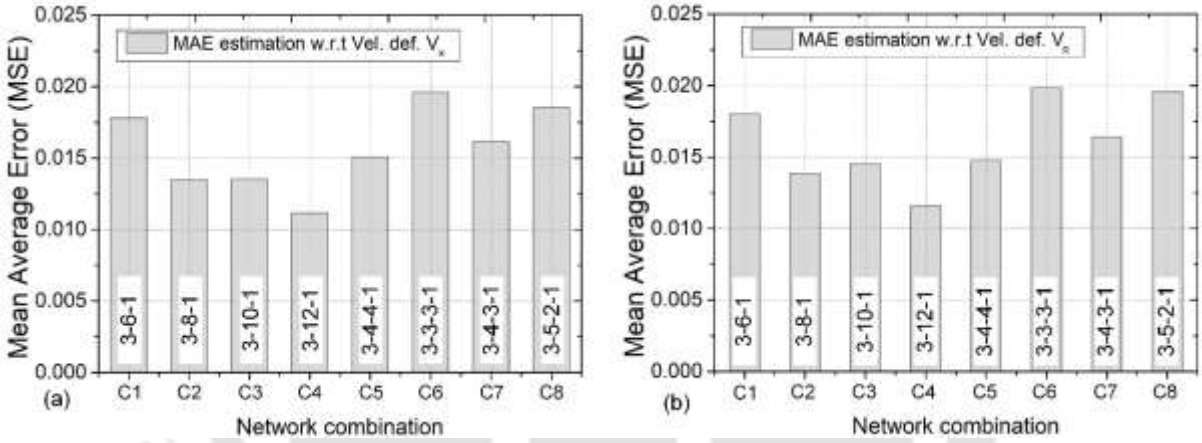

Fig. 9.5. Neural network performance assessment using MAE w.r.t (a) vel. def. V_x, and (b) vel. def. V_R

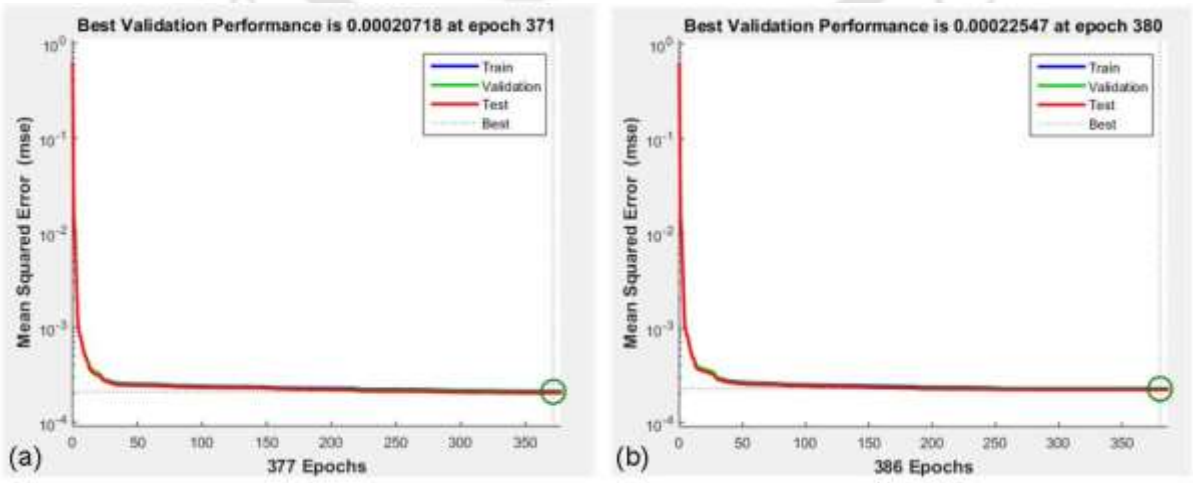

Fig. 9.6. Illustration of training, validation, and testing result of 3-12-1 network model for (a) vel. def. V_x target, and (b) vel. def. of V_R target

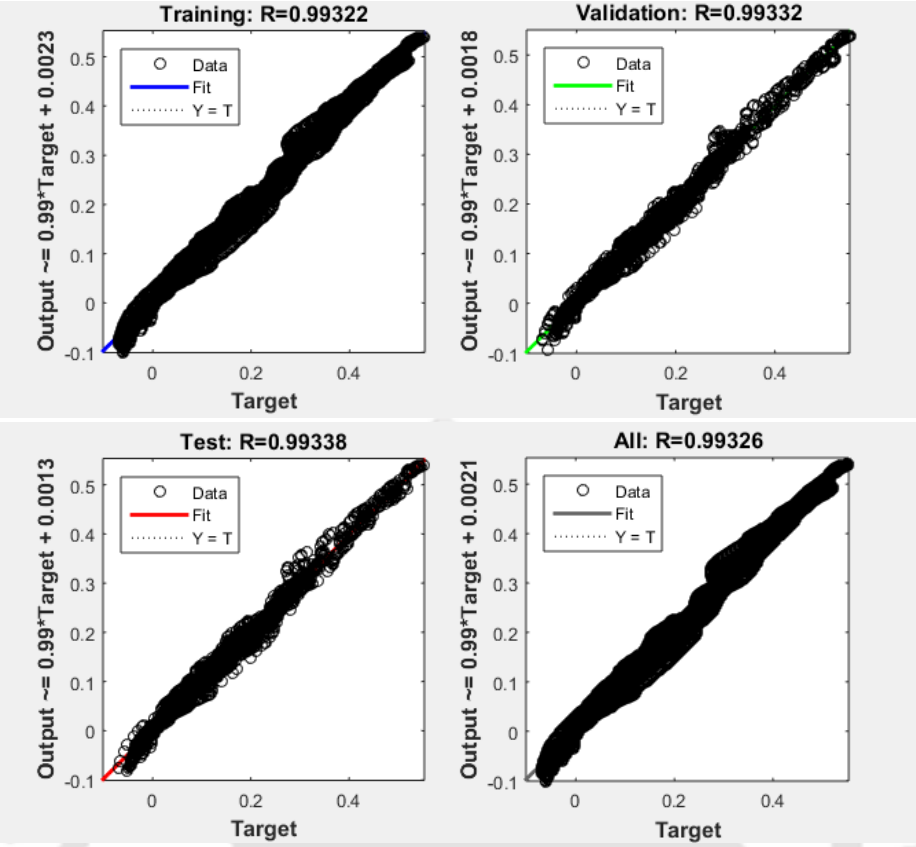

Fig. 9.7. Illustration of post-training regression for the 3-12-1 network for V_x

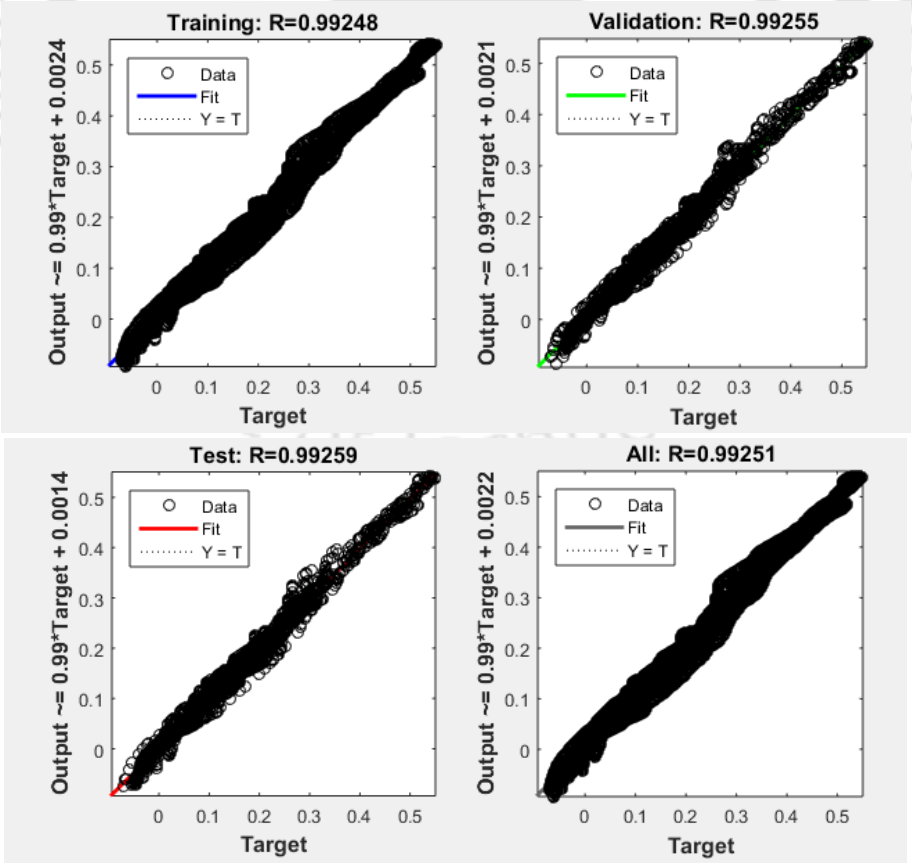

Fig. 9.8. Illustration of post-training regression for the 3-12-1 network for V_R

9.4.2 ANN-based Wake Model Equation

The next important phase of ANN modeling is the ensemble of weight (W) and biases (B) with the normalized variables to form a linear matrix equation, as per Eq. (9.8). The value of W and B for the neural network 3-12-1 is obtained as a simplified aggregate for all the three input parameters based on the number of neurons considered (12), the result is shown in Table 9.2. On the other hand, the normalized independent variables in the input data can be obtained as per Eqs. (9.5). Thereby, upon combining the respective weight with appropriate normalized variables, Eq. (9.6) can be obtained, which can then be associated with the transfer function 'Tansig' as per Eq. (9.7). In the final stage, the resultant expression is obtained after de-normalized the process data to obtain the velocity deficit relationship. The final expression is expressed as per Eq. (9.13) and Eq. (9.14) for velocity w.r.t V_x and V_R, respectively. Following the same procedure, the value of W and B are obtained while considering V_R as the desired output, as shown in Table 9.3.

Table 9.2. The aggregate value of W and B for the normalize input variable in the 3-12-1 network with vel. def. (V_x) as output.

Neuron	$W_{1,i,(x/R)}$	$W_{1,i,(\lambda)}$	$W_{1,i,(y/R)}$	B1
1	0.04879	-0.65824	3.05265	2.686295
2	0.15949	0.77699	-1.41801	1.234939
3	67.81258	41.2986	-4.26799	78.84475
4	0.183809	0.73477	-1.41848	1.277264
5	1.626105	-1.88454	-4.45339	3.214101
6	0.063371	0.52649	3.106434	0.617050
7	0.079217	0.58838	3.151477	0.576238
8	0.927248	-0.36729	-0.00931	0.925595
9	1.765079	-1.22807	1.490155	1.831644
10	-2.368299	1.83912	-2.02351	-2.495208
11	-1.261424	1.81596	1.11272	-1.880918
12	-2.050086	1.514976	-1.76671	-2.151603

Table 9.3. The aggregate value of W and B for the normalize input variable in the 3-12-1 network with vel. def. (V_R) as output.

Neuron	$W_{1,i,(x/R)}$	$W_{1,i,(\lambda)}$	$W_{1,i,(y/R)}$	B1
1	-0.09888	-0.50242	1.10760	0.88498
2	0.31599	1.43817	-1.29376	0.98398
3	-20.16375	40.72549	-13.72464	36.17140
4	-0.33958	0.90300	-1.760498	2.174721
5	-1.65035	-1.96947	-4.72991	3.432042
6	0.112815	0.56042	3.26172	0.543424
7	0.124943	0.61131	3.30963	0.506384
8	0.550930	-0.16294	-0.14268	2.011623
9	-0.045145	-0.52801	1.11156	0.814532
10	-5.721592	1.80501	-1.69970	-5.690883
11	-6.587461	13.6305	1.27363	-11.45387
12	-4.181548	1.58098	-2.13948	-4.401607

ANN model expression for velocity deficit for the streamwise velocity (V_x) and resultant velocity (V_R) using Eq. (9.8) can be presented as per Eq. (9.13) and Eq. (9.14), respectively. The corresponding comparative illustration of experimental and ANN-predicted output for either case is shown in Figs. 9.9 and 9.10, respectively.

$$Vel.def\ (V_x) = 0.21738F_1 - 14.84252F_2 + 0.08111F_3 + 15.31965F_4 + 0.19920F_5 + 7.14429F_6 - 6.99220F_7 + 2.22291F_8 - 17.78548F_9 + 11.97650F_{10} + 0.30376F_{11} - 28.37933F_{12} - 1.61998 \quad (9.13)$$

$$Vel.def\ (V_R) = 7.20202F_1 - 0.86285F_2 + 0.07917F_3 + 1.15928F_4 + 0.19527F_5 + 7.44471F_6 - 7.35761F_7 + 14.20580F_8 - 7.02783F_9 + 1.47121F_{10} + 0.24426F_{11} - 1.37651F_{12} - 14.75587 \quad (9.14)$$

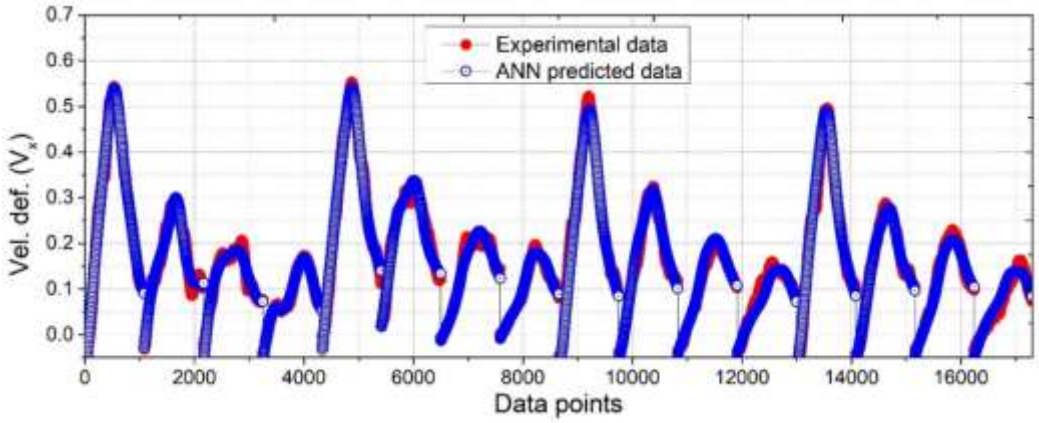

Fig. 9.9. Illustration of predicted data with that of experimental using 3-12-1 network for velocity deficit (V_x)

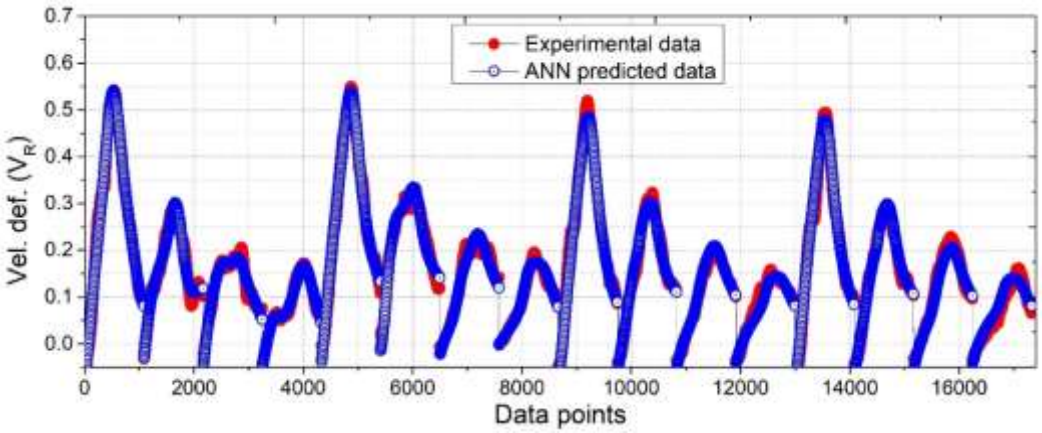

Fig. 9.10. Illustration of predicted data with that of experimental using 3-12-1 network for velocity deficit (V_R)

9.4.3 Comparative Assessment with Analytical Models

To further acknowledged the feasibility of ANN model in predicting the velocity deficit, and deficit profile. A comparative assessment has been carried out with the three renowned analytical wake models; the Jensen model (Jensen, 1988), Frandsen model (Frandsen et al.

2006), and B-P model (Bastankhah and Porté-Agel, 2014). The case study has been performed to estimate the deficit at x/R = 6, 10, 14, and 18, under the low tip speed ratio condition; that is at λ = 2.5. The empirical relation provided in Eq. (9.9) through Eq. (9.12) shows the dependence on C_T; therefore, deficit estimation has been made under two considerations. The first consideration is the ideal scenario when the axial induction factor (a) is 1/3; therefore, the value of C_T as per the relation 4a(1-a) is about 0.889 (Vermeer et al. 2003). The second consideration is as per the experimental data, where the value of 'a' is obtained after mapping the velocity drop just upstream of the rotor plane ($-0.25 < x/R < 0$) using the PIV for the vertical reference $-1.5 < y/R < 1.5$. Accordingly, the average thrust coefficient obtained experimentally ($C_{T,exp}$) is evaluated, which is found to be around 0.30. The reason for adopting uniaxial ($\pm y/R$) 'a' is to relate the corresponding two-dimensional depiction of the deficit field. The estimated velocity deficit using the Jensen model is shown in Fig. 9.11; in both conditions, as expected, the representation is a top-hat shape, and the velocity deficit is maximum at x/R = 6. The value of deficit under the ideal condition is higher than the experimental value (Fig. 9.11b). Figure 9.12 shows the estimated velocity deficit using the Frandsen model; this model also represents a top-hat shape but with a relatively larger wake radius. Figure 9.13 shows the estimated velocity deficit profile using the B-P model (Bastankhah and Porté-Agel, 2014), which represents an axisymmetric Gaussian-like distribution with a maximum deficit at x/R = 6. Thereupon, all three estimated wake profiles under the similar conditions are compared with the experimental and ANN predicted data, as shown in Fig. 9.14. The observation suggests over-estimation of velocity deficit by the analytical wake models, mainly due to the several idealistic assumptions (Steven and Maceveau, 2017). Furthermore, irrespective of the size of the model HAWT rotor, the depiction of downstream flow profile is analogous to the large wind turbine wake that is Gaussian-like distribution but skew or asymmetric.

The present case studies are also unique in the sense that the study on wake deficit at low λ for SHAWT is scarce. Some of the few studies under such circumstances are noted in the reported literatures (Theunissen et al. 2015; Vinnes et al. 2022). The recent work of Vinnes et al. (2022) demonstrated the downstream flow profile by considering a non-uniform rotor/disk (ND) and uniform disk (UD); operating at low λ (= 3.5). The work undertaken was basically meant to complement the actuator disk model employed in most of the classical wake models (Vermeer et al. 2003; Steven and Maceveau, 2017). The wake deficit estimated by these investigations (Theunissen et al. 2015; Vinnes et al. 2022) has been compared and presented in Fig. 9.15. Based on the comparative assessment carried out, it can be outlined that the flow deficit estimated through a data-driven approach offers reliable and accurate results compared analytical models.

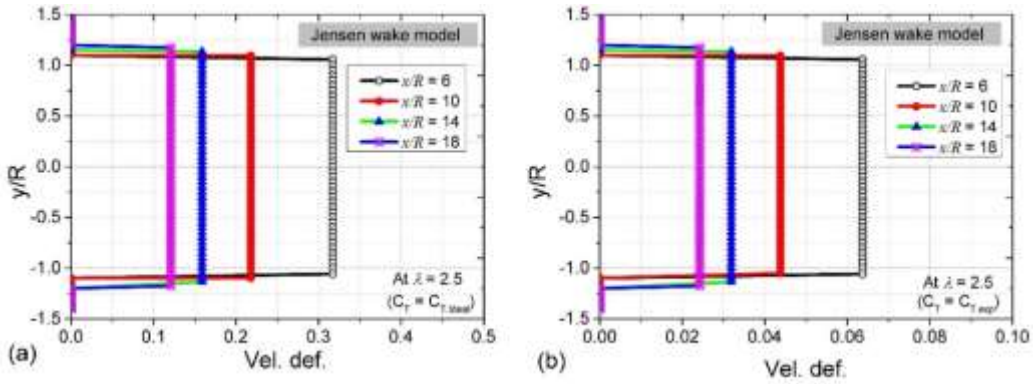

Fig. 9.11. Jensen estimation of downstream V_x deficit for (a) $C_{T,Ideal}$ = 0.889, and (b) $C_T = C_{T,Exp}$

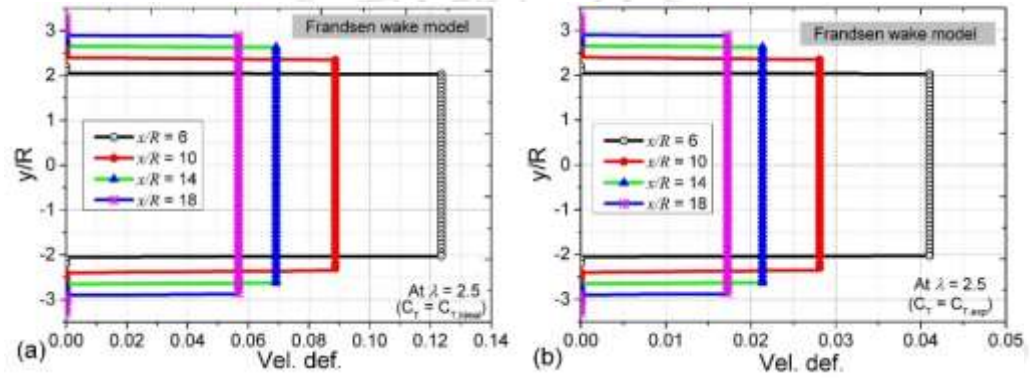

Fig. 9.12. Frandsen estimation of downstream V_x deficit for (a) $C_{T,Ideal}$ = 0.889, and (b) $C_T = C_{T,Exp}$

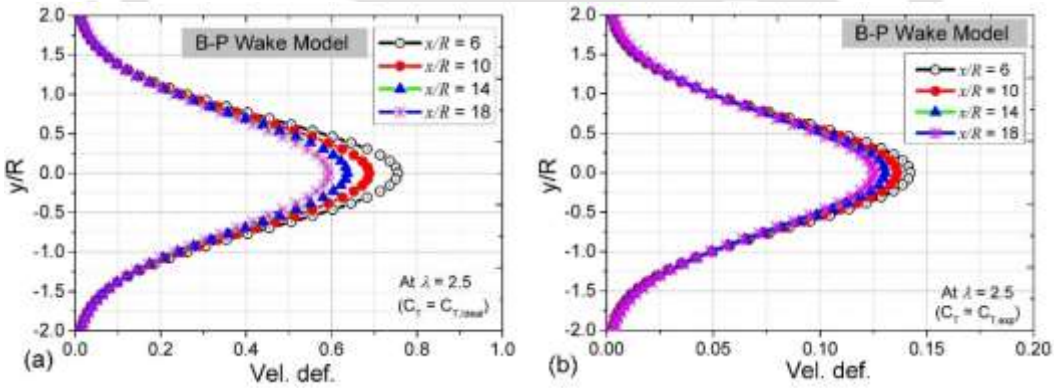

Fig. 9.13. B-P estimation of downstream V_x deficit for (a) $C_{T,Ideal}$ = 0.889, and (b) $C_T = C_{T,Exp}$

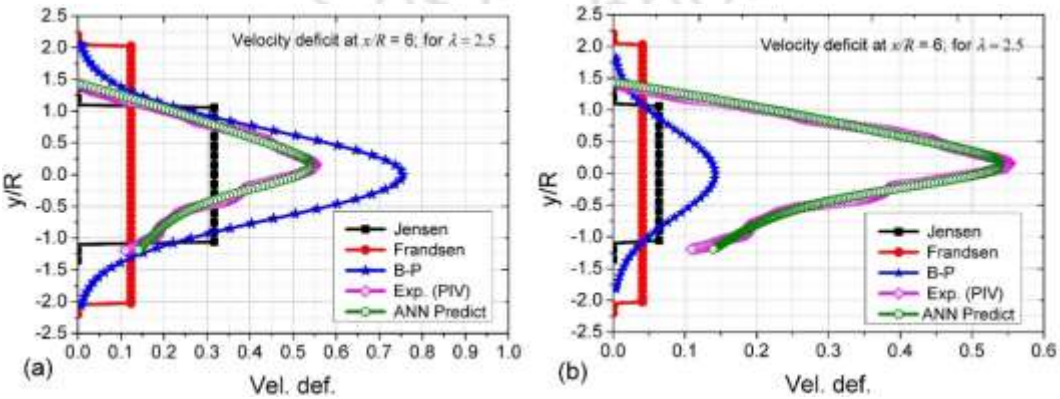

Fig. 9.14. Comparative assessment of downstream V_x deficit for (a) $C_{T,Ideal}$ = 0.889, and (b) $C_T = C_{T,Exp}$

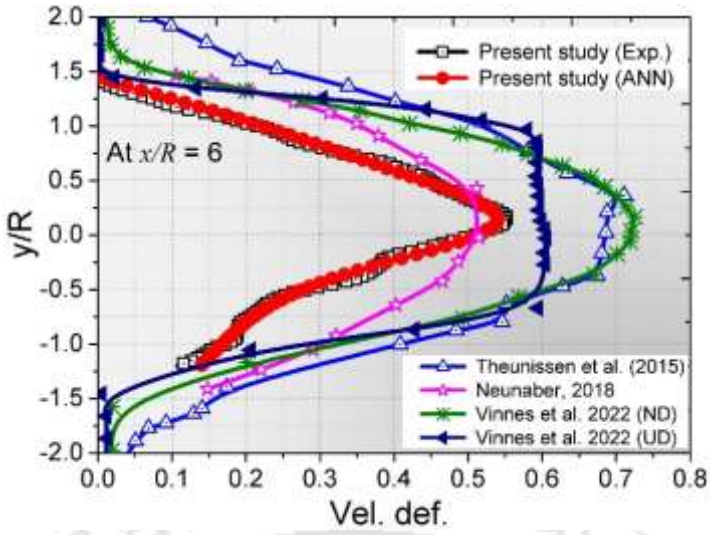

Fig. 9.15. Comparative assessment of the present study with other low tip speed ratio results

9.5 Summary of the Study

In this study, an ML-based wake model is developed to estimate the wake propagation that would help improve the power prediction of multiple turbines or the integration of turbines in a given area/structure. The presented model can reproduce the velocity deficit of the turbine wake using the high-fidelity stereo particle image velocimetry (PIV) data. Driven by a substantial PIV-assessed dataset, the inherent relationship between inflows and wake flows is established using the Artificial Neural Networks (ANN) technique based on the back-propagation algorithm. The model (neural network) selection has been carried out by assessing the mean square error (MSE), sum squared error (SSE), and mean average error (MAE) for three inputs and one output. Thereupon, it is observed that the network combination of 3-12-1 perceptron provides the minimum MSE, SSE, and MAE; this input, hidden neuron (12), and output model produces a correlation coefficient of about R ≈ 0.993 between the predicted output and input target.

The results show about 10-15% deviation, mainly towards the central core (y/R ≈ 0) and towards the brink of wake field. The experimental and ANN-predicted results were then compared with the three classical wake models (Jensen, Frandsen, and B-P). The Jensen and Frandsen wake models, in particular, show a Top-hat profile, while the B-P models depict an axisymmetric Gaussian-like velocity deficit. Because of the several assumptions undertaken by the analytical models, it is observed that there is about 30-40% difference with the experimental results. Furthermore, upon comparing with other low tip speed ratio wake studies, it is observed that experimental and ANN-based models can produce much better and more reliable results than their analytical counterparts.

CHAPTER 10
CONCLUSIONS AND FUTURE SCOPE

10.1 Overview

Fulfilling the demand for renewable energy through wind energy is a promising and potential source in the present and future scenarios. With this aspect, the present investigation explores the applicability of a small horizontal-axis wind turbine (SHAWT) to be employed as a power generating source in places where energy demand is minimal. This study explores the design and testing of SHAWT for low λ and low *Re* conditions. The SHAWT rotor blades were designed using the blade element momentum theory (BEMT) and, thereby, fabricated using the 3D printer. The examined rotors are to be utilized as a multirotor system or in the small wind farm, which would require an in-depth understanding of the rotor's flow characteristics and its effect on the nearby rotors. Thus, a dedicated downstream wake study has been carried out using the constant temperature hot wire anemometry (CTHWA) and stereo particle image velocimetry (PIV) in a subsonic wind tunnel at the Indian Institute of Technology Guwahati.

10.2 Key Highlight of the Research Work

The research work carried out can be broadly classified into two parts (1) design and development of SHAWT, and (2) wake study of SHAWTs for their application in a multirotor system or in the small wind farms. These two requirements have been comprehensively addressed through design and testing assessments, and flow physics studies. Some of the salient highlights of the research work are mentioned below:

- Small wind turbines (SWTs) can be categorized as those a rotors having a rotor diameter less than 5 m, $\lambda < 6$, and $0.3 \times 10^5 < Re < 3 \times 10^5$.
- The low *Re* airfoil that can potentially be used for the design of SHAWT blades is E216, E555, SG6043, NACA63415, NACA0012, E387, and others.
- Based on aerodynamic assessments airfoils E216, SG6043, and NACA63415 are favorable for the SHAWT.
- From BEMT analysis, SHAWT with airfoil E216 produces better C_{pmax}.
- The real-time performance assessment of the three SLT rotors using the RTS reveals the dependence of C_p on β, and also changes the operational range of λ.
- The experimental results show that the SLT rotors should be operated at lower β.
- For the rotors in an array, a substantial drop in both the rotational frequency and the performance is observed. For example, at $x/R = 6$, the C_{pmax} of DsT is obtained to show a drop of about 78.08%.
- It is observed that DsT performance decreases with an increase in the yaw angle (γ).
- The time-resolved PIV shows scatter distribution with a Gaussian-like distribution.
- Time-averaged stream velocity is asymmetric in nature due to the presence of support.

- It is noted that velocity deficits are relatively low at higher λ.
- The observation indicates that at about 9D and beyond, one can expect about 70 – 90% flow recovery.
- Close to the rotor plane, the assessment of V_z velocity reveals two distinct opposite crests towards the upper and lower half of the wake field, which is due to the out-of-the-plane and into-the-plane movement of the wake.
- A data-driven spiral polar plot (SPP) analogy has been introduced that combines the HVL sequence, helical/spiral analogy, and polar coordinates reference.
- ANN-based wake model with a network combination of 3-12-1 perceptron provides the minimum MSE, SSE, and MAE, with a correlation coefficient of about R ≈ 0.993.
- Upon comparing with other low tip speed ratio wake studies, it is observed that experimental and ANN-based models can produce much better and more reliable results than their analytical counterparts.

10.2 Contribution of the Present Work

10.2.1 Design and Testing of SHAWT for Low λ Applications

This study aims at the design, development and testing of SHAWT model rotors meant for low *Re* and low λ conditions. On the basis of literature survey, airfoil E216, SG6043, NACA63415, and NACA0012 have been chosen for developing the model rotors viz., M1, M2, M3, and M4. Furthermore, testing on mixed airfoil SHAWT has also been performed. Following are some of the key findings.

- From BEMT analysis, the C_{pmax} of M1, M2, M3, and M4 at $\lambda = 2.5$ is found to be around 0.37, 0.35, 0.34, and 0.36, respectively, which is about 62.4%, 59.02%, 57.33%, and 60.7% of Betz's limit.
- From wind tunnel studies, the C_{pmax} of M1 at $\theta_{p,design}$ is found to be 0.34 at U = 9 m/s, and this is about 58.01% of Betz's limit. At the same U, the M2 at $\theta_{p,design}$ is capable to produce a C_{pmax} of 0.30 which is about 50.6% of Betz's limit. With a thicker airfoil, the M3 at $\theta_{p,design}$ shows a C_{pmax} of 0.28 at the same U, which is about 47.2% of Betz's limit.
- The testing on mixed airfoil SHAWT suggest that the combination has a favorable performance at lower U and θ_p.
- This study demonstrated the superior performance of SHAWT with E216 profile. And also show promising result when used in mixed airfoil blade.

10.2.2 Design and Testing of SLT Rotors for Low λ Applications

In-line with the prospect of SHAWT as a potential wind power source, an experimental investigation on straight and linearly tapered (SLT) rotors has been carried out. Three models of SHAWT having NACA0012 airfoil have been considered and tested under different λ and

β. The SLT model rotors are differentiated based on the ratio of the root chord by tip chord as M1(1:1), M2(5:3), and M3(5:2). Following are some of the key findings.

- The BEMT prediction of model rotor M0 shows C_{pmax} of 0.35 at λ = 2.5. However, experimental observation on the M0 rotor shows C_{pmax} of 0.15. Thus, the applicability of NACA0012 as a BEMT rotor profile at low *Re* and λ does not seem to be promising due to its highly transitional behavior at low *Re* conditions.
- The favourable models, SLT M1 and SLT M2, can capture 37% and 24% of the Betz-Joukowsky limit while operating at β = 20°. It is suggested to operate SLT rotors at lower β.
- While examining the operational features of SLT rotors, particularly in the case of M1 and M2, a sudden drop in the rotational speed is observed after stall, instead of gradual decrement. The effect is observed to be very much prevailing when β is less than 40°. Therefore, it is suggested to operate such rotors in the potential generation phase of the power characteristics curve.

10.2.3 Wind Tunnel Probe into Array of SHAWTs

To design an integrated SWT system in the form of multirotor system or small wind farm. It is indeed essential to understand the wake propagation and interaction with the nearby turbines, so as to main the cluster efficiency. In this aspect, an experimental investigation has been carried out to assess the wake and performance characteristics of stand-alone rotor and rotor in array, while operating at low λ. Following are some of the key findings.

- The experimentally obtained C_{pmax} of the stand-alone model rotor or upstream rotor (UsT) is found to be 0.30 and 0.34 at 8 m/s and 9 m/s, respectively.
- At x/R = 6, the C_{pmax} of DsT shows a drop in performance by about 78.08% from Betz's limit, however, when installed at x/R = 10 about 46.1% recovery is observed.
- Within the near wake regime (x/R < 6), the velocity deficit profile is marked by the formation of W-shape; however, starts disappearing when POMs are taken at x/R > 8.
- Close to x/R = 12, the downstream flow recovers by about ~70% of the upstream velocity, suggesting the possible inclusion of DsT for potential power extraction.

10.2.4 In-depth Assessment of SHAWT Wake Using Stereo PIV

The intent of this study is to extract the downstream flow field characteristic of wake dissipating from the modelled rotor using the stereo PIV. Following are some of the key findings.

- At x/R = 6, the time-resolved scatter distribution and the time-averaged velocity profile (V_x) has a Gaussian-like distribution. However, profile becomes much stepper at high at x/R > 14.

- It is noted that velocity deficits are relatively low at higher λ, and maximum close to λ = 2.5, which apparently, is also the optimal condition of the model rotor. This leads to an analogy that perhaps; one can expect the maximum deficit when the rotor is operating at or close to the rotor design condition.
- The observation indicates that at about 9D and beyond, one can expect about 70 – 90% flow recovery.
- At x/R = 6, the assessment of V_z velocity reveals two distinct opposite crests towards the upper and lower half of the wake field. And the stereo vector field study suggests such pattern is due to the out-of-the-plane and into-the-plane movement of wake.

10.2.5 Spiral Polar Plot Analogy

A unique methodology/analogy has been introduced that combines the HVL sequence, helical/spiral analogy, and polar co-ordinates reference, thus named as spiral polar plot (SPP). Using SPP, one can easily define the sequence of HVLs at any given polar coordinate position and with respect to blade position. The methodology can dictate the sequence of wake, where each sequence is mark by the passage of HVLs dissipating from the individual blade. For a 'n' number of rotor blade, there will be 'n+1' HVLs to dictate the three-dimensional depiction of the helical vortex.

10.2.5 Implication of Data-Driven Wake Modelling

Finally, an ANN-based wake model is developed to estimate the wake propagation that would help improved the power prediction of multiple turbines placement. The criteria for model selection have been carried out by assessing the mean square error (MSE), sum squared error (SSE), and mean average error (MAE). Following are some of the key findings.

- The model combination of 3-12-1 perceptron provides the minimum MSE, SSE, and MAE, with a correlation coefficient of about R ≈ 0.993.
- The results show about 10-15% deviation between the target and predict data, mainly towards the central core (y/R ≈ 0) and towards the brink of wake field.
- The Analytical model shows higher deficit because of the several assumptions undertaken, it is observed that there is about 30-40% difference with the experimental results.
- Upon comparing with other low tip speed ratio wake studies, it is observed that experimental and ANN-based models can produce much better and more reliable results than their analytical counterparts.

10.3 Application Potential

For minimal energy demand, such as for off-grid individual households, rural communities, small-scale farms, and others, the implication of LWTs may not be viable and economical. Under such circumstances, the need for effective, efficient, and economical small wind turbines (SWTs) comes into play. Based on the design and operation constraints of model rotors presented in this research, the following are some of the possible and potential applications.

- The rotors are most suitable for places where LWT installation is impossible. Such as rooftops, community building, small farms, high-altitude terrain, and others.
- These turbines are also best suited for urban/suburban regions.
- For the specific rotor presented in this work produces about 10 W at $\lambda = 2.5$. Although the power produced is low, the relative comparisons show aggregate potential when integrated into a small wind farm or a multirotor system.
- Wake study on wind turbines operating at low λ is scarce. Therefore, the information presented in this work will be a potential source of wake data analogy for SHAWTs.

10.4 Future Work Scope

The work presented demonstrates several operational and aerodynamic characteristics of SHAWTs. However, it is still a drop in the ocean of wind energy research. Since much of the research work has been carried out within an idealistic scenario (wind tunnel), it would definitely require further examination, especially through an open field test. Following are some of the challenges and possible research opportunities.

- Design and Testing of E216 profile for larger λ and Re range.
- SWTs' spanwise flow is quite strong compared to LWTs; thus, further study is needed.
- Study on the implication of mixed aero foil in SHAWT is scarce; thus, potential research opportunity in this area.
- Rotational characteristics of SHAWTs are quite high and thus possess strong centrifugal action. In this aspect, material and structural analysis are also potential research areas.
- SHAWTs in an integrated system like a multirotor system or small wind farm is a potential research area due to increased power generation capacity.
- The data-driven SPP analogy introduced in this study will be explored quantitatively in future work.
- The data-driven techniques such as ANN, GEP, and others will be explored in future work to integrate the wind turbine wake dynamic with the rotor performance for different array/cluster configurations.

REFERENCES

Abdelsalam, A. M., El-Askary, W. A., Kotb, M. A., and Sakr, I. M., 2021. Experimental Study on Small Scale Horizontal Axis Wind Turbine of Analytically-Optimized Blade with Linearized Chord Twist Angle Profile. Energy, 216, p. 119304.

Abrar, M. A., Mahbub, A. M. I., and Mamum, M., 2014. Design Optimization of a Horizontal Axis Micro Wind Turbine through Development of CFD Model and Experimentation. Procedia Engineering, 90, pp. 333-338.

Adaramola, M. S., and Krogstad, P.-Å., 2011. Experimental investigation of wake effects on wind turbine performance. Renewable Energy 36(8), pp. 2078-2086.

Adhikari, J., Sapkota, R., and Panda, S. K., 2018. Impact of Altitude and Power Rating on Power-to-Weight and Power-to-Cost Ratios of the High-Altitude Wind Power Generating System. Renewable Energy, 115, pp. 16-27.

Aftab, S. M. A., Razak, N. A., Rafie, A. S. M., and Ahmad, K. A., 2016. Mimicking the humpback whale: An aerodynamic perspective. Progress in aerospace sciences, 84, pp. 48-69.

Ainslie, J. F., 1988. Calculating the Flow Field in the Wake of Wind Turbines. Journal of Wind Engineering and Industrial Aerodynamics, 27(1-3), pp. 213-224.

Akour, S. N., Al-Heymari, M., Ahmed, T., and Khalil, K. A., 2018. Experimental and Theoretical Investigation of Micro Wind Turbine for Low Wind Speed Regions. Renewable Energy, 116(A), pp. 215-223.

Al Sam, A., Szasz, R., and Revstedt, J., 2017. An Investigation of Wind Farm Power Production for Various Atmospheric Boundary Layer Height. ASME Journal of Energy Resources Technology, 139(5), p. 051216.

Alhmoud, L., and Wang, B., 2018. A review of the state-of-the-art in wind-energy reliability analysis. Renewable and Sustainable Energy Reviews, 81(2), pp. 1643-1651.

Annoni, J., Howard, K., Seiler, P., and Guala, M., 2016. An Experimental Investigation on the Effect of Individual Turbine Control on Wind Farm Dynamics. Wind Energy, 19(8), pp. 1453-1467.

Astolfi, D., Castellani, F., and Terzi, L., 2019. Definition and Interpretation of Wind Farm Efficiency in Complex Terrain: A Discussion. ASME Journal of Energy Resources Technology, 141(5), p. 055501.

Bahaj, A. S., Molland, A. F., Chaplin, J. R., and Batten, W. M. J., 2007. Power and Trust Measurements of Marine Current Turbines Under Various Hydrodynamic Flow Conditions in a Cavitation Tunnel and a Towing Tank. Renewable Energy, 32(3), pp. 407–426.

Bastankhah, M., and Porté-Agel, F., 2014. A New Analytical Model for Wind-Turbine Wakes. Renewable Energy, 70, pp. 116-123.

Barthelmie, R.J., Rathmann, O., Frandsen, S.T., Hansen, K.S., Politis, E., Prospathopoulos, J., Rados, K., Cabezón, D., Schlez, W., Phillips, J.; et al., 2007. Modelling and measurements of wakes in large wind farms. Journal of Physics Conference Series, 75.

Becerra, M., Morán, J., Jerez, A., Cepeda, F., and Valenzuela, M., 2017. Wind Energy Potential in Chile: Assessment of a Small-Scale Wind Farm for Residential Clients. Energy Conversion and Management, 140, pp. 71–90.

Bechmann, A., Sørensen, N. N., and Zahle, F., 2011. CFD simulations of the MEXICO rotor. Wind Energy, 14, pp. 677–689.

Bilgili, M., Tontu, M., and Sahin, B., 2021. Aerodynamic Rotor Performance of A 3300 Kw Modern Commercial Large-Scale Wind Turbine Installed in a Wind Farm. ASME Journal of Energy Resources Technology, 143(3), p. 031302.

Bishop, M., and Yarusevych, S., 2011. Mitigating Blockage Effects on Flow Over a Circular Cylinder in an Adaptive-Wall Wind Tunnel. ASME Journal of Fluids Engineering, 133(8), p. 081101.

Bruun, H. H., 1995. Hot-Wire Anemometry: Principles and Signal Analysis. Oxford University Press, Oxford

Burton, T. L, Jenkins, N., Bossanyi, E., Sharpe, D., and Graham, M., 2021. Wind Energy Handbook. John Wiley & Sons, 3rd Edition.

Butterfield, C. P., Scott, G., and Musial, W., 1992. Comparison of Wind Tunnel Airfoil Performance Data with Wind Turbine Blade Data. ASME Journal of Solar Energy Engineering, 114(2), pp. 119–124.

Burdett, T. A., and Van Treuren, K. W. van, 2012. Scaling Small-Scale Wind Turbines for Wind Tunnel Testing. ASME Paper No. GT2012-68359, pp. 811-820.

Carrión, M., Woodgate, M., Steijl, R., Barakos, G. N., Gomez-Iradi, S., and Munduate, X., 2015. Understanding Wind-Turbine Wake Breakdown Using Computational Fluid Dynamics. AIAA J., 53(3), pp. 588-602.

Cal, R. B., Lebron, J., Castillo, L., Kang, H. S., and Meneveau, C., 2010. Experimental study of the horizontally averaged flow structure in a model wind-turbine array boundary layer. Journal of Renewable and Sustainable Energy, 2, p. 013106.

Casini, M., 2016. Small Vertical Axis Wind Turbines for Energy Efficiency of Buildings. Journal of Clean Energy Technology, 4, pp. 56-65.

CEA-LGBR, 2019-2020. Load Generation Balance Report (LGBR). http://www.cea.nic.in/reports/ annual/lgbr/ lgbr-2019.pdf.

Cengel, Y. A., and Cimbala, J. M., 2019. Fluid Mechanic- Fundamental and applications. McGraw-Hill, 4th Edition, 28 May.

Chen, X., and Agarwal, R., 2012. Optimization of Flatback airfoils for wind-turbine Blades using a genetic algorithm. Journal of Aircraft, 49(2), pp. 622-629

Chen, T. Y., and Liou, L. R., 2011. Blockage Corrections in Wind Tunnel Tests of Small Horizontal-axis Wind Turbines. Experimental Thermal and Fluid Science, 35(3), pp. 565-569.

Chen, L., and MacDonald, E., 2012. Considering landowner participation in wind farm layout optimization. Journal of Mechanical Design, 134, p. 084506.

Chowdhury, N.E., Shakib, M.A., Xu, F., Salehin, S., Islam, Md R., and Bhuiyan, A.A., 2022. Adverse environmental impacts of wind farm installation and alternative research pathways to their mitigation. Clean Engineering and Technology, 7, p. 100415.

Corbus, D., Hansen, A. C., and Minnema, J., 2006. Effect of blade torsion on modeling results for the small wind research turbine. ASME Journal of Solar Energy Engineering, 128, pp. 481–486.

Costello, S., Costello, C., François, G., and Bonvin, D. Analysis of the Maximum Efficiency of Kite-power Systems. Journal of Renewable and Sustainable Energy, 7, p. 053108.

Crespo, A., Hernandez, J., Fraga, E., and Andreu, C., 1988. Experimental Validation of the UPM Computer Code to Calculate Wind Turbine Wakes and Comparison with Other Models. Journal of Wind Engineering and Industrial Aerodynamics, 27, pp. 77-88.

Dehouck, V., Lateb, M., Sacheau, J., and Fellouah, H., 2018. Application of the Blade Element Momentum Theory to Design Horizontal Axis Wind Turbine Blades. ASME Journal Solar Energy Engineering, 140(1), p. 014501.

Díaz, H., and Soares, C. G., 2020. Review of the Current Status, Technology and Future Trends of Offshore Wind Farms. Ocean Engineering, 209, p. 107381.

Dilimulati, A., Stathopoulos, T., and Parashivoiu, M., 2018. Wind Turbine Designs for Urban Applications: A Case Study of Shrouded Diffuser Casing for Turbines. Journal of Wind Engineering and Industrial Aerodynamics, 175, pp. 179-192.

Duquette, M. M., and Visser, K. D., 2003. Numerical Implications of Solidity and Blade Number on Rotor Performance of Horizontal-Axis Wind Turbine. ASME Journal of Solar Energy Engineering, 125(4), pp. 425-432.

Eriksen, P-E., and Krogstad. P. A., 2017. An Experimental Study of the Wake of a Model Wind Turbine Using Phase-averaging. International Journal of Heat and Fluid Flow, 67(Part B), pp. 52-62.

Esteban, M. D., López-Gutiérrez, J-S., Negro, V., Matutano., García-Flores, F. M., and Millán, M. Á., 2015. Offshore wind foundation design: Some key issues. ASME Journal of Energy Resources Technology, 137(5), p. 051211.

Farsad, S., Ardekani, M. A., and Farhani, F., 2019. Experimental investigation of aerodynamic effects of probe on heat transfer from hot-wire sensors at vertical and horizontal orientations. Flow Measurement and Instrumentation, 70, p. 101642.

Fiedler, B. H., and Bukovsky, M. S., 2011. The Effect of a Giant Wind Farm on Precipitation in a Regional Climate Model. Environ Res. Lett., 6(4), pp. 045101.

Fischer, A., Montuelle, L., Mougeot, M., and Picard, D., 2017. Statistical learning for wind power: A modeling and stability study towards forecasting. Wind Energy, 20(12), pp. 2037–47.

Frandsen, S., Barthelmie, R., Pryor, S., Rathmann, O., Larsen, S., Højstrup, J., and Thøgersen, M., 2006. Analytical Modelling of Wind Speed Deficit in Large Offshore Wind Farms, Wind Energy (2006), 9, pp. 39–53.

Fuglsang, P., Bak, C., Gaunaa, M., and Antoniou, I., 2004. Design and Verification of the Risø-B1 Airfoil Family for Wind Turbines. ASME Journal of Solar Energy Engineering, 126(4), pp. 1003-1010.

Gad-el-Hak, M., 2007. Flow Control: Passive, Active, and Reactive Flow Management. Cambridge University Press, New York.

Giguere, P., and Selig, M. S., 1997. Low Reynolds Number Airfoils for Small Horizontal Axis Wind Turbines. Wind Engineering, 21(6), pp. 367–380.

González-Longatt, F., Wall, P., and Terzija, V., 2012. Wake Effect in Wind Farm Performance: A Steady-State and Dyanmic Behavior. Renewable Energy, 39(1), pp. 329-338.

Grant, I., and Parkin., P., 2000. A DPIV Study of the Trailing Vortex Elements from The Blades of a Horizontal Axis Wind Turbine in Yaw. Experiments in Fluids, 28, pp. 368-376.

Green, J. E., 2008. Laminar flow control-back to the future.? 38th Fluid Dynamics Conference and Exhibit, AIAA 2008-3738.

Gupta, R. K., Warudkar, V., Purohit, R., and Rajpurohit, R. S., 2017. Modelling and Aerodynamic Analysis of Small-Scale, Mixed Airfoil Horizontal Axis Wind Turbine Blade. Materials Today: Proceedings, 4, pp. 5370-5384.

Guo, T., Guo, X., Gao, Z., Li, S., Zheng, X., Gao, X., Li, R., Wang, T., Li, Y., and Li, D., 2021. Nacelle and tower effect on a stand-alone wind turbine energy output- A discussion on field measurements of a small wind turbine. Applied Energy, 303, 117590. https://doi.org/10.1016/j.apenergy.2021.117590

Hernandez, C. O. M., Shadman, M., Amiri, M. M., Silva, C., Estefen, S. F., and Rovere, E. L., 2021. Environmental Impacts of Offshore Wind Installation, Operation and Maintenance, and Decommissioning Activities: A Case Study of Brazil. Renewable and Sustainable Energy Reviews, 144, p. 110994.

Han, T., 2011. The assessment of dynamic wake effects on loading. The Netherland: Department of Aerospace Engineering Delft University of Technology. MS Thesis, Technical University of Denmark.

Hancock, P. E., and Pascheke, F., 2014. Wind-Tunnel Simulation of the Wake of a Large Wind Turbine in a Stable, Boundary Layer: Part 1, the Wake Flow. Boundary-Layer Meteorology, 151, pp. 23–37.

Hasan, M., El-Shahat, A., and Rahman, M., 2017. Performance Investigation of Three Combined Airfoils Bladed Small-Scale Horizontal Axis Wind Turbine by BEM and CFD Analysis. Journal of Power and Energy Engineering, 5(5), pp. 14-27.

Hirahara, H., Hossain, M. Z., and Nonomura, Y., 2005. Testing Basic Performance of a Very Small Wind Turbine Designed for Multi-Purposes. Renewable Energy, 30(8), pp. 1279–97.

Howell, R., Qin, N., Edwards, J., and Durrani, N., 2010. Wind Tunnel and Numerical Study of a Small Vertical-axis Wind Turbine. Renewable Energy 35(2), pp. 412-422.

Hsiao, F. B., Bai, C. J., and Chong, W. T., 2013. The Performance Test of Three Different Horizontal Axis Wind Turbine (HAWT) Blade Shapes Using Experimental and Numerical Methods. Energies, 6, pp. 2784-2803.

IEA, 2021. World Energy Outlook 2021. IEA, Paris. https://www.iea.org/reports/worldenergy-outlook-2021.

IRENA Renewable Capacity Statistics, 2020. https://irena.org/publications/2020/Mar/Renewable-Capacity-Statistics-2020.

Ismail, K. A. R., Canale, T., and Lino, F. A. M., 2022. Effects of The Airfoil Section, Chord and Twist Angle Distributions on the Starting Torque of Small Horizontal Axis Wind Turbine. ASME Journal of Energy Resources Technology, 144(5), p. 051301.

Istvan, M. S., and Yarusevych, S., 2018. Effects of free-stream turbulence intensity on transition in a laminar separation bubble formed over an airfoil. Experiments in Fluids, 59, p. 52.

Jain, S., and Saha, U. K., 2019. The State-of-the-Art Technology of H-Type Darrieus Wind Turbine Rotor. ASME Journal of Energy Resources Technology, 142(3), p. 030801.

Jackson, R. S., and Amano, R., 2017. Experimental Study and Simulation of a Small-Scale Horizontal-Axis Wind Turbine. ASME Journal of Energy Resources Technology, 139(5), p. 051207.

Jauch, C., Islam, S. M., Sørensen, P., and Jensen, B. B., 2007. Design of a wind turbine pitch angle controller for power system stabilization. Renewable Energy, 32, pp. 2334–2349.

Jeong, J., Park, K., Jun, S., Song, S., and Lee, D., 2012. Design optimization of a wind turbine blade to reduce the fluctuating unsteady aerodynamic load in turbulent wind. Journal of Mechanical Science and Technology, 26(3), pp. 827-838.

Jensen, N. O., 1983. A Note on Wind Generator Interaction. Risø national laboratory report, Riso-M-2411, DK-4000 Roskilde- Denmark, November.
Karthikeyan, N., Murugavel, K., Kumar, S. A., and Rajakumar, S., 2015. Review of aerodynamic developments on small horizontal axis wind turbine blade. Renewable Sustainable Energy Reviews, 42, pp. 801–822.
Katic, I, Højstrup, J., and Jensen, N. O., 1987. A Simple Model for Cluster Efficiency. Proceedings of European Wind Energy Association Conference and Exhibition, Rome, Italy, 06- October, 1, pp. 407-410.
Keisar, D., Troyer, T. D., and Greenblatt, D., 2020. Concept and Operation of a Wind Turbine Driven by Dynamic Stall. AIAA Journal, 58(6), pp. 2370-2376.
Kober, T., Schiffer, H.W., fDensing, M., and Panos, E., 2020. Global energy perspectives to 2060 – WEC's world energy scenarios 2019. Energy Strategy Reviews, 31, p. 100523.
Koch, P. H., and Jacobsen, H. K., 2019. Comparing Offshore and Onshore Wind Development Considering Acceptance Costs. Energy Policy, 125, pp. 9-19.
King, L. V., 1914. On The Convection of Heat from Small Cylinders in A Stream of Fluid. Phil. Trans. Roy. Soc., 214A, pp. 373-432.
Kishore, R. A., and Priya, S., 2013. Design and Experimental Verification of a High Efficiency Small Wind Energy Portable Turbine (SWEPT). Journal of Wind Engineering and Industrial Aerodynamics, 118, pp. 12–19.
Krogstad, P. –Å., and Lund, J. A., 2012. An Experimental and Numerical Study of the Performance of a Model Turbine. Wind Energy, 15(3), pp. 443-457.
Kuo J. Y. J., Romero, D. A., and Amon, C. H., 2015. A Mechanistic Semi-Empirical Wake Interaction Model for Wind Farm Layout Optimization. Energy, 93, pp. 2157-2165.
Kusiak, A., Zheng, H., and Song, Z., 2009. Wind farm power prediction: a data-mining approach. Wind Energy. International Journal of Progress Applied Wind Power Conversion Technology, 12(3) pp. 275–93.
Lanzafame, R., and Messina, M., 2010. Power Curve Control in Micro Wind Turbine Design. Energy, 35(2), pp. 556–561.
Larsen, G. C., 1988. A Simple Wake Calculation Procedure. Risø National Laboratory, Report Risø-M-2760, Roskilde, Denmark, pp. 1–53.
Larsen, G. C., and Réthoré, P.-E., 2009. A Simple Stationary Semi-Analytical Wake Model. Risø National Laboratory, Report Risø-R-1713(EN), Roskilde, Denmark.
Lee, S. H., and Han, Y. O., 2019. Experimental Investigation of High Angle of Attack Aerodynamics of Low Aspect Ratio Rectangular Wings Configure with NACA0012 Airfoil Section. International Journal of Aeronautical and Space Sciences, 21, pp.303–314.
Leger, J. A., Pascoa, J. C., and Xisto, C. M., 2015. Analytical Modeling of a Cyclorotor in Hovering State. Proceedings of the Institution of Mechanical Engineering, Part G, 229(12), pp. 2163–2177.
Li, L., Gao, Y., Yuan, Z., Day, S., Hu, Z., 2018. Dynamic response and power production of a floating integrated wind, wave and tidal energy system. Renewable Energy, 116, pp. 412–422
Lienard, C., Boisard, R., and Daudin, C., 2020. Aerodynamic Behavior of a Floating Offshore Wind Turbine. AIAA Journal, 58(9), pp. 3835-3847.
Lipian, M., Dobrev, I., Karczewski, M., Massouh, F., and Jozwik, K., 2016. Small Wind Turbine Augmentation: Experimental Investigation of Shrouded and Twin-rotor Wind Turbine Systems. Energy, 186, pp. 115855.
Lissaman, P. B. S., 1979. Energy effectiveness of arbitrary arrays of wind turbines. AIAA, pp. 079-0114.
Liu, J., Lin, H., and Zhang, J., 2019. Review on the technical perspective and commercial viability of vertical-axis wind turbines. Ocean Engineering, 182, pp. 608-626.
Lucas, A., 2005, "Wind, Water, Work," Leiden, The Netherlands: Brill Publication, 29 November.
Manwell, J. F., Mcgowan, J. G., and Rogers, A. L., 2009. Wind Energy Explained: Theory, Design and Application. 2nd Edition, Wiley publication, UK.
MacPhee, D. W., and Beyene, A., 2019. Performance analysis of a small wind turbine equipped with flexible blades. Renewable Energy, 132, pp. 497-508.
Marini, M., Baccoli, R., Mastino, C. C., Bella, A. D., Bernardini, C., and Masullo, M., 2017. Assessment of the Noise Generated by Wind Turbines at Low Frequencies. ASME Journal of Energy Resource and Technology, 139(5), p. 051215.

Massouh, F., and Dobrev, I., 2007. Exploration of the vortex wake behind of wind turbine rotor. Journal of Physics: Conference Series 75, p. 012036.

Matsumiya, H., Ito, R., Kawakami, M., Matsushita, D., Iida, M., and Arakawa, C., 2010. Field Operation and Track Tests of 1-Kw Small Wind Turbine Under High Wind Conditions. ASME Journal of Solar Energy Engineering, 132(1), p. 011002.

Medici, D., and Alfredsson, P. H., 2006. Measurements on a Wind Turbine Wake: 3D Effects and Bluff Body Vortex Shedding. Wind Energy, 9(3), pp. 219–236.

Medici, D., and Alfredsson, P. H., 2008. Measurements Behind Model Wind Turbines: Further Evidence of Wake Meandering. Wind Energy, 11(2), pp. 211–217.

McKay, P., Carriveau, R., and Ting D. S-K., 2013. Wake impacts on downstream wind turbine performance and yaw alignment. Wind Energy, 16, pp. 221–34.

McTavish, S., Feszty, D., and Nitzsche, F., 2013. Evaluating Reynolds Number Effects in Small-Scale Wind Turbine Experiments. Journal of Wind Engineering and Industrial Aerodynamics, 120, pp. 81-90.

MNRE Annual report, 2019-2020. https://mnre.gov.in/img/documents/uploads/file_f-1585710569965.pdf.

Neagoe, M., Saulescu, R., Jaliu, C., and Simionescu, P. A., 2020. A Generalized Approach to the Steady-State Efficiency Analysis of Torque-Adding Transmissions Used in Renewable Energy Systems. Energies, 13, p. 4568.

Nguyen, L., and Metzger, M., 2017. Optimization of a Vertical-axis Wind Turbine for Application in an Urban/suburban Area. Journal of Renewable and Sustainable Energy, 9, p. 043302.

Niayifar, A., and Porté-Agel, F., 2016. Analytical modelling of wind farms: A new approach for power prediction. Energies, 9, p. 741.

NLDC Annual report, 2018-2019. https://nrldc.in/download/annual-report-2019 20/?wpdmdl=8184.

Okulov, V. L., and van Kuik, G. A. M., 2012a.The Betz-Joukowsky limit: On the contribution to rotor aerodynamics by the British, German and Russian scientific schools. Wind Energy, 15(2), pp. 335–344.

Okulov, V. L., Mikkelsen, R., Sørensen, J. N., Naumov, I. V., and Tsoy, M. A., 2017. Power Properties of Two Interacting Wind Turbine Rotors. ASME Journal of Energy Resources Technology, 139(5), p. 051210.

Orrell, A., Kazimierczuk, K., and Sheridan, L., 2021. Distributed Wind Market Report: 2020 Edition. Report, U. S Department of Energy (2021). https://www.energy.gov/eere/wind/articles/distributed-wind-market-report-2021-edition-released

Ossmann, D., Seiler, P., Milliren, C., and Danker, A., 2021. Field Testing of Multi-Variable Individual Pitch Control on a Utility-Scale Wind Turbine. Renewable Energy, 170, pp. 1245-1256.

Polat, O., and Tuncer, L. H., 2013. Aerodynamic Shape Optimization of Wind Turbine Blades Using a Parallel Genetic Algorithm. Procedia Engineering, 61, pp. 28-31.

Pope, A., and Harper, J. J., 1966. Low Speed Wind Tunnel Testing. John Wiley and Sons, New York.

Pourrajabian, A., Mirzaei, M., Ebrahimi, R., and Wood, D., 2014. Effect of Air Density on the Performance of a Small Wind Turbine Blade: A case study in Iran. Journal of Wind Engineering and Industrial Aerodynamics, 126, pp. 1–10.

Rahgozar, S., Pourrajabian, A., Kazmi, S. A. A., and Kazmi, S. M. R., 2020. Performance analysis of a Small Horizontal Axis Wind Turbine under the use of Linear/Nonlinear Distributions for the Chord and Twist Angle. Energy for Sustainable Development, 58, pp. 42–49.

Rathod, U. H., Talukdar, P. K., Kulkarni, V., and Saha, U. K., 2019. Effect of Capped Vents on Torque Distribution of a Semicircular-Bladed Savonius Wind Rotor. ASME. Journal of Energy Resources Technology, 141(10), 101201.

Refan, M., and Hangan, H., 2012. Aerodynamic Performance of a Small Horizontal Axis Wind Turbine. ASME Journal of Solar Energy and Engineering, 134(2), p. 021013.

Ritchie, H., Roser, M., 2020. Energy. Published online at OurWorldInData.org. Retrieved from. https://ourworldindata.org/energy.

Rocha, P. A. C., Araujo, J. W. C., Lima, R. J. P., Silva, M. E. V., Albiero, D., Andrade, C. F., and Carneiro, F. O. M., 2018. The Effects of Blade Pitch Angle on the Performance of Small-Scale Wind Turbine in Urban Environments. Energy, 148, pp. 169-178.

Roser, M., Ritchie, H., Ortiz-Ospina, 2019. World Population Growth. https://ourworldindata.org/world-population-growth. 2019

Sadorsky, P., 2021. Wind Energy for Sustainable Development: Driving Factors and Future Outlook. Journal of Cleaner Production, 289, p. 125779.
Schlichting, H., 2014. Boundary-Layer Theory. McGraw Hill Education, 7th Edition, 15 January, ISBN-10: 9332902828.
Schwanitz, V.J., and Wierling, A., 2016. Offshore wind Investments-Realism about cost developments is necessary. Energy, 106, pp. 170–181.
Schubel, P. J., and Crossley, R. J., 2012. Wind Turbine Blade Design Review. Wind Engineering, 36(4), pp. 365-388.
Sedaghatizadeh, N., Arjomandi, M., Kelso, R., Cazzolato, B., and Ghayesh, M. H., 2019. The Effect of the Boundary Layer on the Wake of a Horizontal Axis Wind Turbine. Energy, 182, pp. 1202-1221.
Selig, M. S., and McGranahan, B. D., 2004. Wind Tunnel Aerodynamic Tests of Six Airfoils for Use on Small Wind Turbines. ASME Journal of Solar Energy Engineering, 126(4), pp. 986-1001.
Shakoor, R., Hassan, M. Y., Raheem, A., and Rasheed, N., 2016. Wind farm layout optimization using area dimensions and definite point selection techniques. Renewable Energy, 88, pp. 154-163.
Sheldahi, R. E., and Klimas, P. C., 1981. Aerodynamic Characteristics of Seven Symmetrical Airfoil Sections Through 180-Degree Angle of Attack for use in Aerodynamic Analysis of Vertical Axis Wind Turbines. SAND80-2114, March 1981.
Shen, X., Yang, H., Chen, J., Zhu, X., and Du, Z., 2016. Aerodynamic Shape Optimization of Non-Straight Small Wind Turbine Blades. Energy Conversion Management, 119, pp. 266–278.
Siddall, R. G., and Davies, T. W., 1972. An Improved Response Equation for Hot-Wire Anemometry," Internal Journal of Heat Mass Transfer, 15, pp. 367-368.
Singh, R. K., Ahmed, M. R., Zullah, M. A., and Lee, Y-H., 2012. Design of a Low Reynolds Number Airfoil for Small Horizontal Axis Wind Turbines. Renewable Energy, 42, pp. 66–76.
Singh, R. K., and Ahmed, M. R., 2013. Blade Design and Performance Testing of a Small Wind Turbine Rotor for Low Wind Speed Applications. Renewable Energy, 50, pp. 812–9.
Simpson, R. L., Heizer, K. W., and Nasburg, R. E., 1979. Performance characteristics of a simple linearized hot-wire anemometer. ASME Journal of Fluids Engineering, 101(3), pp. 381-382.
Snel, H., Schepers, J. G., and Montgomerie, B., 2009. MEXICO project: The database and results of data processing and interpretation. AIAA 2009-1217.
Song, Q., and Luitz, W. D., 2014. Design and Testing of a New Small Wind Turbine Blade. ASME Journal of Solar Energy Engineering, 136(3), p. 034502.
Souaissa, K., Ghiss, M., Chrigui, M., Bentaher, H., and Maalej, A., 2019. A comprehensive analysis of aerodynamic flow around H-Darrieus rotor with camber-bladed profile. Wind Engineering, 43(5), pp. 459-475.
Sørensen, N. N., Bechmann, A., Réthoré, P-E., and Zahle, F., 2014. Near wake Reynolds-averaged Navier–Stokes predictions of the wake behind the MEXICO rotor in axial and yawed flow conditions. Wind Energy, 17(1), pp. 75-86.
Stainback, P. C, and Nagabushana, K. A., 1997. Review of Hot-Wire Anemometry in Transonic and Subsonic Slip Flows. ASME Journal of Fluids Engineering, 119(1), pp. 14-18.
Steven, R. J. A. M., and Meneveau, C., 2017. Flow Structure and Turbulence in Wind Farms. Annual Review of Fluid Mechanics, 49: pp. 311-339.
Sun, S., Luo, D., Huang, D., and Wu, G., 2012. Numerical Study on Coupling Effects Among Multiple Savonius Turbines. Journal of Renewable and Sustainable Energy, 4, p. 053107.
Sun, H., and Yang, H., 2020. Numerical investigation of the average wind speed of a single wind turbine and development of a novel three-dimensional multiple wind turbine wake model. Renewable Energy 147, pp. 192–203.
Talavera, M., and Shu, F., 2017. Experimental study of turbulence intensity influence on wind turbine performance and wake recovery in a low-speed wind tunnel. Renewable Energy, 109, pp. 363-371.
Tangler, W., and Rooij, R. V., 2003. Summary of the Delft University Wind Turbine Dedicated Airfoils," ASME Journal of Solar Energy Engineering, 125(4), pp. 488–96.

Tasneem, Z., Noman, A. A., Das, S. K., Saha, D. K., Islam, M. R., et al., 2020. An analytical review on the evaluation of wind resource and wind turbine for urban application: Prospect and Challenges. Developments in the Built Environment, 4, p. 100033.

Tian, L., Zhu, W., Shen, W., Song, Y., and Zhao, N., 2017. Prediction of multi-wake problems using an improved Jensen wake model. Renewable Energy, 102, p. 457-469.

Tieleman, H., 1992. Wind Characteristics in the Surface Layer Over Heterogeneous Terrain. Journal of Wind Engineering and Industrial Aerodynamics, 41(1–3), pp. 329–40.

Treuren, K. W. V., 2015. Small-Scale Wind Turbine Testing in Wind Tunnels Under Low Reynolds Number Conditions. ASME Journal of Energy Resources Technology, 137(5), p. 051208.

Tummala, A., Velamati, R. K., Sinha, D. K., Indraja, V., and Krishna, V. H., 2016. A Review on Small Scale Wind Turbines. Renewable Sustainable Energy Reviews, 56, pp. 1351–1371.

Yavuzkurt, S., 1984. A Guide to Uncertainty Analysis of Hot-Wire Data. ASME Journal of Fluids Engineering, 106, pp. 181-186.

Yoon, J.-H., and Lee, S.-J., 2004. Stereoscopic PIV measurements of flow behind an isolated low-speed axial-fan. Experimental Thermal and Fluid Science, 28, pp. 791–802.

Uemura, Y., Tanabe, Y., Mamori, H., Fukushima, N., and Yamamoto, M., 2017. Wake Deflection in Long Distance from a Yawed Wind Turbine. ASME Journal of Energy Resource Technology, 139(5), p. 051212.

Vardar, A., and Alibas, I., 2008. Research on Wind Turbine Rotor Models using NACA Profiles. Renewable Energy, 33, pp. 1721-1732.

Venters, R., and Helenbrook, B. T., 2016. Ducted Wind Turbine Optimization. 34th AIAA Applied Aerodynamic Conference, 13-17 June 2016, Washington, USA.

Vermeer, L. J., Sørensen, J. N., and Crespo, A., 2003. Wind Turbine Wake Aerodynamics. Progress in Aerospace Sciences, 39(6-7), pp. 467-510.

Vermeulen, P. E. J., 1980. An experimental analysis of wind turbine wakes. Proc. 3rd International Symposium on Wind Energy Systems, Lyngby- Denmark, 26-29 August 1980, pp. 431-450.

Wang, C., and Prinn, R. G., 2010. Potential Climatic Impacts and Reliability of Very Large-Scale Wind Farms. Atmospheric Chemistry and Physics, 10(4), pp. 2053–61.

Werle, M. J., 2010. Wind Turbine Wall-Blockage Performance Corrections. AIAA Journal of Propulsion and Power, 26(6), pp. 1317-1321.

Winslow, J., Otsuka, H., Govindarajan, B., et al., 2018. Basic understanding of airfoil characteristics at low Reynolds numbers (10^4–10^5). Journal of Aircraft, 55(3), pp. 1050–1061

Whale, C. G., Anderson, R., and Bareiss, S., 2000. Wagner. An experimental and numerical study of the vortex structure in the wake of a wind turbine. Journal of Wind Engineering and Industrial Aerodynamics, 84(1), pp. 1-21.

Wu, B., Song, M., Chen, K., He, Z., and Zhang, X., 2014. Wind power prediction system for wind farm based on auto regressive statistical model and physical model. Journal of Renewable and Sustainable Energy, 6(1), p. 013101.

Xisto, C. M., Páscoa, J. C., and Trancossi, M., 2016. Geometrical Parameters Influencing the Aerodynamic Efficiency of a Small-Scale Self-Pitch High-Solidity VAWT. ASME Journal of Solar Energy Engineering, 138(3), p. 031006.

Zhang, W., Corey, Markfort, D., and Porte´-Agel, F., 2012. Near-wake flow structure downwind of a wind turbine in a turbulent boundary layer. Experiment in Fluids, 52, pp. 1219–1235.

Zhao, Z., Su, D., Wang, T., Xu, B., Wu, H., and Zheng, Y., 2019. A Blade Pitching Approach for Vertical-axis Wind Turbines Based on the Free Vortex Method. Journal of Renewable and Sustainable Energy, 11, p. 053301.

Zhong, W., Shen, W. Z., Wang T, et al. 2020. A tip loss correction model for wind turbine aerodynamic performance prediction. Renewable Energy, 147(1), pp. 223–238.

APPENDIX-A

CALIBRATION OF CONSTANT TEMPERATURE HOT-WIRE ANEMOMETRY

A.1 Methodology of Noise Reduction

The Pitot-static pressure or dynamic pressure is expressed as

$$\Rightarrow \qquad P_d = P_o - P_s = \frac{1}{2}\rho U^2 \tag{A1}$$

The simplified King's law defining the relation between the voltage response of HWA with respect to change in inflow velocity is expressed as

$$\Rightarrow \qquad E^2 = A + BU^n \tag{A2}$$

The sensitivity (S) of the HWA probe is obtained by differentiating Eq. (A2) with respect to *U*, considering velocity index factor as 0.5.

$$\Rightarrow \qquad S = \frac{dE}{dU} = \frac{B}{4E\sqrt{U}} \tag{A3}$$

The HWA voltage and velocity signal can be discretized as

$$\Rightarrow \qquad E(t) = \bar{E} + e; \text{ and } U(t) = \bar{U} + u \tag{A4}$$

The turbulence intensity (TI) can be express as

$$\Rightarrow \qquad TI = \frac{\sigma}{U} = \frac{u_{rms}}{U} \tag{A5}$$

$$\text{where, } \sigma = u_{rms} = \left(\overline{u^2}\right)^{0.5} = \left[\frac{1}{T}\int_0^T u^2 dt\right]^{0.5} \tag{A6}$$

$$\Rightarrow \qquad TI = \frac{\sigma}{U} = \frac{\left[\frac{1}{T}\int_0^T u^2 dt\right]^{0.5}}{U} = \frac{\sqrt{\overline{u^2}}}{U} \times 100\ \% \tag{A7}$$

The King's power law can be further extended by incorporating Eq. (A4) in Eq. (A2), considering velocity index factor as 0.5.

$$\Rightarrow \qquad \left(\bar{E} + e\right)^2 = A + B\sqrt{\left(\bar{U} + u\right)} \tag{A11}$$

$$\Rightarrow \qquad \overline{E^2} + e^2 + 2e\bar{E} = A + B\sqrt{\bar{U}}\left(1 + \frac{u}{\bar{U}}\right)^{1/2} \tag{A12}$$

Expressing, $\left(1 + \frac{u}{\bar{U}}\right)^{1/2}$ in terms of Binomial expression as; $(x+y)^n = \sum_{k=0}^{n} \binom{n}{k} x^{n-k} y^k$

$$\Rightarrow \qquad \overline{E^2} + 2e\bar{E} = A + B\sqrt{\bar{U}}\left(1 + \frac{1}{2}\frac{u}{\bar{U}} + \frac{u^2}{\overline{U^2}} + \ldots\right) \tag{A13}$$

Or, $\overline{E^2} + 2e\bar{E} = A + B\sqrt{\bar{U}} + \frac{Bu}{2\sqrt{\bar{U}}}$; Neglecting higher terms

$$\Rightarrow \qquad 2e\bar{E} = \frac{Bu}{2\sqrt{\bar{U}}} \tag{A14}$$

$$\Rightarrow \qquad e = \frac{Bu}{4\bar{E}\sqrt{\bar{U}}} = Su; \quad \text{(From Eq. A3)} \tag{A15}$$

The measured fluctuating voltage (e_{meas}) can be expressed in terms of gain factor (G) as

$$\Rightarrow \quad e_{meas} = e.G \text{ ; where G is product of AC and DC gain.} \tag{A16}$$

$$\Rightarrow \quad e = \frac{e_{meas}}{G} = Su; \quad \text{(From Eq. A15)} \tag{A17}$$

Therefore, the TI from e can be obtained as per following expressions

$$\Rightarrow \quad u^2 = \left(\frac{e_{meas}}{G.S}\right)^2 \text{ Or, } \overline{u^2} = \frac{\overline{e_{meas}^2}}{(G.S)^2} \tag{A18}$$

$$\text{Or, } \sqrt{\overline{u^2}} = \frac{\sqrt{\overline{e_{meas}^2}}}{G.S} = \text{Turbulent velocity or RMS of } u.$$

$$\Rightarrow \quad TI = \frac{\sqrt{\overline{u^2}}}{U} \times 100 = \frac{\sqrt{\overline{e_{meas}^2}}}{G.S.U} \times 100 = \text{Turbulent Intensity (\%)} \tag{A19}$$

The acquired instantaneous fluctuating signal comprise of fluctuation imparted by the flow (e_s) and the noise in the signal (e_n) that can express as

$$\Rightarrow \quad e = e_n + e_s \tag{A20}$$

When $U = 0$, then $e_s = 0$, $\quad e|_{U=0} = e_n + \cancel{e_s}$ (A21)

$$\Rightarrow \quad e|_{U=0} = e_{meas} = e_n \text{ or, } e_{meas}^2|_{U=0} = e_n^2$$

$$\Rightarrow \quad \overline{e_{meas}^2}|_{U=0} = \overline{e_n^2} \tag{A22}$$

Now, when $U \neq 0$, then $e_s \neq 0$, $\quad e|_{U\neq 0} = e_n + e_s = e_{meas}$ (A23)

$$\text{Or, } \overline{e_{meas}^2} = \overline{e_n^2} + \overline{e_s^2} + \overline{2e_n.e_s}; \text{ where mean of fluctuation } (\bar{e}) = 0. \tag{A24}$$

$$\text{Using Eq. (A23), we get, } \quad \overline{e_s^2} = \overline{e_{meas}^2} - \overline{e_n^2} = \overline{e_{meas}^2}|_{U\neq 0} - \overline{e_{meas}^2}|_{U=0} \tag{A25}$$

Now, incorporating Eq. A25 with Eq. A19, the relation for TI can be expression as

$$\text{Turbulent velocity} = \sqrt{\overline{u^2}} = \frac{\sqrt{\left(\overline{e_{meas}^2}|_{U\neq 0} - \overline{e_{meas}^2}|_{U=0}\right)}}{S.G}$$

$$\Rightarrow \quad TI(\%) = \sqrt{\overline{u^2}}/U = \frac{\sqrt{\left(\overline{e_{meas}^2}|_{U\neq 0} - \overline{e_{meas}^2}|_{U=0}\right)}}{S.G.U} \times 100 \tag{A26}$$

The deviation between indirectly quantified velocity evaluated through HWA with of velocity measured through Pitot-static probe is express as

$$\%Deviation = \left(\frac{U(\zeta) - U(Pr)}{U(Pr)}\right)\% \tag{A27}$$

The methodology describe above is further refined by adding necessary analog/digital filters. For digital signal, low pass filtered has been applied to extract the low frequency signal whereas high pass signal has been applied to extract the fluctuating signal. Some of the key features to be taken into account while processing the hot-wire signal is mentioned in APPENDIX-B.

B.1 Signal Filtering Considerations

The signal acquired through CTHWA is further processed to extract the low frequency and high frequency signals. The signal processing has been carried out using the LABVIEW program, where a third order Butterworth filter has been employed. The order selected is well enough to produce higher roll-off rates between stopband and passband, also ensures that required attenuation of the cut-off is achieved. To extract the dominating low frequency signal, a low pass (LP) filter is applied whereas to extract the fluctuating velocity, a high pass (HP) is applied. In most of cases, the values of sampling frequency (f_s) and cut-off (f_c) will differ as per the flow structure or the type of HWA unit opted. So, a more general parameter has to be considered. The relation between f_s and f_c has been expressed in the dimensionless parameter defined by Eq. (B1). It has to be ensured that the value follows the Nyquist filtering criterion, as $0 < \zeta < 0.5$. This post-processing operation can also be applied to instantaneous velocity *U(t)*, which is evaluated from *E(t)* through the simplification of Eq. (B2), as per Eq. (B1) considering velocity index factor as 0.5. Figure B1 through Figure B4, shows the signal response at different cut-off condition. Such assessment prior to processing is essential to limit the cut-off frequency and its effect on the signal response.

$$\zeta = f_c / f_s \tag{B1}$$

$$U(t) = \left(\frac{\{E(t)\}^2 - A}{B} \right)^2 \tag{B2}$$

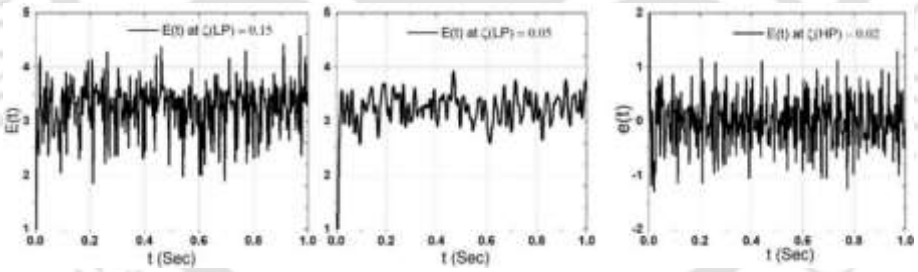

Fig. B1: Sample test signals processed with LP and HP filters

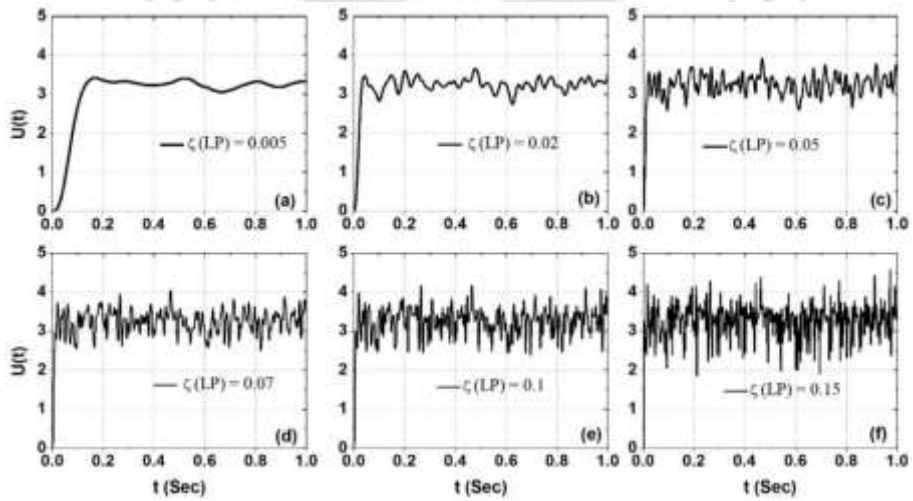

Fig. B2: Visual depiction of fluctuation response at different LP cut-off frequency

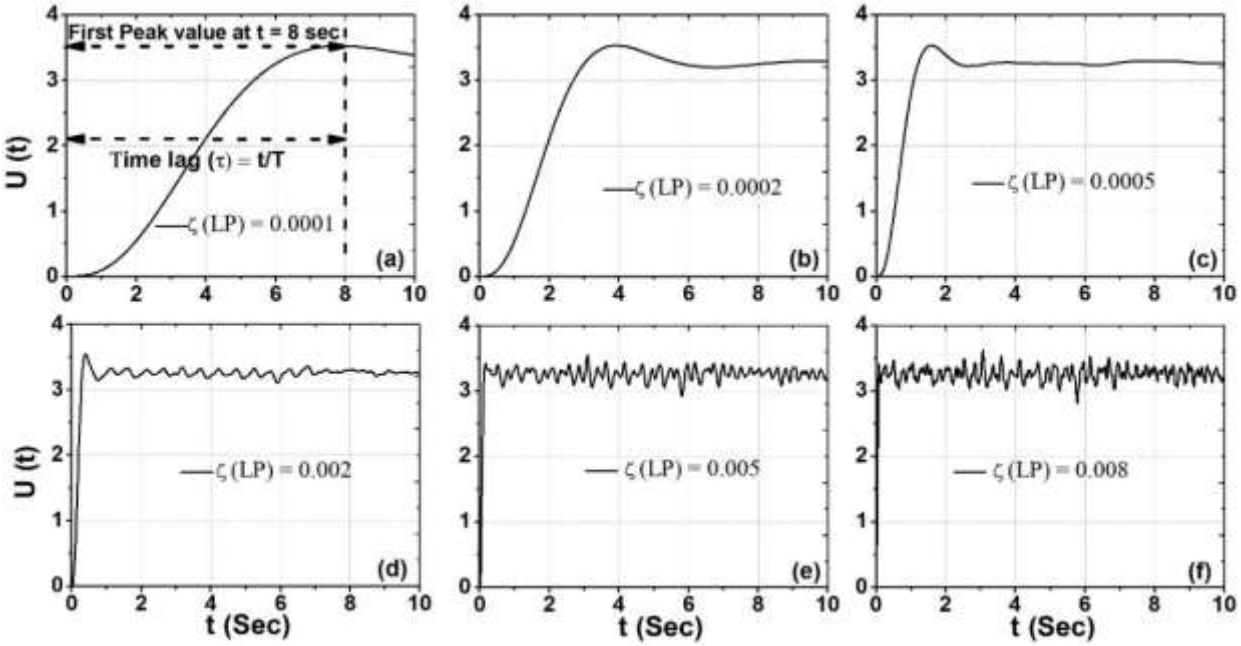

Fig. B3: Time lag response behaviour at very low LP filter cut-off frequency

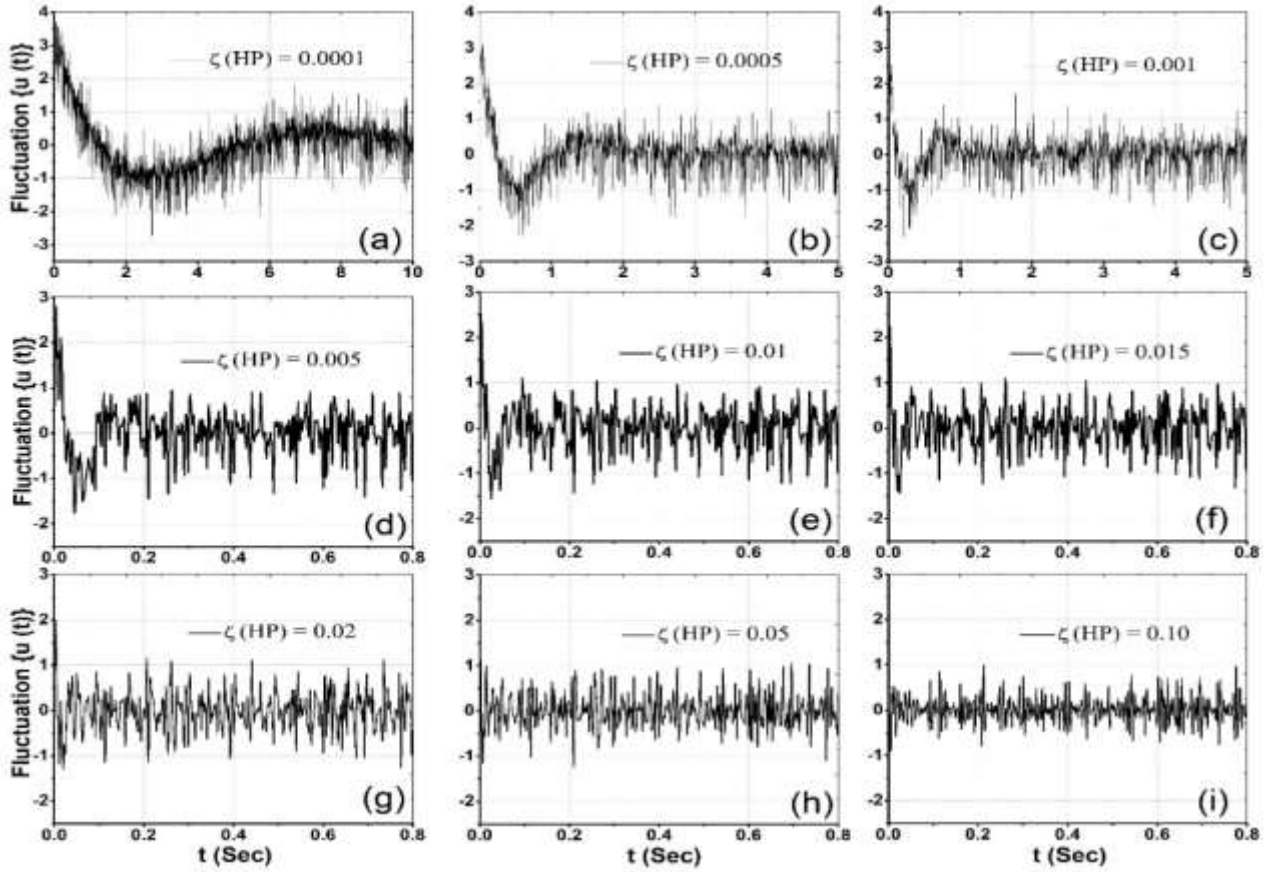

Fig. B4: Time lag response behaviour at very low HP filter cut-off frequency

A SHAWT blades designed using the BEMT has been fabricated using the fuse deposition modeling (FDM) 3D printer. Simultaneously, the hub and other coupling components were fabricated using the same printer. The dimensional configuration and pictorial depiction of components are shown in following figures.

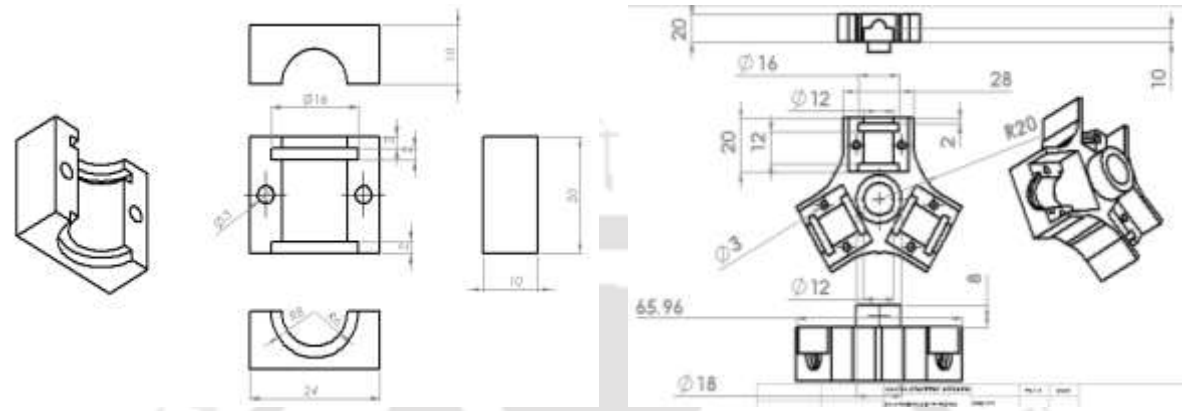

Fig. C1. (a) Blade outer casing, and (b) back side view Hub casing

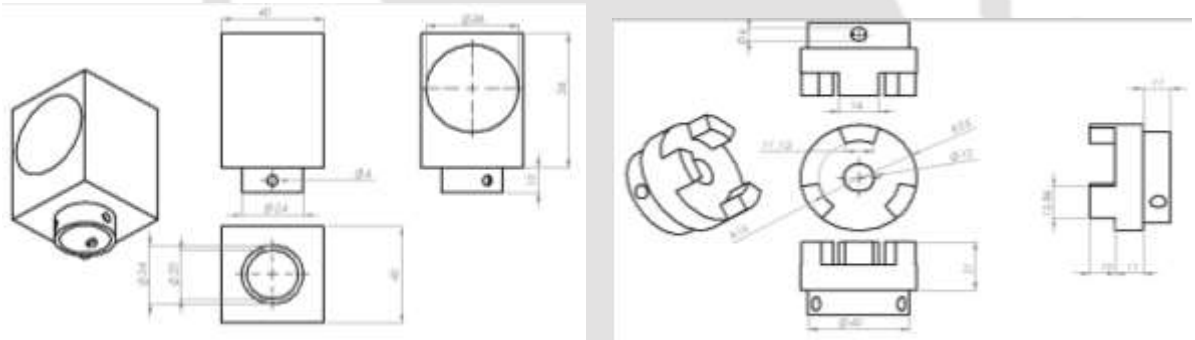

Fig. C2. (a) Nacelle casing, and (b) Custom made coupling

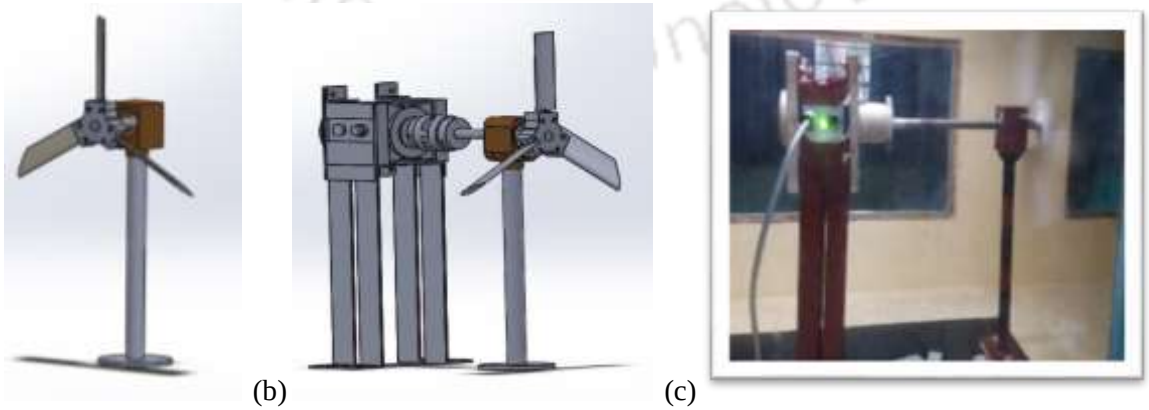

(a) (b) (c)

Fig. C3. CAD Illustration of (a) Model rotor, (b) Rotor with RTS, and (c) Prototype model with RTS

APPENDIX-D

MEASUREMENT DEVICES SPECIFICATIONS

Following are some of the instruments with their specifications used in the investigation.

1. Wind Tunnel
   - Type: Open Circuit Wind Tunnel
   - Test Section Size: 600 mm x 600 mm x 2000 mm, with max. wind speed of 50 m/s
   - Fan (Axial Flow): Diameter- 1.3 m; Max. rpm: 1450; No. of Blades: 12; Hub Dia.: 500 mm
   - Contraction ratio: 9:1; Contraction length: 1.8 m
   - Settling Chamber Size: 1800 mm x 1800 mm
   - Entry section: Bell Mouthed Entry.
   - Honey Comb Size: 25 mm x 25 mm x 200 mm
   - Screens: Two screens with 8 mesh and 16 mesh stainless steel.
   - Power: 22 kW AC motor (3-phase input), with variable speed control panel.

2. Stepper Motor Controller Multi-Axis Traverse (3D Traverse System)
   - Model: 3D.TRA.003.600.2A. YZ
   - Three-axis: X, Y, and Z-axis; Max. displacement: 600 mm
   - Linear movement block for rigidity and ball-screw for manual as well as stepper motor-controlled movement of the LM block.
   - Diameter of screw: 5 mm; Pitch of the screw: 15 mm
   - 100 divisions circular disc fixed to the shaft. This gives a movement of 0.05 mm/division.
   - CAN BUS connector to stepper motor controller.
   - Power supply: 12 V DC, 3 Amps; Transfer: RS232 link for PC communication.

3. Rotary Torque Sensor (RTS)
   - Model: RWT410/420 Series Transducer (RWT421-DE-KG)
   - Range (full scale): 20 Nm, and 20000 rpm
   - Maximum deflection: 0.5 degree (@rated torque)
   - Mode of operation: Surface Acoustic Wave
     (Upon deflection of shaft, the two SAW devices sense the change and thereby, results in change in resonant frequency. This change is further processed to provide a torque reading)
   - Output: Analog and Digital lead
   - Online/PC Monitoring: TOURQVIEW Software
   - Analog/Digital connector: 15 ways 'D' type connector to 12 pin Lumberg.
   - Transducer Signal Breakout Unit (SBU): Communication with PC via USB and RS232 ports.
   - Accuracy and resolution: 0.25% and 0.02%, respectively.
   - Power supply: 12-32 V DC, minimum 1 Amps current.

4. Electronic Manometer
   - Model: EM0901
   - Range of Pressure Transducer: 0 to 210 mm (mm of H_2O)
   - Zero Adjustment: 11 mV to 13 mV
   - Maximum Sampling rate: 100 sample/sec; Max. sample duration: 99 sec
   - Power Input: 230 V AC; Requirement: 12 V DC; Transfer: USB and RS232 Link

3. Particle Image Velocimetry (PIV) System
   - **Laser**
     - Model: Litron LD-527
     - Power Supply Unit (PSU): 220-250 V, 21 Amps, 50/60 Hz
     - Mode of pulse generation: CW-pumped Q-switched
     - Original/source Wavelength: 1053 nm (Infrared laser light); Max. power output: 150 W
     - Wavelength Converter/Harmonic Generator: Intra-cavity Harmonic Generation Assembly
     - Output Wavelength: 527 nm (Green)
     - Double pulse with inter-pulse separating time of less than 10 nanoseconds.
     - Laser medium: Neodymium: Yttrium Lithium Fluoride (Nd: YLF)
     - Cooling Equipment: Litron DPSS (Diode Pumped Solid State); Input: 220-250 V AC, 32 Amps; Thermal Load to Air/Ambient: ~1500 W; Operating Temp.: 23 - 30ºC
   - Camera
     - Model: Phantom 640 L
   - Seeding Particle: Di-ethyl Hexyl (Size: 1.0 micrometers)

APPENDIX-E
EXPERIMENTAL UNCERTAINITIES

The experimental output often carries some level of errors and these errors could be instrumental, human, approximation, and some other physical errors. Hence, it is needed to obtain the uncertainty involved in the ultimate parametric or numeric output. The uncertainty in the calculation can be evaluated by the relation propounded by Moffat and Kline. Finding the uncertainties help in mitigating the errors over the expected performance of the rotor throughout the operation and over the period of time. Assuming Y be the dependent parameter which is a function of various independent variables such as x_1, x_2, x_2…, x_n, it can be expressed as.

$$Y = Y(x_1, x_2, x_3, ..., x_n) \tag{E1}$$

If ΔY is the overall uncertainty created by uncertainties of all the independent variables such as ΔY_1, ΔY_2, ΔY_3..., ΔY_n, then the uncertainty involved with the dependent variable (Y) in percentage can be expressed by Eq. (E2).

$$\frac{\Delta Y}{Y} = \frac{1}{Y}\left[\left(\frac{\delta Y}{\delta x_1}\Delta Y_1\right)^2 + \left(\frac{\delta Y}{\delta x_2}\Delta Y_1\right)^2 + \left(\frac{\delta Y}{\delta x_3}\Delta Y_1\right)^2 + ...+ \left(\frac{\delta Y}{\delta x_n}\Delta Y_n\right)^2\right]^{0.5} \textit{(In \%)} \tag{E2}$$

Subsequently, the uncertainties involved with other dependent parameters can be calculated with similar approach. For example, the uncertainties in τ (torque), N (rpm), and U (velocity) are found to be about 1.0%, 1.2%, and 1.0% respectively. Further, using Eqs. (E3) through (E6), the uncertainty in the measured C_p is found to be about 3.4%.

$$C_p = \frac{P_{output}}{0.5\rho_{air}\pi R^2 U^3} = \frac{2\pi N\tau/60}{0.5\rho_{air}\pi R^2 U^3} = \frac{\tau N}{KU^3} \tag{E3}$$

where

$$\mathrm{K} = \frac{2\pi}{0.5\rho_{air}\pi(0.12)^2 60} = 3.78$$

$$\frac{\Delta C_p}{C_p} = \frac{1}{C_p}\left[\left(\frac{\delta C_p}{\delta\tau}\Delta\tau\right)^2 + \left(\frac{\delta C_p}{\delta N}\Delta N\right)^2 + \left(\frac{\delta C_p}{\delta U}\Delta U\right)^2\right]^{0.5} (\%) \tag{E4}$$

$$\frac{\delta C_p}{\delta\tau}\Delta\tau / C_p = \left(\frac{\Delta\tau}{\tau}\right); \quad \frac{\delta C_p}{\delta N}\Delta N / C_p = \left(\frac{\Delta N}{N}\right) \textit{ and } \frac{\delta C_p}{\delta U}\Delta U / C_p = \left(-3\frac{\Delta U}{U}\right) \tag{E5}$$

$$\therefore \frac{\Delta C_p}{C_p} = \left[(0.01)^2 + (0.012)^2 + 9(0.01)^2\right]^{0.5} \% = 3.4\% \tag{E6}$$

1. Wind Tunnel Calibration Data

Tunnel RPM	***Avg. U* (m/s)**	***SD* in *U* *(m/s)***	**Avg. *E* (Volt)**	***SD* in E (Volt)**	$\sqrt{U}$	E^2
127	3.370	0.033	1.539113	0.778995	1.835756	2.371281
155	4.353	0.030	1.586337	0.598655	2.086384	2.518223
185	5.390	0.025	1.631455	0.643923	2.321637	2.663728
215	6.398	0.027	1.672051	0.600591	2.529427	2.797812
243	7.427	0.020	1.710291	0.605447	2.725344	2.927215
269	8.330	0.021	1.739318	0.566595	2.886174	3.027208
298	9.350	0.018	1.769727	0.484054	3.057777	3.133784
328	10.40	0.018	1.798519	0.501697	3.224903	3.236673
350	11.130	0.020	1.816773	0.484763	3.336165	3.302662
400	12.870	0.017	1.858639	0.465361	3.587478	3.456519
430	13.875	0.016	1.882509	0.409672	3.724916	3.545671
470	15.250	0.015	1.912029	0.490595	3.905125	3.657868
500	16.270	0.016	1.931861	0.505988	4.033609	3.734143
530	17.340	0.018	1.952618	0.536309	4.164133	3.814906
570	18.730	0.015	1.977866	0.407612	4.327817	3.913822
600	19.810	0.017	1.99659	0.398117	4.450843	3.988246
630	20.860	0.017	2.015345	0.448766	4.567275	4.063626
670	22.640	0.016	2.036685	0.457530	4.758151	4.150152
700	23.730	0.016	2.052858	0.356409	4.871345	4.215955

#The data present is a sample of calibration value since there were several experiments, and during each experiment, the wind tunnel calibration was performed. Thus, presenting all the calibrated data is not possible, though the author will be happy to share any specific data on request.

LIST OF PUBLICATIONS

PUBLICATIONS – JOURNALS

- **Siram, O.,** Sahoo, N., and Saha, U. K., 2022, "Wind Tunnel Tests of a Model Small-Scale Horizontal-Axis Wind Turbine Developed from Blade Element Momentum Theory," ASME Journal of Energy Resources Technology, 144(6), p. 064502.
- **Siram, O.,** Kesharwani, N., Sahoo, N., and Saha, U. K., 2022, "Aerodynamic Design and Wind Tunnel Tests of Small-scale Horizontal-axis Wind Turbines for Low Tip Speed Ratio Applications," ASME Journal of Solar Energy Engineering, 144(4), p. 041009.
- **Siram, O.,** Kumar, R., Saha, U. K., and Sahoo, N., 2022, "Wind Tunnel Probe into an Array of Small-scale Horizontal-axis Wind Turbines Operating at Low Tip Speed Ratio Conditions," ASME Journal of Energy Resources Technology, 144(9), p. 091303.
- **Siram. O.,** and Sahoo N., 2022, "Performance Assessment of Straight and Linearly Tapered Rotors Through Wind Tunnel Investigation for Off-Grid Applications," Wind Engineering, 46(4), pp. 1291-1310.
- **Siram, O.,** Kumar, R., Saha, U. K., and Sahoo, N., 2022, "A Comprehensive Review on Analytical Formulations of Wind Turbine Wake Models and Future Scope in the Development of Wind Farms of Assorted Configurations." ASME Journal of Energy Resources Technology, 144(11), p. 110801.
- **Siram, O.,** Sahoo, N., and Saha, U. K., 2022, "Changing Landscape of India's Renewable Energy and the Contribution of Wind Energy," Cleaner Engineering and Technology, 8, p. 100506.
- **Siram, O.,** Saha, U. K., and Sahoo, N., 2022, "Blade Design Consideration of Small Wind Turbines: From Classical to Bio-inspired Shapes/Profiles," AIP Journal of Renewable and Sustainable Energy, 14, p. 042701.
- **Siram, O.,** Barhate, S. C., and Sahoo, N., 2022, "Modelling and Estimation of Horizontal-Axis Wind Turbine Wake Through Data-Driven Approach," Submitted in AIP Journal of Renewable and Sustainable Energy.

PUBLICATIONS – CONFERENCES

- **Siram, O.,** and Sahoo, N., 2019, "Near Wake Regime Study on Wind Turbine Blade Tip Vortex," Paper No: GTINDIA2019-2493, ASME 2019 Gas Turbine India Conference. Dec. 5–6, IIT Madras.
- **Siram, O.,** and Sahoo, N., 2021, "Characterizing the Helical Vortex Frequency of HAWT," In: Bose M., Modi A. (eds) Proceedings of the 7th International Conference

on Advances in Energy Research. Springer Proceedings in Energy. Springer, Singapore.

- **Siram, O.,** and Sahoo, N., 2019, "Experimental Study on Horizontal Axis Wind Turbine Wakes for Wind Farm Modelling," Proceedings of the 25th National and 3rd International ISHMT-ASTFE Heat and Mass Transfer Conference (IHMTC-2019), December 28-31, 2019, IIT Roorkee, India, IHMTC2019-ENE-741.
- **Siram, O.,** and Sahoo, N., 2019, "Vortex Stability Analysis of Horizontal Axis Wind Turbine Wake," The Institution of Engineers (India), All India Seminar on Scope and Opportunity of Small Hydro & Wind Power in NER of India- Mizoram, 02-03 August 2019.
- Kumar, R., **Siram, O.,** Sahoo, N., and Saha, U. K., 2021, "Characterizing the Transitional Behaviour of Wind Turbine Wake from Near to Far Wake Regimes," Paper no. POWER2021-65959, ASME 2021 Power Conference (Virtual), July 20–22.
- **Siram O.,** and Sahoo, N., 2022, "A statistical approach to determine and discretize the turbulent flow signature acquired using hot-wire anemometry," Indo-German International Conference on Metrology for the Deployment of Green Hydrogen and Renewable Fuels in India, 4^{th} – 6^{th} April, 2022.
- **Siram, O.,** Barhate, S. C., and Sahoo, N., 2022, "Spiral Polar Plot Analogy to Dictate the Two-Dimensional Depiction of Helical Vortex Lines (HLVs)," 67^{th} Congress of the Indian Society of Theoretical and Applied Mechanics (ISTAM), Paper ID: PA0242, December 14-16, IIT Mandi, India.
- Barhate, S. C., **Siram, O.,** and Sahoo, N., 2022, "Wake Modelling of Horizontal-axis Wind Turbine Using Sparse Identification of Non-Linear Dynamics (SINDy)," 67^{th} Congress of the Indian Society of Theoretical and Applied Mechanics (ISTAM), Paper ID: PA0220, December 14-16, IIT Mandi, India.

AWARDS

- **Ojing Siram** and Niranjan Sahoo. Characterizing the helical vortex frequency of HAWT. Best Paper award at 7^{th} International Conference on Advances in Energy Research (ICAER), December 10-12, 2019, IIT Bombay, Mumbai, India.
- **Ojing Siram**, Abhinay Rawat and Niranjan Sahoo. Wind Farm Modeling for Horizontal Axis Wind Turbine. Best oral presentation in Research Conclave 17th March 2019, IITG.
- **Ojing Siram** and Anand Verma. Experimental Characterization of Subsonic Wind Tunnel. Best poster presentation in Research Conclave 16th March 2019, IITG.